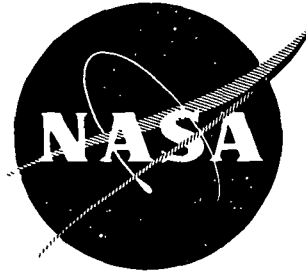*HTS   64480*

N 7 3   2 2 7 2 7

NASA CR-121095
AiResearch 72-8421

HIGH-TIP-SPEED, LOW-LOADING TRANSONIC FAN STAGE
(PART 1-AERODYNAMIC AND MECHANICAL DESIGN)

April 1973

by L.C. Wright, N.G. Vitale, T.C. Ware, and J.R. Erwin

AIRESEARCH MANUFACTURING COMPANY,
A DIVISION OF
THE GARRETT CORPORATION
Los Angeles, California

Prepared for

NATIONAL AERONAUTICS AND SPACE ADMINISTRATION

NASA Lewis Research Center

Contract NAS 3-13498

1 Report No NASA CR-121095	2 Government Accession No	3 Recipient's Catalog No
4 Title and Subtitle HIGH-TIP-SPEED, LOW-LOADING, TRANSONIC FAN STAGE (PART I - AERODYNAMIC AND MECHANICAL DESIGN)		5 Report Date April 1973
		6 Performing Organization Code
7 Author(s) L. C. Wright, N. G. Vitale, T. C. Ware, and J. R. Erwin		8 Performing Organization Report No 72-8421
		10 Work Unit No
9 Performing Organization Name and Address AiResearch Manufacturing Company A Division of the Garrett Corporation Los Angeles, California 90509		11 Contract or Grant No NAS 3-13498
		13 Type of Report and Period Covered Contractor Report
12 Sponsoring Agency Name and Address National Aeronautics and Space Administration Washington, D.C. 20546		
		14 Sponsoring Agency Code

15 Supplementary Notes

Project Manager, E. E. Bailey, NASA-Lewis Research Center, Cleveland, Ohio 44135

16 Abstract

A high-tip-speed, low-loading transonic fan stage was designed to deliver an overall pressure ratio of 1.5 with an adiabatic efficiency of 86 percent. The design flow per unit annulus area is 42.0 lbm/s-ft^2 (205.1 kgm/s-m^2). The fan features a hub/tip ratio of 0.46, a tip diameter of 28.74 in. (0.73 m) and operates at a design tip speed of 1600 fps (488.6 m/s). For these design conditions, the rotor blade tip region operates with supersonic inlet and supersonic discharge relative velocities. A sophisticated quasi-three-dimensional characteristic section design procedure was used for the all-supersonic sections and the inlet of the midspan transonic sections. For regions where the relative outlet velocities are supersonic, the blade operates with weak oblique shocks only.

17 Key Words (Suggested by Author(s)) Transonic Fan Stage Low Loading, High Tip Speed	18 Distribution Statement Unclassified-unlimited		
19 Security Classif (of this report) Unclassified	20 Security Classif (of this page) Unclassified	21 No of Pages 182	22 Price* $3.00

Page Intentionally Left Blank

CONTENTS

CONTENTS (Continued)

CONTENTS (Continued)

LIST OF ILLUSTRATIONS

LIST OF ILLUSTRATIONS (Continued)

LIST OF ILLUSTRATIONS (Continued)

SUMMARY

A high-tip-speed, low-pressure-ratio transonic fan stage was designed. The objective of this design was the provision of a rotor design that could deliver good efficiency at low work input via elimination of strong shock losses and shock-induced separation in the high-Mach-number tip region. In the rotor blade tip region, the design incorporates near oblique shocks only, with supersonic relative outlet velocities. In order to accomplish this, a relatively sophisticated quasi-three-dimensional characteristic section design procedure was used for the all-supersonic sections and for the inlet of the midspan transonic sections.

The subsonic hub sections were designed on the basis of conventional empirical cascade data and sections of the three regions (tip, pitch, and hub) were analytically joined via a special stage-stacking program to form an aerodynamically and structurally compatible blade. Special attention was focused on inlet losses, the boundary layer growth rate, and the physical passage contraction ratio to ensure passage "starting" below the rotor design speed.

Although the rotor relative velocities were well into the supersonic range, the stator velocities were at modest, subsonic levels. Hence, the stator design is conventionally subsonic and has the primary role of turning the flow back to the axial direction.

The final fan design calculations resulted in the following values of stage design parameters.

Overall pressure ratio	1.5
Adiabatic efficiency	0.86
Equivalent total flow	148 lb/s (6.71 kgm/s)
Flow per unit annulus area	42.0 lb/s-ft^2 (205.1 kgm/s-m^2)
Equivalent tip speed	1600 ft/s (488.6 m/s)
Inlet hub-to-tip radius ratio	0.46
Tip diameter	28.74 in. (0.73 m)

It is anticipated that stages designed as described herein would permit the selection of high-bypass-ratio fan speeds which minimize the number of fan drive turbine stages without compromising fan or fan turbine efficiency. Other supplementary benefits, such as reduced hub loading and/or the ability to utilize lower radius ratios for a given stage pressure ratio, should also result.

INTRODUCTION

The recent need for power plants to propel large transport aircraft capable of long-range flights has spurred the development of very-high-bypass-ratio turbofan engines (bypass ratios between 8 and 12 or even higher are being explored). The fan component of these high-bypass-ratio engines, in general, controls the engine diameter and requires large drive-turbine work. In addition, the engine configurational constraints restrict the direct-drive turbine diameter to a fraction of that of the fan, leading to low turbine wheel speeds. Consequently, the resulting fan turbine usually consists of a large number of highly loaded stages and/or compromised turbine efficiency. Alternatively, the fan may be run up to tip speeds substantially above those for which good efficiency has been achieved for the fan pressure ratios commonly used in high-bypass-ratio engines. The ultimate compromise has usually meant acceptance of the penalties associated with a large number of fan turbine stages, compromised turbine efficiency, or compromised fan efficiency, or some combination of these. Such penalties could be reduced or conceivably eliminated by use of a fan capable of high efficiency at high rotative speeds and the low pressure ratios compatible with high bypass ratios. The purpose of the current investigation is to do precisely this, to design for, and demonstrate, good efficiency for a high-tip-speed, relatively low-total-pressure-ratio, axial-flow fan stage. A design tip speed of 1600 ft/s (488.6 m/s) and a stage total pressure ratio of 1.50 were specified for these purposes. The principles to be examined are

(1) Whether low losses and therefore good efficiency could be obtained by designing a transonic rotor for weak oblique shock waves in the high-Mach-number tip region at design-point operation (thereby avoiding normal shock losses and the potential blade suction surface and casing boundary layer separation)

(2) Whether adequate stall margin would be obtained, particularly in the presence of distorted inlet flow, with this type operation

Achievement of the objectives of this investigation would permit much improved fan and fan turbine compatibility, thereby minimizing the penalties previously mentioned. Still further, the concept could reduce substantially the problems associated with the inherent hub and tip mismatch in work potential from which all low-radius-ratio rotors (whether fan or multistage compressor inlet stage) suffer. Indeed, the advantages of being able to select the appropriate hub speed for a given multistage compressor first-stage pressure ratio without penalty to the tip region performance may be equally as important as the benefits of matching the high-bypass fan to the fan turbine. Further, the current interest in turbojets with very high flow per unit of frontal area dictates use of low-inlet-radius-ratio, high-inlet-Mach-number rotors. The ability to use the minimum structurally feasible radius ratio reduces the required inlet Mach number (and hence the required total axial diffusion) for a given specific flow. In addition, there may be the potential for reduced noise through the minimization of upstream shock strengths for the selected rotor tip speed.

The rotor used for demonstration was selected to be approximately 30 in. (0.762 m) in diameter, a size which permits accurate measurement with conventional instrumentation. The rotor blade inlet radius ratio of 0.50, aspect ratio of 2.5 to 3, and airflow per square ft of annulus area of 40 to 42 lb/s (195.3 to 205.1 kgm/s) were selected as being representative of current aircraft propulsion fan design practice.

This report outlines the design procedures and presents the aerodynamic and mechanical design results.

AERODYNAMIC DESIGN

DESIGN CONCEPTS AND OBJECTIVES

Several new rotor aerodynamic concepts influenced the design of the current rotor. A design objective was to avoid tip normal shock losses by substitution of oblique shocks in the high-Mach-number tip region. In addition, the strengths of the oblique shocks were restricted to values for which the static pressure rise would not exceed the separation criteria generally accepted for turbulent boundary layers on flat plates. The static pressure rise and the total pressure ratio values were kept below the maximum values obtainable from rotors of 1600 fps (488.6 m/s) tip speed to make them consistent with near-optimum hub potential. Lower losses and an improved stall margin were anticipated to result from this design approach. Another feature essential to this approach was the calculation of the rotor design outlet velocity diagrams that satisfied radial equilibrium with supersonic rotor-tip relative leaving velocities. In spite of the excess tip speed (for the design pressure ratio), the design value of rotor-tip static density rise was small enough so that axial velocity did not incur a significant reduction. Accordingly, the use of negative camber at the rotor tip proved to be unnecessary for the radially constant stage pressure ratio.

To terminate the necessary supersonic waves at the blade trailing edges, a characteristic procedure allowing for change in radius and stream filament thickness was used for the wholly supersonic sections. The locations of the points for expansions and compressions and their points of impingement on opposite surfaces were carefully controlled to cancel all oblique shocks inside the blade passage. The shocks were also separated to prevent the accumulating effect from causing separation. The weak shocks that began at the blade leading edges were prevented from increasing (in the high Mach number outboard region) by utilizing small leading-edge thicknesses and wedge angles. At the design condition, no tip waves emanated upstream of the cascade. An important design consideration involved the magnitude of the speed at which supersonic flow could be initiated in the tip region (i.e., the starting Mach number). The contraction ratio was prescribed to be sufficiently small to permit tip starting at a speed somewhere below design speed.

The principle design objectives were set by contract. Others were selected for convenience of procurement and testing, but were consistent with the basic objectives. The contract-specified parameters are listed below:

Overall total pressure ratio	1.5
Flow per unit annulus area	42.0 lb/s-ft^2 (205.1 kgm/s-m^2)
Equivalent tip speed	1600 ft/s (488.6 m/s)
Rotor and stator aspect ratios	3.0 (originally)
Rotor inlet hub-to-tip radius ratio	0.50 max.
Rotor tip solidity	1.4 (approx.)

4

The following parameters were specified by the designer for the final design.

Objective adiabatic efficiency	0.86
Equivalent total flow	148 lb/s (6.71 kgm/s)
Rotor inlet hub-to-tip radius ratio	0.462
Tip diameter	28.74 in. (0.73 m)

FLOW PATH AND VELOCITY DIAGRAM DETERMINATION

General Procedure

The subject fan design was initiated utilizing the procedure of the usual quasi-three-dimensional compressor design approach. That is, the flow path and the blade inlet and outlet velocity diagrams were determined under the assumption of axisymmetric, inviscid flow utilizing the AiResearch stream filament computer program. In this approach the assumed axisymmetric surfaces are represented in the radial-axial plane by streamlines (fig. 1). The radial component of the equations of motion is solved to obtain the radial variations of the flow conditions between blade rows. The mass flow is then summed or integrated along radial or near-radial lines from hub to tip using the previously calculated radially varying flow conditions. When the calculated mass flow at one axial position equals the prescribed flow rate, both continuity and radial equilibrium are satisfied at that station and the same calculation is performed at the next station. As in most such programs, after satisfaction of continuity at every compressor calculation station, a curve-fit routine is used to connect points of constant mass flow. These connecting streamlines then provide new streamline curvatures and slopes in the meridional plane which permit a repeat solution of the radial equilibrium equation with the new streamline geometry. Subsequently, a new set of streamlines is defined. The process may be continued until a compatible flow field is defined within the initial assumptions and further iteration leads to no appreciable changes in streamline curvatures. In addition, a new AiResearch axisymmetric computational procedure using a finite difference solution to the radial component of the equations of motion with interior grid points was used. In general, the agreement was good.

Both procedures permit arbitrary definition of the radial variations of enthalpy and entropy (or losses). In general, the radial variation may be specified for any two of the three quantities: pressure ratio, temperature ratio, and efficiency (or other equivalent). The bases for these specifications are empirical with due consideration being given to the objective aerodynamic operating modes.

Rotor Annulus Convergence

Because a high rotor aspect ratio (which was originally specified to be 3.0) was contractually required, the projected chord of the blade was short, leading to relatively steep inner and outer casing slopes as illustrated in fig. 1. These slopes and the accompanying concave inner- and outer-wall contours upstream of the rotor resulted in a parabolic inlet absolute velocity distribution with low inner- and outer-wall values at the rotor inlet and a high velocity near the pitch. Conversely, at the rotor exit the convex wall
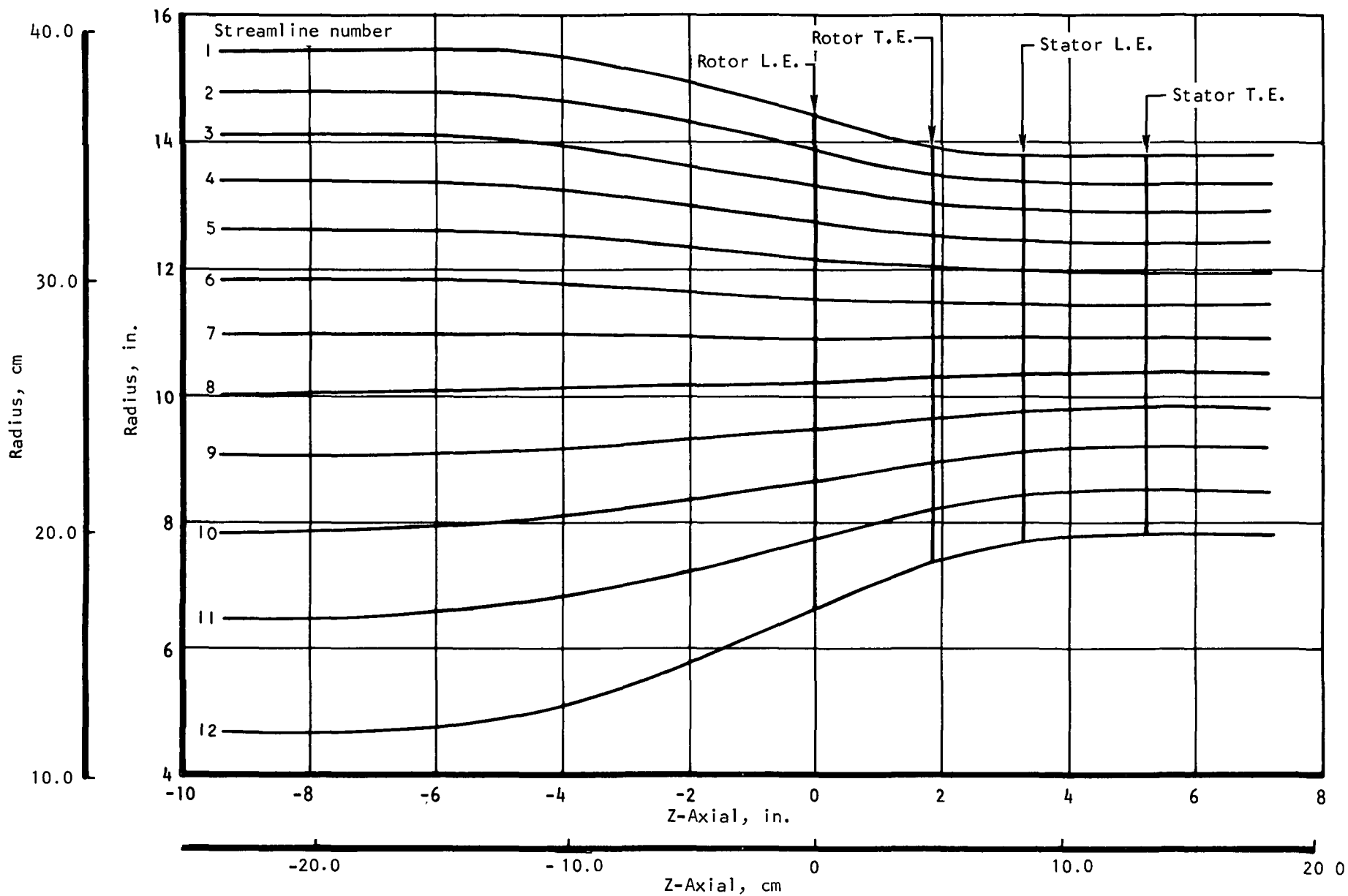
Figure 1.--Design Fan Flow Path.

S-71933

contour and the decreasing wall slopes resulted in a rotor exit meridional velocity distribution with low velocity near the pitch radius and high velocity on the walls. These meridional velocity distributions have pronounced effects (some beneficial) on the rotor configuration.

The meridional velocity ratios (V_{m2}/V_{m1}) resulting from the rotor inlet and exit distributions varied from about unity at hub and tip to approximately 0.85 in the central flow region. The low values in the central flow region were believed to be tolerable because the diffusion factors and static pressure rise coefficients were conservative and the region was not adjacent to wall boundary layers. A matter that could be of greater concern was the effect of the resulting mid-blade camber and its structural implications. Due to the modest work input (for this wheel speed) required of this rotor, the change in tangential velocity produced is relatively low. With a low value of the meridional velocity ratio V_{m2}/V_{m1} (large diffusion), the required change in tangential velocity could be accomplished at an almost constant relative flow direction with essentially uncambered blade sections. Also, since the mid-passage flow is to be transonic, thin airfoil sections are desired for low losses. It is difficult to obtain the desired mechanical stiffness for such blades. Hence, in hopes of achieving a satisfactory rotor blade mechanical design with a single part-span damper, an aspect ratio change from 3.0 to 2.5 was permitted by NASA.

A detrimental effect of the rotor meridional velocity ratios imposed by the flow path convergence results from the relocation of the maximum static pressure ratio region to the center sections instead of at the tip. Because the rotor inlet relative Mach number normally increases with radius and the allowable shock static pressure rise is proportional to the preshock Mach number (e.g., see refs. 1 and 2), the problem of shock-induced separation on the pitch sections becomes critical. The use of multiple shocks provides a theoretical solution. However, little information exists regarding the distance between shocks that is required before the boundary layer is restored to a healthy profile after the shock interaction. In spite of this uncertainty, spaced multiple shocks were incorporated in the mid-passage region for the current design to reduce each shock static pressure ratio below the value allowable for a single shock at the mid-passage Mach number.

ROTOR DESIGN REGIONS

Method of Classification

The output from the axisymmetric, radial-equilibrium program yielded three types of rotor velocity diagrams based on rotor design-point inlet and outlet Mach numbers. Each of these three velocity diagram types characterizes a blade design region requiring a different section design procedure. These are summarized below.

Section type	Inlet relative Mach number	Outlet relative Mach number	Approx flow division at design point, percent
Outboard	Supersonic	Supersonic	35
Central	Supersonic	Subsonic	45
Inboard	Subsonic	Subsonic	20

7

To define a single, structurally feasible blade composed of the three separately designed blade types listed above, new computational programs were written. The all-supersonic outboard sections can be completely designed analytically with the aid of several assumptions. The subsonic-entry, subsonic-exit hub sections can be derived from well-established empirical incidence and deviation angle rules and a selection of a meanline shape (circular arc, multiple circular arc, polynomial, etc.). The inlet region of the mid-span transonic sections can also be calculated. However, the terminal shock configuration and location must be determined by somewhat less formal methods for the conventional transonic sections. Still, the blade design program described herein did yield transonic sections that gave a smooth aerodynamic transition and a structurally satisfactory stacking between the supersonic tip and subsonic hub regions.

Theoretically, a blade section is defined as the contour generated by the intersection of the rotor blade surfaces and the appropriate axisymmetric stream surface. From the picture of the final axisymmetric stream surfaces shown in fig. 1, they may be seen to be very closely approximated by conical surfaces through the blade leading- and trailing-edge streamline intercepts. Therefore, for our purposes the blade sections referred to hereafter will be on these conical surfaces.

Since the outboard section has supersonic inlet and outlet relative velocities, an approximate method of characteristic was used. Because the principle is more easily understood for the two-dimensional problem, the application of the approximate method of characteristics is first illustrated for the two-dimensional flow field, and later generalized for the quasi-three-dimensional flow field.

In the following presentation, the equations and formulas define relationships among angles and other geometrical parameters, where the angles are correctly expressed in radians. However, illustrative calculations and diagrams present angles in degrees for easier interpretation.

Outboard Section Design Theory (2-D)

An idealized two-dimensional (2-D) section is shown in fig. 2. As shown in this figure, a simple 2-D section to meet the design conditions would have reverse camber. Let the leading- and trailing-edge shock strengths (in terms of deflection angle) be denoted by δ_1 and δ_2, respectively, as illustrated in fig. 2. Then the relation between the relative flow angle β_u upstream of the leading-edge shock and the flow angle β_2 downstream of the trailing-edge is given by the expression

$$\beta_2 = \beta_u - \delta_1 + \delta_2 \tag{1}$$

Similarly, for weak shocks the relation between the upstream and downstream Prandtl-Meyer expansion angles ν_u and ν_2 is closely represented by the expression

$$\nu_2 = \nu_u - \delta_1 - \delta_2 \tag{2}$$

8

Rotation

(1)

$\nu = 14.86$

Leading edge shock

$M = 1.6, \beta = 70 \text{ deg}$

Trailing edge shock

$1.47, 66.1$

First captured Mach line

$\delta_1 = 3.85$

(u)

$\delta_2 = 7.45$

$1.2, 73.6$

2

$\nu = 3.56, \beta = 73.60 \text{ deg}$

Mean streamline
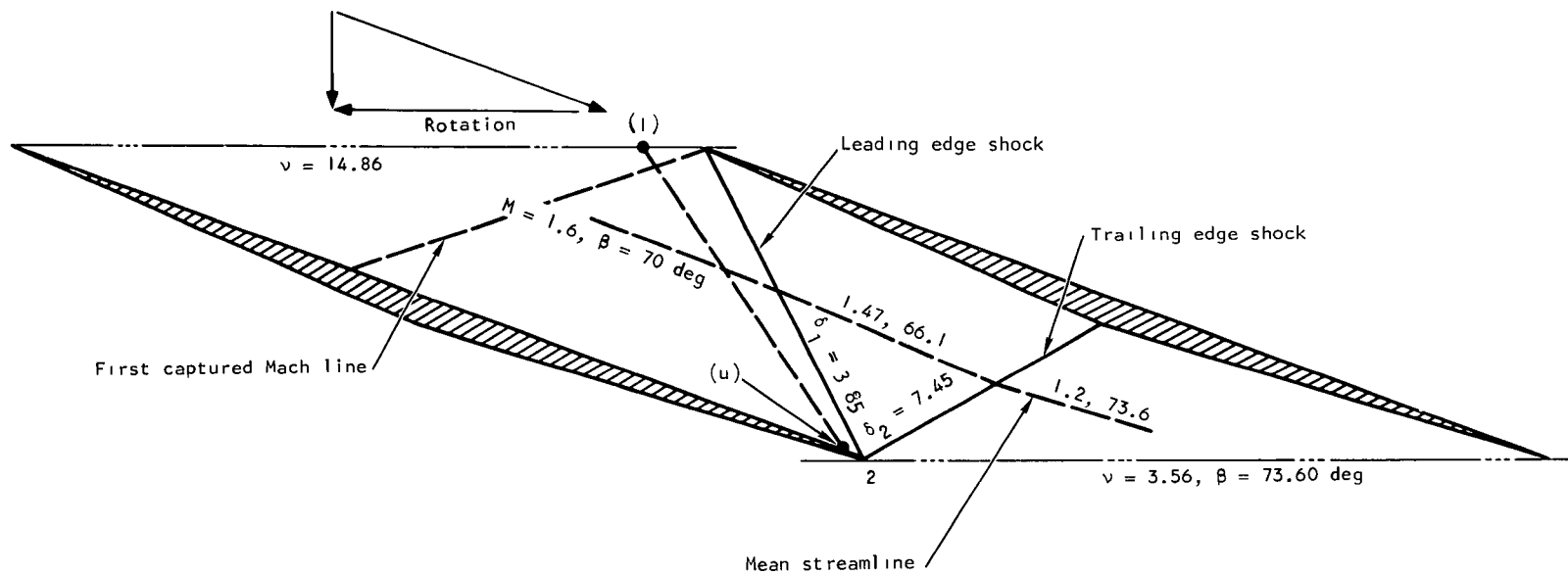
S-72475

Figure 2.--Sample Two-Dimensional Wave Pattern Illustrating Design Logic
for the Compressions Contained in Leading-and Trailing-Edge
Shocks.

The sum of eqs. (1) and (2) yields the leading edge shock strength δ_1

$$\delta_1 = \bar{\xi}_u - \bar{\xi}_2 \tag{3}$$

where

$$\bar{\xi} \equiv \frac{\nu + \beta}{2}$$

As a consequence of the fact that the leading-edge shock has a greater slope than a corresponding upstream Mach (or characteristic) line, it follows that there is some point on the inlet line of the blade (denoted as point 1 in fig. 2) whose negative characteristic line intersects the blade surface at point u. For a steady supersonic reversible adiabatic flow of a perfect gas with constant specific heats in the absence of body forces, the two-dimensional theory of characteristics states that the value of the characteristic parameter $\bar{\xi}$ remains constant along the negative characteristic, independent of the manner in which the characteristic line may weave through the flow field. Hence, it follows that

$$\bar{\xi}_u = \bar{\xi}_1 \tag{4}$$

Since the flow conditions are uniform along the inlet line of the blade, it follows that the value of $\bar{\xi}_u$ is determined by the section inlet flow condition, i.e.,

$$\bar{\xi}_u = \frac{\nu_1 + \beta_1}{2} \tag{5}$$

In an analogous manner, the value of $\bar{\xi}_2$ is determined directly from the discharge flow condition, i.e.,

$$\bar{\xi}_2 = \frac{\nu_2 + \beta_2}{2} \tag{6}$$

It now follows from eqs. (3), (5), and (6) that the leading-edge wedge angle of the simple section shown in fig. 2 is uniquely determined by the upstream and downstream flow conditions for the hypothesized blade and wave configurations. As an example, for the section shown in fig. 2, $\nu_1 = 14.86$, $\beta_1 = 70$ deg, $\nu_2 = 3.56$, and $\beta_2 = 73.6$ deg; hence, $\bar{\xi}_1 = 42.43$ deg and $\bar{\xi}_2 = 38.58$ deg; and therefore, the leading edge wedge angle is 3.85 deg from eq. (3).

Development of the trailing-edge shock-strength δ_2 begins by subtracting eq. (2) from eq. (1) at the rotor blade trailing edge:

$$\delta_2 = \xi_u^+ - \xi_2^+$$

where

$$\xi^+ \equiv \frac{\nu - \beta}{2}$$

10

The value of ξ_2^+ is determined directly from the downstream flow conditions as

$$\xi_2^+ = \frac{\nu_2 - \beta_2}{2} \qquad (8)$$

The value of ξ_u^+ can be determined from the value of ξ_u^- and the blade surface angle at point u as

$$\xi_u^+ = \xi_u^- - \beta_u$$

or from eq. (4),

$$\xi_u^+ = \xi_1^- - \beta_u \qquad (9)$$

Hence, it follows from eqs. (7), (8), and (9) that for the configurations assumed above, the trailing-edge shock strength is determined by the inlet and discharge flow conditions and by the blade surface angle just upstream of the leading-edge shock.

For the section shown in fig. 2, $\xi_2^+ = -35.02$ deg, $\xi_1^- = 42.43$ deg, and $\beta_u = \beta_1 = 70$ deg, hence, $\delta_2 = 7.45$ deg.

Trailing-edge shock strength effect.--Although the leading-edge shock strength is uniquely determined by the inlet and discharge flow conditions, some degree of freedom is available to the designer relative to the choice of trailing-edge shock strength. The effect of the trailing-edge shock strength on the section aerodynamic and mechanical properties is discussed below.

As a consequence of eqs. (7), (8), and (9), it follows that

$$\delta_2 + (\beta_u - \beta_1) = \frac{\nu_1 - \nu_2}{2} + \frac{\beta_2 - \beta_1}{2} \qquad (10)$$

The left hand side of eq. (10) represents the total suction surface compression from the first captured Mach wave to the blade trailing edge. Since the right-hand side of eq. (10) is determined by the inlet and discharge flow conditions, it follows that the total net suction surface compression is fixed.

The wave pattern for the nominal trailing-edge shock strength, defined as the shock strength corresponding to $\beta_1 = \beta_u$ (no suction surface compression or expansion forward of the final shock), is illustrated in fig. 2. For this case, the net required turning is simply the difference between the trailing-edge and leading-edge shock strengths. For trailing-edge shock strengths below nominal,

11

Rotation

1.85

$\delta_1 = 3.85$

$\delta_2 = 5.6$
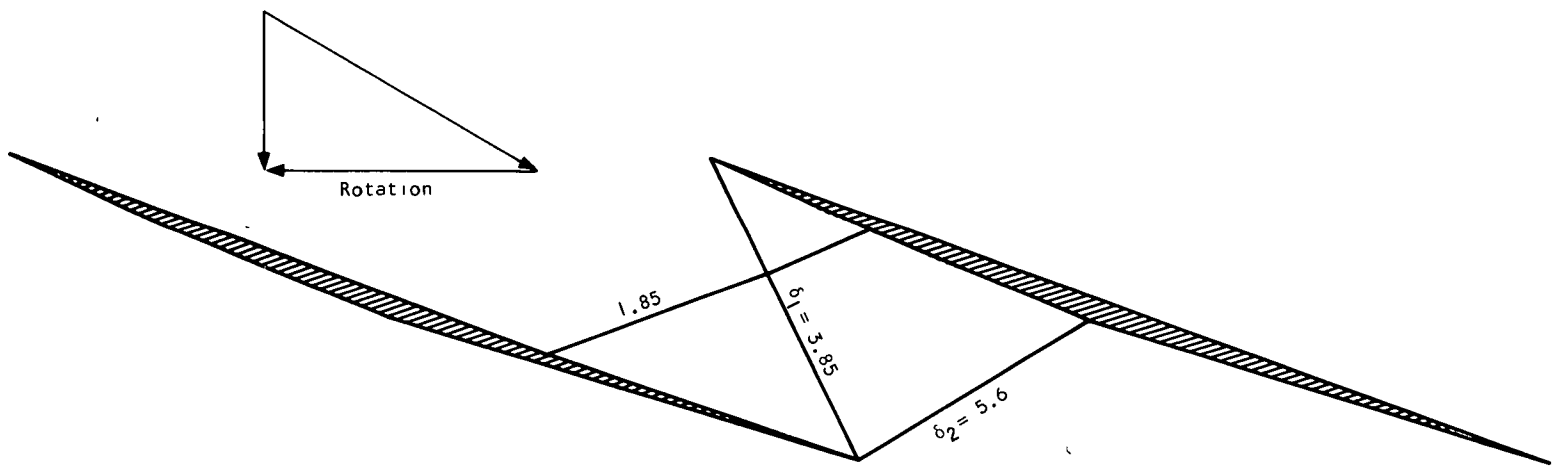
S-72473

Figure 3.--Sample Wave Pattern Showing 1.85 Degrees of the Trailing-
Edge Shock Shifted Part-way Forward.
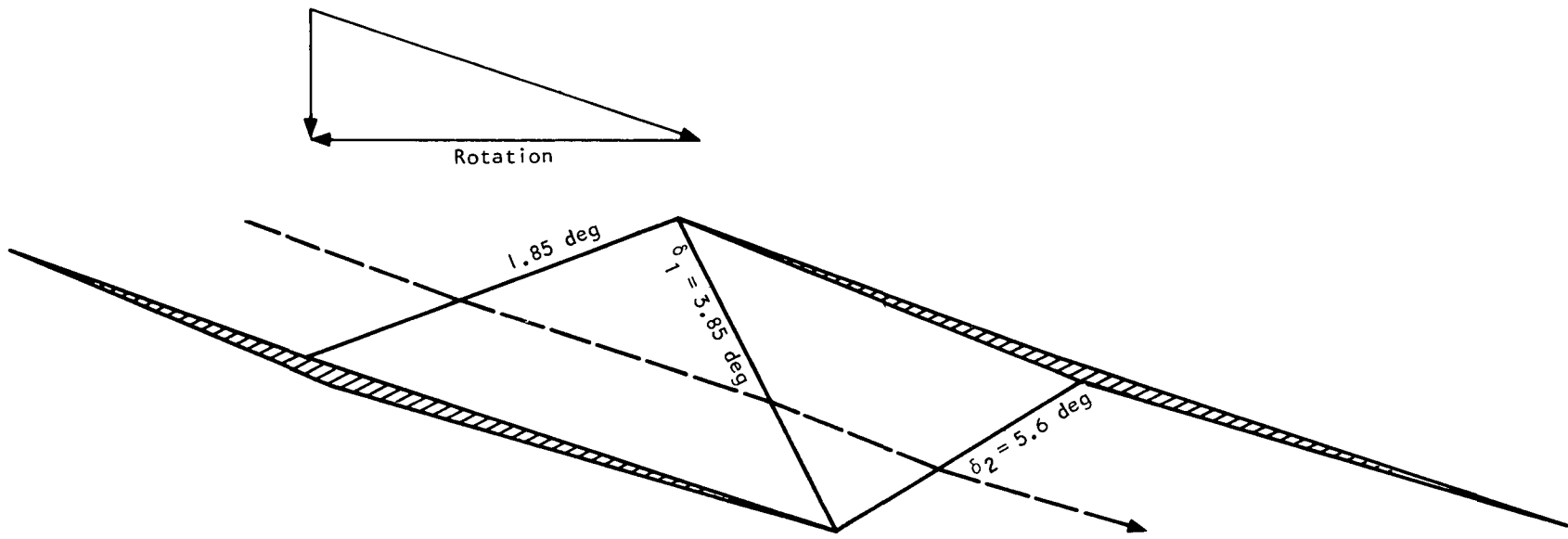
Figure 4.--Sample Wave Pattern Showing 1.85 Degrees of
Trailing-Edge Shock Shifted Fully Forward.

Rotation

$\delta_1 = 3.85$ deg

$\delta_2 = 3.85$ deg
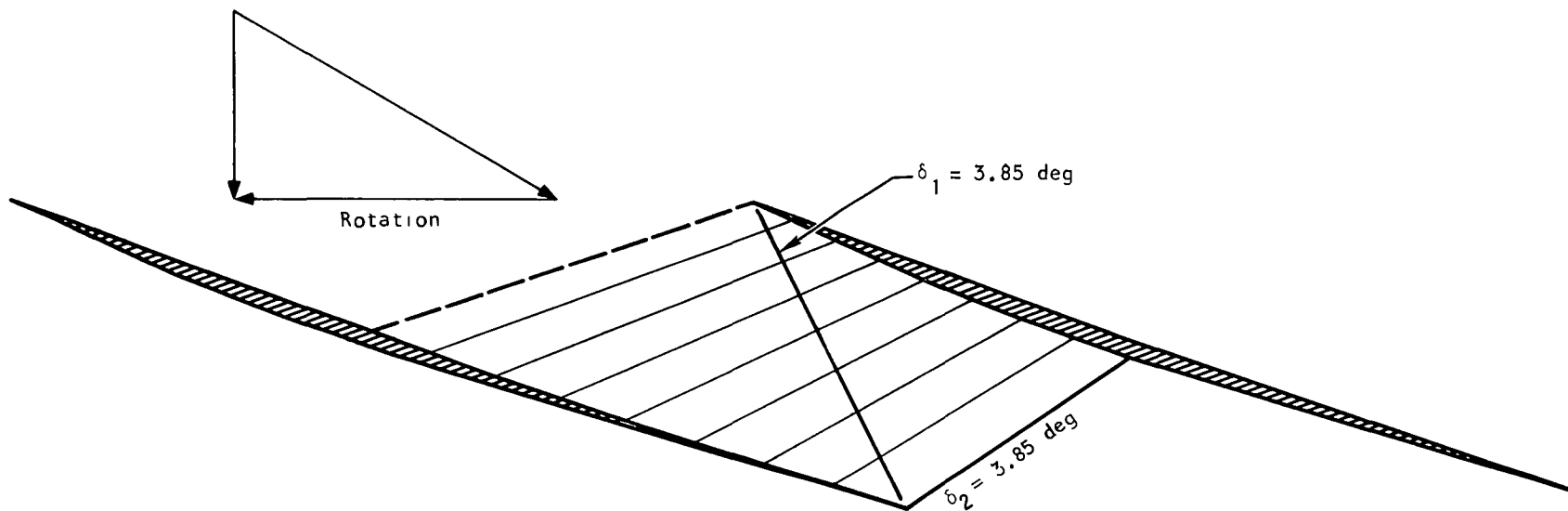
S-72477

Figure 5.--Sample Wave Pattern Showing Residual Trailing-Edge Shock
Compression Distributed Along Suction Surface.

Leading edge shock

Rotation

Trailing edge shock

Imaginary blade section
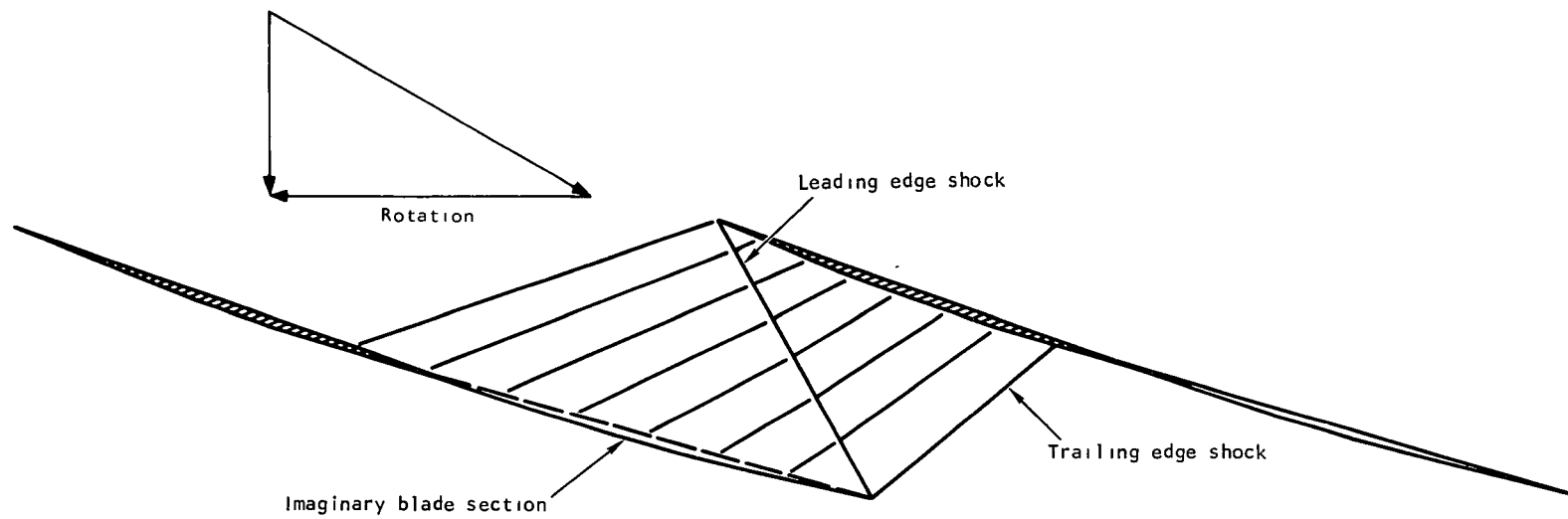
S-72469

Figure 6.--Blade Section Using Distributed Suction Surface Compressions
to Weaken the Trailing-Edge Shock Below the Leading-Edge
Shock Strength Resulting in an Imaginary Blade Aft Section.

15

additional suction surface compression must be provided, either as a finite wave emanating from the suction surface (figs. 3 and 4), or as distributed turning (fig. 5). For the type of blade section shown in fig. 2, where the leading-edge shock terminates at the adjacent-blade trailing edge, the minimum trailing-edge shock strength is established by mechanical considerations. For the section of fig. 2, the trailing-edge wedge angle δ_{TE} is

$$\delta_{TE} = \delta_2 - \delta_1 \tag{11}$$

Accordingly, δ_{TE} vanishes as δ_2 approaches δ_1 and becomes negative for $\delta_2 < \delta_1$, thereby yielding a nonphysical section (fig. 6).

The trailing-edge shock can be made stronger than nominal by offsetting the excess compression with an equivalent distributed expansion on the suction surface between the points u and l.

Aerodynamically, changing the trailing edge shock strength affects the blade surface Mach number distribution, and hence indirectly the blade viscous and profile losses. In addition, as a result of raising or lowering the mean Mach number level in the passage portion of the blade, the trailing-edge shock affects the ability of the section to start.

Weakening the trailing-edge shock results in a reduction of the average surface Mach numbers, and hence should result in a reduction in viscous losses. In addition, distributing the overall blade diffusion and using the weaker trailing-edge shock should reduce the tendency of the boundary layer to separate and eliminate the profile losses associated with separation. On the other hand, section changes that weaken the trailing-edge shock tend to reduce the mean passage Mach number and, hence, will make the section more difficult to start. This latter effect is partially offset by the reduced Mach number into the bow shock in the unstarted operating condition where upstream compressions usually precede the cascade.

Using similar reasoning, it is anticipated that section suction surface changes that strengthen the trailing-edge shock will increase the blade losses and, at the same time, make the resulting section easier to start.

Solidity effects.--A section of higher solidity than is portrayed in figs. 2 through 6 will cause the leading-edge shock to impinge on the suction surface. Cancellation of this wave by an expansion corner decreases β on the suction surface, downstream of the expansion kink, by the magnitude δ_1. Denoting this value as β_t yields, in general,

$$\delta_{TE} = \beta_2 - \beta_t$$

From eq. (1),

$$\beta_u = \beta_2 + \delta_1 - \delta_2$$

16

therefore,

$$\beta_t = \beta_2 - \delta_2$$

and, finally, for the high-solidity section of fig. 7,

$$\delta_{TE} = \delta_2 \qquad\qquad (12)$$

For this type of section, the trailing-edge shock strength δ_2 can evidently be less than for the section shown in fig. 2 before the trailing-edge region becomes excessively thin.

It is apparent from a comparison of figs. 2 and 7 that the section solidity can significantly influence the section mechanical properties. In particular, increasing the section solidity tends to increase the section thickness in the trailing-edge region. As will be seen later, three-dimensional sections have higher than minimum solidity in order to take advantage of these effects.

From an aerodynamic point of view, the increased solidity (as a result of its effect on the trailing-edge wedge angle) allows a weaker trailing-edge shock to be used than would otherwise be possible. In addition, it allows some distance for the suction surface boundary layer to energize after its encounter with the leading-edge shock. This latter effect should tend to reduce profile losses, and may more than offset the increase in viscous losses due to the increase in section wetted surface.

Outboard Section Design Theory (3-D)

The three-dimensional (3-D) characteristic procedure used in the actual design of the rotor outboard sections is basically analogous to the 2-D method just described. The leading-edge shock strength may still be defined in terms of the characteristic parameters, eq. (3). However, because of the effects of the stream tube contraction, the radius change, and the blade row rotation, eq. (4) is no longer valid and $\xi_u \neq \xi_1$. The procedure by which the actual outer blade sections are derived utilizes the simple two-dimensional characteristic equations modified to reflect changes with axial distance in both stream tube thickness and radius. With this type of flow field, the two-dimensional variations in wave strength may be altered or even change signs as they move in the axial direction. That is, the variations are functions of stream tube contractions (or expansions) as well as blade turning.

The actual 3-D sections contain modifications which make them consistent with:

(1) The effects of blade row rotation, radius changes, and variations in stream tube height on the flow field

(2) Certain necessary mechanical constraints such as leading- and trailing-edge radii and blade section thicknesses

(3) The calculated shock and viscous losses

Rotation
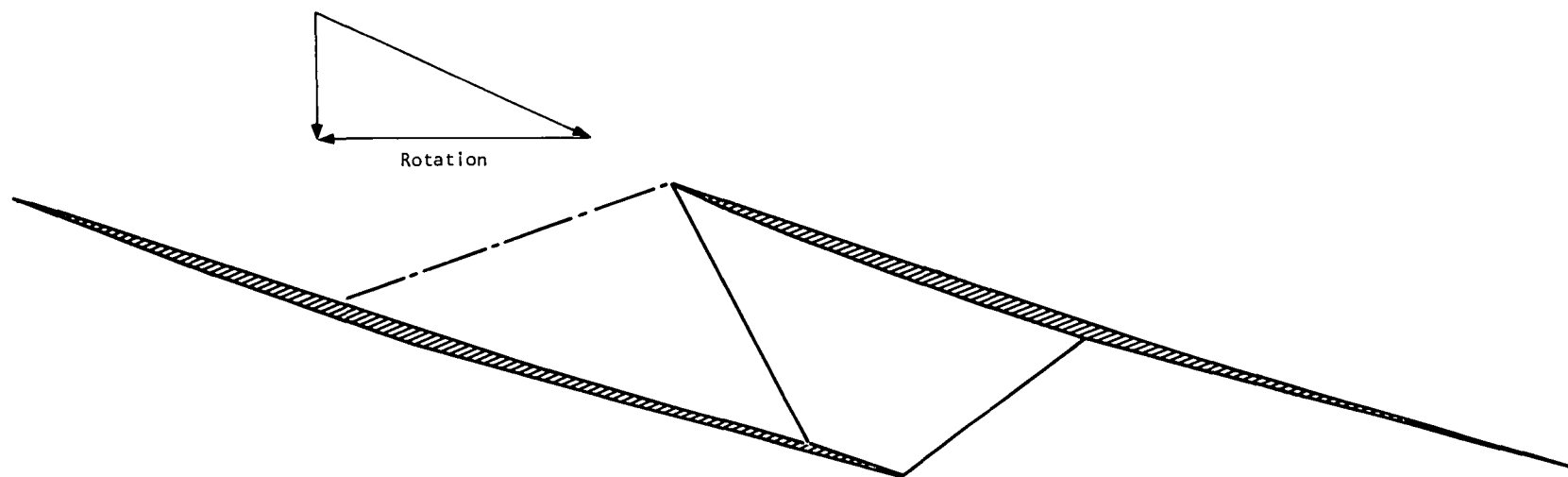
S-72470

Figure 7.--Sample Wave Patterns Showing Leading- and Trailing-Edge
Shock Cancellation with Increased Solidity Which Allows
Separation of Leading- and Trailing-Edge Shock.

(4)   Blade passage area variations which permit a reasonable passage
      "starting" speed (sufficiently below design speed)

(5)   Adjacent sections of the same and different types

Characteristic equations.--As developed in Appendix A, the theory of characteristics gives the differential $d\bar{\xi}$ at any point on the negative characteristic joining the points 1 and u, fig. 2.

$$d\bar{\xi} = \bar{\epsilon} \ (r, \alpha, \omega, \frac{1}{h}\frac{dh}{dm}, \nu, \beta) \tag{13}$$

where r, α, and $\frac{1}{h}\frac{dh}{dm}$ are all functions of the meridional location (m) of the point on the characteristic. Since ω is a design constant, eq. (13) may then be written as

$$d\bar{\xi} = \bar{\epsilon}_2 \ (m, \nu, \beta) \quad dm \tag{14}$$

where the ϵ-function is defined in Appendix A by the expression of eq. (A-22).

In general, the ν and β distributions on the negative characteristic joining the points 1 and u are not known a priori and depend upon the detailed contouring of the blade suction surface. Hence, the exact relationship between $\bar{\xi}_1$ and $\bar{\xi}_u$ cannot be determined without a detailed calculation of

the intervening flow field. This calculation would be costly and time consuming. However, examination of the function $\bar{\epsilon}_2$ indicates that under certain conditions it may be closely approximated by substituting the inlet values ν_1 and β_1 for the local values of ν and β. Then

$$d\bar{\xi} \approx \bar{\epsilon}_2 \ (m, \nu_1, \beta_1) \quad dm \tag{15}$$

or

$$\bar{\xi}_u - \bar{\xi}_1 \approx \int_{m_1}^{m_u} \bar{\epsilon}_2 \ (m, \nu_1, \beta_1) \quad dm \tag{16}$$

In addition to the above approximations the conditions at the cascade exit (point 2) are assumed to be equal to the core conditions as calculated from the trailing edge mixing analysis (Appendix B). Further, the inlet conditions (point 1) are taken to be the inlet conditions after the leading edge blockage calculation described in Appendix C. The final equation for the leading edge shock strength in three-dimensional flow, analogous to eq. (3) for two-dimensional flow, is then

$$\delta_1 = \bar{\xi}_{1, corr} + \int_{m_1}^{m_u} \bar{\epsilon}_2 \ (m, \nu_{1 \ corr}, \beta_{1 \ corr}) \quad dm - \bar{\xi}_{2, core} \tag{17}$$

where the first two terms on the right represent $\bar{\xi}_u$, the subscript corr denotes the cascade inlet conditions corrected for leading-edge blockage, and the subscript core denotes inviscid flow conditions corrected for blockage.

As a consequence of eq. (17), it follows that the leading-edge shock strength is uniquely determined in a manner which is essentially the same as the technique explained for the two-dimensional sections. For fixed inlet and outlet velocity diagrams (fixed $\bar{\xi}_{1,\ corr}$ and $\bar{\xi}_{2,\ core}$), the leading-edge shock strength can be varied without altering the cascade wave configuration only by changing the integral term in eq. (17). This, in turn, can be done only by the blade annulus area distribution (stream tube height). This procedure allows some design freedom for altering the blade thickness.

Using the values of $M_{1\ corr}$ and $\beta_{1\ corr}$ as calculated in Appendix D and values of M_{core} and β_{core} from Appendix B, the leading-edge shock strength may be calculated as indicated in the following illustrative example.

$$M_{1\ corr} = 1.502$$

$$\beta_{1\ corr} = 62.17 \text{ deg}$$

$$M_{core} = 1.143$$

$$\beta_{core} = 59.35 \text{ deg}$$

The corresponding values of $\bar{\xi}_{1\ corr}$ and $\bar{\xi}_{core}$ are:

$$\bar{\xi}_{1\ corr} = 37.07 \text{ deg}$$

$$\bar{\xi}_{core} = 30.79 \text{ deg}$$

The value of the integral term in eq. (17) is

$$\int_{m\ =\ 0}^{m\ =\ 1.787} \bar{\epsilon}(m, \nu, \beta)\ dm = -1.94 \text{ deg}$$

The corresponding value of leading-edge shock strength as calculated by eq. (17) is therefore

$$\delta_1 = 37.07 - 1.94 - 30.79$$

or

$$\delta_1 = 4.34 \text{ deg}$$

20

Accuracy evaluation of approximate $\bar{\varepsilon}$ function.--In the design of the 2-D section, the suction surface from the leading edge to the first captured Mach line was made straight in order to eliminate waves which would escape upstream of the rotor. The analogous procedure for 3-D sections consists of defining the suction surface from the leading edge to the first captured Mach line to be coincident with the 3-D free streamline. This streamline is the locus of the path which the flow would take in the absence of blades if it entered the blade annulus axisymmetrically with the blade row inlet values of Mach number and flow angle and if it was restrained to flow within the same axisymmetric stream tube geometry for which the blade section is being designed. This free streamline may be referred to as the no-work streamline, and its flow field represents an exact solution of the fluid flow equations defined for the free streamline constraints. As a consequence it can be used as a partial check of the validity of the approximate eq. (15).

Using the actual rotor design defined herein, a comparison of the characteristic parameter $\bar{\xi}$ calculated for the free streamline flow field and from eq. (16) is shown in fig. 8. As can be seen, the comparison is excellent up to the point of free streamline choke.

Description of 3-D methods.--The conical development of the passage between two adjacent blade sections associated with streamline number 4 (a representative section) is shown in fig. 9. Similar developments for streamlines 1, 6 9 and 12 are shown in figs. 10a through 10d. The grid shown in the figure is the conical development of lines of constant Z (lines A-A) and lines of constant θ (lines B-B) on the conical surface. For purposes of discussion, the significant points on the section are labeled from ① to ⑨, as follows.

Point Number	Description
①	Suction-surface, leading edge radius tangency point
②	Intersection of first captured Mach line with suction surface
③	Point just upstream of the intersection of the leading-edge shock with the shock surface
④	Point just downstream of the intersection of the leading-edge shock with the suction surface
⑤	Suction surface trailing-edge radius tangency point
⑥	Pressure surface trailing-edge radius tangency point
⑦	Point just downstream of the intersection of the trailing-edge shock with the pressure surface
⑧	Point just upstream of the intersection of the trailing-edge shock with the pressure surface
⑨	Pressure surface leading-edge radius tangency point
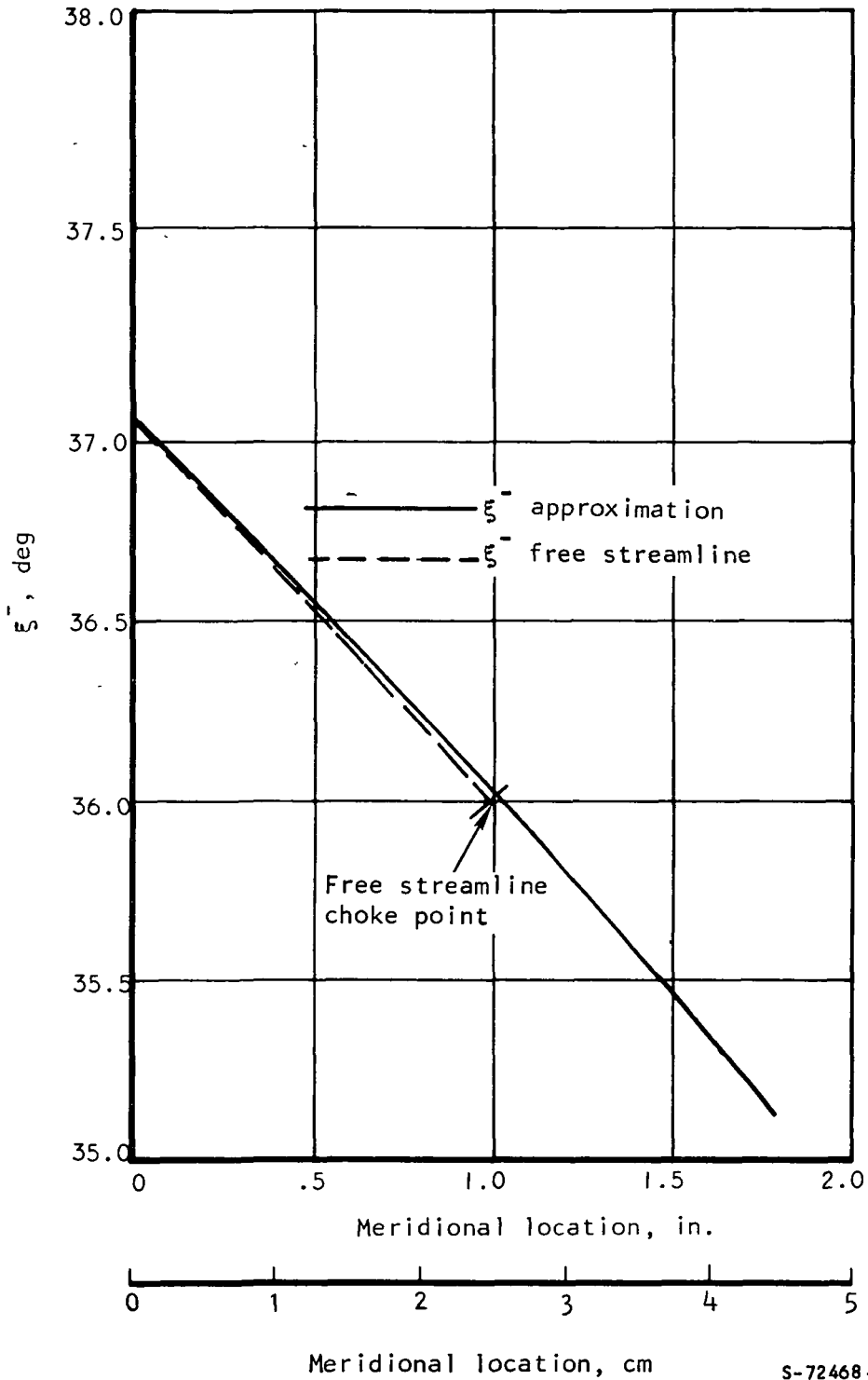
Figure 8.--$\bar{\xi}$ Approximation and $\bar{\xi}$ Free Streamline for Streamline No. 4.
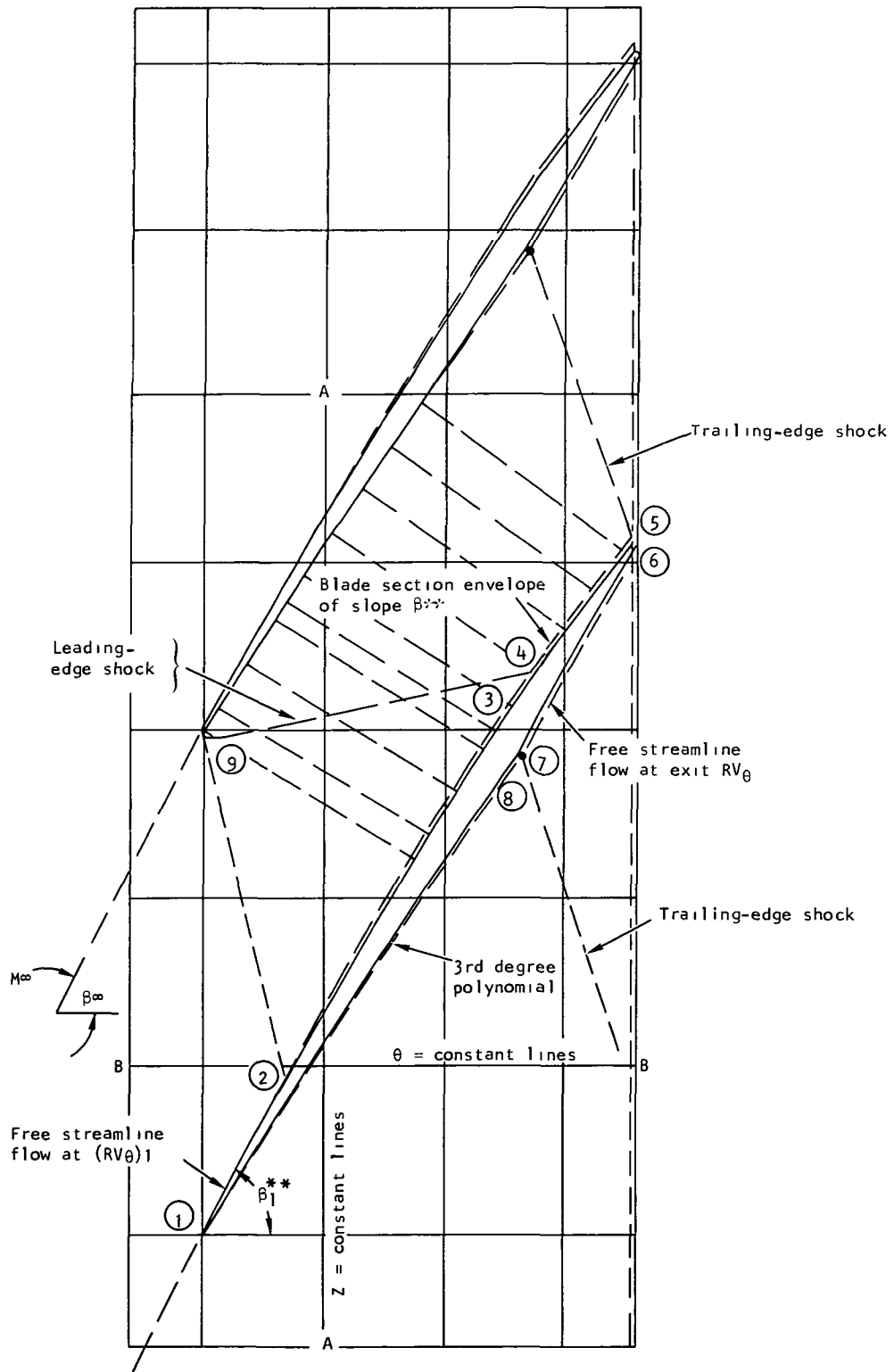
Figure 9.--Representative Rotor Section (Streamline No. 4) Showing Pertinent Design Blade Segments and Points.

23
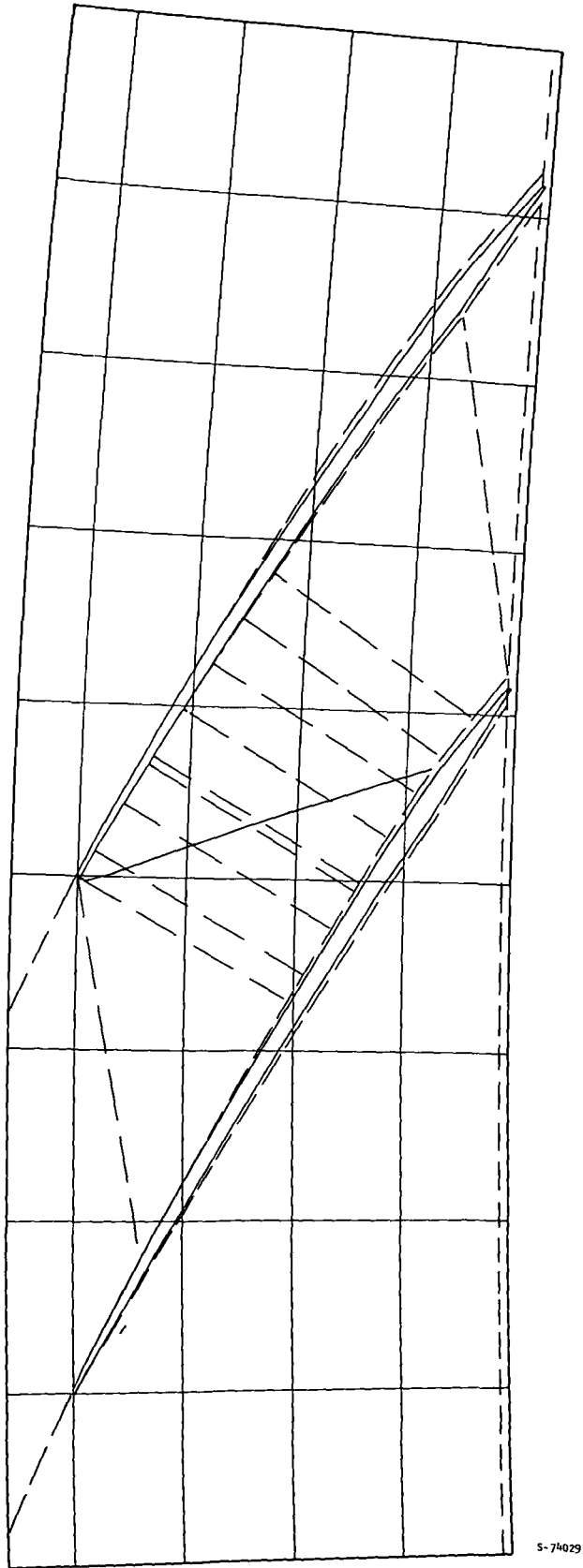
Figure 10a.--Streamline No. 1 Conical Development.

S-74029

24
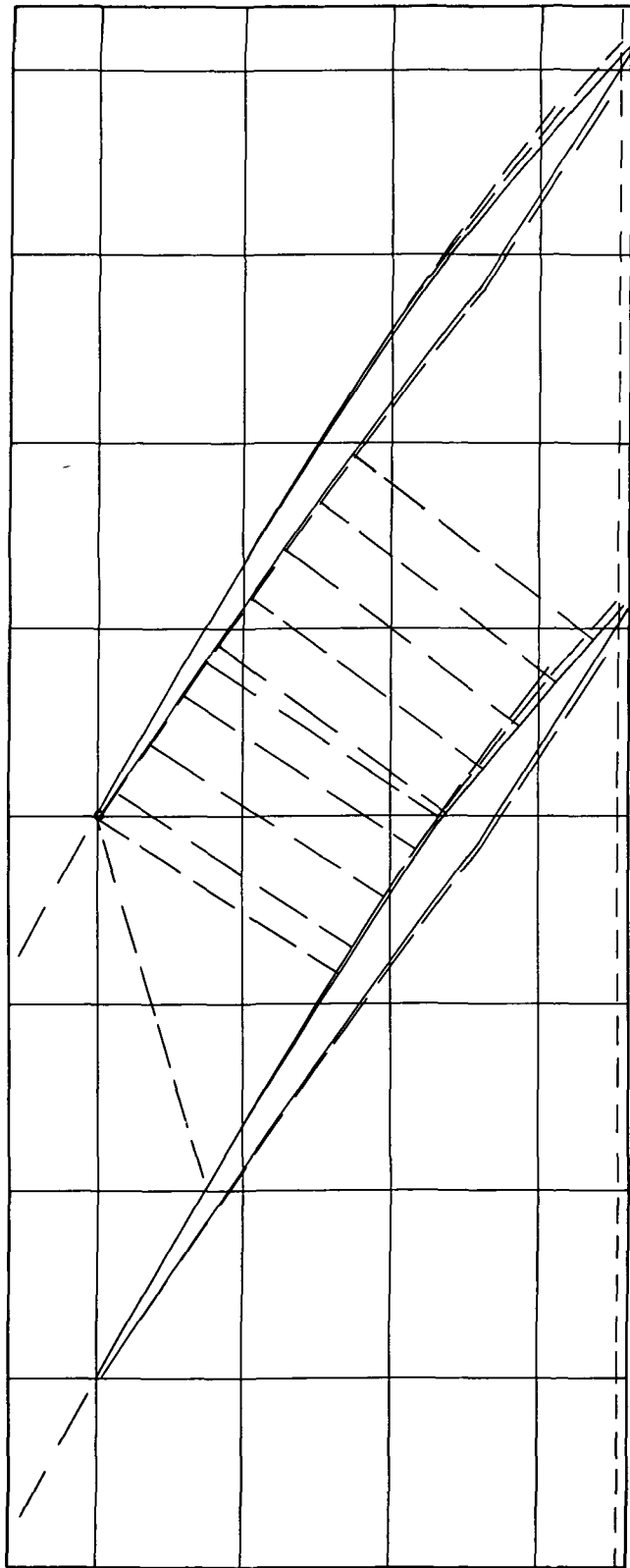
S-74030

Figure 10b.--Streamline No. 6 Conical Development.
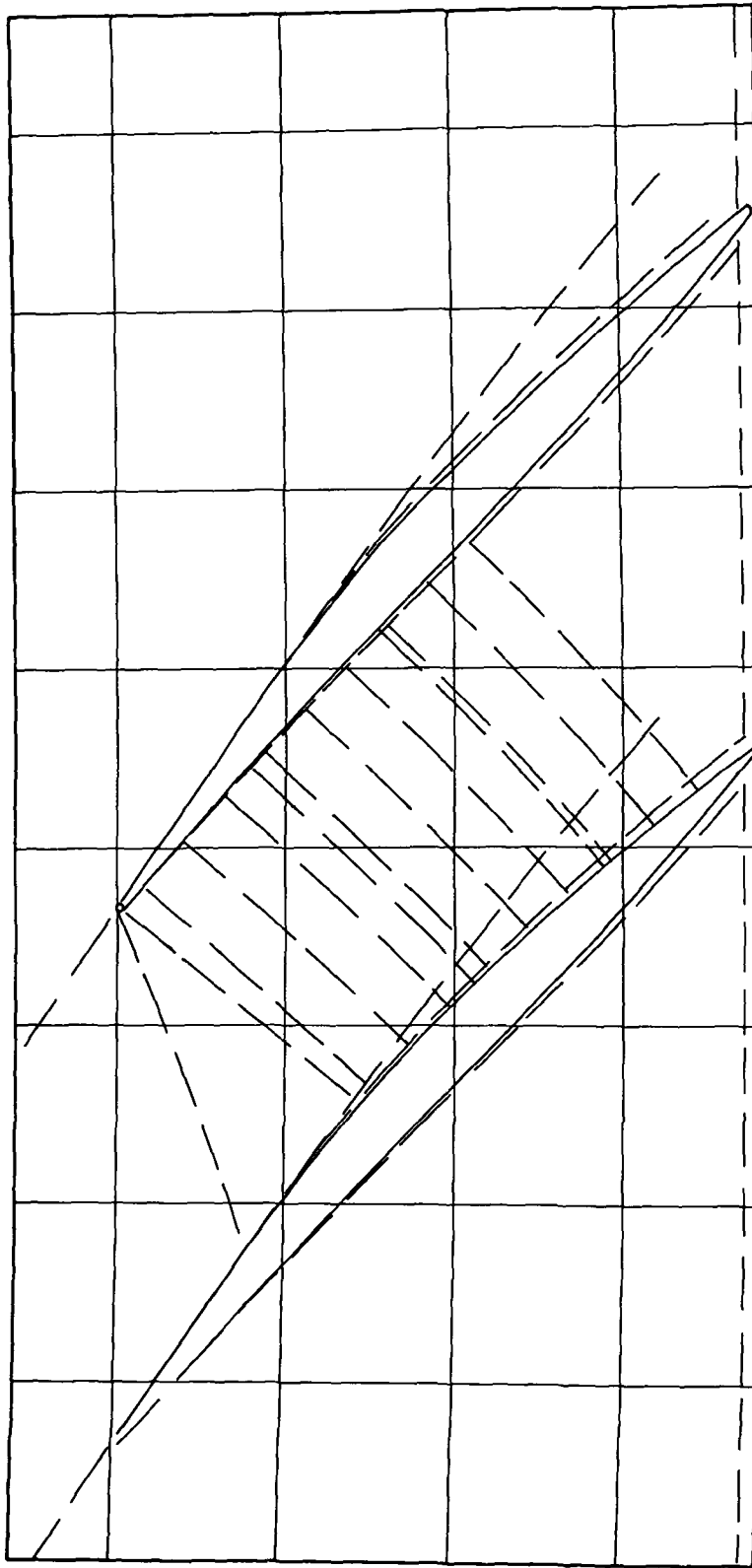
S-74027

Figure 10c.--Streamline No. 9 Conical Development.
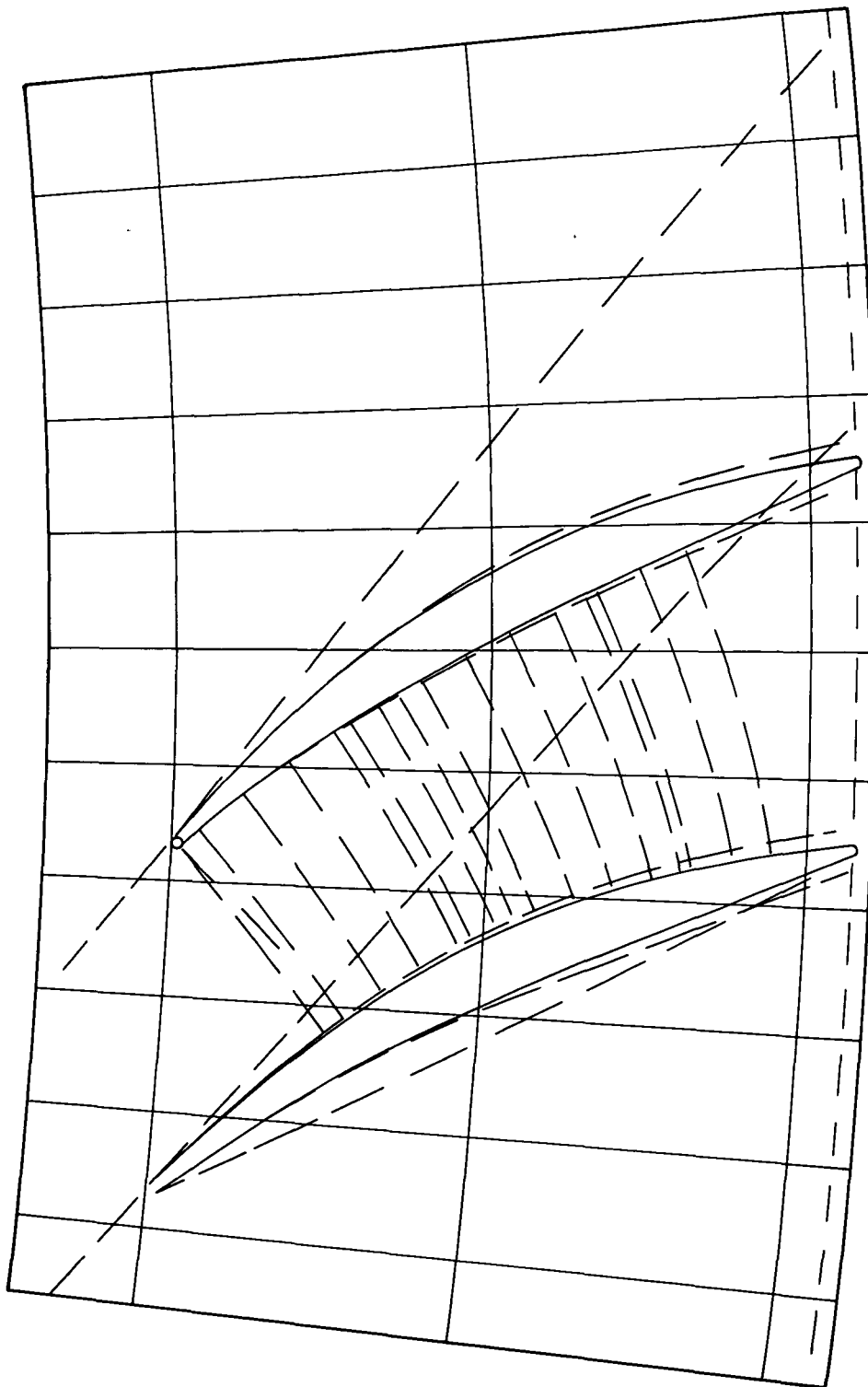
S-74028

Figure 10d.--Streamline No. 12 Conical Development.

27

The line running across the passage from point ⑨ to point ③ represents the leading-edge shock, and the line running from point ⑤ to point ⑧ represents the trailing-edge shock. The dashed line running from point ② to point ⑨ represents the first captured Mach line. The dashed lines running across the interblade passage are used during the calculation of the blade passage area distribution. The dashed line surrounding the blade section represents the section envelope which was calculated in the design process. The solid line within the envelope represents the blade surfaces which are obtained by subtracting the boundary layer displacement thickness from this envelope.

The conical development of the section envelope can be conveniently divided into five steps dealing with the following segments.

Step number	Segment of section envelope developed
1	Point ① to point ②
2	Point ② to point ⑤
3	Point ⑤ to point ⑥
4	Point ⑥ to point ⑦
5	Point ⑧ to point ⑨

The techniques associated with each step segment are presented below.

The first step covering segment ① - ② comprises calculation of the free streamline or "no work streamline". The initial values of Mach number and flow angle used for the no work streamline calculation differ from the axisymmetric program output by the blockage effects associated with the section leading-edge radius and the detached portion of the leading-edge shock. The equations used to calculate the magnitude of the changes are developed as indicated in Appendixes C and D. The net effect of these corrections is as follows:

$$\beta_i = \beta_1 - (i_f + i_s)$$

where i_s and i_f are given by eqs. D-8 and D-9 of Appendix D, respectively.

In addition,

$$M_i = M(\nu_i)$$

where ν_i, the Prandtl-Meyer angle, is calculated from

$$\nu_i = \nu_1 + (\beta_1 - \beta_i)$$

The section envelope angle $\beta_{①}^{**}$ at point ① is set equal to β_i.

28

It was found to be most practical to assign i_f as an input item to the computer program developed to implement this design procedure. The program then calculates an exact value of i_f for use in the next iterative design pass.

Since β_i is assigned to be the suction surface envelope angle $\beta^{**}_{\textcircled{1}}$ it can be seen that the suction-surface incidence angle with respect to the cascade entrance conditions is zero. With respect to the free-stream inlet flow, the leading-edge suction surface incidence angle is $i_f + i_s$.

In addition to defining the forward portion of the section envelope, the free streamline calculation also defines the flow field in the forward region of the section. The location of point $\textcircled{2}$ on the section envelope is determined by constructing a Mach line from the pressure surface leading edge of the adjacent section through the known free streamline flow field until it intersects the section envelope suction surface. The section envelope angle at point $\textcircled{2}$, $\beta^{**}_{\textcircled{2}}$, is equal to the free streamline angle at that point.

The portion of the section envelope suction surface developed in step 2 consists of two smooth curves between points $\textcircled{2}$ - $\textcircled{3}$ and $\textcircled{4}$ - $\textcircled{5}$, separated by a discontinuity between points $\textcircled{3}$ and $\textcircled{4}$. For simplicity, the rate of change of β^{**} with respect to meridional distance on these two smooth surfaces was held constant $(\frac{\partial \beta}{\partial m} = K)$. This rate, defined as K, is

$$K = \frac{(\beta^{**}_{\textcircled{5}} - \beta^{**}_{\textcircled{2}}) - (\beta^{**}_{\textcircled{4}} - \beta^{**}_{\textcircled{3}})}{m_{\textcircled{5}} - m_{\textcircled{2}}} \tag{18}$$

The angle $\beta^{**}_{\textcircled{2}}$ is determined from step 1. The angle $\beta^{**}_{\textcircled{5}}$ is calculated as the difference between the discharge flow angle of the inviscid core and the flow deflection across the trailing edge shock, ie.,

$$\beta^{**}_{\textcircled{5}} = \beta_{core} - \delta_2 \tag{19}$$

The technique used to calculate β_{core} is described in Appendix B. The quantity δ_2 is calculated from the expression

$$\delta_2 = \delta_1 + \Delta\delta \tag{20}$$

where δ_1 is the leading-edge shock strength, and $\Delta\delta$ is the designer-specified difference between the trailing- and leading-edge shock strengths. The technique used to calculate δ_1 was described in the preceding description of the outboard 3-D section design procedure.

For the current designs the magnitude of the leading-edge shock is assumed to be constant across the passage with complete cancellation at point ③. As a consequence

$$\beta^{**}_{③} - \beta^{**}_{④} = \delta_1 \tag{21}$$

The value of β^{**} at any meridional location on the section envelope between points ② and ⑤ is given by

$$\beta^{**}(m) = \beta^{**}_{②} + K(m - m_{②}) \qquad \text{for } m < m_{③}$$
$$\beta^{**}(m) = \beta^{**}_{②} + K(m - m_{②}) - \delta_1 \qquad \text{for } m > m_{③} \tag{22}$$

and the corresponding angular location of the envelope is given by

$$\theta^{**} = \theta^{**}_{②} + \int_{m_{②}}^{m} \frac{\tan \beta^{**}}{r} \, dm \tag{23}$$

The techniques used to determine the location of the leading-edge shock, and subsequently the value of $m_{③}$, are presented in Appendix C.

In the blade layout, step 3 is simply an angular translation at the trailing edge of the section envelope to account for the blockage effects of the suction and pressure surface boundary layers and the physical blockage of the trailing-edge radius. It is apparent from fig. 9 that a significant percentage of the section envelope thickness arises directly as a consequence of the trailing-edge blockage. The magnitude of the trailing-edge blockage is evaluated by means of a mixing loss analysis which is described in Appendix B.

For a 2-D section, the trailing edge region between points ⑥ and ⑦ would be straight in order to eliminate wave disturbances downstream of the section. Correspondingly, in the 3-D design, the pressure surface from points ⑥ to ⑦ is designed so as to be coincident with the free-streamline path corresponding to the cascade outlet inviscid core flow conditions and passing through point ⑥ so as to eliminate wave disturbances downstream of the cascade. In addition, the free streamline analysis provides a detail description of the core flow field in the vicinity of the trailing edge. This information, along with the knowledge of the strength of the trailing-edge shock, is sufficient to determine the approximate location of the shock in the flow field. The intersection of the free streamline and the trailing-edge shock from the adjacent blade determines the location of point ⑦.

In theory, knowledge of the pressure-surface flow conditions downstream of the leading-edge shock and upstream of the trailing-edge shock, along with a reasonable assumption of the Mach number distribution (e.g., linear) between points ⑧ and ⑨, is sufficient to allow the pressure surface contour to be extended analytically from point ⑧ to point ⑨. An assumed Mach number distribution yields a corresponding β-distribution, from which the polar coordinates can be computed by numerical integration from point ⑧ to point ⑨. However,

the resulting value of $\theta^{**}_{\text{⑨}}$ would not necessarily agree with the previously calculated value. In view of this fact, this approach to completing the section envelope was not employed in the present design method. Instead, the angular location of each point on this surface was assumed to be a cubic function of the meridional distance, m, so that

$$\theta^{**} = am^3 + bm^2 + cm + d \tag{24}$$

The location of the surface at points ⑧ and ⑨ is known as a result of the previous construction steps. The corresponding slopes at these points are also known since

$$\beta^{**}_{\text{⑨}} = \beta^{**}_{\text{①}} - \delta^{**}_1 \tag{25}$$

$$\beta^{**}_{\text{⑧}} = \beta^{**}_{\text{⑦}} - \delta_k \tag{26}$$

where δ^{**}_1, the leading-edge envelope wedge angle, is equal to δ_1; and δ_k, the pressure-surface kink angle, equals δ_2, the trailing-edge shock strength (eq. 20)). Hence, the four coefficients of eq. (24) can be easily evaluated.

It might be noted at this point, that in the previous construction steps it was implicitly assumed that the flow deflection across the leading edge shock was the same at the suction and pressure surfaces. A similar assumption was made relative to the trailing edge shock. The validity of this assumption is related directly to the shape of the surface from point ⑧ to point ⑨ and any consequent waves from that surface. For the small changes in β that take place along the subject surfaces, the pressure surface compression waves are not expected to affect significantly the leading-edge and trailing-edge shock wave profiles. As stated previously, the suction-surface rate of change of β^{**} with respect to the meridional coordinate is constant. On the pressure surface, eq. (24) means that

$$\frac{d(\tan \beta^{**})}{dm} = km$$

Accordingly, for small changes in β^{**}, the two surfaces are similar in contour and an appreciable degree of wave cancellation should result.

In order to calculate the blade section from the section envelope it is necessary to choose a distribution of boundary layer displacement thickness on the section surfaces. In the present design procedure, the boundary layer distribution on the suction and pressure surfaces is assumed to be a quadratic function of meridional distance. The three quadratic coefficients are defined by assuming that the displacement thickness at the leading edge is zero; and by specifying the rate of growth of the boundary layer at the leading edge, and the

magnitude of the displacement thickness at the trailing edge (see sketch below).
The sum of the pressure and suction surfaces displacement thicknesses is evalu-
ated using the mixing calculation described in Appendix B. The magnitude of
the individual thickness was determined by assuming the suction surface thick-
ness to be 20 percent larger than the pressure surface thickness. For simpli-
city, the rate of change of boundary layer displacement thickness at the lead-
ing edge is specified´in terms of the angle between the section envelope and
the metal surface.

Meridional distance

S-74118

32
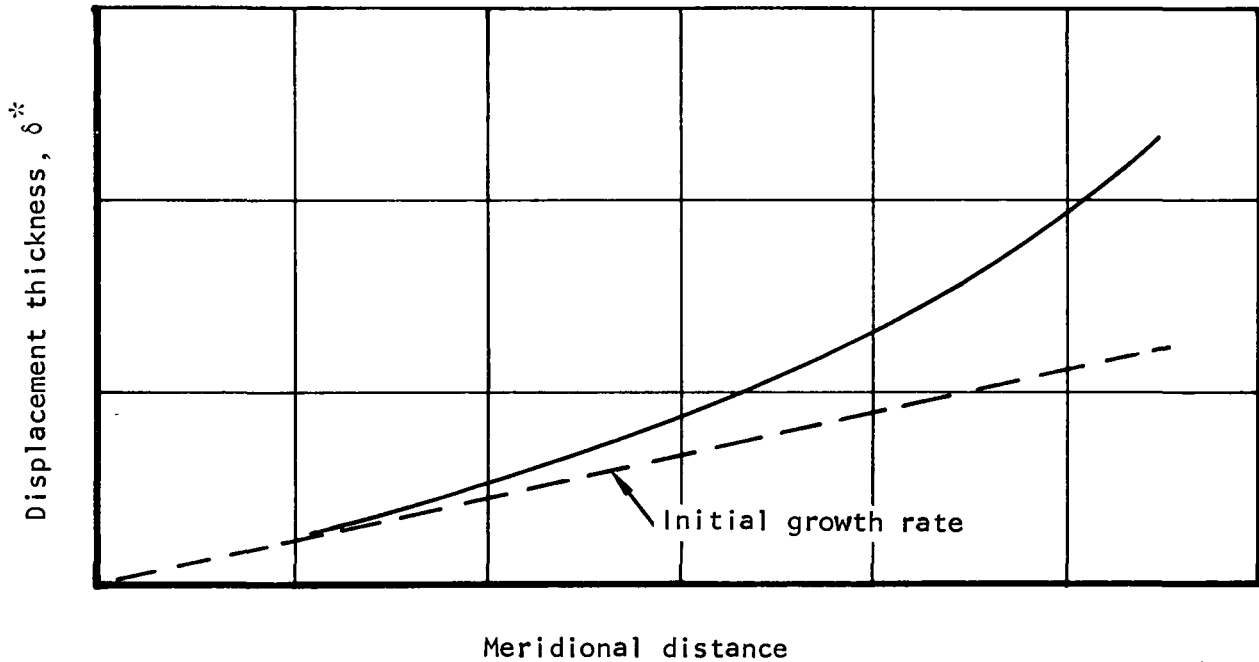
One approach to specifying the initial rate of boundary layer growth would be to evaluate the displacement thickness at the location of the first captured Mach line, and then to choose an initial growth rate consistent with this value. This approach was not used in the development of the present design; rather, an initial growth angle of 0.2 deg was assumed for each blade section.

Summary of outer-section design sequence.—The input to the outer section design procedure can be divided into two categories: (1) the input supplied by the axisymmetric program, and (2) the input supplied by the designer. The former includes the inlet and discharge flow conditions, the streamtube geometry, and the axial chord of the section. The primary and secondary input supplied by the designer is listed in the following table.

Primary input	Description
$\Delta\delta$	Difference between trailing-edge and leading-edge shock strength
δ_k	Pressure surface kink angle

Secondary input	
Q_p	The profile loss factor to be used in the mixing calculation
i_f	Suction surface incidence factor (see Appendix D)
$r_{L.E.}$	The leading-edge radius
$r_{T.E.}$	The trailing-edge radius
α_s	The suction surface initial boundary layer growth angle
α_p	The pressure surface initial boundary layer growth angle
H	The trailing-edge boundary layer shape factor
f	The ratio of the suction surface to total boundary layer displacement thickness

The secondary input parameters are those quantities which are generally held fixed during the design process. The only primary input variable with which the designer can influence the outboard section properties is $\Delta\delta$. The choice of this variable directly affects the section maximum thickness and the minimum passage area. If the maximum section thickness is specified from mechanical design considerations, then the value of $\Delta\delta$ and consequently the minimum passage area are determined. If the value of minimum passage area is not acceptable then the solidity, i.e., the axial projection of the section must be changed. The design process can be speeded up considerably if the axial projection is treated as a primary design parameter, with the condition that the axial projection value used in the final axisymmetric pass and the final blade design pass correspond.

Inboard Section Design Theory

The inner rotor sections, by definition, have subsonic inlet and discharge Mach numbers. As a consequence, the analytical techniques used in the design of the outer sections are no longer valid and an alternate design approach must be used. One of the main considerations in choosing the inner section design technique was that the method should provide, automatically, a simple means of fairing the inner and outer sections in a smooth, continuous, and structurally acceptable manner. For this reason, a design technique which was identical in structure to that used for the outboard design was selected rather than the simpler and more conventional multiple-circular-arc approach.

The outer section was developed in six basic steps, two steps to develop the suction surface, two steps to develop the pressure surface, and one step each to develop the section envelope blockage and the blade metal surface. The inner section is developed in four steps, one each for the pressure and suction envelope surfaces and one each for the blockage and metal section development. The suction and pressure surface steps are individually divided into two steps each so that the final section is consistent with the six-step outboard section. Consequently, construction steps 1 and 2, and steps 4 and 5 are considered together in the following description. The manner in which the inner and outer sections are faired smoothly into one another is discussed in the description of the central section design technique.

Description of inboard section design methods.--Steps 1 and 2 encompass the generation of the section envelope suction surface. For the inner sections, the surface angle variations along this envelope are defined by

$$\frac{d\beta^{**}}{dm} = K(1 + \lambda \frac{m}{m_{\circled{5}}})$$

(27)

The parameter λ allows the designer to control the distribution of suction surface curvature. For $\lambda = 0$, the distribution of curvature is the same as was used for the outer sections. For $\lambda > 0$, the surface curvature tends to shift towards the trailing edge, and for $\lambda < 0$, the surface curvature tends to shift towards the leading edge. Integrating eq. (27) from the leading edge ($m = 0$) to a general point on the surface yields

$$\beta^{**} - \beta^{**}_{\circled{1}} = Km (1 + \frac{\lambda}{2} \frac{m}{m_{\circled{5}}})$$

(28)

where the subscripts identify locations designated in fig. 9. Eq. (28) can be used to evaluate K in terms of the change in section envelope surface angle from the known overall change in β^{**}:

$$K = \frac{\beta^{**}_{\circled{5}} - \beta^{**}_{\circled{1}}}{m_{\circled{5}} (1 + \lambda/2)}$$

34

Accordingly, eq. (28) becomes

$$\beta^{**} = \dot{\beta}^{**}_1 + \frac{(\beta^{**}_{\text{⑤}} - \beta^{**}_{\text{①}})(1 + \frac{\lambda}{2}\frac{m}{m_{\text{⑤}}})\frac{m}{m_{\text{⑤}}}}{(1 + \frac{\lambda}{2})} \tag{29}$$

It will be noted that $\lambda = 0$ results in

$$\beta^{**} = \beta^{**}_1 + \frac{\beta^{**}_{\text{⑤}} - \dot{\beta}^{**}_{\text{①}}}{m_{\text{⑤}}} m$$

which displays the same form as eq. (22).

The suction surface angle $\beta^{**}_{\text{①}}$ at the leading edge is evaluated from

$$\beta^{**}_{\text{①}} = \beta_{\text{①}} - \frac{2r_{\text{L.E.}}}{Y \cos \beta_\infty} - i_f \tag{30}$$

The second and third terms on the right of eq. (30) are analogous to the leading-edge thickness and shock blockage terms used in the outboard section development. The leading-edge thickness blockage term has been chosen so as to just offset the loss in blade passage area for a two-dimensional cascade with a straight suction surface. The shock blockage term, now more correctly referred to as simply as an incidence correction factor, is an input quantity in the inboard section design procedure. It is by means of this term that section incidence is controlled.

The section angle (e.g., $\beta_{\text{⑤}}$, fig. 9) at the trailing edge is evaluated from

$$\beta^{**}_{\text{⑤}} = \beta_{\text{core}} - \delta^{**}_s \tag{31}$$

where β_{core} is the inviscid core flow angle, and δ^{**}_s is the section envelope suction surface deviation angle. The suction surface deviation factor is evaluated as

$$\delta^{**}_s = \delta^{**} + \frac{\delta^{**}_{TE}}{2} \tag{32}$$

where δ^{**} and δ^{**}_{TE} are two parameters supplied by the designer, the former being the deviation angle and the latter the trailing-edge wedge angle of the section envelope. The reason for specifying δ^{**} and δ^{**}_{TE} instead of δ^{**}_s directly is that these two quantities are closely related to the corresponding quantities of the metal section and it is convenient to be able to control these quantities independently during the design process.

Once the parameters i_f, δ^{**}_{TE}, δ^{**}, and λ are specified, the section envelope at each point can be calculated from

$$\beta^{**} = \beta_1^{**} + \int_o^m \frac{d\beta^{**}}{dm}\, dm \tag{33}$$

and the corresponding section envelope angular location from

$$\theta^{**} = \int_o^m \frac{\tan \beta^{**}}{r}\, dm \tag{34}$$

With the suction surface specified by eqs. (33) and (34), only the position of the point corresponding to the outboard section point ③ and ④ on the surface in a manner consistent with the outer section remains. In the outer section development, this position is determined by extending a Mach line (the first captured Mach line) from the leading edge of an adjacent blade to the suction surfaces. For sections toward the hub (lower relative Mach numbers), this Mach line tends to approximate a leading-edge passage normal. For the inner sections, where such a Mach line does not exist, the leading-edge normal is used in its place.

The third step for the inner sections is identical to step 3 for the outer section. It specifies the location of point ⑥ on the section envelope via the angular translation of the coordinate to account for the total effective blade and displacement thickness blockage. Steps 4 and 5 encompass the definition of the section envelope pressure surface. The angle of this surface at the leading edge was previously evaluated in eq. (25) as $\beta_{⑨}^{**} = \beta_{①}^{**} - \delta_1^{**}$ where $\beta_{①}^{**}$ is the angle of the suction surface as calculated in step 1 and δ_1^{**} is the section envelope leading-edge wedge angle specified by the designer. The angle of the pressure surface at the trailing edge is evaluated as

$$\beta_{⑥}^{**} = \beta_{core} - \delta_p^{**} \tag{35}$$

where δ_p^{**} is the section envelope pressure surface deviation factor. This quantity is evaluated from the section envelope deviation angle, and the section envelope trailing edge wedge angle as

$$\delta_p^{**} = \delta^{**} - \frac{\delta_{TE}^{**}}{2} \tag{36}$$

Eqs. (25) and (35) serve to define the pressure surface angle at the leading- and trailing-edge points. The location of the leading-edge point is calculated from the location of point ① and the designer's choice of leading-edge radius; the location of the trailing-edge point is determined from step 3. With the

location and slope of the surface specified at the leading and trailing edge, the remainder of the surface is defined by a cubic curve, i.e.,

$$\theta^{**} = am^3 + bm^2 + cm + d \qquad (37)$$

Step 6 encompasses the generation of the metal section within the section envelope. This operation is performed in the same manner as for an outer section.

Summary of inboard section design sequence.--The design of an inner rotor section using the techniques described above requires two types of input: (1) input supplied from the axisymmetric program, and (2) input supplied by the designer. The input supplied by the axisymmetric program includes the inlet and discharge flow conditions, and the streamtube geometry, and the axial length of the section. The primary and secondary input supplied by the designer is listed in the table below.

Primary input	Description
λ	Suction surface curvature factor
i_f	Suction surface incidence factor
δ^{**}	Envelope deviation angle with respect to envelope mean line
δ^{**}_{TE}	Section envelope trailing-edge wedge angle
δ^{**}_1	Section envelope leading-edge wedge angle

Secondary input	
Q_P	Profile loss factor for use in mixing calculation
H	Trailing-edge boundary layer shape factor
α_s	Suction surface initial boundary layer growth angle
α_p	Pressure surface initial boundary layer growth angle
$r_{L.E.}$	Leading-edge radius
$r_{T.E.}$	Trailing-edge radius

The primary input values represent those quantities which are varied by the designer in the process of obtaining an acceptable metal section. The secondary input quantities, in general, are fixed during the iteration process. The manner in which the primary quantities tend to affect the section properties are discussed in the following paragraphs.

37

The leading- and trailing-edge section envelope wedge angles control the magnitude and location of the section maximum thickness. Increasing either wedge angle tends to increase the maximum thickness. Increasing the leading-edge wedge angle tends to shift the maximum thickness forward, and increasing the trailing-edge wedge angle tends to shift the maximum thickness aft. The section envelope deviation factor controls the metal section deviation angle. The suction surface curvature and incidence factors control the blade passage area distribution. In actuality, there is some cross-coupling between each input parameter and all the section properties. This cross-coupling is in general small.

The section passage area distribution can be described quantitatively in terms of the value and location of the passage minimum area, and qualitatively in terms of how quickly the area distribution opens up downstream of the minimum value. In general, it was found that shifting the suction surface curvature aft tended to shift the passage minimum area in the same direction, and increasing the incidence factor tends to increase the value of the minimum area. In the development of the hub section, these two factors were chosen so as to achieve a minimum passage five percent larger than the critical area at the passage inlet, with a continuous increase in area downstream of this location. The hub deviation factor was chosen to achieve a section deviation angle of 10 deg, and the leading- and trailing-edge wedge angles were chosen so as to achieve a t_m/C of 0.08 located slightly aft of the mid-chord position.

Central Section Design Theory

The central sections, by definition, have supersonic inlet and subsonic discharge relative Mach numbers. At present no theoretical technique is readily available for analyzing entire sections of this type. In developing the central sections, consideration was given to the following:

(1) Achievement of a smooth transition from inboard to outboard sections

(2) Achievement of adequate choke margin

(3) Achievement of adequate section thickness

(4) Avoidance of excessive suction surface Mach numbers in the leading-edge region

A main requirement of the central section design technique is that it be structured in a manner which is consistent with item (1) above, and have sufficient flexibility to allow the designer to satisfy items (2) through (4). In order to satisfy item (1), the middle section is developed in six construction steps.

Central section design methods.--In the following paragraphs, the techniques used in each step are discussed in detail. In certain instances where a nonnumerical description of a particular step is inconvenient, a finite difference description of the step is presented. The finite difference procedures are basically those that are used in a computer program that was developed to automate the blade generation technique.

38

Step 1 encompasses the generation of the suction surface of the section envelope from the leading edge to the first captured Mach line (point 2, fig. 9). For all three types of sections the shape of this surface is defined by specifying the surface angle at a finite number of meridional locations. If conditions at the jth point are denoted by subscript j, then for the central sections

$$\beta_{①}^{**} = \beta_1 - \left[\left(2-F_s\right)\left(\frac{r_{L.E.}}{(Y\cos\beta_1)(\tan\beta_1 - \sqrt{M_1^2-1})}\right) + i_f\right]$$

$$\beta_j^{**} = F_s\,\beta_{fs_j} + \left(1-F_s\right)\left[\beta_{j-1}^{**} + K'\left(1 + \frac{\lambda m_j}{m_5}\right)\left(m_j - m_{j-1}\right)\right] \tag{38}$$

where the subscript f_s denotes the "no work" streamline.

When $F_s = 1$, eq. (38) reduces to the definition used for the outer surface; where $F_s = 0$, it reduces to the definition used for the inner surface. The parameter K' in the above equation is defined as follows:

$$K' = \frac{\beta_{⑤}^{**} - \beta_{①}^{**} + F_s\delta_1}{m_{⑤}\left(1 + \frac{\lambda}{2}\right)} \tag{39}$$

where the numbered subscripts denote points indicated on the reference blade section (fig. 9).

With the surface angle defined at each discrete point j, the corresponding angular location of the surface θ_j^{**} is calculated incrementally as

$$\theta_j^{**} = \theta_{j-1}^{**} + \left(\frac{\tan\beta_j^{**} + \tan\beta_{j-1}^{**}}{r_j + r_{j-1}}\right)\left(m_j - m_{j-1}\right) \tag{40}$$

The angular location of the first point (at the leading edge) is specified as zero.

For the outboard sections, the termination point of the above surface is determined by its intersection with the first captured Mach line, the first captured Mach line being constructed from the free streamline angle, the Mach number distribution, and blade spacing. For the inboard sections, the termination point is determined by the intersection of the surface with the passage inlet normal. For the central sections, the termination point is determined by its intersection with a pseudo-Mach-line defined in terms of the surface angle and the free streamline Mach number distribution. The term " pseudo-Mach-line" is employed in recognition of the fact that the coordinates of this line

are calculated for a meridional distribution of Mach number that has not been corrected for adjustments to the suction-surface free streamline beta distribution imposed by eq. (38). This pseudo-Mach-line reduces to a true Mach line for the outboard sections where the surface and free streamline angles are identical. Similarly, it reduces to a passage normal close to the inboard sections as the free streamline Mach number approaches unity.

Step 2 encompasses the generation of the section-envelope suction surface from point ②, fig. 9, to the trailing edge. The surface is defined in two substeps, the first referred to as the preliminary surface definition, and the second as the final surface definition. The preliminary surface definition is used in determining the incidence point of the leading edge shock. Once this point is located, appropriate modification of the preliminary surface downstream of this location yields the final surface definition.

The preliminary angle distribution for the critical sections is generated by the finite difference equation

$$\beta_j^{**} = \beta_{j-1}^{**} + K''' (m_j - m_{j-1}) \tag{41}$$

where

$$K''' = F_s K'' + (1-F_s) K' \left(1 + \lambda \frac{m_j}{m_{⑤}}\right) \tag{42}$$

$$K'' = \frac{(\beta_{⑤}^{**} + F_s \delta_1 - \beta_{②}^{**})}{m_{⑤} - m_{②}} \tag{43}$$

and K' is given by eq. (39).

To demonstrate that the structure of eqs. (41) through (43) applies also to outboard and inboard blade section design, eqs. (41) and (42) can be combined to display the finite-difference approximation $d\beta^{**}/dm$ in the region between points ② and ③

$$\frac{d\beta^{**}}{dm} \approx \frac{\beta_j^{**} - \beta_{j-1}^{**}}{m_j - m_{j-1}} = F_s K'' + (1-F_s) K' \left(1 + \lambda \frac{m_j}{m_{⑤}}\right) \tag{44}$$

For outboard sections ($F_s = 1$), eq. (44) becomes

$$\frac{\beta_j^{**} - \beta_{j-1}^{**}}{m_j - m_{j-1}} = \frac{\beta_{⑤}^{**} + \delta_1 - \beta_2^{**}}{m_{⑤} - m_{②}} \tag{45}$$

which is equivalent to eq. (18). (Note that the term $(\beta_4^{**} - \beta_3^{**})$ of eq. (18) equals $-\delta_1$.) For inboard sections ($F_s = 0$) eq. (44) reduces to

$$\frac{\beta_j^{**} - \beta_{j-1}^{**}}{m_j - m_{j-1}} = \frac{\beta_{⑤}^{**} - \beta_{①}^{**}}{m_{⑤}\left(1 + \frac{\lambda}{2}\right)} \left(1 + \lambda \frac{m_j}{m_{⑤}}\right) \tag{46}$$

40

which is identical to eq. (27).

The location of point $\textcircled{3}$, the shock intercept point, is determined from the interception of the leading-edge shock and the preliminary suction surface. For cases in which the leading-edge wedge is too large to support an attached shock or where the designer wishes to control the location of the "kink" independently of the shock, the intersection location is specified manually. The expression used to determine the suction surface angle distribution downstream of the intersection is

$$\beta_{\textcircled{4}}^{**} = \beta_{\textcircled{3}}^{**} - F_s \, \delta_1 \tag{47}$$

where F_s is a specified parameter and δ_1 is the leading-edge shock strength (see eq. (17)). For $F_s = 1$, the suction surface technique described above generates a surface which is consistent with the outer surface technique, and for $F_s = 0$, generates a surface consistent with the inner surface definition.

The technique used in step 3 is identical to that used in the outer section procedure for defining the change in θ^{**} between points $\textcircled{5}$ and $\textcircled{6}$.

Step 4 encompasses the generation of the pressure surface from point $\textcircled{6}$ to point $\textcircled{7}$. For the outboard sections, the surface angles between points $\textcircled{6}$ and $\textcircled{7}$ are set equal to the corresponding trailing-edge free streamline angles computed from the trailing edge RV_θ, and point $\textcircled{7}$ is determined by the intersection of the adjacent blade suction surface trailing-edge shock with the free streamline surface. For the inboard section, the surface angle is defined by a cubic curve fit and the location of point $\textcircled{7}$ is specified at input. For a point j between points $\textcircled{6}$ and $\textcircled{7}$, let the section surface angle as calculated by the outboard section design method be denoted as β_j^{**o}, and let the surface angle as calculated by the inboard section method be β_j^{**i}. Then the central surface angle is defined as

$$\beta_j^{**} = F_p \, \beta_j^{**o} + (1 - F_p)\beta_j^{**i} \tag{48}$$

where F_p is a parameter governing the transition from inboard to output sections. For $F_p = 1$, the surface corresponds to an outboard section surface and for $F_p = 0$, the surface corresponds to an inboard section surface.

Step 5 defines the generation of the section envelope pressure surface from point $\textcircled{8}$ to point $\textcircled{9}$. For both inboard and outboard sections, the surface is generated by a cubic equation whose parameters are defined by the location and the surface angles at points $\textcircled{8}$ and $\textcircled{9}$. Since the location of point $\textcircled{8}$ is already known from the above steps and point $\textcircled{9}$ can be easily located in terms of the location of point $\textcircled{1}$, only the angles need to be specified to complete the definition of the middle section. The angle at point $\textcircled{9}$ is defined in the same manner for all three types of sections, i.e.,

$$\beta_{\textcircled{9}}^{**} = \beta_{\textcircled{1}}^{**} - \delta_1 \tag{49}$$

41

For point⑧, the central section angle is defined as

$$\beta_{⑧}^{***} = \beta_{⑦}^{***} - F_p \delta_k \qquad (50)$$

where F_p and δ_k are now parameters specified by the designer. For $F_p = 0$, the angles at points ⑦ and ⑧ are the same and the surface definition is identical to the inboard section specification. Similarly with $F_p = 1$, and the kink angle δ_k set equal to the trailing-edge shock strength, the central section reduces to the outboard section specification.

Step 6 consists of the development of the blade section within the section envelope. It is performed in the same manner as described for an outboard section by subtracting the boundary layer displacement thickness from the section envelope.

Summary of central section design sequence.--The central section design procedure is the most complex of the three design procedures discussed in this report. This is so because the midsection procedure must be capable of producing (with appropriate input parameters) either an outboard or an inboard section or any section in between. In fact, in the computer program that has been written to automate the section design procedure, only the midsection procedure was actually programmed. The input to this program for each type of section is identical in format, although many of the input parameters are not used for the outboard sections since the parameters can be calculated internally. The major aspects of the transition from inner to outer sections are controlled by two parameters denoted by F_s and F_p as discussed in the previous section. The parameter F_s controls the transition of the suction surface, and the parameter F_p controls the transition of the pressure surface.

The section using the mid-section design technique requires two types of input: (1) input supplied by the axisymmetric program, and (2) input supplied by the designer. The input supplied by the axisymmetric program includes the inlet and discharge flow conditions, the streamtube geometry, and the axial length of the section. The input parameters supplied by the designer are further divided into two categories: primary and secondary parameters. The latter refers to quantities that are, in general, held constant during the design of the section. The former refers to quantities that are varied during the design process and by means of which the designer controls the section mechanical and aerodynamic properties. The primary and secondary input quantities required for development of the mid-sections are tabulated as follows.

Primary input	Description
λ	Suction surface curvature factor
i_f^{***}	Suction surface incidence factor
δ^{***}	Section deviation angle with respect to envelope meanline
δ_1^{***}	Section envelope leading-edge wedge angle

42

δ_{TE}^{**} Section envelope trailing-edge wedge angle

F_s Suction surface transition factor

F_p Pressure surface transition factor

$m_{③}$ Meridional location of point 3

$m_{⑦}$ Meridional location of point 7

Secondary input

Q_p Profile loss factor for use in mixing calculation

H Trailing-edge boundary layer shape factor

α_s Suction surface initial boundary layer growth angle

α_p Pressure surface initial boundary layer growth angle

$r_{L.E.}$ Leading-edge radius

$r_{T.E.}$ Trailing-edge radius

The manner in which the primary quantities tend to affect the section properties is discussed in the following paragraphs.

The leading- and trailing-edge section envelope wedge angles together control the magnitude and location of the section maximum thickness. Increasing either wedge angle tends to increase the maximum thickness. For small suction and pressure surface angle discontinuities, these two angles also tend to control the location of the section maximum thickness. Increasing the leading-edge wedge angle tends to shift the maximum thickness forward, and increasing the trailing-edge wedge angle tends to shift the maximum thickness aft. For larger suction and pressure surface "kinks", the location of the kinks tends to control the location of the maximum thickness (unless the kinks are placed far forward or far aft on the section). This is because the sections tend to become single or double wedge shapes with the maximum thickness located at or between the wedge vertexes.

The section envelope deviation factor controls the metal section deviation angle. The suction surface curvature and incidence factors and the location and magnitude of the surface angle discontinuities control the blade passage area distribution as well as the suction surface Mach number distribution.

Overall Rotor Design Procedure

In the previous sections of this report, the techniques used to design the outboard, central, and inboard rotor sections were discussed in detail. In the present section, the manner in which these techniques were used to arrive at the final geometry is discussed.

The axisymmetric calculations indicated that the five outermost rotor sections (streamlines 1 through 5, fig. 1) were fully supersonic, and hence they were designed using the outboard section design techniques. The primary variables associated with the design of these sections are the axial projection of the sections, and the difference between the leading- and trailing-edge shock strengths. The major section parameters monitored during the design process were the maximum thickness-to-chord ratio t_m/C and the start margin.

The start margin as calculated by the methods of Appendix D varied from approximately 5.5 percent at the tip to approximately 2.5 percent at section 5. The t_m/C values were set equal to values previously deemed acceptable from mechanical design considerations. Using the program described herein and observing the constraints resulted in a set of sections having gradually decreasing chord lengths and increasing shock strength difference radially inward from the tip. The increasing shock strength difference was necessary in order to keep the section passages sufficiently open. That is, the channel Mach number in the exit region was increased by means of additional turning towards the axis downstream of the expansion kink (eq. 19)). Turning the channel towards the axis increases its flow area.

As a consequence of designing the five outboard sections first, some guidance in the selection of the variables required as input for the design of central and inboard sections could be gained. Specifically, this information included (1) the envelope leading- and trailing-edge wedge angles, (2) the locations of the suction and pressure surface kinks, (3) the magnitudes of the respective kinks, i.e., the values of F_s and F_p, (4) the magnitudes of the incidence factors, and (5) the magnitudes of the deviation angles.

In order to gain some idea as to the probable behavior of the above variables from section 6 on down, section 12 was developed next. This section has subsonic inlet and discharge Mach numbers and hence was designed as an inboard section (no kinks on the pressure or suction surface). In choosing the input variables for this section, the major parameters monitored were the passage area distribution, the t_m/C, and the inlet incidence angle. The location of the hypothetical suction surface kink was specified just aft of the passage inlet normal. The location of the hypothetical pressure surface kink was determined by extrapolation from the outboard sections.

With the central input variables specified in the outboard region and at the hub, the approximate values of the variables at the other sections were determined by curve fitting. The variables were modified somewhat in the design of the remaining sections in order to achieve acceptable distributions of passage area suction surface Mach number, start margin, and t_m/C.

After the final smoothing of the input, r, θ , and z coordinates of each section were input into the rotor "stacking program". This program was specifi- cally written as a part of the present design effort to handle sections with surface angle discontinuities on the pressure and suction surfaces. The program maintains the integrity of the kinks during the stacking and twist operations, and fairs the kinks over a specified surface distance after development of the section onto planar surfaces. In the present design, all kinks were faired over a 0.2 in. surface distance. In addition to fairing the kinks, the program also fairs a leading and trailing edge ellipse to each section. In the present design, a 2:1 ellipse was used for all sections as a compromise between achievable manu- facturing tolerances and optimum aerodynamics.

DESIGN RESULTS AND DISCUSSION

The rather elaborate design procedure used in this program for the rotor design was felt to be justified on the basis that a conclusive evaluation of a new compressor concept was desired. The stator design procedure was standard inasmuch as the stator flow was entirely conventional with respect to both turn- ing angle and Mach number. The fan stage which resulted from these design efforts is summarized and discussed below.

Flow Path and Velocity Diagrams

The flow path was determined considering influences of blade blockage, boundary layer allowance, shock and profile loss coefficients, and work input distribution within the blade row. The resulting iterated flow path showing the locus of the rotor and stator leading and trailing edges and design stream- lines is presented in fig. 1. The 12 streamlines shown divide the flow into 11 actual flow annuluses.

The final velocity diagram values for streamline Nos. 1, 6, and 12 at design speed and airflow are presented in fig. 11. The most noteworthy factors are the supersonic exit Mach number relative to the rotor tip and the small amount of fluid flow turning required at streamline No. 6. The tip inlet Mach number of 1.647 is higher than present commercial practice, but not beyond pub- lished data for transonic and supersonic compressors (refs. 3 and 4). The maxi- mum absolute Mach number leaving the rotor is only 0.732 at an angle of 39.3 deg from the axial direction (at the hub). Providing that the flow leaving the rotor is as uniform as the design concept predicts and the flow parameters have approximately the design values, a low-loss stator design appears routine.

Rotor Design Summary

The overall summary of the final rotor design is presented in tabular form in table 1. Because the axisymmetrical flow calculations are carried out along stream surfaces, all of the design values are presented as functions of the streamline numbers rather than the dimensional radius. However, for orientation purposes, plots of streamline location at rotor blade inlet and outlet are pre- sented in fig. 12. In addition, 4 rotor sections defined along the conical sur- faces representing streamlines 1, 6, 9, and 12 are presented in figs. 10a through 10d. The presentation of the aerodynamic design results is completed by the following discussion and the accompanying figures.
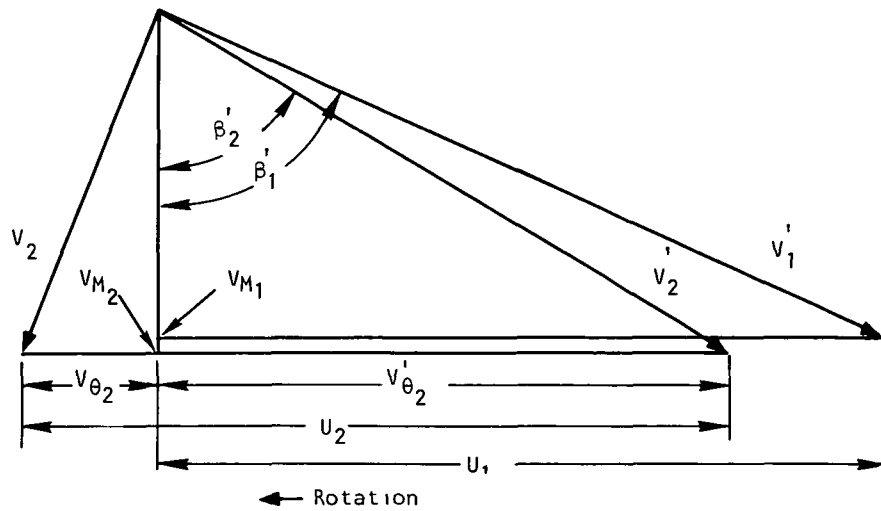
Streamline No.	1	6	12
U_1, ft/s (m/s)	1603.0 (488.6)	1295.1 (394.7)	740.7 (225.8)
V_1'	1773.1 (540.4)	1478.3 (450.6)	952.0 (290.2)
V_{M1}	750.0 (228.6)	701.0 (213.7)	596.0 (181.7)
V_1	750.0 (228.6)	701.0 (213.7)	596.0 (181.7)
U_2	1555.1 (474.0)	1284.0 (391.4)	825.5 (251.6)
V_2'	1470.0 (448.0)	1110.1 (338.4)	708.0 (215.8)
$V_{\theta 2}'$	1259.0 (383.7)	939.0 (286.2)	302.0 (92.1)
V_2	813.0 (247.8)	688.0 (209.7)	828.8 (252.6)
V_{M2}/V_{M1} (Dimensionless)	1.011	0.8463	1.074
M_1'	1.647	1.356	0.875
M_1	0.704	0.653	0.549
M_2'	1.291	0.962	0.625
M_2	0.715	0.596	0.732
β_1', deg	64.7	61.2	51.1
β_2', deg	58.9	57.7	25.3

S-74024

Figure 11.--Rotor Velocity Diagram Values for Tip, Mid-Span, and Hub Stream Surfaces of Design.

46

TABLE I

ROTOR AERODYNAMIC SUMMARY

P_{TI} = 14 696 psia = 10 133 N/cm²
T_{TI} = 518.69 °R = 288 16°K
N/√θ = 12 781 rpm = 1338 4 rad/s
W√θ/δ = 147 91 lbm/s = 6 709 kgm/s
U_{TI} = 1603 0 ft/sec = 488 594 m/s
r_{TI} = 14 370 in = 36 50 cm

Blockage factor = 0 980   <u>Inlet</u>

Streamline	1	2	3	4	5	6	7	8	9	10	11	12
r_I/r_{TI}	1 0000	0 9613	0 9258	0 8877	0 8484	0 8079	0 7613	0 7140	0 6625	0 6047	0 5400	0 4621
% Flow	0 0	9 09	18 18	27 27	36 36	45 45	54 55	63 64	72 73	81 82	91 91	100 0
P_T/P_I	1 0	1 0	1.0	1 0	1 0	1 0	1 0	1 0	1 0	1 0	1 0	1 0
T_T/T_I	1 0	1 0	1 Q	1 0	1 0	1 0	1 0	1 0	1 0	1 0	1 0	1 0
U/U_{TI}	1 0000	0 9613	0 9258	0 8877	0 8484	0 8079	0 7613	0 7140	0 6625	0 6047	0 5400	0 4621
V_θ/U_{TI}	1 0000	0.9613	0.9258	0.8877	0 8484	0 8079	0 7613	0 7140	0 6625	0 6047	0 5400	0 4621
V_M/U_{TI}	0 4682	0 4615	0 4542	0 4524	0.4450	0 4371	0 4303	0 4234	0 4166	0 4072	0 3902	0 3717
φ	-15 0	-11 2	-8 2	-6 2	-4 5	-3.2	-0 5	1 9	4 4	7 7	12 9	23 3
V/U_{TI}	0 4682	0 4615	0 4542	0 4524	0 4450	0 4371	0 4303	0 4234	0 4166	0 4072	0 3902	0 3717
V'/U_{TI}	1 1061	1 0680	1 0349	0 9988	0 9607	0 9220	0 8765	0 8334	0 7860	0 7349	0 6737	0 5939
β'	64 70	64 20	63.50	62 70	62 00	61.20	60.20	59 00	57 40	55 50	53 50	51 10
β	0	0	0	0	0	0	0	0	0	0	0	0
i_{MCL}	2 79	2 75	2 79	2 85	2 95	3 10	3 27	3 78	4.50	4 89	3.77	4 36
i_{SS}	0 69	0 81	0.79	0.73	0 81	0 95	0 99	1.43	1 78	1 65	0 01	-0.58
M'	1 647	1 591	1 526	1.479	1 420	1 356	1 291	1 225	1 150	1 068	0 973	0 875
M	0 704	0 693	0 681	0 678	0 666	0 653	0 642	0 631	0 620	0 605	0 578	0 549

<u>Overall Parameters</u>

	1	2	3	4	5	6	7	8	9	10	11	12
$\bar{r}/r_{TI}$	0 9847	0 9499	0 9158	0 8810	0 8441	0 8045	0 7613	0 7168	0 6674	0 6130	0 5560	0 4885
$\Delta T/T_I$	0 1473	0 1417	0.1398	0 1396	0 1407	0 1442	0 1488	0 1498	0 1446	0 1400	0 1377	0 1388
$\bar{\omega}$	0 080	0 065	0 060	0 061	0 068	0 085	0 110	0 120	0 100	0 082	0 073	0 080
D	0 216	0 235	0 252	0 270	0 290	0 315	0 347	0 382	0 405	0 414	0 400	0 370
η_{ad}	0.854	0 880	0.892	0.894	0 886	0 867	0 839	0 837	0.870	0.900	0.920	0.927
σ	1.620	1 615	1 612	1 614	1 623	1 648	1 664	1 689	1.727	1 773	1 869	2 080

Blockage factor = 0 955   <u>Exit</u>

	1	2	3	4	5	6	7	8	9	10	11	12
r_2/r_{TI}	0 9701	0 9388	0 9068	0 8747	0.8392	0.8010	0 7613	0 7189	0 6722	0 6228	0 5713	0 5150
P_T/P_I	1.5120	1 5097	1 5091	1 5090	1 5093	1 5097	1.5106	1 5116	1 5127	1 5143	1 5168	1 5274
T_T/T_I	1 1473	1 1418	1 1398	1 1394	1 1407	1 1442	1 1488	1 1498	1 1444	1 1400	1 1375	1 1388
U/U_{TI}	0 9701	0 9388	0 9068	0 8747	0 8392	0 8010	0 7613	0 7189	0 6722	0 6228	0 5713	0.5150
V_θ/U_{TI}	0 7854	0 7573	0 7168	0 6818	0 6376	0 5858	0 5253	0 4660	0 4117	0 3512	0 2789	0 1884
V_M/U_{TI}	0 4735	0 4317	0 4086	0 3893	0 3774	0 3699	0 3656	0 3637	0 3643	0 3755	0 3930	0 3993
φ	-11 5	-8 2	-6 4	-4 3	-2.5	-0 7	0 8	2 7	4 0	7 6	12.0	17 7
V/U_{TI}	0 5072	0.4654	0 4510	0 4354	0 4298	0 4292	0.4361	0 4429	0 4479	0 4641	0 4910	0 5170
V'/U_{TI}	0 9170	0.8715	0.8260	0 7835	0 7405	0 6925	0 6400	0 5908	0 5496	0 5140	0 4822	0 4417
β'	58 9	60 3	60.4	60 2	59 4	57 7	55 1	52 0	48 5	43 1	35 4	25 3
β	21 0	21 7	25.0	26 6	28.6	30 5	32 8	34 8	35 5	35 9	36 7	39 3
M'	1 291	1 221	1 152	1 093	1 031	0 962	0 888	0 821	0.766	0 720	0 680	0 625
M	0 715	0 652	0 630	0 607	0 598	0.596	0 605	0 615	0 624	0 650	0 692	0 732
δ°	3 72	3 73	3 89	4 14	4.28	4 30	4 34	4 27	4 36	5 21	6 52	10 08

47
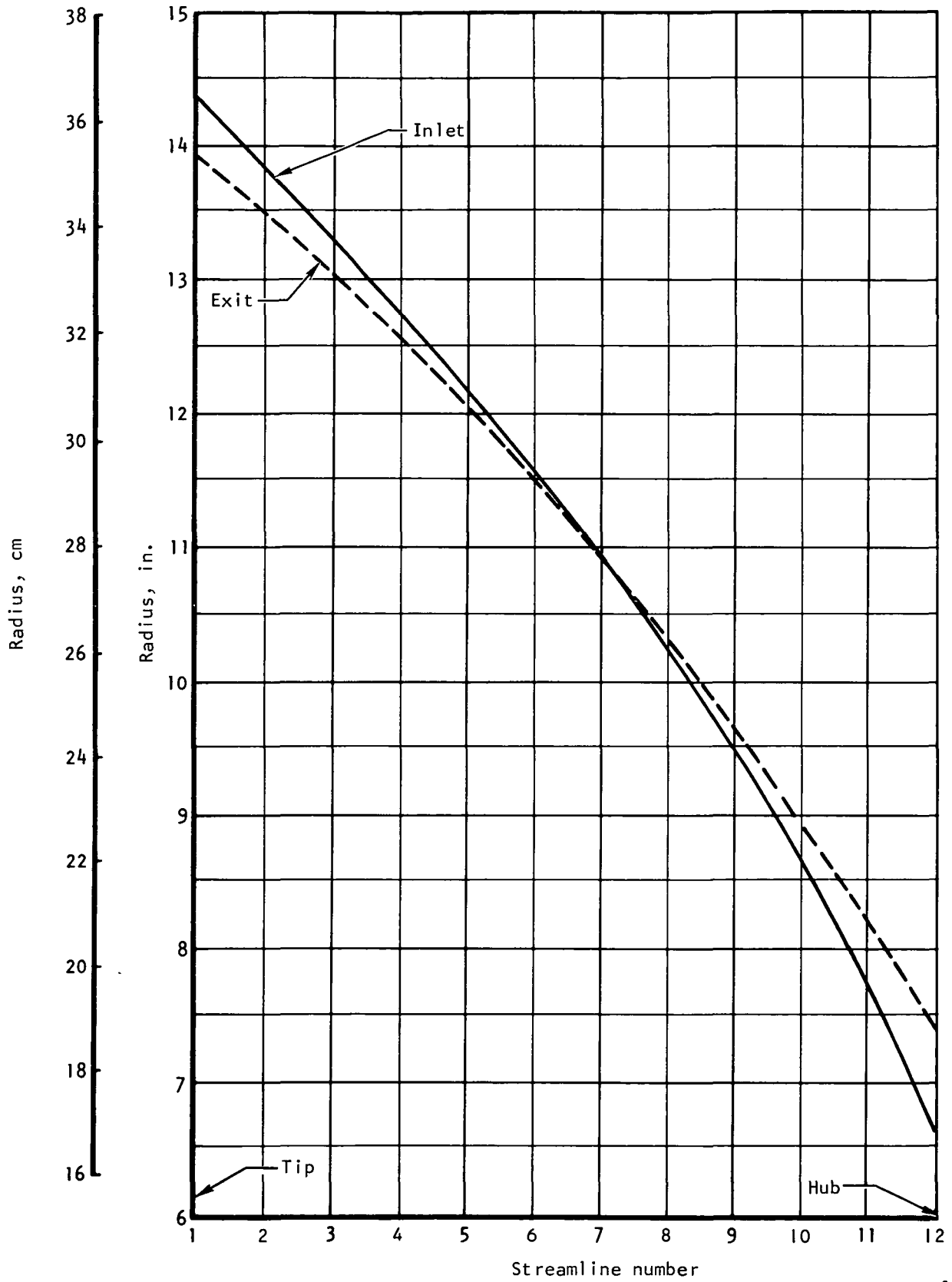
Figure 12.--Rotor Inlet and Exit Radial Streamline Locations.

S-71879

48

Design flow regimes.--The Mach numbers relative to the rotor at inlet and exit are presented in fig. 13. At rotor inlet the outer half of the flow may be considered supersonic and the inner half transonic. Flow exiting from the rotor is supersonic from the tip to streamline no. 5, and subsonic inboard from that location.

Relative flow angles.--The distribution of the airflow angles relative to the rotor blade at the rotor inlet and outlet are presented in fig. 14. The relatively high values of the inlet flow angles, varying from about 50 to 65 deg, reflect the high rotational speed of this rotor. The distribution of the rotor blade outlet flow angles is somewhat unusual, showing a maximum value at streamline no. 4 with the minimum required turning angle occurring in this zone. As mentioned previously, this variation of rotor outlet flow angle and of the required turning angle, β_1' minus β_2', results from the wall curvature effects on the radial variation of rotor inlet and outlet meridional velocity.

Section solidity and thickness.--The rotor blade solidity and section thickness to chord ratio (t_m/C), figs. 15 and 16, respectively, result from compromises between the aerodynamic and mechanical design considerations. The rotor tip solidity of about 1.62 was chosen solely from aerodynamic design considerations. The number of rotor blades, their taper, and average chord were fundamentally fixed by the contractually specified aspect ratio and structurally allowable chord and cross-sectional area taper. Initially a linear variation with radius of maximum thickness in percent of chord length was assumed. The final distribution shown in fig. 16 does not vary greatly from this selection. Fig. 17 gives the chordwise location of the maximum thickness as a function of streamline number.

Total pressure ratio and loss coefficients.--The objective radial distribution of stage pressure ratio for this transonic fan is constant. The variation in rotor outlet total pressure ratio (fig. 18) therefore reflects the expected higher total pressure loss in the stator end wall regions. The rotor outlet total pressure ratio is highest at the hub because the Mach number, turning requirements, and hence loss for the stator vane sections are greatest at the hub. The rotor diffusion factor calculated using the axisymmetric program is presented in fig. 19. The profile component of the rotor total loss coefficient, $\bar{\omega}_p$, is considered to be a function of the diffusion factor and radius. The variation of this profile loss coefficient, $\bar{\omega}_p$, is presented in fig. 20 and shows the trend with streamline number as would be expected from diffusion factor variations. The component of rotor total loss coefficient at design operation due to supersonic flow and shock waves is expected to be different in this rotor from any previous design because of the avoidance of strong tip shock.

There is no direct precedent upon which to estimate the total pressure loss coefficients for this design wherein the total is composed of shock and profile losses. In the all-supersonic outboard region only weak oblique shocks are expected so the shock losses are anticipated to be very low. This should also be true near the hub contour where the relative flow has either subsonic or low
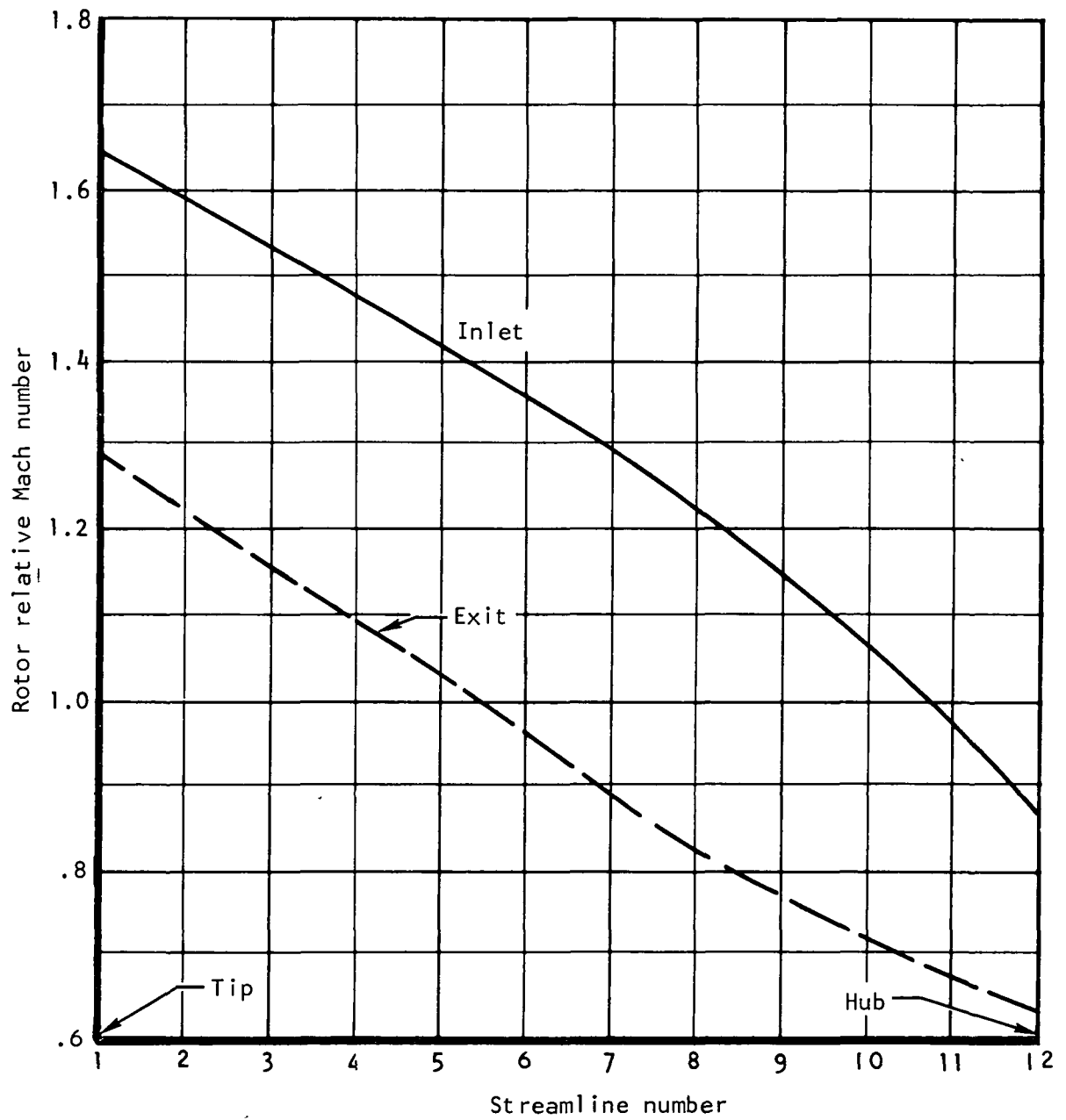
Figure 13.--Rotor Relative Mach Number.

S-71924

50
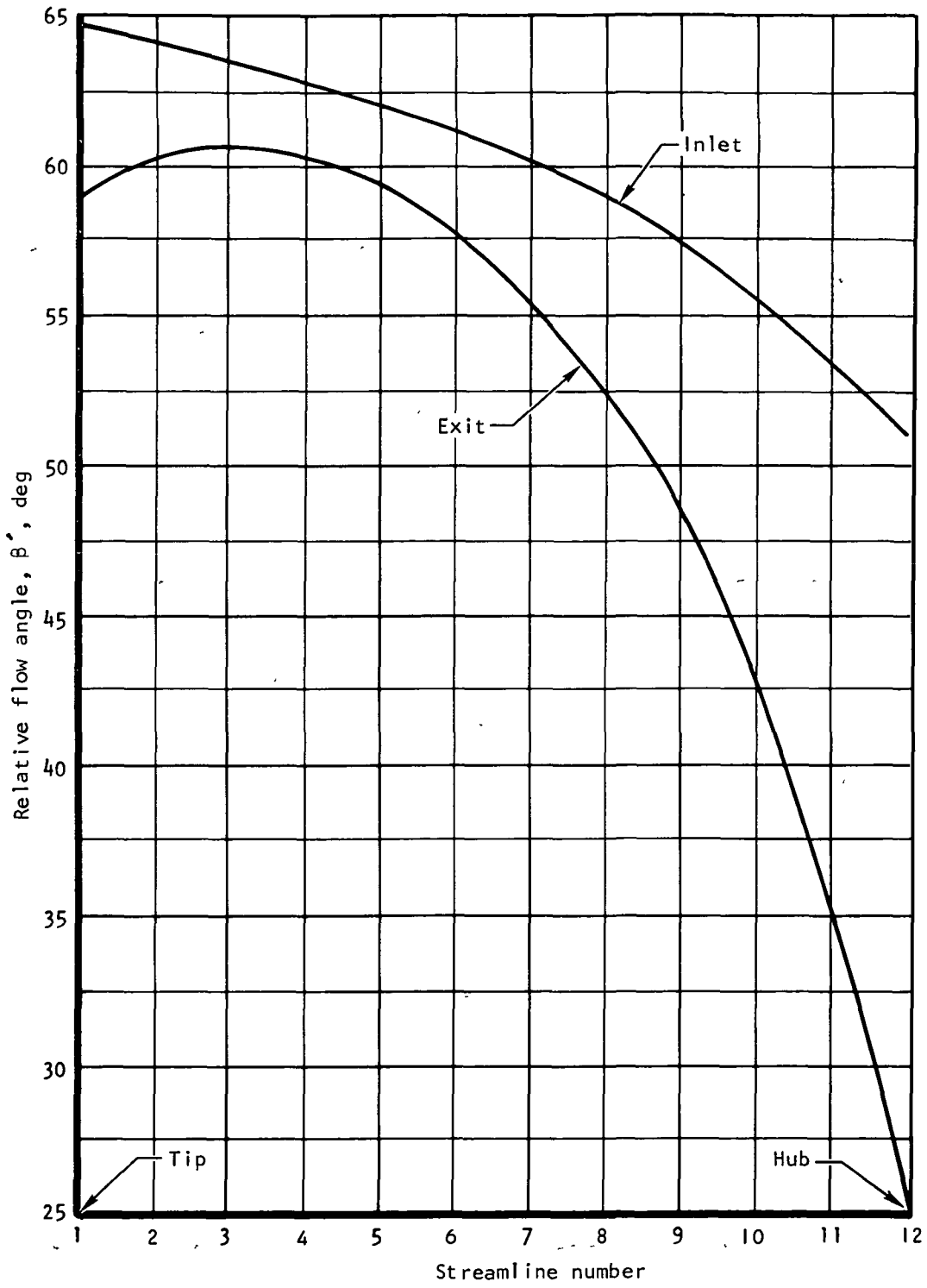
Figure 14.--Rotor Relative Flow Angles.
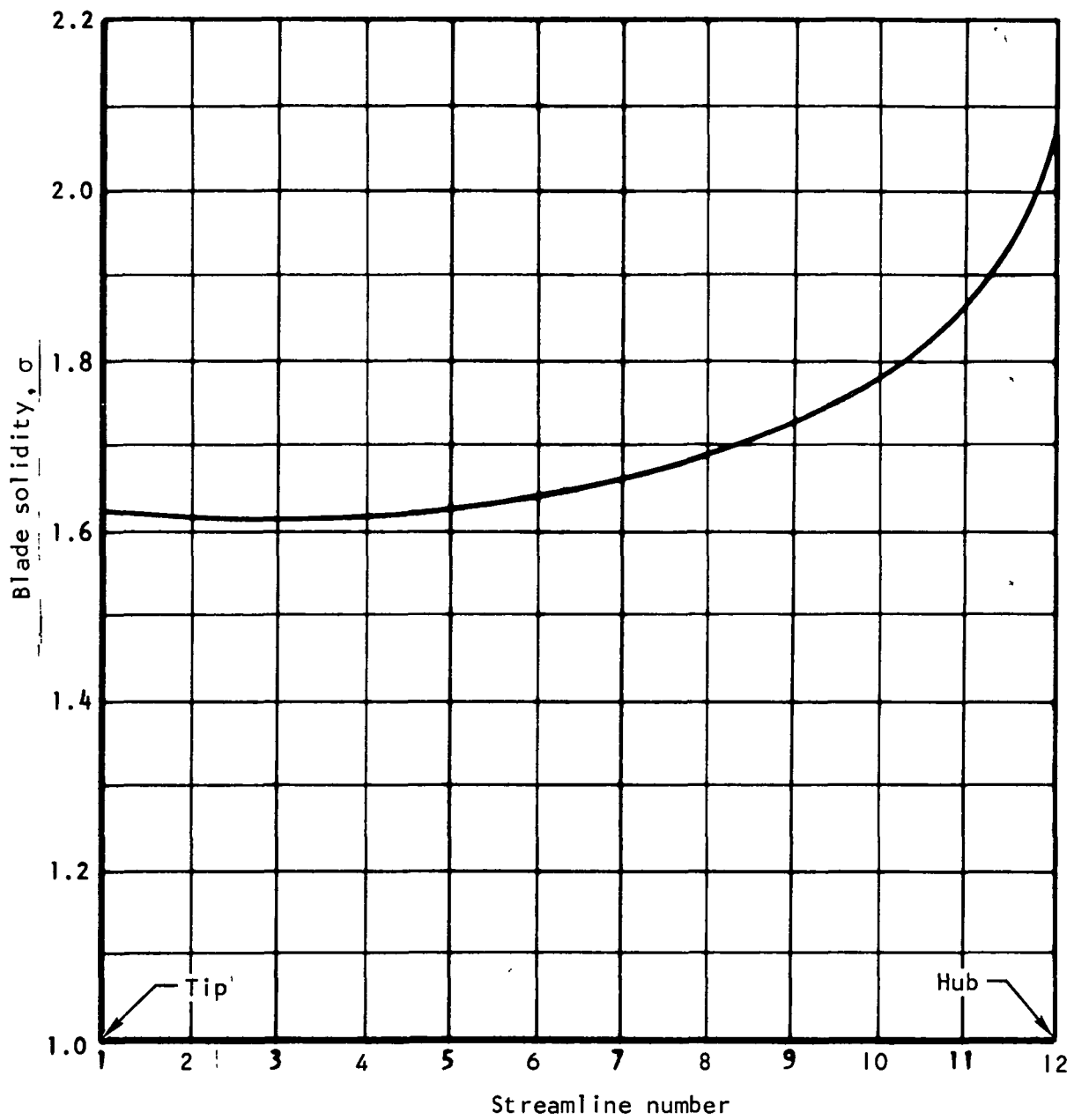
S-71915

51

Figure 15 .--Rotor Blade Solidity.

S-71891

52
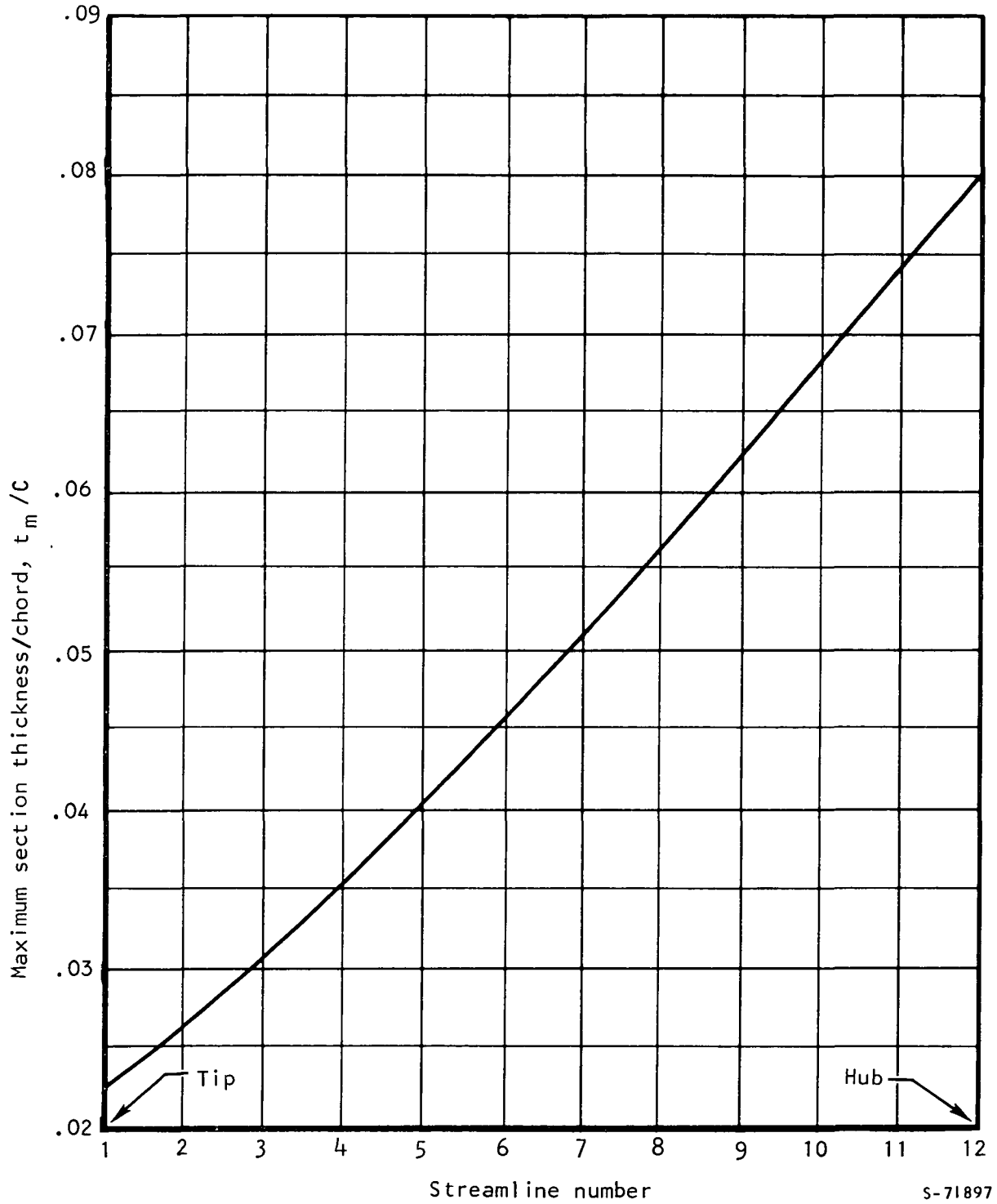
Figure 16.--Rotor Section Maximum Thickness-to-Chord Ratio.
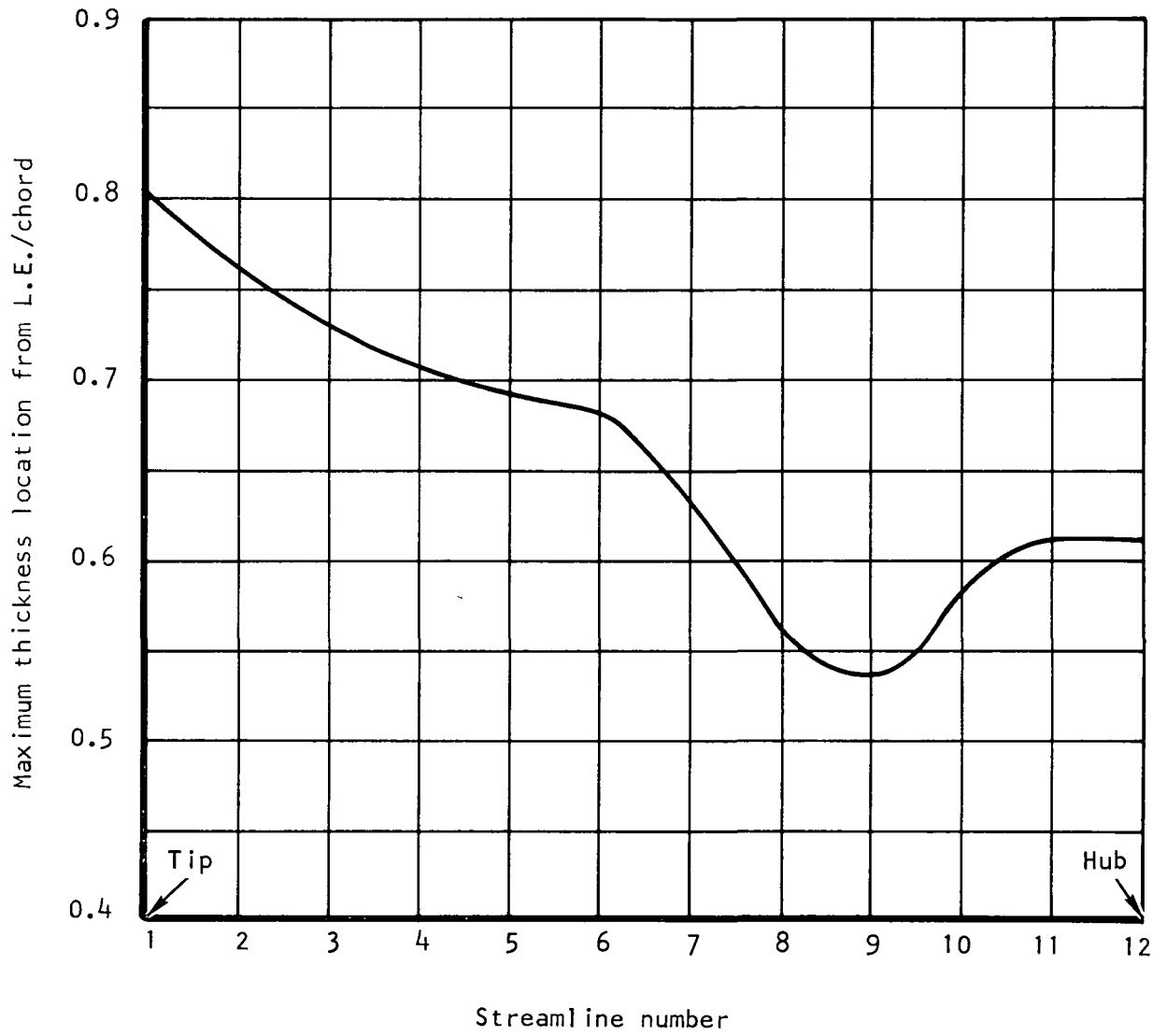
Figure 17 .--Rotor Maximum Thickness Location.

S-74103

54
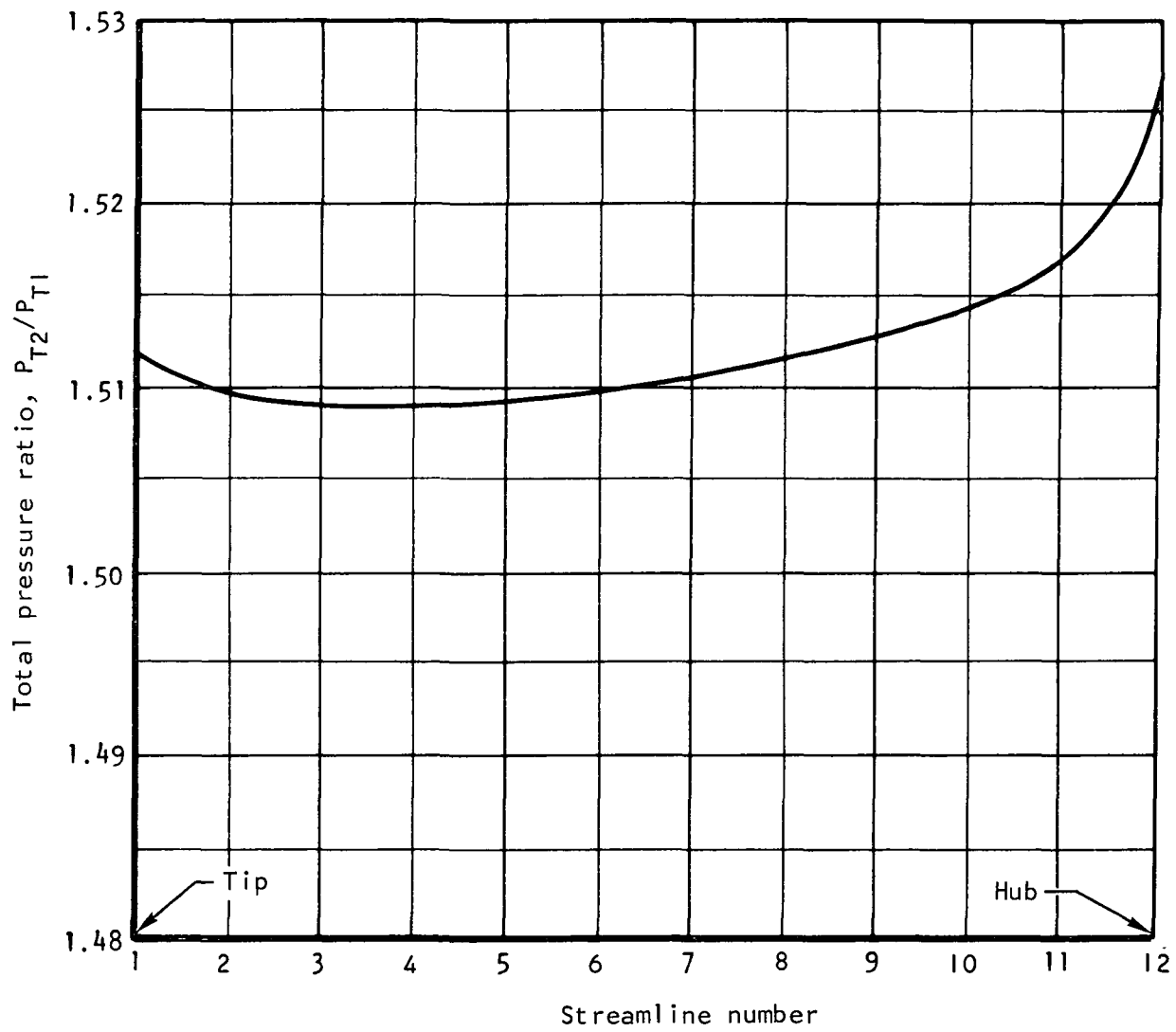
Figure 18.--Rotor Total Pressure Ratio.

S-71901
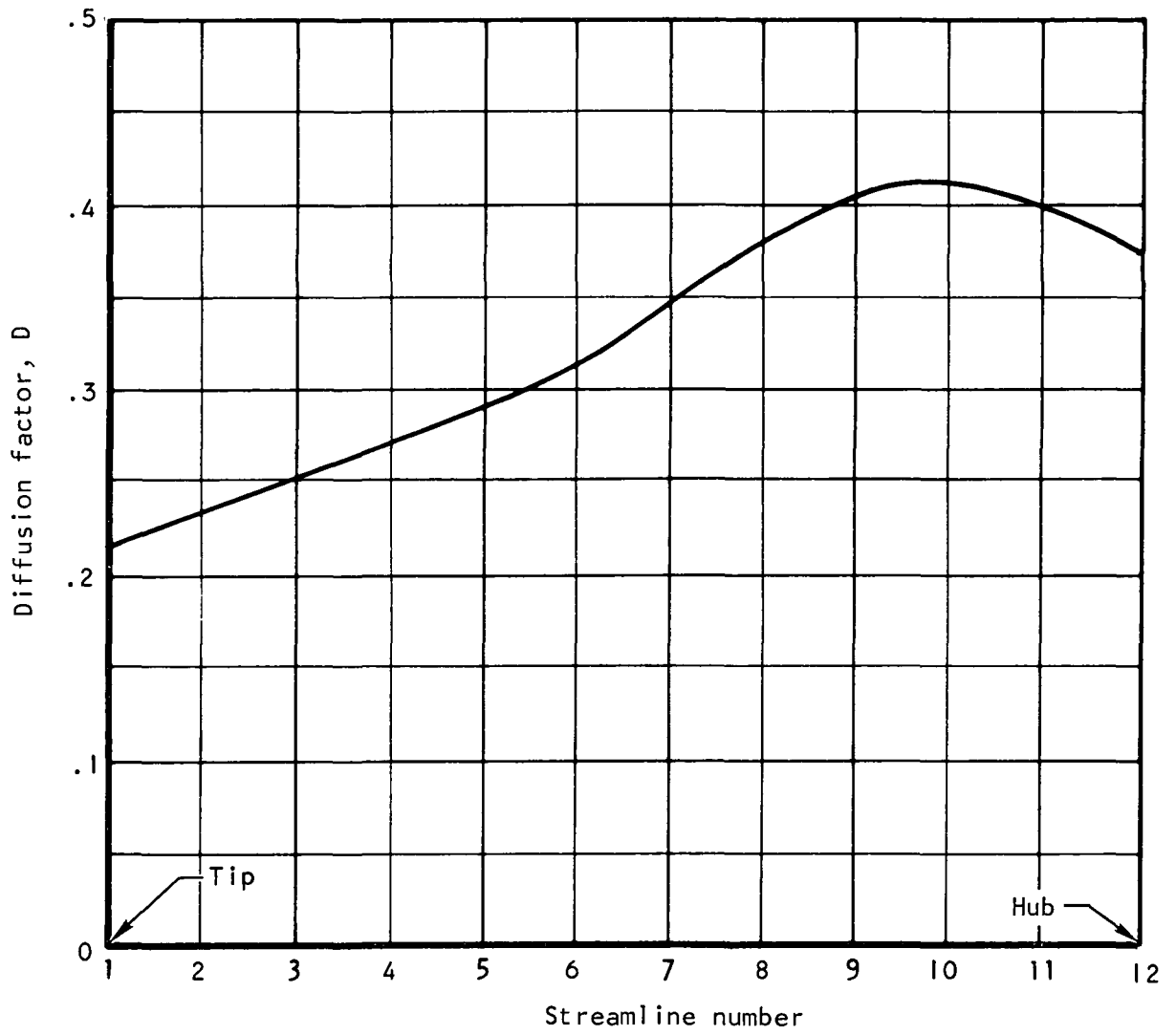
Figure 19.--Rotor Diffusion Factor.

S-71896

56
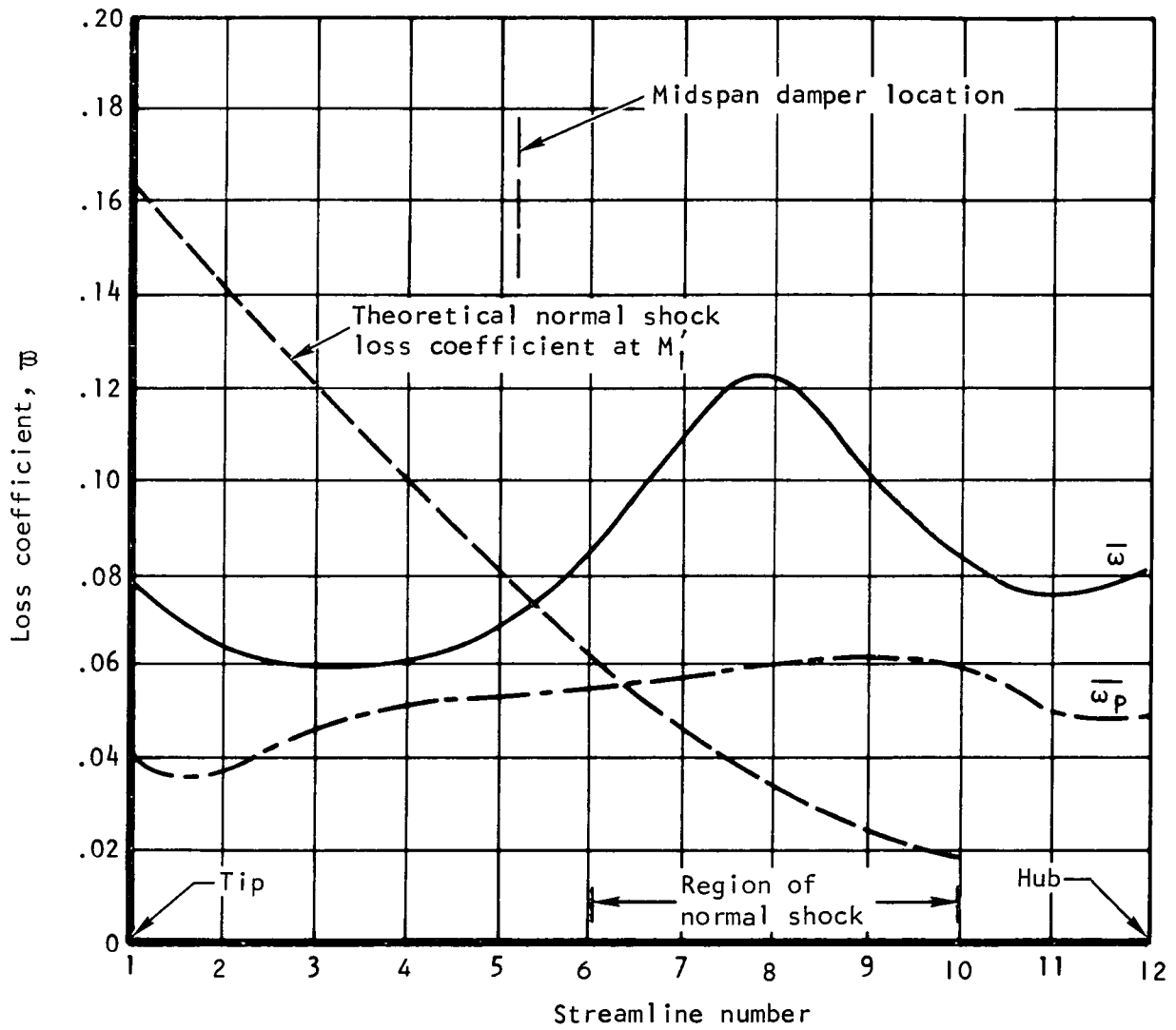
Figure 20.--Design Loss Coefficient.

transonic values. In the intermediate zone between streamlines nos. 6 and 10, bow waves are anticipated. The strong shocks are expected to occur in the region around streamline no. 8 (see fig. 20). The additional total pressure loss due to rapid boundary layer growth and probable separation is expected to be maximum in_this region. For this reason, the additional component of loss coefficient, ω_s, attributable to shock losses, has been given a maximum value of twice the normal shock loss in this zone (fig. 20). From this maximum, additive values of ω_s have been tapered off smoothly to low values in the subsonic and in the all-supersonic regions. At both walls, the loss coefficient has been increased to reflect wall boundary layer and clearance effects, but the increase is anticipated to be small due to the design condition of low diffusion across this rotor and particularly across the hub and tip elements where high calculated meridional velocity ratios exist at the walls. These considerations result in the fig. 20 variation of shock loss coefficient with radius. The resulting combined total-pressure-loss coefficient is also indicated in fig. 20.

Although a localized loss associated with the midspan damper will occur, the decision was taken to distribute a 1-percent loss in relative total pressure uniformly across the rotor exit. This distributed loss is included in fig. 20. The reason for not attempting to model the loss locally is that for an essentially constant total pressure ratio the computer program would tend to give a locally increased camber yielding small local blade irregularities which could compromise mechanical integrity in the high stress region of the midspan damper. Due to the high sweep angle of the damper (71 deg) and the low normal Mach number (0.67), there is reason to expect minimum flow disturbance by the damper even though the relative Mach number of 1.43 is higher than used in current practice.

Element temperature rise and efficiency.--The normalized rotor total temperature rise presented in fig. 21 reflects the work input required in order to produce the desired stage total pressure ratio while considering the combined total loss coefficient anticipated to occur. The calculated element efficiency of the rotor for each streamline is shown in fig. 22, presenting a near mirror image of the fig. 21 temperature rise distribution. In practice, it might be expected that lower efficiencies than the 85 percent calculated at the tip may occur in that region and that higher values than the 82 percent minimum calculated between the streamlines nos. 7 and 8 may also be realized. However, the calculated mass-averaged rotor efficiency of approximately 86.7 percent (including the distributed one percent total pressure loss allowance for the midspan damper) appears to be a valid expectation.

Incidence, deviation, and blockage.--The incidence was primarily influenced by the section incidence correction as defined in Appendix D. The resulting incidence angles with respect to the suction surface and mean camber line are shown in fig. 23.

In the all-supersonic outboard region of the rotor, the deviation angles, fig. 24, were determined by aerodynamic analysis during the calculation of the airfoil sections. For the inboard zone of the rotor having subsonic exit Mach number, the deviation angle was calculated using Carter's rule with an adjusted additive factor shown in fig. 24.
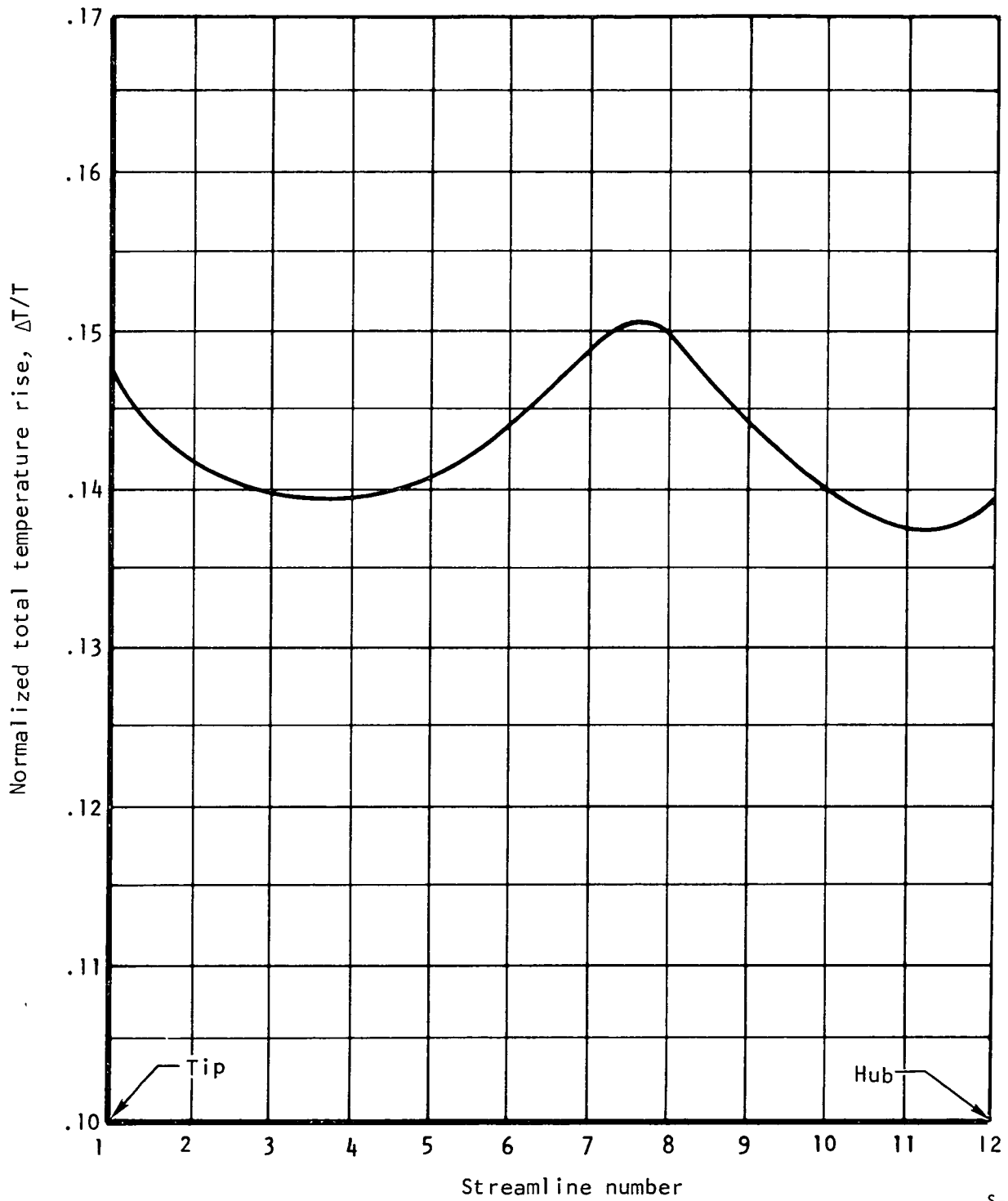
Figure 21.--Normalized Rotor Total Temperature Rise.

S-71912

59
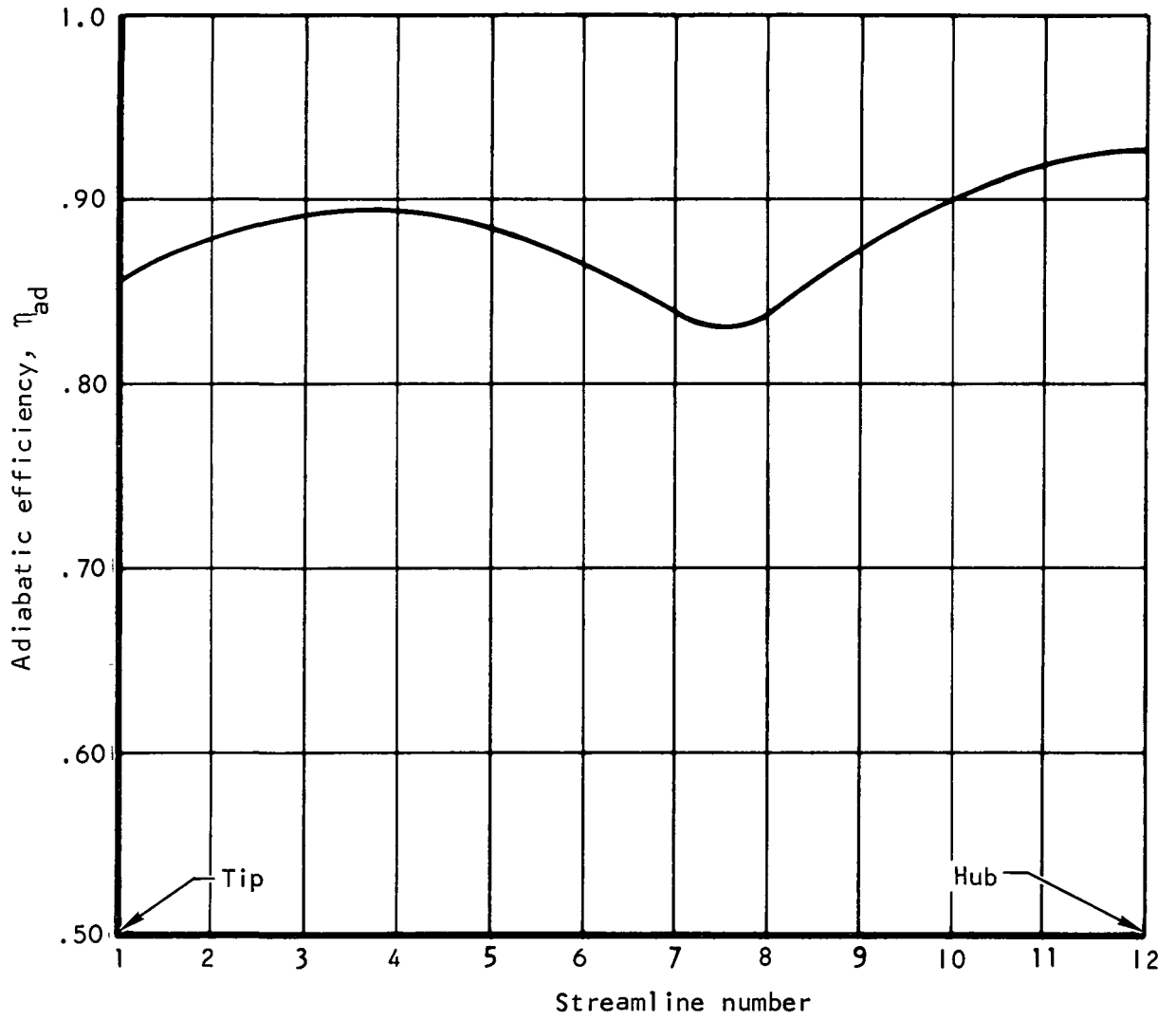
Figure 22.—Rotor Element Adiabatic Efficiency.

S-71913

60
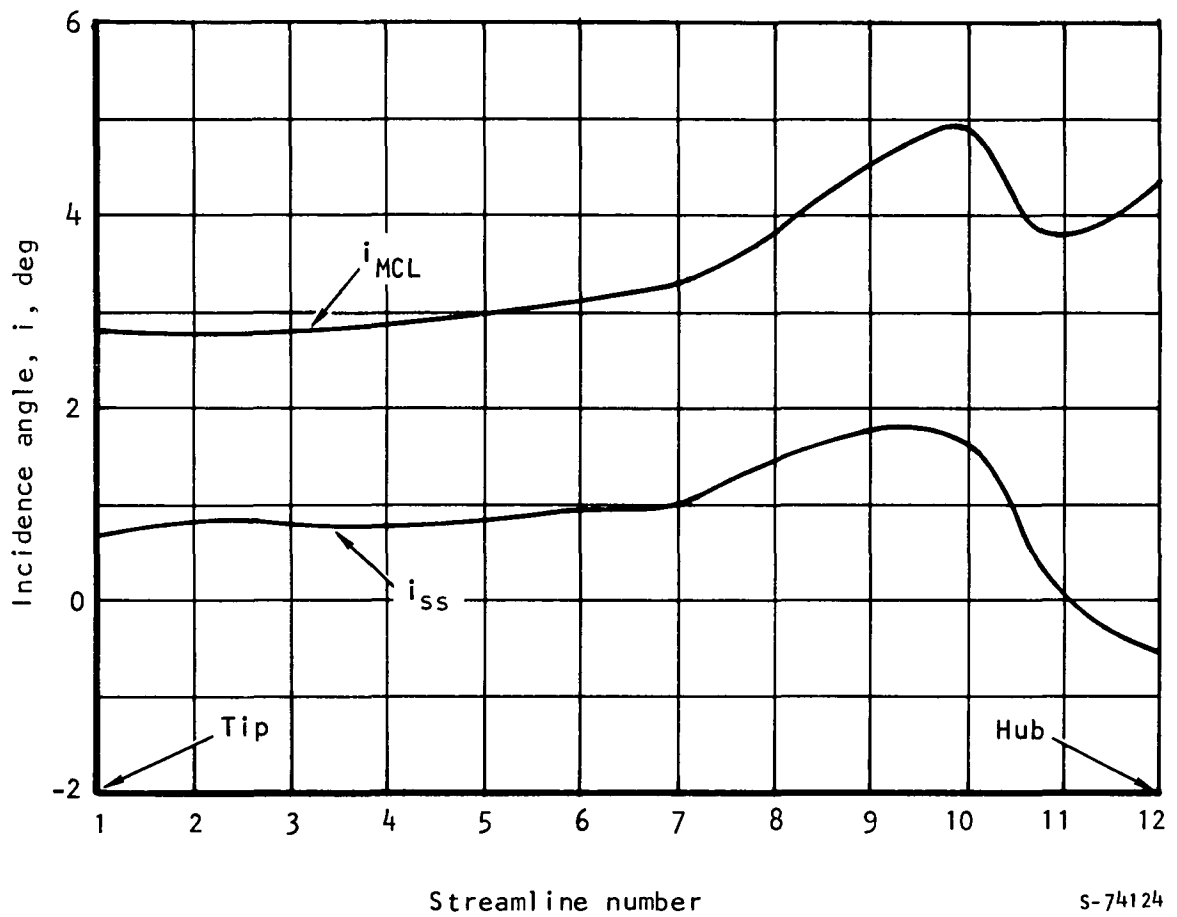
Figure 23.--Rotor Incidence Angles.

S-74124

61
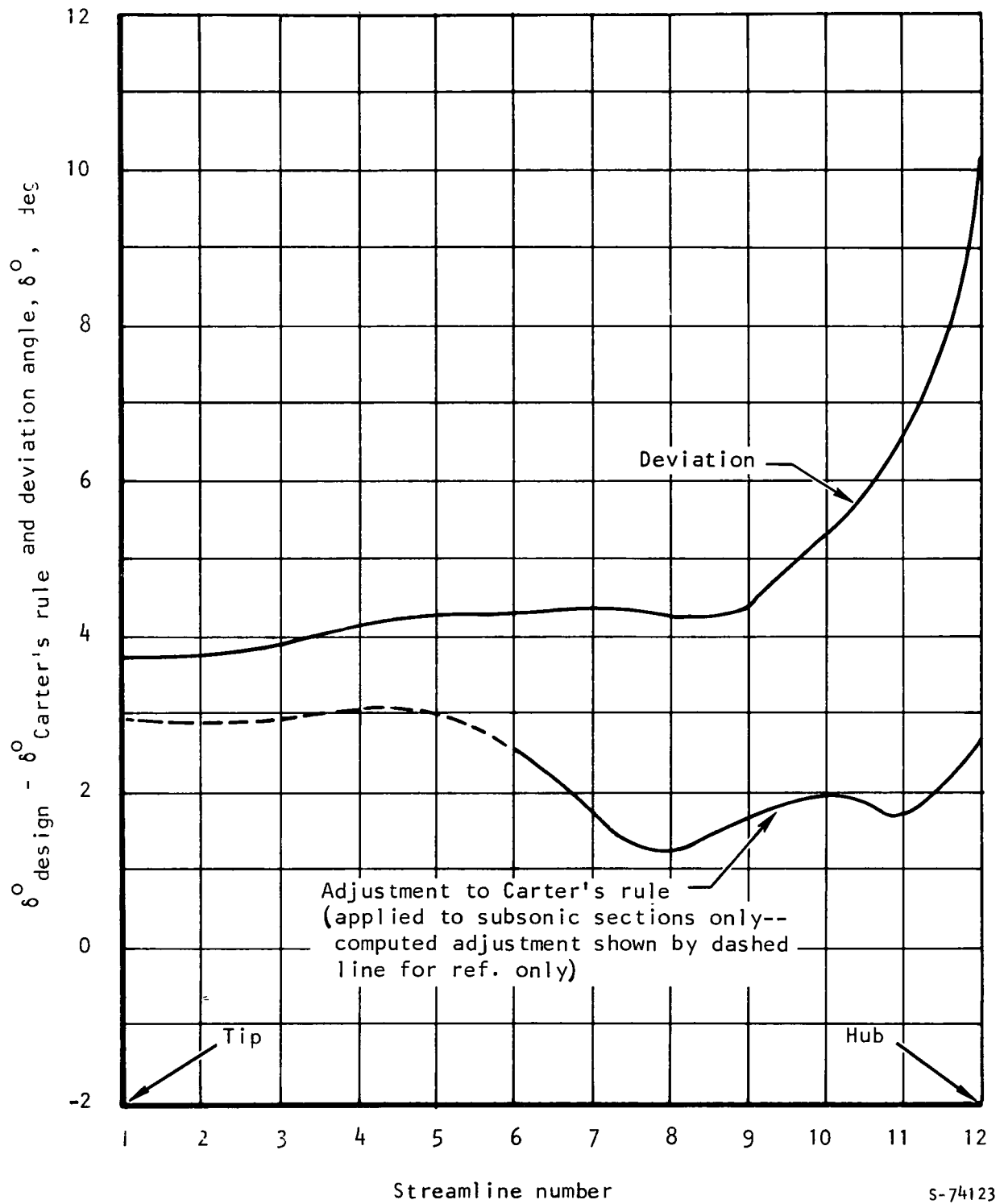
Figure 24.--Rotor Deviation and Carter's Rule Adjustment.

62

An inlet total blockage factor of 0.98 and an exit total blockage factor of 0.955 were assumed for the design pass and held constant span-wise. Realistic blockages based on a preliminary design were used through the blade. Typical rotor blockages for streamlines 1, 6, and 12 are listed below.

Streamline	Percent Axial Chord								
	0	12.5	25.0	37.5	50	62.5	75.0	87.5	100
1	0.980	0.945	0.928	0.919	0.910	0.903	0.894	0.898	0.955
6	0.980	0.960	0.916	0.896	0.870	0.834	0.831	0.890	0.955
12	0.980	0.870	0.820	0.794	0.781	0.784	0.810	0.860	0.955

Rotor start margin.--The rotor starting margin for streamlines 1 through 8, which include the all-supersonic outboard sections and sections similar in shape to these outboard sections, was calculated by the procedures described in Appendix D. Start margin is defined as the percentage by which the channel flow area exceeds the minimum area needed to pass the normal shock. These characteristics are presented in fig. D-1, Appendix D. As shown therein, the start margin varies from approximately 5 percent for section 1 to about 2.5 percent for section 8.

Additional rotor calculations.--In the process of the current design, three separate versions of the axisymmetric design program were used.

(1) The streamfilament program with calculational stations at the inlet and outlet of the blade rows (total of 14 computational stations)

(2) The streamfilament program with calculational stations at seven axial positions inside the blade row (total of 28 computational stations)

(3) A new axisymmetric program using a finite difference solution to the radial component of the equations of motion with blade interior grid points

All aerodynamic results presented prior to this point were obtained from program (3) above. The calculated flow conditions including relative angle agreed well for all calculational procedures except for relative angle at the rotor trailing-edge station. The results are indicated in fig. 25, showing a significant difference, particularly at the inner radii. The finite difference results were selected for the final design because it was felt that the particular calculation appeared to handle the blade blockage just upstream of the rotor trailing edge somewhat better than the stream filament program.

Stator Design Summary

The stator design is based on inlet and outlet velocity diagrams compatible with the rotor final aerodynamic design and zero stator outlet swirl. The axisymmetric computer pass on which this design was based utilized calculating stations at the blade row leading and trailing edges. A blockage factor of 0.955 which was compatible with the rotor trailing-edge value was used at the inlet to the stator. On the basis of available empirical data this blockage was assumed to decrease to 0.940 at the stator exit plane. A tabulated summary of aerodynamic parameters at the leading- and trailing-edge stations is presented in table 2 with some of the more pertinent parameters plotted in figs. 26 through 28.

63
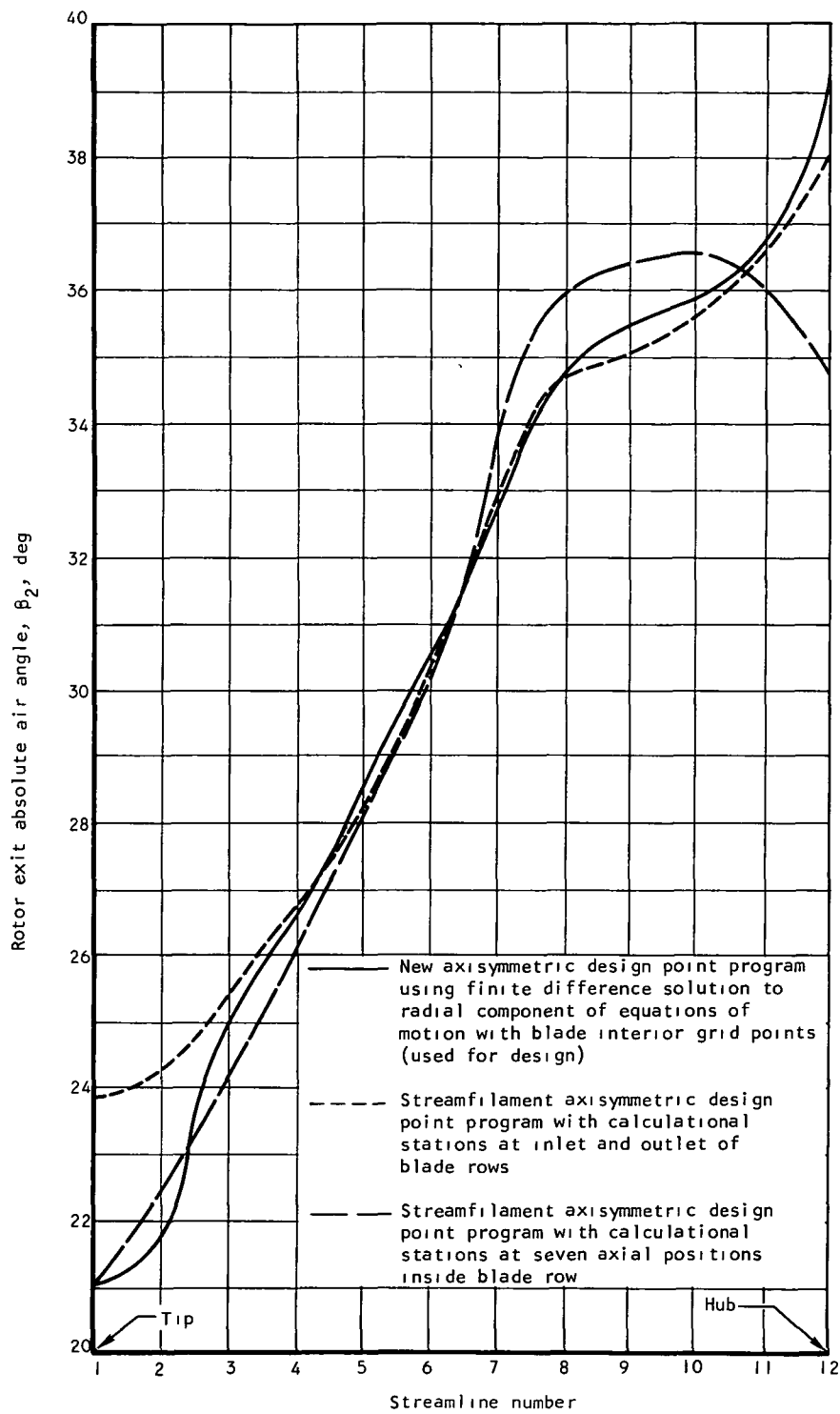
Figure 25.--Rotor Exit Absolute Air Angles.

S-72471

64

TABLE 2

STATOR AERODYNAMIC SUMMARY

$$P_{TI} = 14.696 \text{ psia} = 10.133 \text{ N/cm}^2$$
$$T_{TI} = 518.69 \text{ }^\circ R = 288.16 \text{ }^\circ K$$
$$N/\sqrt{\theta} = 12781 \text{ rpm} = 1338.4 \text{ rad/s}$$
$$W\sqrt{\theta}/\delta = 147.91 \text{ lbm/s} = 6.709 \text{ kgm/s}$$
$$U_{TI} = 1603.0 \text{ ft/s} = 488 \text{ } 594 \text{ m/s}$$
$$r_{TI} = 14.370 \text{ in.} = 0.3650 \text{ m}$$

Blockage factor = <u>0.955</u> Inlet

Streamline	1	2	3	4	5	6	7	8	9	10	11	12
r_2/r_{T_I}	0.9605	0.9313	0.9008	0 8690	0.8354	0 7999	0.7623	0 7221	0.6797	0 6351	0.5879	0 5377
% Flow	0	9 09	18.18	27 27	36 36	45.45	54 55	63 64	72 73	81.82	91 91	100.0
P_T/P_{T_I}	1.512	1.510	1.509	1 509	1.509	1 510	1.511	1 512	1.513	1 514	1 516	1 527
T_T/T_{T_I}	1.1474	1 1421	1 1399	1.1396	1.1406	1.1441	1.1488	1 1498	1 1443	1 1397	1 1374	1 1388
V_θ/U_{T_I}	0.1878	0.1871	0.1903	0 1965	0 2065	0.2208	0.2389	0.2539	0 2601	0.2695	0.2863	0 3163
V_M/U_{T_I}	0.4423	0.4292	0.4242	0 4180	0.4117	0.4080	0.4042	0.4049	0.4124	0.4230	0.4410	0.4729
V/U_{T_I}	0.4810	0.4685	0.4654	0.4616	0.4604	0.4635	0 4697	0.4779	0.4872	0.5016	0 5259	0.5689
β	23.0	23.5	24.1	25.2	26.6	28.4	30.6	32.1	32.2	32.5	32.4	33.7
M	0.669	0.653	0.649	0 643	0.641	0 645	0.653	0.665	0.681	0 704	0.743	0 811
i_{MCL}	-2.90	-2.62	-2.30	-1.87	-1.32	-0.62	0.25	0.80	1.05	1.28	1.70	2.30
i_{ss}	-9.05	-8.98	-8.88	-8.88	-7.60	-6.80	-5.80	-5.46	-5.20	-4.89	-5.20	-4.10

Overall parameters

	1	2	3	4	5	6	7	8	9	10	11	12
$\bar{r}$	0.9605	0 9308	0.9001	0 8681	0.8345	0 7994	0 7623	0 7230	0 6815	0 6377	0.5912	0.5415
$\Delta T/T_{T_I}$	0.1473	0 1417	0.1398	0.1396	0 1407	0.1442	0 1488	0.1498	0 1446	0 1400	0.1377	0.1388
$\bar{\omega}$	0.030	0.025	0.024	0 025	0.026	0.027	0.0285	0 030	0.0315	0 033	0 035	0 050
D	0.344	0.321	0.314	0.309	0.308	0.316	0 330	0.342	0.348	0.358	0 379	0 424
η_{ad}	0.834	0.866	0.878	0.879	0.873	0 852	0.826	0.820	0 851	0 879	0 894	0 885
σ	1.010	1.043	1.080	1.119	1.165	1.220	1.283	1 359	1.445	1.542	1.643	1.825

Blockage factor = <u>0.940</u> Exit

	1	2	3	4	5	6	7	8	9	10	11	12
r_3/r_{T_I}	0.9605	0.9303	0.8993	0 8672	0.8337	0.7988	0 7623	0 7238	0.6832	0.6403	0 5945	0.5452
P_T/P_{T_I}	1.500	1.500	1 500	1.500	1.500	1 500	1 500	1.500	1.500	1 500	1.500	1 500
T_T/T_{T_I}	1.1474	1.1421	1 1400	1 1396	1.1407	1.1441	1.1489	1 1498	1.1444	1.1398	1.1374	1 1388
V_θ/U_{T_I}	0	0	0	0	0	0	0	0	0	0	0	0
V_M/U_{T_I}	0.4080	0.4074	0 4074	0.4074	0 0474	0.4074	0.4080	0 4080	0 4080	0 4092	0 4124	0 4148
V/U_{T_I}	0.4080	0.4074	0.4074	0.4074	0.0474	0.0474	0 4080	0 4080	0 4080	0.4092	0 4124	0 4148
β	0	0	0	0	0	0	0	0	0	0	0	0
M	0.561	0.562	0.562	0.562	0 562	0.561	0.561	0 561	0.562	0.565	0 570	0 573
δ°	7.50	7.50	7.60	7.85	8.39	9.00	9.95	10.40	9.86	9.50	9.19	8.95
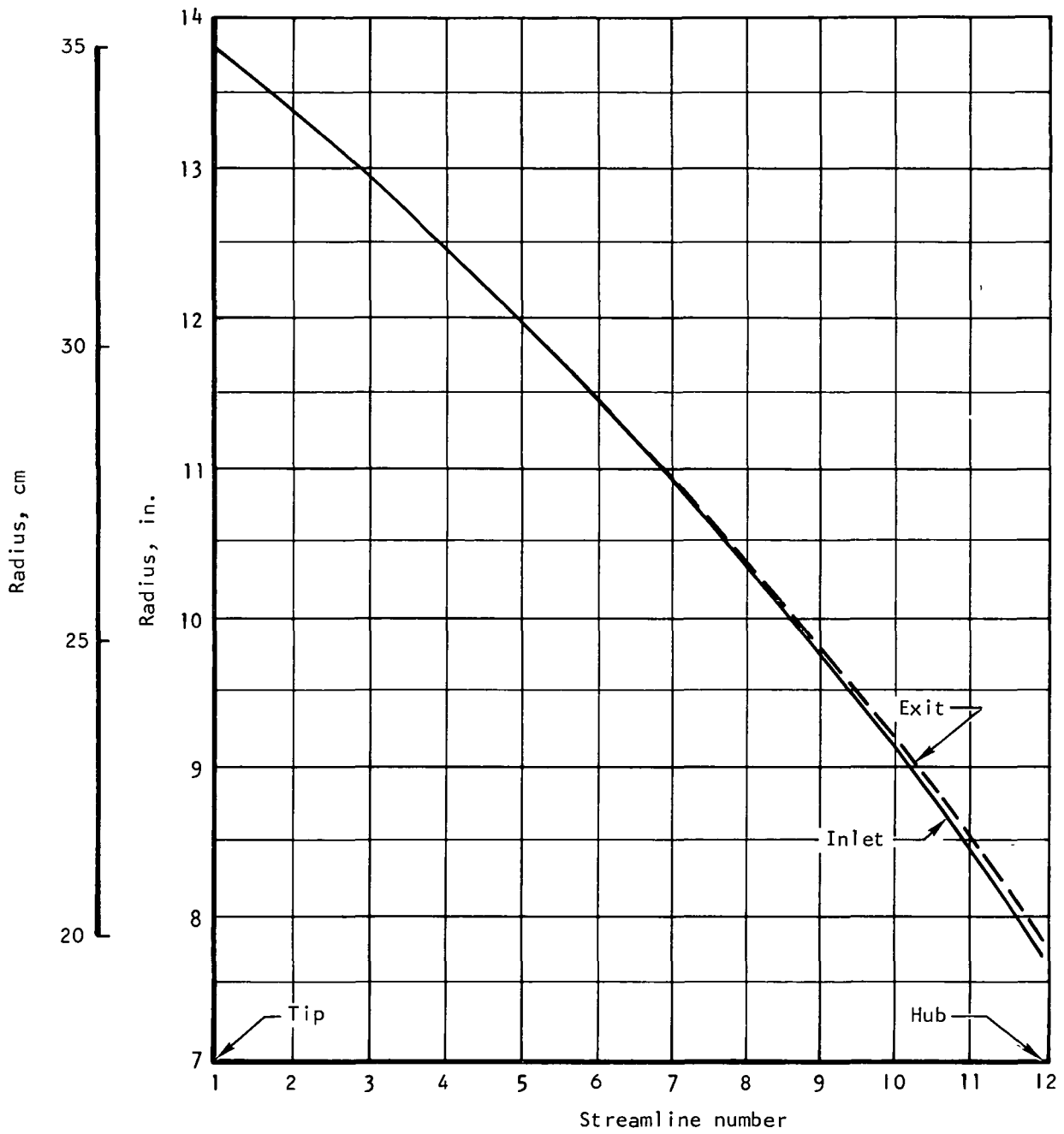
Figure 26.--Stator Inlet and Exit Radial Streamline Locations.

S-71898

66
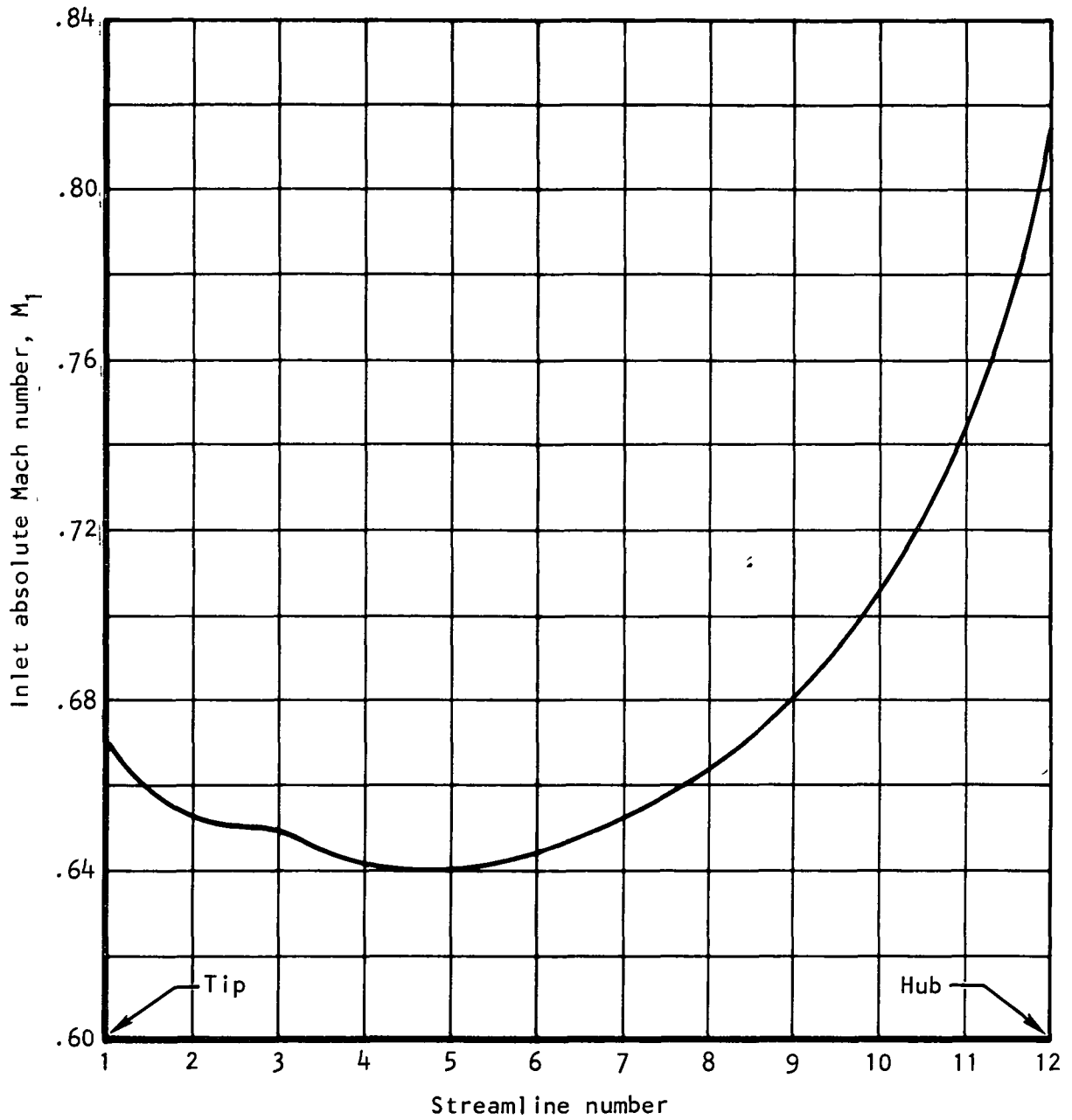
Figure 27.--Stator Inlet Absolute Mach Number.

S-74119
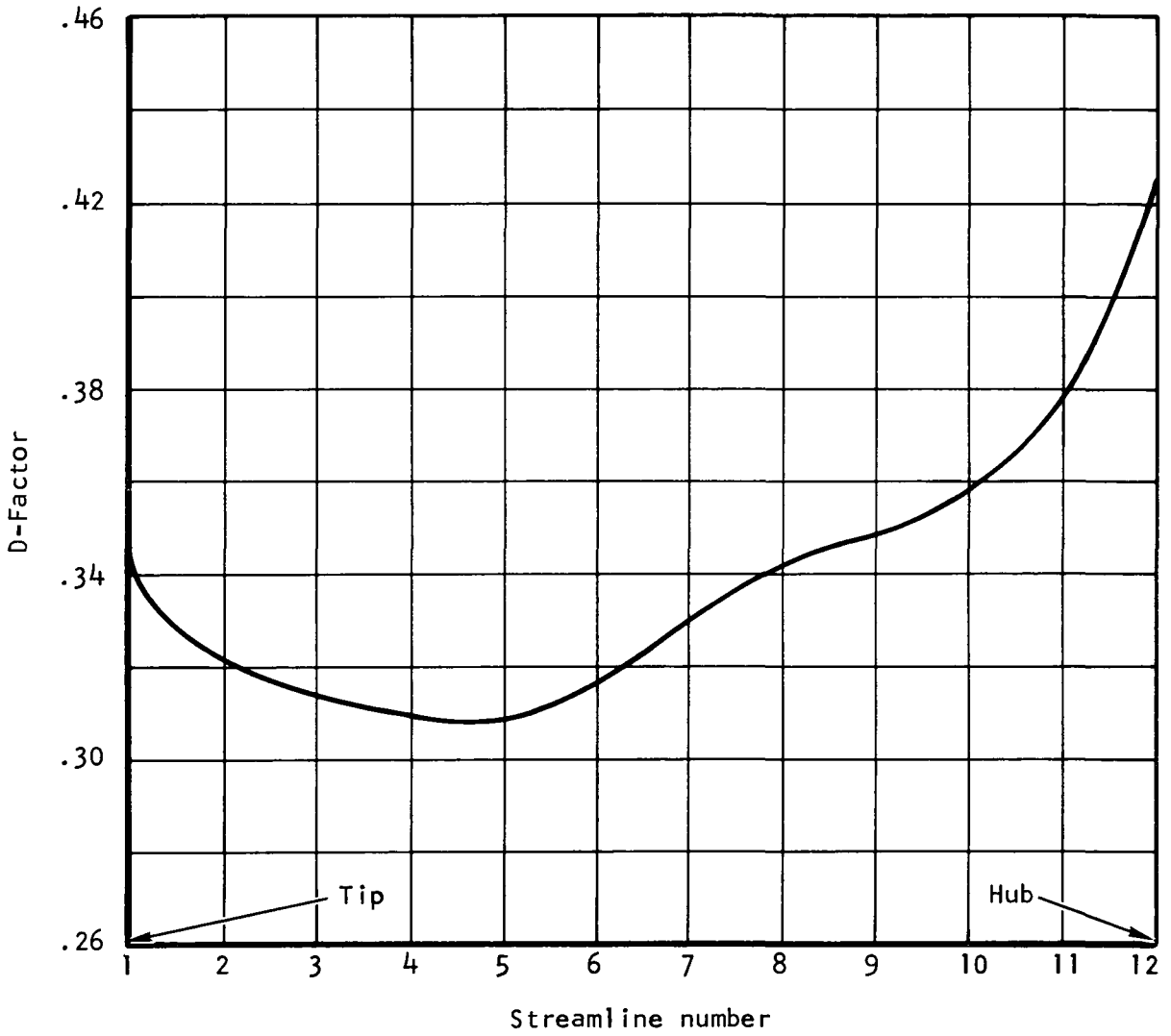
Figure 28.-- Stator D-Factor Variation.

Vane selection.--Both a special uncambered leading edge section and a double-circular-arc (DCA) section were considered for this design. The inlet hub Mach number of only 0.811 (maximum)and corresponding diffusion factor of less than 0.43 (solidity of 1.82) seemed near ideal conditions for a DCA stator. However, a general survey was made of the published literature on high and moderately high Mach number stators, and recent AiResearch experience on stators at inlet Mach numbers up to 0.94 was examined. The study showed strong evidence that DCA sections would perform at a level equal to or better than any other section type at the design Mach number and turning level (see table 2 and fig. 27). To further verify the suitability of DCA stator sections, a suction surface velocity option in the axisymmetric computer program incorporating 7 intra-blade-row stations (for both the rotor and stator) was used to approximate the stator pressure and suction surface velocity and Mach number levels. The results are shown in figs. 29 and 30 for the hub and tip streamlines. A linear variation (with axial chord) of turning and loss was assumed and the calculations based on moment of momentum change between the designated stations. Realistic blockages based on a preliminary design were used through the vane. Typical stator blockages used are tabulated below for streamlines 1, 6, and 12. For the above assumptions, the resulting peak suction surface velocity for the critical streamline (hub) is less than sonic at the design point. It also can be seen from fig. 29 that the ratio of peak suction surface velocity to trailing edge velocity is less than 1.7.

Percent axial chord									
Streamline	0	12.5	25.0	37.5	50.0	62.5	75.0	87.5	100
1	0.955	0.9135	0.8948	0.8833	0.8804	0.8847	0.8947	0.9104	0.9400
6	0.955	0.9054	0.8835	0.8699	0.8670	0.8723	0.8848	0.9041	0.9400
12	0.955	0.8829	0.8513	0.8323	0.8288	0.8376	0.8569	0.8862	0.9400

Losses.--The assumed spanwise loss distribution for the stator shown in fig. 31 is compatible with that of ref. 5 for similar type blading, inlet conditions, and loading.

Incidence and deviation.--The stator vane parameters of blade angle and camber angle corresponding to a given set of velocity triangles were defined utilizing the procedures given in Chapter VII of ref. 6. Some of the more pertinent parameters are plotted as figs. 32 through 35. The design mean-camber-line incidence is shown in fig. 36. The deviation based on Carter's Rule plus an additive factor is also indicated by fig. 36 with the additive factor shown separately in fig. 37. Small adjustments to original calculated blading parameters were made to obtain smooth leading and trailing edges. All the above tables and figures reflect the final design.

Choking incidence.--The designed stator was evaluated for the incidence angle corresponding to sonic flow at the throat. This incidence angle, denoted the ideal choking incidence angle, imposes the minimum permissible design angle. This choking incidence angle is shown in fig. 38. The procedure for determining the ideal choking incidence angle is thoroughly explained in ref. 7.
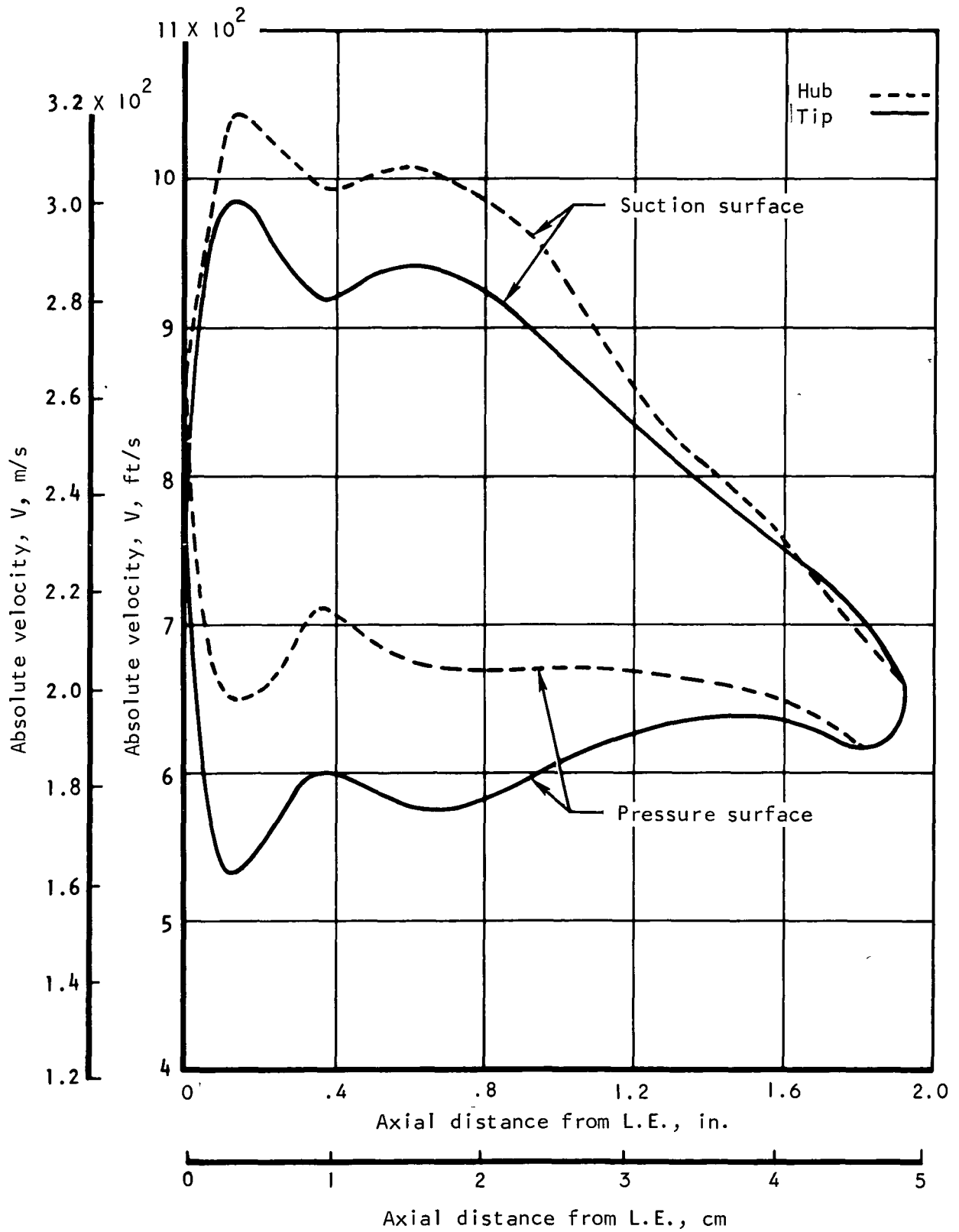
Figure 29.--Stator Surface Velocity Distributions.

S-71928

70
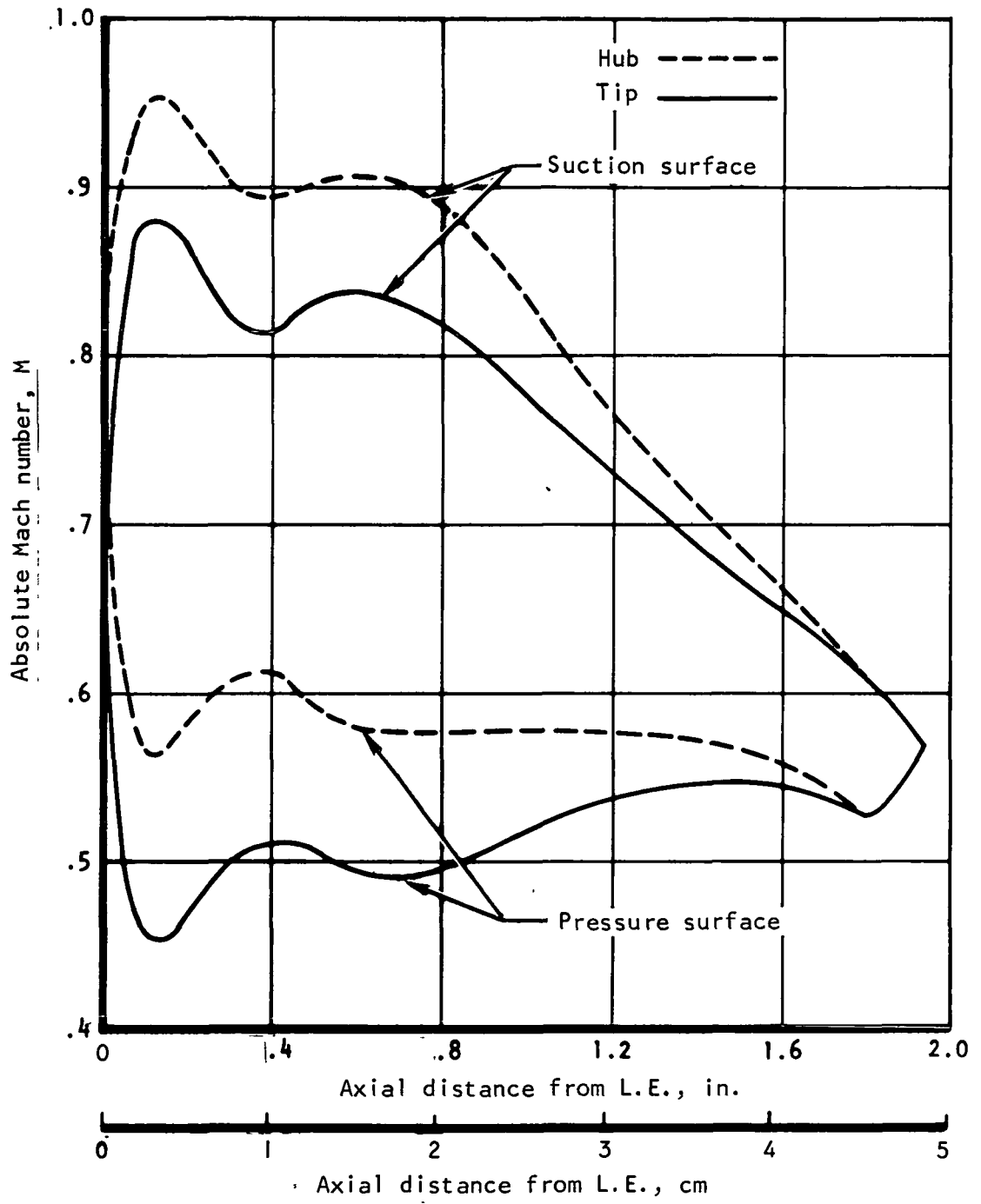
Figure 30.--Stator Surface Mach Number Distributions.   S-71902
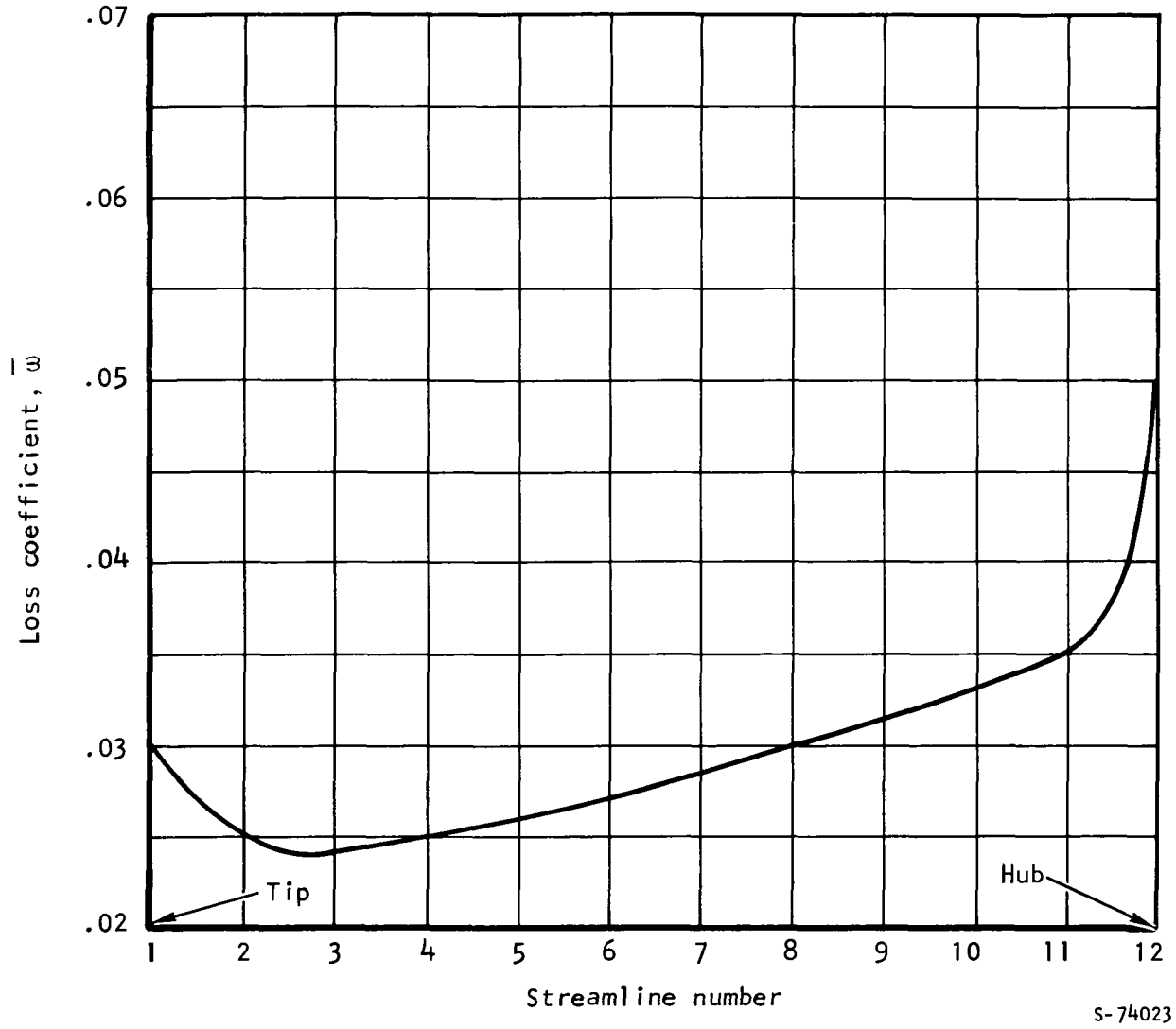
Figure 31.-- Stator Loss Coefficient.

S-74023
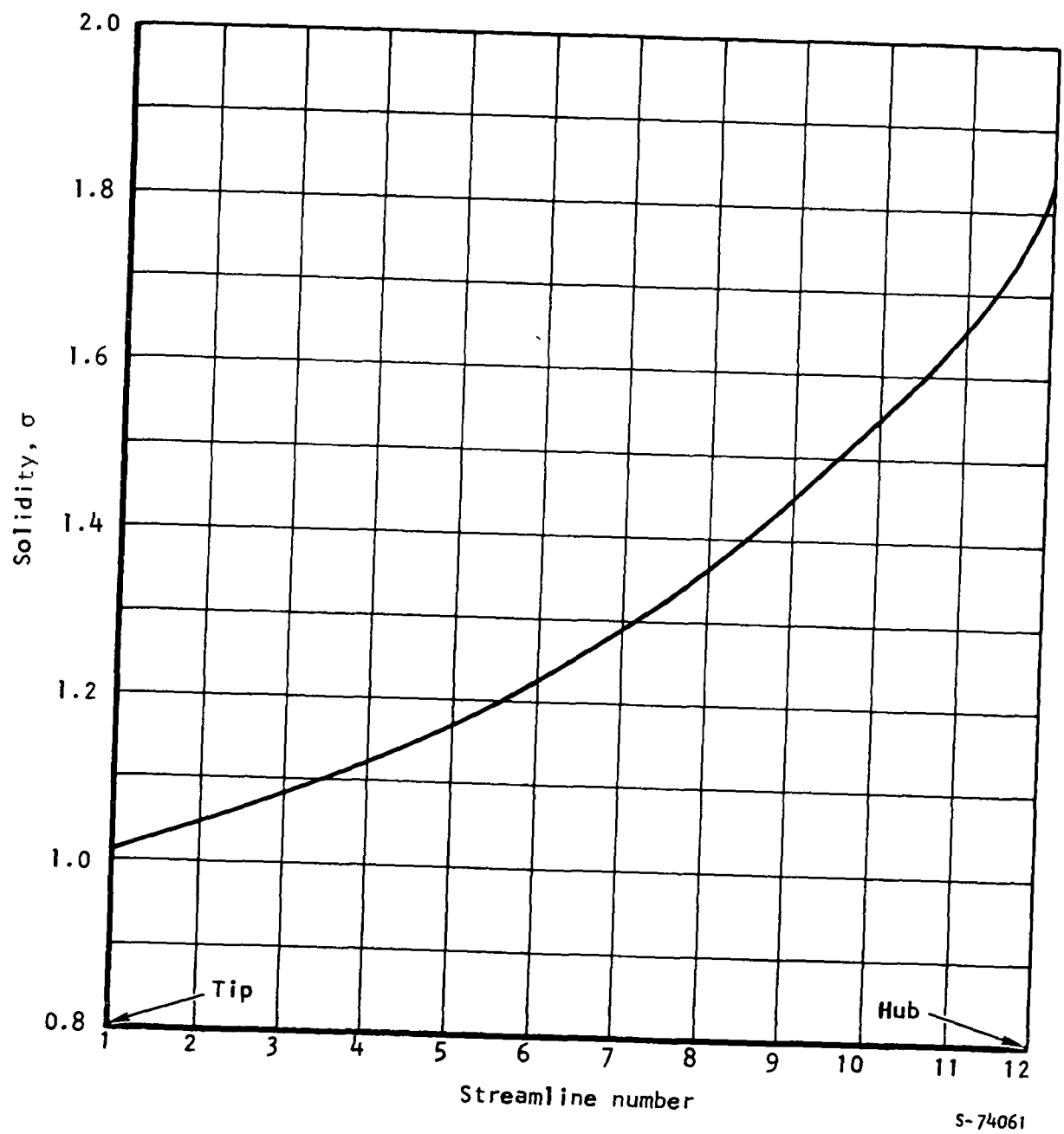
Figure 32.--Stator Solidity.

S-74061

73
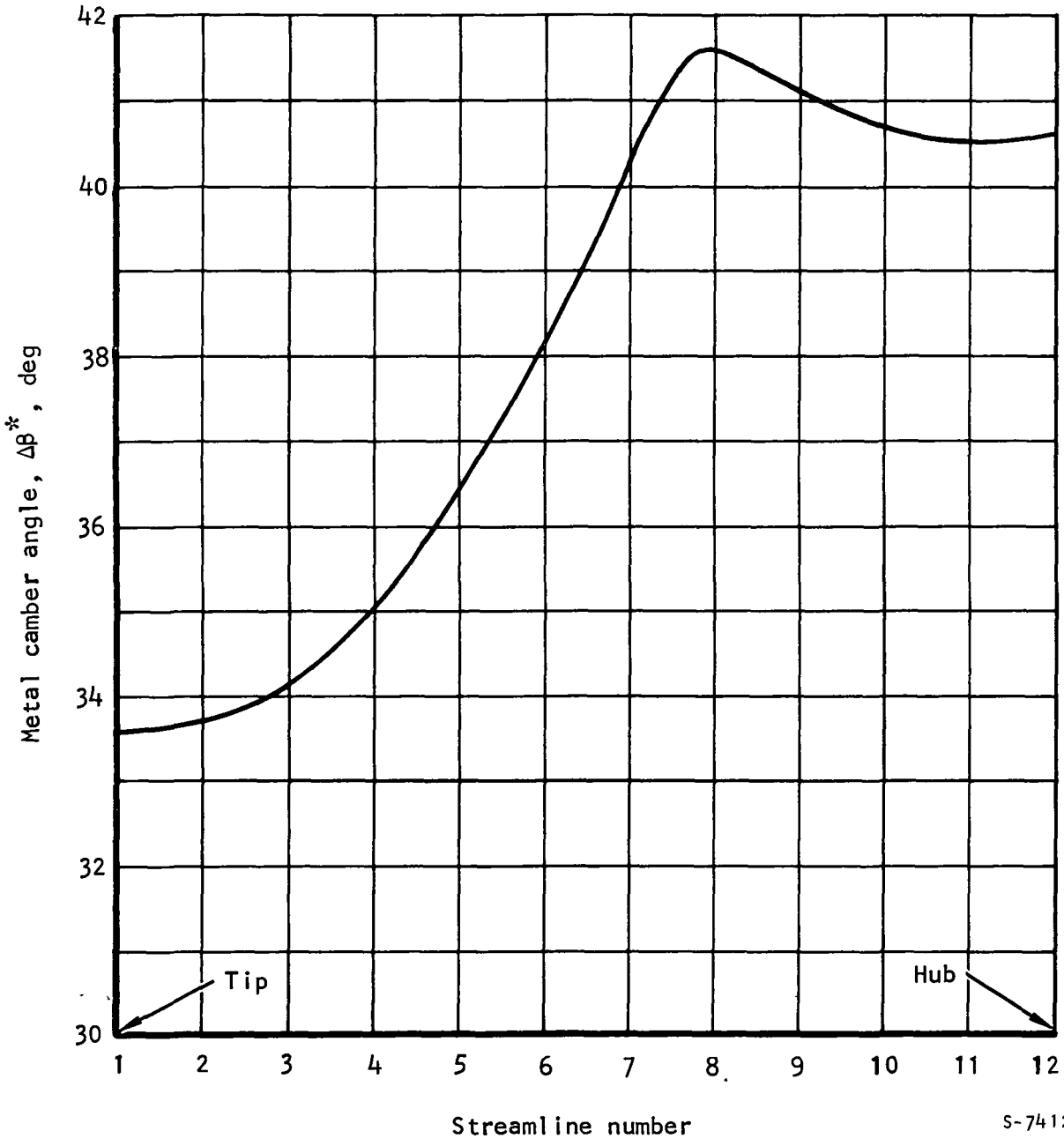
Figure 33.--Stator Metal Camber Angle.

74
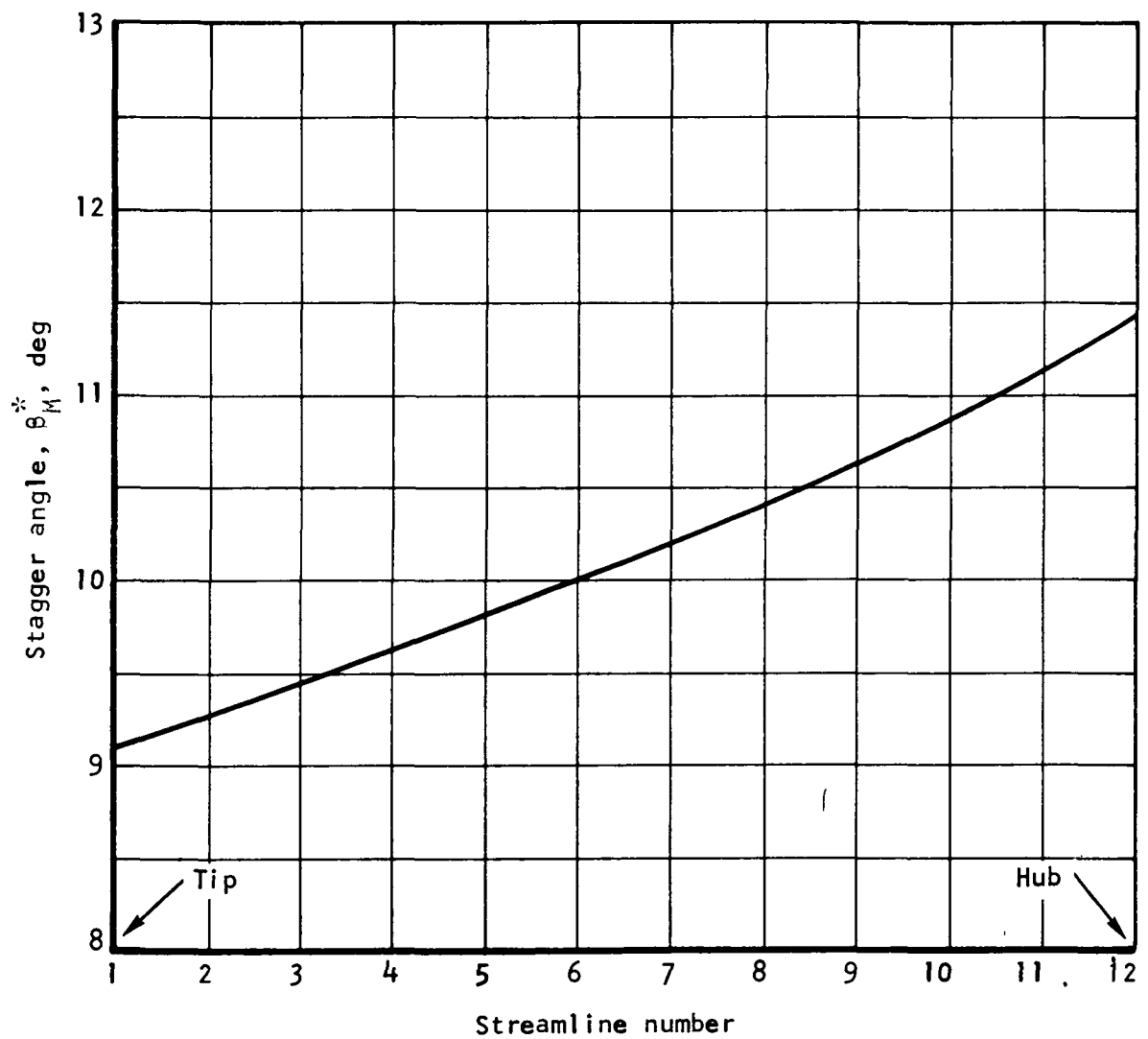
Figure 34.—Stator Stagger Angle.

S-74060
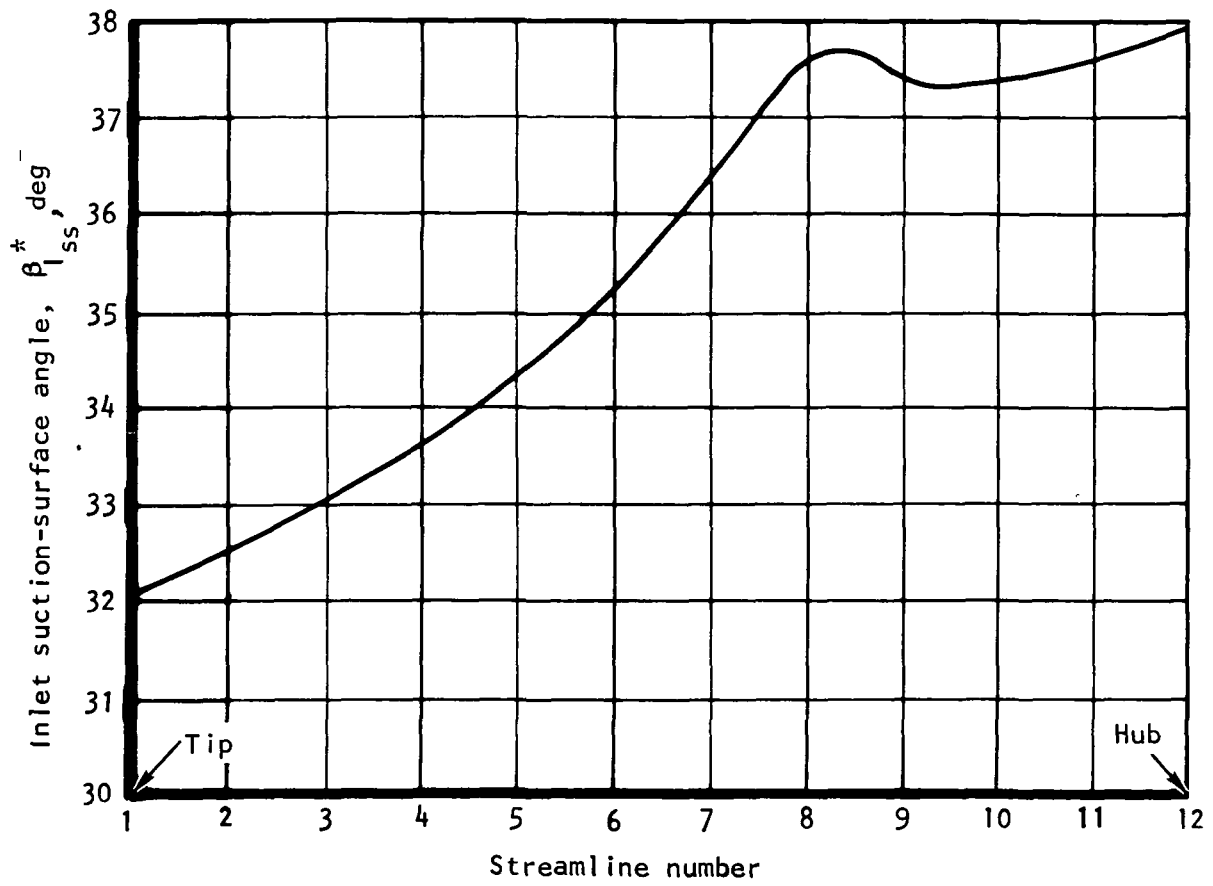
Figure 35.--Stator Suction Surface Angles.
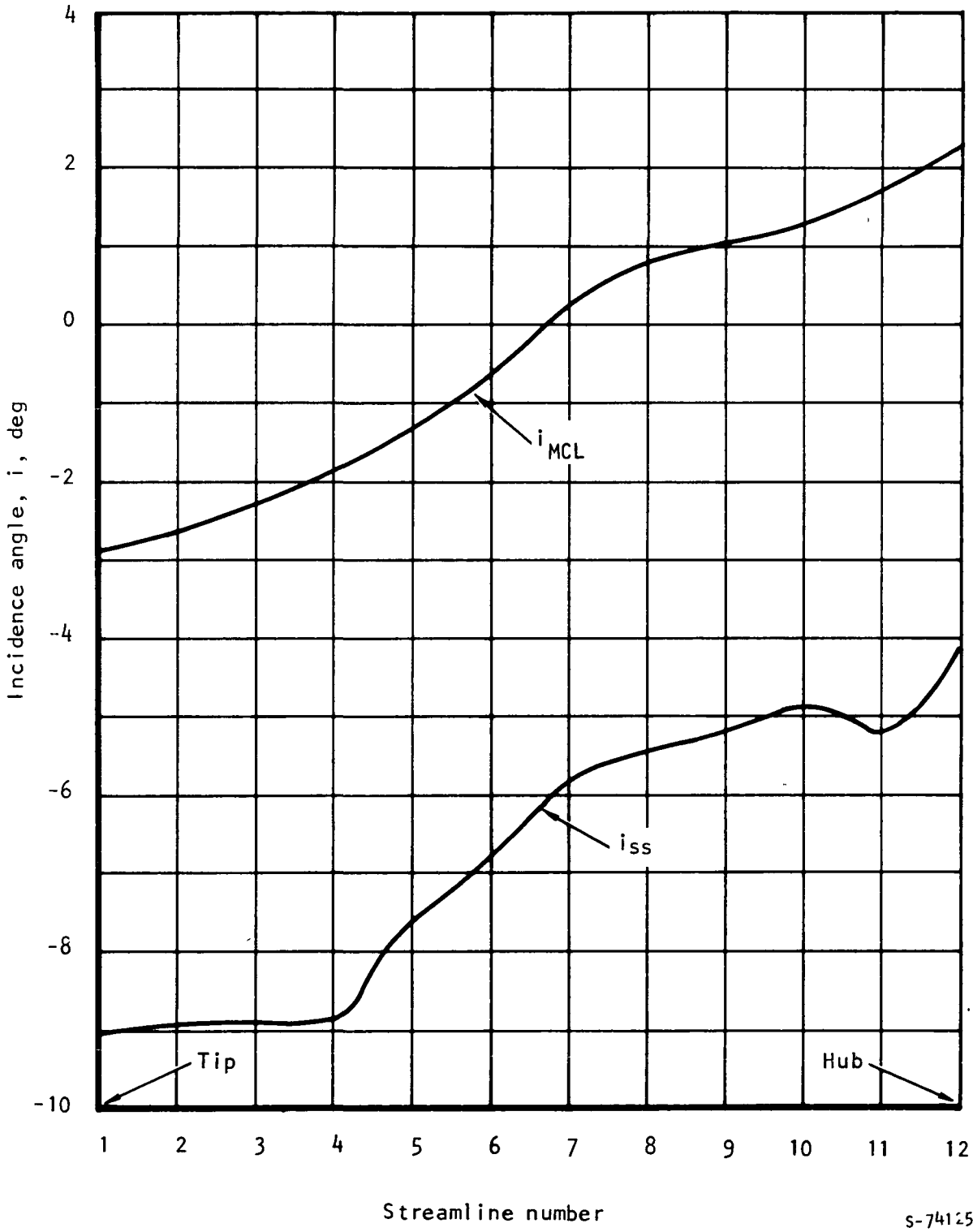
Figure 36.--Stator Incidence Angles.
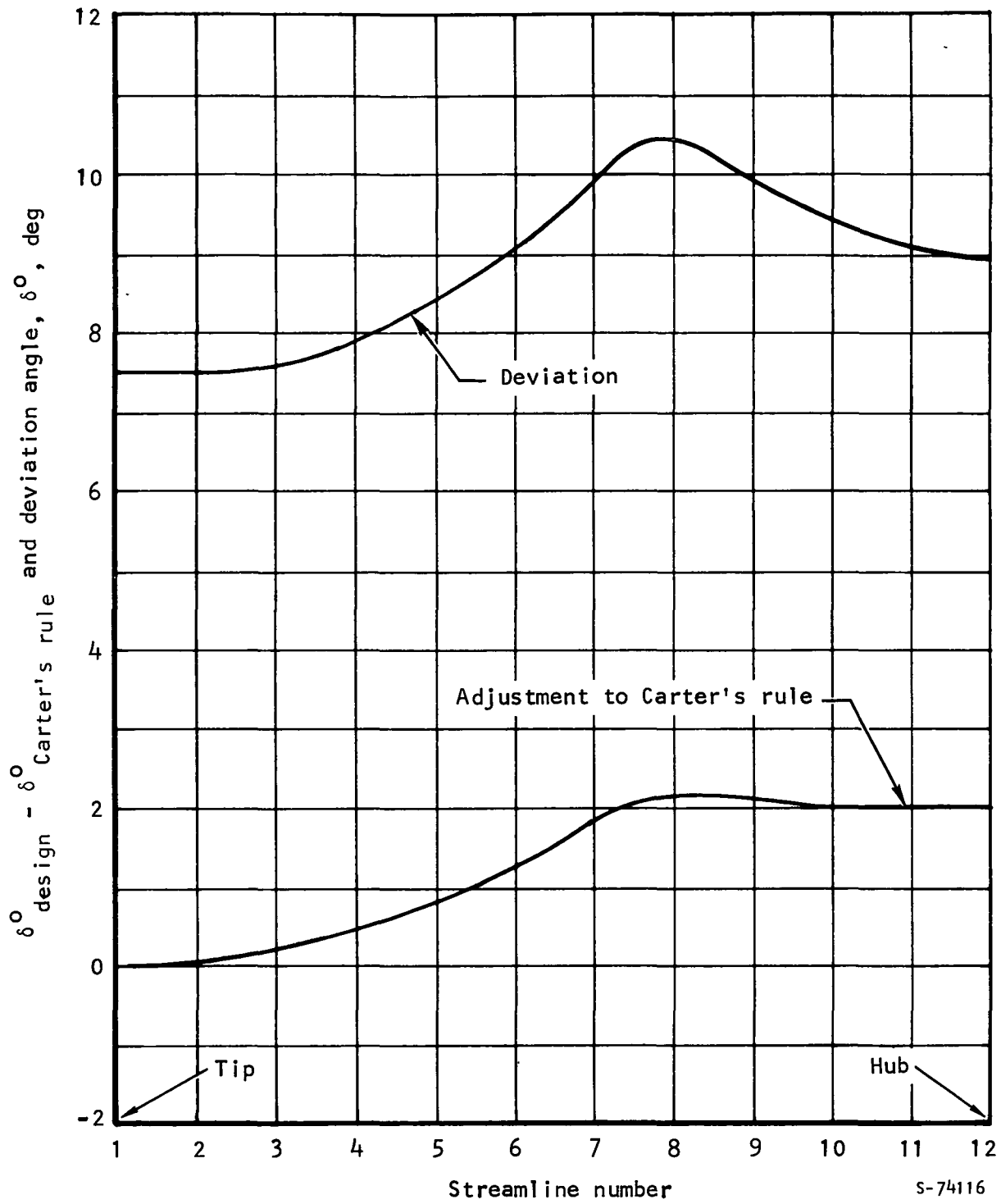
Figure 37.--Stator Deviation and Carter's Rule Adjustment.

78
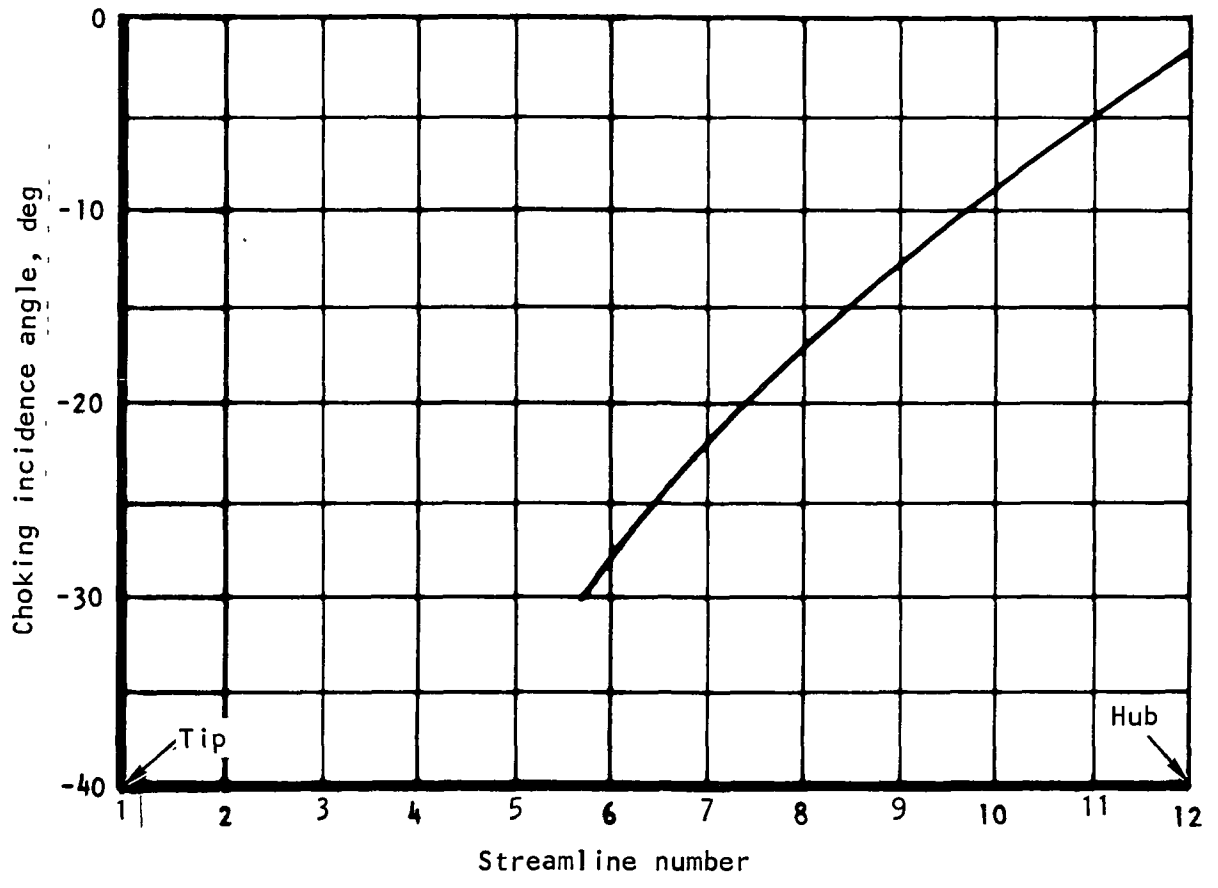
Figure 38.--Stator Choking Incidence Angle.

S-71916

79

MECHANICAL DESIGN

A relatively elaborate mechanical design was carried out on the subject transonic fan rotor because of the combination of relatively high tip speed and high aspect ratio and the aerodynamic necessity for a thin blade.

This section presents the details of that analysis. Design criteria, applicable steady-state and vibratory stresses, as well as margins of safety are summarized herein. The study encompassed the rotor blades, fan disk, disk/blade attachments, stator vanes and rotor critical speeds.

DESIGN CONCEPTS AND OBJECTIVES

The design criteria cover the allowable stress levels, anticipated operating conditions, and material properties used to size the critical components.

Material Properties

The materials selected for the critical components are as follows:

Component	Material (Specification)
Fan blade	Ti-6Al-4V (AMS 4928)
Fan disk	Ti-6Al-4V (AMS 4928)
Stator vane	17-4 PH (AMS 5643)

The material strengths that form the bases for the allowable stresses are from MIL-HDBK-5B (ref. 8) and are tabulated below:

	Fan blade (AMS 4928)	Fan disk (AMS 4928)	Stator vane (AMS 5643)
Temperature, $^{\circ}$F ($^{\circ}$K)	250 (395)	200 (367)	300 (422)
Ft_U, ksi (N/cm^2)	113 (779×10^2)	117 (806×10^2)	135 (930×10^2)
Ft_Y, ksi (N/cm^2)	102 (702×10^2)	107 (737×10^2)	115 (792×10^2)

Allowable Design Parameter Values

The following allowable design stresses refer to minimum material properties based on MIL-HDBK-5B definition (ref. 8).

Rotor blade.--The blade design limits were set on the basis of the following critical safety margin requirements:

(1) The maximum steady-state airfoil stress allowed is 82 ksi
(566×10^2 N/cm^2) which is 80 percent of the minimum 0.2-percent yield stress.

(2) The maximum midspan damper stress allowed is 102 ksi (703×10^2 N/cm^2) which is 100 percent of the minimum 0.2-percent yield stress.

(3) Airfoil vibratory stresses shall not exceed 50 percent of the smooth specimen endurance strength based on a combined stress Goodman diagram at 10^7 cycles.

Disk.--The disk was sized based on the following allowable limits:

(1) The maximum allowable bore stress is 91 ksi (626×10^2 N/cm^2) which is 85 percent of the minimum 0.2-percent yield stress (100 percent of the minimum 0.2-percent yield stress locally where bending exists)

(2) The maximum web stress is 85.5 ksi (590×10^2 N/cm^2) which is 80 percent of the minimum 0.2-percent yield stress (100 percent of the minimum 0.2-percent yield stress locally where bending exists).

(3) Disk burst speed is 125 percent of the design mechanical speed at the maximum disk metal temperature, based on 90 percent of the minimum ultimate tensile stress of 105 ksi (723×10^2 N/cm^2).

Blade/disk attachment.--The maximum allowable attachment stresses listed in table 3 were based on the following limits:

(1) Peak neck tension or tang bending stresses do not exceed 90 percent of the minimum 0.2-percent yield stress of the material.

(2) Peak combined fillet stresses do not exceed 125 percent of the minimum 0.2-percent yield stress.

(3) Peak maximum fillet stresses do not exceed the low-cycle-fatigue allowable stress for 10 000 cycles from rest to 110 percent speed.

(4) Peak bearing stresses do not exceed 125 percent of the minimum 0.2-percent yield stress.

(5) Peak tang shear stresses do not exceed 58 percent of the neck tension allowable stress.

Stator vane.--The principal stationary aerodynamic component is the stator vane row. The stator vane design is based on an allowable limit of airfoil maximum stress of less than 80 percent of the minimum 0.2-percent yield stress and a margin of 2 on smooth specimen endurance strength based on combined stresses.

Operating Conditions

From the mechanical design viewpoint, the most pertinent operating speeds were the following:

Aerodynamic design speed (100%)	12 800 rpm (1340.4 rad/s)
Mechanical design speed (110%)	14 100 rpm (1476.6 rad/s)
Maximum blade temperature	250°F (395°K)
Maximum disk temperature	200°F (367°K)

DESIGN RESULTS AND DISCUSSION

Rotor Blade

Geometric definition.--The geometric summary of the final rotor blade design is presented in tabular form in table 3. The rotor airfoil coordinates of the resulting 12 rotor blade sections are presented in table 4. The coordinates are L-plane blade sections defined by the intersection of the blade with planes tangent to the cylindrical surfaces. A typical L-section is presented in fig. 39.

Steady stress.--The blade nominal centrifugal stress versus radius is shown in fig. 40. This stress does not include any bending stress and, therefore, is useful as a basis for optimizing the blade tilt.

The airfoil combined stress distributions due to aerodynamic and centrifugal loads including blade untwist are shown in fig. 41a. These stresses were calculated at the aerodynamic design speed (100 percent) with the blade tilted tangentially 0.0175 in./in. (cm/cm) to optimize the stress distribution. The airfoil stresses caused by design aerodynamic loads only are shown in fig. 41b. The effect of blade tilt on the stress distribution is 5 percent per 0.010 in./in. (cm/cm) tangential tilt. The effect of dimensional tolerance is less than ±2 percent of the blade stresses.

TABLE 3

ROTOR GEOMETRIC SUMMARY

[L-Plane Blade Sections, defined by the intersection of the blade with planes tangent to cylindrical surfaces]

Blade height = 7.728 in. (19.63 cm) Number of blades ≈ 40

Hub/tip ratio = 0.462 Aspect ratio = 2.76

Radius	in.	14.372	13.800	13.100	12.399	11.700	11.700	10.300	9.600	8.899	8.201	7 500	6.641
	cm	36.50	35.05	33.27	31.49	29.72	27.94	26.16	24 38	22.60	20.83	19.05	16.87
β_1^* design		63.17	62.21	61.20	60.06	58.86	57.64	56.06	54.20	52.61	51.88	51.24	50 21
β_2^* design		52.74	55.47	56.93	56.25	54.38	51.63	48.14	44.14	37.52	28 07	15.13	2.42
β_M^* design		59.82	59.76	59.36	58.15	56.45	54.25	51.35	48.07	44.10	39.50	34.25	27.87
β_1^* static		63.17	62.43	61.93	61.13	60.06	58.84	57.11	54.98	53.02	52.00	51.26	50.21
β_2^* static		52.74	55.69	57.66	67.32	55.58	52.83	49.19	44.92	37.93	28.19	15.15	47.79
β_M^* static		59.82	59.98	60.09	59.22	57.65	55.45	52.40	48.85	44.51	39.62	34.27	27.87
Pretwist		0.00	0.22	0.73	1.07	1.20	1.20	1.05	0.78	0.41	0.12	0.02	0.00
$\Delta\beta^*$		10.43	6.74	4.27	3.81	4.48	6.01	7.92	10.06	15.09	23.81	36.11	47 79
Axial chord	in.	1.792	1.740	1.702	1.675	1.669	1.687	1.702	1.726	1 761	1 791	1 825	1 866
	cm	4.55	4.42	4.32	4.25	4.24	4.28	4.32	4.38	4.47	4.55	4.64	4.74
Chord	in.	3 714	3.565	3.357	3.194	3.065	2.939	2.795	2.664	2.526	2 394	2.285	2.184
	cm	9.43	9.06	8.53	8.11	7.79	7.47	7.10	6.77	6.42	6.08	5.80	5.50
$T_{max.}/C$		0.0177	0.0248	0.0306	0.0370	0.0445	0.0493	0 0558	0.0612	0.0673	0.0722	0 0782	0.0858
$r_{L.E.}/C$ (a)		0.0015	0.0016	0.0019	0.0022	0.0025	0.0029	0.0033	0 0038	0.0045	0.0052	0.0059	0 0065
$r_{T.E.}/C$ (a)		0.0014	0.0016	0.0019	0.0022	0.0026	0.0030	0.0036	0.0043	0.0052	0.0064	0.0072	0.0080

(a) Leading and trailing edge radii are defined to be the semi-minor axes of 2-to-1 ellipses

TABLE 4

ROTOR AIRFOIL COORDINATES
[Section no. 1; radius 14.372 in. (36.505 cm)]

| [a]Coordinates, in. | | [a]Coordinates, cm | |
X	Y	X	Y
-.9624	-1.6271	-2.4445	-4.1328
-.9605	-1.6316	-2.4395	-4.1442
-.9559	-1.6313	-2.4305	-4.1434
-.9529	-1.6277	-2.4203	-4.1343
-.9314	-1.5590	-2.3659	-4.0360
-.7472	-1.2521	-1.8978	-3.1802
-.5103	-.8200	-1.2962	-2.0829
-.2697	-.3832	-.6851	-.9733
-.0233	.0537	-.0591	.1365
.2515	.4901	.5876	1.2449
.4971	.9236	1.2626	2.3459
.5795	1.0505	1.4716	2.6661
.6024	1.0857	1.5300	2.7577
.6251	1.2112	1.5876	2.6477
.6474	1.1568	1.6443	2.9363
.6692	1.1923	1.6997	3.0297
.6866	1.2220	1.7440	3.1637
.7741	1.3675	1.9662	3.4734
.8573	1.4964	2.1775	3.8008
.9063	1.5687	2.3020	3.9645
.9091	1.5763	2.3091	4.0037
.9079	1.5794	2.3060	4.0116
.9045	1.5798	2.2975	4.0125
.9002	1.5773	2.2865	4.0062
.8955	1.5721	2.2745	3.9930
.8454	1.5128	2.1472	3.8426
.7919	1.4484	2.0114	3.6788
.7377	1.3818	1.8738	3.5097
.6829	1.3132	1.7346	3.3356
.6604	1.2645	1.6774	3.2627
.6337	1.2489	1.6095	3.1722
.6076	1.2127	1.5438	3.0601
.5827	1.1756	1.4801	2.9866
.5584	1.1385	1.4182	2.8918
.4588	.9822	1.1653	2.4947
.1392	.4551	.3536	1.1558
-.4717	-.6420	-1.1981	-1.6307
-.9415	-1.5800	-2.3914	-4.0132
-.9618	-1.6232	-2.4430	-4.1228

[a]Coordinates on L-plane blade sections defined by the intersection of the blade with planes tangent to cylindrical surfaces.

TABLE 4.--Continued

ROTOR AIRFOIL COORDINATES
[Section no. 2; radius 13.800 in. (35.052 cm)]

aCoordinates, in.		aCoordinates, cm	
X	Y	X	Y
-.9567	-1.5929	-2.4299	-4.0455
-.9546	-1.5976	-2.4246	-4.0575
-.9507	-1.5973	-2.4148	-4.0571
-.9464	-1.5935	-2.4037	-4.0474
-.9256	-1.5576	-2.3514	-3.9561
-.7586	-1.2601	-1.9207	-3.2006
-.5449	-.8796	-1.3839	-2.2341
-.3305	-.4998	-.8394	-1.2694
-.1128	-.1197	-.2865	-.3040
.1115	.2614	.2830	.6639
.3430	.6397	.8712	1.6247
.4078	.7414	1.0356	1.8831
.4316	.7794	1.0961	1.9797
.4546	.8179	1.1546	2.0773
.4769	.8567	1.2114	2.1759
.4987	.8959	1.2660	2.2754
.5306	.9557	1.3478	2.4274
.6477	1.1667	1.6450	2.9634
.7609	1.3640	1.9325	3.4646
.8263	1.4777	2.1036	3.7532
.8510	1.4656	2.1107	3.7740
.8306	1.4683	2.1095	3.7862
.8272	1.4901	2.1020	3.7849
.8235	1.4687	2.0916	3.7612
.8190	1.4844	2.0801	3.7704
.7895	1.4462	2.0053	3.6734
.7300	1.3684	1.8543	3.4757
.6699	1.2887	1.7016	3.2732
.6093	1.2072	1.5475	3.0663
.5597	1.1400	1.4215	2.8954
.5337	1.1038	1.3555	2.8035
.5084	1.0671	1.2914	2.7103
.4839	1.0299	1.2290	2.6160
.4600	.9924	1.1683	2.5205
.4365	.9542	1.1087	2.4237
.1769	.5210	.4492	1.3233
-.2185	-.1742	-.5549	-.4424
-.7739	-1.2176	-1.9658	-3.0927
-.9547	-1.5853	-2.4249	-4.0266
-.9506	-1.5916	-2.4297	-4.0425

aCoordinates on L-plane blade sections defined by the intersection of the blade with planes tangent to cylindrical surfaces.

TABLE 4.--Continued

ROTOR AIRFOIL COORDINATES
[Section no. 3; radius 13.100 in. (33.274 cm)]

Coordinates, in.		Coordinates, cm	
X	Y	X	Y
-.9092	-1.5035	-2.3092	-3.8185
-.9069	-1.5066	-2.3036	-3.8316
-.9027	-1.5083	-2.2927	-3.8311
-.8976	-1.5042	-2.2804	-3.8205
-.8703	-1.4713	-2.2313	-3.7363
-.7264	-1.2074	-1.8451	-3.0668
-.5320	-.8701	-1.3513	-2.2099
-.5375	-.5350	-.8573	-1.3586
-.1425	-.2030	-.3620	-.5157
.0537	.1244	.1364	.3160
.2517	.4459	.6391	1.1323
.2977	.5188	.7560	1.3170
.3210	.5567	.8154	1.4139
.3436	.5950	.8727	1.5113
.3654	.6338	.9281	1.6098
.3865	.6730	.9816	1.7093
.4070	.7128	1.0337	1.8106
.4925	.8776	1.2506	2.2290
.6229	1.1243	1.5821	2.8556
.7032	1.3624	1.9365	3.5112
.7691	1.3952	1.9533	3.5436
.7692	1.3973	1.9538	3.5490
.7686	1.4003	1.9522	3.5567
.7655	1.4022	1.9443	3.5616
.7608	1.4005	1.9323	3.5572
.7553	1.3956	1.9200	3.5447
.7238	1.3509	1.8535	3.4312
.6591	1.2603	1.6740	3.2012
.5936	1.1682	1.5077	2.9672
.5274	1.0745	1.3396	2.7293
.4791	1.0057	1.2168	2.5545
.4537	.9693	1.1523	2.4620
.4238	.9324	1.0691	2.3653
.4046	.8951	1.0277	2.2735
.3811	.8573	.9679	2.1776
.3582	.8192	.9097	2.0807
.2855	.6956	.7250	1.7667
.0245	.2432	.0622	.6176
-.4876	-.6825	-1.2385	-1.7335
-.8904	-1.4620	-2.2616	-3.7134
-.9083	-1.4986	-2.3071	-3.8063

Coordinates on L-plane blade sections defined by the intersection of the blade with planes tangent to cylindrical surfaces.

TABLE 4.--Continued

ROTOR AIRFOIL COORDINATES
[Section no. 4; radius 12.400 in. (31.496 cm)]

^aCoordinates, in.		^aCoordinates, cm	
X	Y	X	Y
-.8889	-1.4215	-2.2578	-3.6106
-.8865	-1.4270	-2.2517	-3.6244
-.8819	-1.4267	-2.2399	-3.6236
-.8765	-1.4223	-2.2262	-3.6125
-.6580	-1.3920	-2.1793	-3.5356
-.7130	-1.1498	-1.8110	-2.9205
-.5285	-.8430	-1.3418	-2.1411
-.3437	-.5397	-.8729	-1.3708
-.1589	-.2410	-.4036	-.6120
.0262	.0522	.0664	.1326
.2118	.3388	.5376	.8605
.2492	.3953	.6329	1.0041
.2733	.4326	.6940	1.0985
.2965	.4703	.7530	1.1944
.3188	.5085	.8098	1.2914
.3403	.5472	.8643	1.3398
.3611	.5865	.9171	1.4897
.4543	.7624	1.1538	1.9365
.5932	1.0208	1.5066	2.5927
.7432	1.2952	1.8876	3.2895
.7499	1.3098	1.9046	3.3268
.7501	1.3120	1.9052	3.3325
.7494	1.3154	1.9034	3.3409
.7460	1.3176	1.8947	3.3465
.7407	1.3157	1.8814	3.3417
.7353	1.3103	1.8077	3.3261
.6975	1.2590	1.7715	3.1978
.6209	1.1548	1.5770	2.9332
.5432	1.0486	1.3797	2.6634
.4645	.9404	1.1799	2.3895
.3850	.8303	.9779	2.1090
.3690	.8079	.9373	2.0521
.3437	.7713	.8729	1.9591
.3191	.7343	.8104	1.8651
.2951	.6968	.7495	1.7699
.2718	.6589	.6903	1.6736
.2104	.5571	.5344	1.4149
-.0289	.1522	-.0733	.3866
-.5000	-.6803	-1.2699	-1.7279
-.8711	-1.3825	-2.2125	-3.5116
-.8879	-1.4160	-2.2553	-3.5965

^aCoordinates on L-plane blade sections defined by the intersection
of the blade with planes tangent to cylindrical surfaces.

TABLE 4.--Continued

ROTOR AIRFOIL COORDINATES
[Section no. 5; radius 11.700 in. (29.718 cm)]

[a]Coordinates, in.		[a]Coordinates, cm	
X	Y	X	Y
-.3805	-1.3431	-2.2371	-3.4115
-.3783	-1.3459	-2.2308	-3.4262
-.3732	-1.3486	-2.2179	-3.4298
-.8672	-1.3440	-2.2026	-3.4137
-.8497	-1.3167	-2.1581	-3.3443
-.7057	-1.0861	-1.7925	-2.7637
-.5236	-.8024	-1.3299	-2.0361
-.3416	-.5214	-.8676	-1.3242
-.1596	-.2451	-.4053	-.6225
.0224	.0260	.0569	.0659
.1215	.1711	.3086	.4346
.2090	.3014	.5305	.7656
.2939	.4334	.7465	1.1007
.3765	.5667	.9561	1.4394
.4569	.7014	1.1606	1.7816
.5258	.8199	1.3355	2.0824
.6714	1.0712	1.7052	2.7207
.7603	1.2245	1.9311	3.1103
.7639	1.2356	1.9404	3.1383
.7633	1.2390	1.9387	3.1470
.7596	1.2415	1.9293	3.1534
.7536	1.2397	1.9145	3.1487
.7476	1.2340	1.8959	3.1344
.6988	1.1729	1.7746	2.9792
.5993	1.0481	1.5233	2.6622
.4992	.9200	1.2678	2.3367
.3972	.7886	1.0089	2.0029
.3385	.7113	.8597	1.8067
.2568	.5987	.6523	1.5207
.1781	.4841	.4523	1.2296
.1019	.3678	.2588	.9341
.0279	.2499	.0707	.6348
-.1024	.0371	-.2601	.0941
-.5275	-.6906	-1.3398	-1.7541
-.8640	-1.3066	-2.1944	-3.3192
-.8796	-1.3369	-2.2342	-3.3955

[a]Coordinates on L-plane blade sections defined by the intersection of the blade with planes tangent to cylindrical surfaces.

TABLE 4.--Continued

ROTOR AIRFOIL COORDINATES
[Section no. 6; radius 11.000 in. (27.940 cm)]

[a]Coordinates, in.		[a]Coordinates, cm	
X	Y	X	Y
-.0746	-1.2516	-2.2213	-3.1794
-.8720	-1.2576	-2.2148	-3.1948
-.8064	-1.2577	-2.2007	-3.1947
-.5590	-1.2526	-2.1839	-3.1820
-.8433	-1.2265	-2.1419	-3.1205
-.6977	-1.0104	-1.7721	-2.5664
-.5154	-.7440	-1.5039	-1.8892
-.3331	-.4640	-.8460	-1.2293
-.1509	-.2291	.3831	-.5817
.0313	.0220	.0775	.0557
.1357	.1646	.3446	.4161
.2155	.2746	.5473	.6980
.2941	.3659	.7470	.9001
.3714	.4978	.9434	1.2644
.4474	.6107	1.1362	1.5512
.5458	.7610	1.3865	1.9330
.6966	.7964	1.7743	2.5358
.7920	1.1456	2.0117	2.9097
.7965	1.1580	2.0230	2.9412
.7959	1.1612	2.0216	2.9474
.7920	1.1642	2.0117	2.9569
.7656	1.1625	1.9953	2.9528
.7786	1.1568	1.9775	2.9362
.7151	1.0662	1.8164	2.7569
.5671	.9416	1.4911	2.5917
.4576	.7924	1.1622	2.0127
.5270	.6386	.6306	1.6221
.2542	.5513	.6457	1.4003
.1738	.4509	.4415	1.1453
.0967	.3662	.2455	.8644
.0223	.2434	.0567	.6162
-.0496	.1368	-.1258	.3475
-.1119	.0411	-.2643	.1043
-.3714	-.3745	-.9434	-.9512
-.7475	-1.0188	-1.8987	-2.5878
-.8711	-1.2403	-2.2126	-3.1502
-.6743	-1.2490	-2.2207	-3.1725

[a]Coordinates on L-plane blade sections defined by the intersection
of the blade with planes tangent to cylindrical surfaces.

TABLE 4.--Continued

ROTOR AIRFOIL COORDINATES
[Section no. 7; radius 10.300 in. (26.162 cm)]

aCoordinates, in.		aCoordinates, cm	
X	Y	X	Y
-.6767	-1.1427	-2.2263	-2.9025
-.6741	-1.1490	-2.2201	-2.9164
-.6656	-1.1492	-2.2043	-2.9168
-.6606	-1.1439	-2.1660	-2.9056
-.8452	-1.1230	-2.1467	-2.8523
-.6976	-.9193	-1.7719	-2.3349
-.5149	-.6775	-1.5077	-1.7209
-.3321	-.4444	-.8435	-1.1288
-.1494	-.2169	-.3793	-.5508
.0334	.0082	.0848	.0209
.1467	.1481	.3726	.3761
.2193	.2383	.5566	.6052
.2914	.3288	.7400	.8351
.3629	.4197	.9216	1.0661
.4338	.5112	1.1019	1.2984
.4826	.5752	1.2262	1.4611
.6460	.7945	1.6407	2.0179
.6169	1.0360	2.0799	2.6314
.8302	1.0526	2.1086	2.6736
.8326	1.0613	2.1147	2.6957
.8305	1.0666	2.1095	2.7091
.6247	1.0676	2.0947	2.7120
.6166	1.0642	2.0746	2.7039
.8047	1.0532	2.0439	2.6750
.6509	.9049	1.6533	2.2963
.4880	.7418	1.2395	1.8840
.3243	.5713	.8237	1.4511
.1603	.3935	.4072	.9993
.0678	.2889	.1721	.7338
-.0079	.1979	-.0200	.5025
-.0606	.1045	-.2048	.2655
-.1506	.0092	-.3629	.0233
-.2186	-.0879	-.5553	-.2232
-.2831	-.1831	-.7190	-.4650
-.6045	-.6848	-1.5353	-1.7393
-.8620	-1.1120	-2.1894	-2.8243
-.8750	-1.1347	-2.2224	-2.8820

aCoordinates on L-plane blade sections defined by the intersection of the blade with planes tangent to cylindrical surfaces.

90

TABLE 4.--Continued

ROTOR AIRFOIL COORDINATES
[Section no. 8; radius 9.600 in. (24.384 cm)]

aCoordinates, in.		aCoordinates, cm	
X	Y	X	Y
-.5967	-1.0490	-2.2775	-2.6644
-.6967	-1.0494	-2.2775	-2.6654
-.6940	-1.0554	-2.2708	-2.6605
-.8911	-1.0564	-2.2634	-2.6833
-.8674	-1.0559	-2.2540	-2.6819
-.8553	-1.0538	-2.2456	-2.6767
-.8791	-1.0505	-2.2330	-2.6683
-.8735	-1.0440	-2.2186	-2.6516
-.8642	-1.0321	-2.1951	-2.6215
-.8065	-.9584	-2.0456	-2.4343
-.7150	-.8449	-1.8161	-2.1459
-.6235	-.7348	-1.5835	-1.8664
-.5319	-.6279	-1.3510	-1.5949
-.4403	-.5237	-1.1183	-1.3301
-.3487	-.4217	-.8856	-1.0709
-.2571	-.3214	-.6530	-.8163
-.1655	-.2224	-.4202	-.5649
-.0738	-.1243	-.1675	-.3158
.0178	-.0266	.0452	-.0676
.1094	.0712	.2779	.1807
.1446	.1089	.3672	.2765
.1779	.1447	.4517	.3674
.2111	.1805	.5361	.4565
.2443	.2165	.6204	.5498
.2773	.2525	.7044	.6412
.3103	.2886	.7881	.7329
.3431	.3248	.8715	.8249
.3758	.3611	.9546	.9172
.4084	.3976	1.0373	1.0096
.4408	.4342	1.1196	1.1028
.4813	.4602	1.2224	1.2196
.5693	.5825	1.4459	1.4795
.6572	.6675	1.6693	1.7462
.7451	.7952	1.8924	2.0196
.8432	.9188	2.1418	2.3337
.8528	.9309	2.1661	2.3643
.8568	.9366	2.1762	2.3788
.8599	.9455	2.1840	2.4015
.8599	.9465	2.1841	2.4041
.8596	.9491	2.1833	2.4107

aCoordinates on L-plane blade sections defined by the intersection of the blade with planes tangent to cylindrical surfaces.

TABLE 4.--Continued

ROTOR AIRFOIL COORDINATES
[Section no. 8--continued; radius 9.600 in. (24.384 cm)]

aCoordinates, in.		aCoordinates, cm	
X	Y	X	Y
.ඨ58Ũ	.ყ518	2.1793	2.4175
.ඨ554	.9533	2.1726	2.4214
.ඨ51ඨ	.953ඨ	2.1ඨ35	2.42ඨ2
.ඨ475	.9527	2.15ඨ6	2.41ყඨ
.ඨ42ඨ	.95Ũඨ	2.14Ũ7	2.4144
.ඨ5ඨ1	.ඨ474	2.12ඨ7	2.4Ũඨ4
.ඨ2ඨ5	.939ඨ	2.1Ũ44	2.ඨඨ71
.7423	.ඨ716	1.ඨඨ53	2.213ඨ
.ඨ46ඨ	.7933	1.ඨ417	2.Ũ14ඨ
.5ඨŨ4	.7123	1.3ඨ7ඨ	1.ඨŨყ1
.4543	.ඨ285	1.153ඨ	1.ඨඨඨඨ
.35ඨ2	.ඨ418	.ყŨყඨ	1.37ඨ1
.2622	.4522	.ඨඨ5ඨ	1.14ඨ6
.1ඨ61	.ඨඨ96	.42ඨ9	.ყ13ඨ
.Ũ7Ũ2	.2639	.17ඨ4	.ඨ7Ũඨ
-.Ũ227	.1679	-.Ũ577	.4265
-.Ũ5ඨඨ	.13ඨ3	-.152Ũ	.325ඨ
-.Ũ963	.Ũඨඨ1	-.2446	.ඨ237
-.1321	.Ũ473	-.33ඨ4	.12Ũ2
-.1672	.ŨŨ60	-.42ඨ7	.Ũ153
-.ඨŨ17	-.Ũ35ඨ	-.ඨ12ඨ	-.Ũყ0ඨ
-.23ඨ7	-.Ũ781	-.59ඨ6	-.19ඨ2
-.26ඨ1	-.12Ũඨ	-.6ඨ3ඨ	-.ඨŨඨඨ
-.3ඨ19	-.1640	-.76ඨඨ	-.416ඨ
-.3343	-.2Ũ76	-.ඨ4ყŨ	-.ඨ272
-.ඨ772	-.ඨ664	-.9ඨ7ඨ	-.6766
-.ඨ173	-.465ඨ	-1.313ඨ	-1.1ඨ31
-.ඨ57ඨ	-.ඨ742	-1.ඨ7Ũඨ	-1.7125
-.79ඨ1	-.ඨඨ97	-2.Ũඨඨ6	-2.2597
-.ඨඨ25	-1.0201	-2.2414	-2.5ඨ1Ũ
-.ඨ91ඨ	-1.Ũඨ46	-2.2ඨ5Ũ	-2.6ඨ7ඨ
-.ඨ945	-1.Ũ39ඨ	-2.272Ũ	2.ඨ4Ũ9
-.ඨ962	-1.Ũ44ඨ	-ඨ.2763	-2.65ඨඨ
		-2.2775	-2.6644

aCoordinates on L-plane blade sections defined by the intersection of the blade with planes tangent to cylindrical surfaces.

TABLE 4.—Continued

ROTOR AIRFOIL COORDINATES
[Section no. 9; radius 8.900 in. (22.606 cm)]

[a]Coordinates, in.		[a]Coordinates, cm	
X	Y	X	Y
-.9164	-.9565	-2.3326	-2.4294
-.9177	-.9605	-2.3306	-2.4396
-.9124	-.9644	-2.3175	-2.4496
-.9084	-.9640	-2.3072	-2.4484
-.9036	-.9619	-2.2955	-2.4432
-.8990	-.9564	-2.2834	-2.4344
-.8925	-.9514	-2.2668	-2.4106
-.8835	-.9413	-2.2449	-2.3903
-.8253	-.8726	-2.0963	-2.2163
-.7336	-.7667	-1.8633	-1.9524
-.6419	-.6669	-1.6305	-1.6990
-.5503	-.5729	-1.3977	-1.4551
-.4586	-.4801	-1.1649	-1.2193
-.3670	-.3901	-.9322	-.9906
-.2754	-.3024	-.6996	-.7681
-.1839	-.2167	-.4670	-.5502
-.0924	-.1324	-.2346	-.3362
-.0009	-.0492	-.0023	-.1248
.0905	.0334	.2298	.0848
.1381	.0764	.3506	.1940
.1683	.1037	.4275	.2633
.1986	.1310	.5043	.3326
.2287	.1583	.5809	.4021
.2589	.1857	.6575	.4716
.2890	.2131	.7340	.5412
.3190	.2406	.8103	.6110
.3490	.2662	.8864	.6811
.3789	.2958	.9623	.7513
.4087	.3236	1.0380	.8218
.4756	.3666	1.2084	.9619
.5705	.4777	1.4490	1.2133
.6654	.5711	1.6900	1.4506
.7603	.6670	1.9312	1.6941
.8666	.7767	2.2011	1.9727
.8771	.7875	2.2278	2.0003
.8822	.7935	2.2407	2.0154
.8866	.8031	2.2520	2.0397
.8868	.8054	2.2525	2.0457
.8867	.8071	2.2522	2.0500
.8853	.8103	2.2486	2.0581

[a]Coordinates on L-plane blade sections defined by the intersection of the blade with planes tangent to cylindrical surfaces.

93

TABLE 4.--Continued

ROTOR AIRFOIL COORDINATES
[Section no. 9--continued; radius 8.900 in. (22.606 cm)]

aCoordinates, in.		aCoordinates, cm	
X	Y	X	Y
.8626	.8124	2.2417	2.0635
.8786	.8133	2.2316	2.0656
.8637	.8130	2.2192	2.0649
.8662	.8114	2.2053	2.0663
.8625	.8066	2.1907	2.0538
.8520	.8025	2.1641	2.0362
.7576	.7471	1.9241	1.8976
.6526	.6816	1.6576	1.7313
.5477	.6126	1.3912	1.5560
.4429	.5393	1.1249	1.3698
.3361	.4616	.8567	1.1729
.2334	.3799	.5926	.9650
.1286	.2935	.3271	.7453
.0243	.2025	.0617	.5143
-.0800	.1057	-.2030	.2709
-.0963	.0968	-.2446	.2366
-.1510	.0573	-.3327	.1454
-.1652	.0233	-.4195	.0590
-.1988	-.0113	-.5050	-.0286
-.2319	-.0463	-.5891	-.1174
-.2646	-.0817	-.6720	-.2075
-.2967	-.1176	-.7536	-.2987
-.3284	-.1540	-.8340	-.3910
-.3596	-.1907	-.9132	-.4844
-.3903	-.2279	-.9913	-.5788
-.4315	-.2286	-1.0956	-.7077
-.5625	-.4485	-1.4286	-1.1391
-.6940	-.6274	-1.7626	-1.5936
-.8260	-.8139	-2.0981	-2.0671
-.9036	-.9277	-2.2956	-2.3563
-.9124	-.9403	-2.3175	-2.3884
-.9156	-.9459	-2.3256	-2.4026
-.9177	-.9515	-2.3306	-2.4167

aCoordinates on L-plane blade sections defined by the intersection of the blade with planes tangent to cylindrical surfaces.

TABLE 4.--Continued

ROTOR AIRFOIL COORDINATES
[Section no. 10; radius 8.200 in. (20.828 cm)]

ªCoordinates, in.		ªCoordinates, cm	
X	Y	X	Y
-.9364	-.6710	-2.3763	-2.2123
-.9357	-.8753	-2.3765	-2.2231
-.9303	-.8797	-2.3622	-2.2343
-.9250	-.8793	-2.3509	-2.2333
-.9205	-.8772	-2.3379	-2.2279
-.9152	-.8735	-2.3245	-2.2186
-.9080	-.8662	-2.3062	-2.2000
-.8997	-.8569	-2.2851	-2.1765
-.8413	-.7920	-2.1367	-2.0116
-.7502	-.6950	-1.9054	-1.7653
-.6592	-.6029	-1.6743	-1.5312
-.5685	-.5152	-1.4435	-1.3085
-.4775	-.4316	-1.2129	-1.0962
-.3868	-.3517	-.9824	-.8931
-.2962	-.2750	-.7522	-.6985
-.2056	-.2013	-.5222	-.5112
-.1152	-.1300	-.2925	-.3302
-.0248	-.0608	-.0628	-.1544
.0655	.0067	.1664	.0170
.1224	.0485	.3106	.1232
.1496	.0686	.3805	.1742
.1773	.0887	.4502	.2251
.2047	.1087	.5200	.2759
.2322	.1286	.5896	.3266
.2597	.1486	.6596	.3773
.2872	.1686	.7295	.4281
.3147	.1886	.7993	.4789
.3422	.2066	.8690	.5297
.3696	.2287	.9386	.5807
.4634	.2981	1.1769	.7571
.5655	.3745	1.4364	.9513
.6682	.4521	1.6972	1.1483
.7714	.5308	1.9593	1.3481
.8576	.6196	2.2544	1.5738
.8987	.6282	2.2827	1.5955
.9049	.6335	2.2983	1.6090
.9114	.6433	2.3149	1.6338
.9122	.6475	2.3169	1.6447
.9122	.6477	2.3169	1.6451
.9112	.6515	2.3145	1.6548

ªCoordinates on L-plane blade sections defined by the intersection of the blade with planes tangent to cylindrical surfaces.

TABLE 4.--Continued

ROTOR AIRFOIL COORDINATES
[Section no. 10--continued; radius 8.200 in (20.828 cm)]

aCoordinates, in.		aCoordinates, cm	
X	Y	X	Y
.9066	.6544	2.3078	1.6621
.9044	.6562	2.2972	1.6667
.8990	.6568	2.2835	1.6662
.8927	.6562	2.2674	1.6665
.8693	.6543	2.2500	1.6620
.8747	.6502	2.2216	1.6515
.7741	.6134	1.9662	1.5577
.6626	.5671	1.6825	1.4403
.5311	.5153	1.3998	1.3087
.4599	.4560	1.1172	1.1633
.3283	.3950	.8351	1.0032
.2181	.3262	.5540	.8286
.1077	.2514	.2734	.6384
-.0026	.1701	-.0066	.4320
-.1126	.0821	-.2860	.2634
-.1434	.0554	-.3641	.1406
-.1759	.0272	-.4468	.0691
-.2080	-.0014	-.5263	-.0035
-.2397	-.0305	-.6086	-.0773
-.2710	-.0599	-.6882	-.1522
-.3019	-.0898	-.7667	-.2261
-.3323	-.1201	-.8441	-.3051
-.3625	-.1508	-.9206	-.3850
-.3922	-.1819	-.9961	-.4620
-.4216	-.2133	-1.0707	-.5413
-.4660	-.2620	-1.1835	-.6654
-.5926	-.4083	-1.5051	-1.0371
-.7195	-.5659	-1.8275	-1.4376
-.8466	-.7354	-2.1504	-1.8679
-.9214	-.8515	-2.3403	-2.1374
-.9297	-.8533	-2.3614	-2.1673
-.9333	-.8594	-2.3704	-2.1827
-.9355	-.8654	-2.3762	-2.1980
-.9364	-.8708	-2.3763	-2.2119

aCoordinates on L-plane blade sections defined by the intersection of the blade with planes tangent to cylindrical surfaces.

TABLE 4.--Continued

ROTOR AIRFOIL COORDINATES
[Section no. 11; radius 7.500 in. (19.050 cm)]

aCoordinates, in.		aCoordinates, cm	
X	Y	X	Y
-.9460	-.7918	-2.4028	-2.0110
-.9453	-.7962	-2.4010	-2.0222
-.9393	-.8010	-2.3858	-2.0344
-.9346	-.8007	-2.3737	-2.0336
-.9291	-.7985	-2.3599	-2.0282
-.9234	-.7947	-2.3454	-2.0186
-.9158	-.7873	-2.3260	-1.9997
-.9077	-.7787	-2.3054	-1.9779
-.8499	-.7175	-2.1587	-1.8225
-.7601	-.6273	-1.9307	-1.5934
-.6707	-.5427	-1.7034	-1.3785
-.5815	-.4681	-1.4769	-1.1762
-.4526	-.3883	-1.2511	-.9861
-.4039	-.3177	-1.0260	-.8070
-.3156	-.2511	-.8015	-.6377
-.2275	-.1880	-.5777	-.4774
-.1396	-.1280	-.3546	-.3252
-.0520	-.0709	-.1321	-.1800
.0352	-.0162	.0895	-.0411
.0934	.0190	.2371	.0481
.1186	.0342	.3017	.0868
.1443	.0493	.3665	.1251
.1699	.0643	.4314	.1633
.1955	.0792	.4964	.2011
.2211	.0940	.5616	.2388
.2468	.1088	.6269	.2763
.2726	.1235	.6923	.3135
.2964	.1381	.7578	.3507
.3242	.1527	.8234	.3877
.3350	.1588	.8509	.4033
.4465	.2209	1.1340	.5610
.5591	.2821	1.4199	.7166
.6728	.3422	1.7089	.8690
.7879	.4006	2.0012	1.0175
.9192	.4639	2.3347	1.1782
.9311	.4696	2.3649	1.1927
.9375	.4732	2.3811	1.2018
.9427	.4773	2.3945	1.2123
.9483	.4862	2.4086	1.2349
.9465	.4881	2.4091	1.2398

aCoordinates on L-plane blade sections defined by the intersection
of the blade with planes tangent to cylindrical surfaces.

TABLE 4.--Continued

ROTOR AIRFOIL COORDINATES
[Section no. 11--continued; radius 7.500 in. (19.050 cm)]

aCoordinates, in.		aCoordinates, cm	
X	Y	X	Y
.9482	.4904	2.4064	1.2455
.9462	.4940	2.4032	1.2547
.9423	.4969	2.3933	1.2621
.9369	.4989	2.3797	1.2671
.9302	.4995	2.3628	1.2694
.9221	.4996	2.3436	1.2690
.9108	.4981	2.3134	1.2652
.8037	.4647	2.0413	1.2310
.6852	.4617	1.7404	1.1726
.5673	.4310	1.4408	1.0947
.4496	.3926	1.1424	.9971
.3328	.3464	.8451	.8795
.2161	.2923	.5489	.7424
.0999	.2302	.2536	.5847
-.0160	.1598	-.0405	.4059
-.1314	.0807	-.3338	.2050
-.1759	.0466	-.4467	.1184
-.2067	.0229	-.5249	.0582
-.2371	-.0012	-.6023	-.0030
-.2672	-.0258	-.6787	-.0654
-.2970	-.0507	-.7542	-.1287
-.3263	-.0761	-.8289	-.1932
-.3554	-.1013	-.9026	-.2586
-.3841	-.1280	-.9755	-.3250
-.4124	-.1545	-1.0475	-.3925
-.4405	-.1815	-1.1187	-.4609
-.4410	-.1820	-1.1200	-.4621
-.4674	-.2280	-1.2380	-.5790
-.6105	-.3579	-1.5506	-.9091
-.7340	-.5011	-1.8643	-1.2728
-.8579	-.6598	-2.1789	-1.6757
-.9306	-.7615	-2.3641	-1.9343
-.9389	-.7729	-2.3846	-1.9630
-.9427	-.7793	-2.3943	-1.9794
-.9451	-.7857	-2.4005	-1.9956
-.9460	-.7915	-2.4028	-2.0103

aCoordinates on L-plane blade sections defined by the intersection of the blade with planes tangent to cylindrical surfaces.

TABLE 4.--Continued

ROTOR AIRFOIL COORDINATES
[Section no. 12; radius 6.641 in. (16.868 cm)]

aCoordinates, in.		aCoordinates, cm	
X	Y	X	Y
-.9449	-.6987	-2.4000	-1.7700
-.9442	-.7013	-2.3982	-1.7812
-.9382	-.7063	-2.3829	-1.7940
-.9333	-.7001	-2.3706	-1.7939
-.9277	-.7041	-2.3563	-1.7839
-.9215	-.7005	-2.3413	-1.7792
-.9142	-.6936	-2.3220	-1.7616
-.9064	-.6859	-2.3022	-1.7422
-.8508	-.6310	-2.1610	-1.6026
-.7644	-.5504	-1.9416	-1.3981
-.6785	-.4755	-1.7233	-1.2077
-.5929	-.4058	-1.5058	-1.0306
-.5076	-.3410	-1.2893	-.8660
-.4228	-.2807	-1.0737	-.7130
-.3362	-.2249	-.8591	-.5711
-.2541	-.1730	-.6453	-.4393
-.1703	-.1249	-.4325	-.3172
-.0869	-.0803	-.2206	-.2039
-.0040	-.0390	-.0100	-.0990
.0523	-.0129	.1329	-.0327
.0762	-.0021	.1935	-.0052
.1002	.0086	.2544	.0218
.1242	.0191	.3154	.0485
.1465	.0295	.3765	.0748
.1724	.0397	.4376	.1008
.1966	.0499	.4992	.1266
.2208	.0599	.5607	.1521
.2450	.0698	.6223	.1773
.2693	.0797	.6840	.2024
.3005	.0926	.7631	.2351
.4246	.1403	1.0784	.3564
.5505	.1850	1.3981	.4697
.6763	.2260	1.7229	.5739
.8083	.2627	2.0530	.6673
.9583	.2988	2.4366	.7590
.9711	.3019	2.4664	.7667
.9776	.3039	2.4834	.7716
.9843	.3070	2.5000	.7797
.9921	.3149	2.5200	.7999
.9930	.3189	2.5223	.8100

aCoordinates on L-plane blade sections defined by the intersection of the blade with planes tangent to cylindrical surfaces.

TABLE 4.--Continued

ROTOR AIRFOIL COORDINATES

[Section no. 12--continued; radius 6.641 in. (16.868 cm)]

aCoordinates, in.		aCoordinates, cm	
X	Y	X	Y
.9930	.3193	2.5222	.8109
.9916	.3236	2.5190	.8213
.9885	.3275	2.5106	.8317
.9833	.3308	2.4974	.8402
.9765	.3334	2.4803	.8467
.9686	.3349	2.4602	.8507
.9559	.3361	2.4279	.8536
.8412	.3464	2.1365	.8799
.7148	.3479	1.8154	.8836
.5893	.3396	1.4967	.8624
.4046	.3216	1.1800	.8166
.3407	.2941	.8654	.7470
.2176	.2571	.5527	.6530
.0952	.2104	.2416	.5344
-.0267	.1539	-.0676	.3908
-.1476	.0871	-.3753	.2211
-.2076	.0486	-.5272	.1235
-.2364	.0298	-.6004	.0757
-.2650	.0106	-.6729	.0270
-.2932	-.0089	-.7448	-.0226
-.3212	-.0289	-.8159	-.0733
-.3489	-.0493	-.8862	-.1251
-.3763	-.0701	-.9557	-.1779
-.4033	-.0913	-1.0244	-.2319
-.4300	-.1130	-1.0922	-.2870
-.4564	-.1352	-1.1591	-.3434
-.4597	-.1379	-1.1675	-.3503
-.5041	-.1772	-1.2804	-.4500
-.6221	-.2914	-1.5800	-.7401
-.7406	-.4217	-1.8809	-1.0711
-.8596	-.5700	-2.1833	-1.4478
-.9298	-.6668	-2.3615	-1.6936
-.9375	-.6776	-2.3813	-1.7209
-.9415	-.6841	-2.3912	-1.7376
-.9440	-.6906	-2.3976	-1.7541
-.9449	-.6965	-2.4000	-1.7690

aCoordinates on L-plane blade sections defined by the intersection of the blade with planes tangent to cylindrical surfaces.
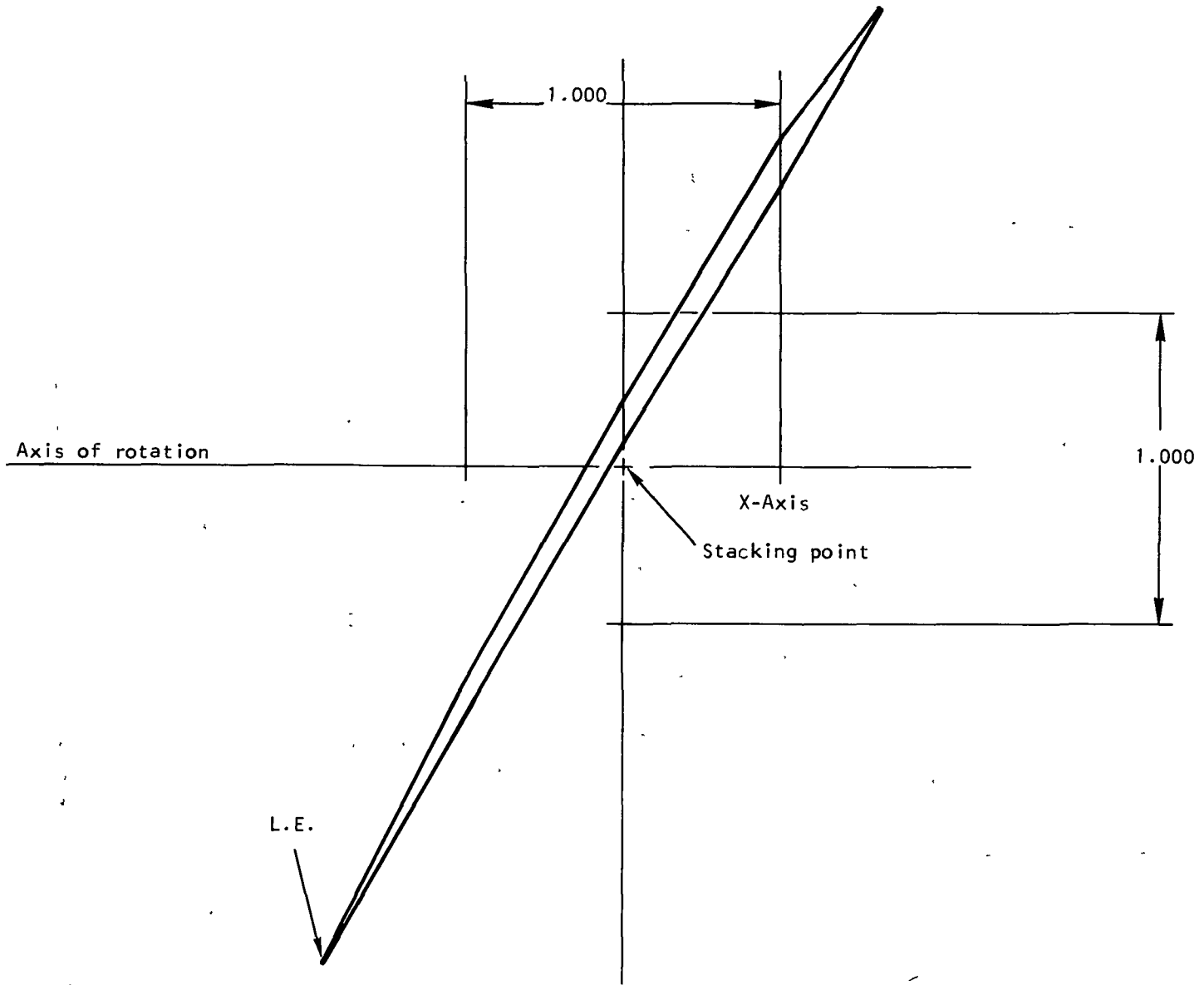
Figure 39.--Typical L-Section.

S-74025
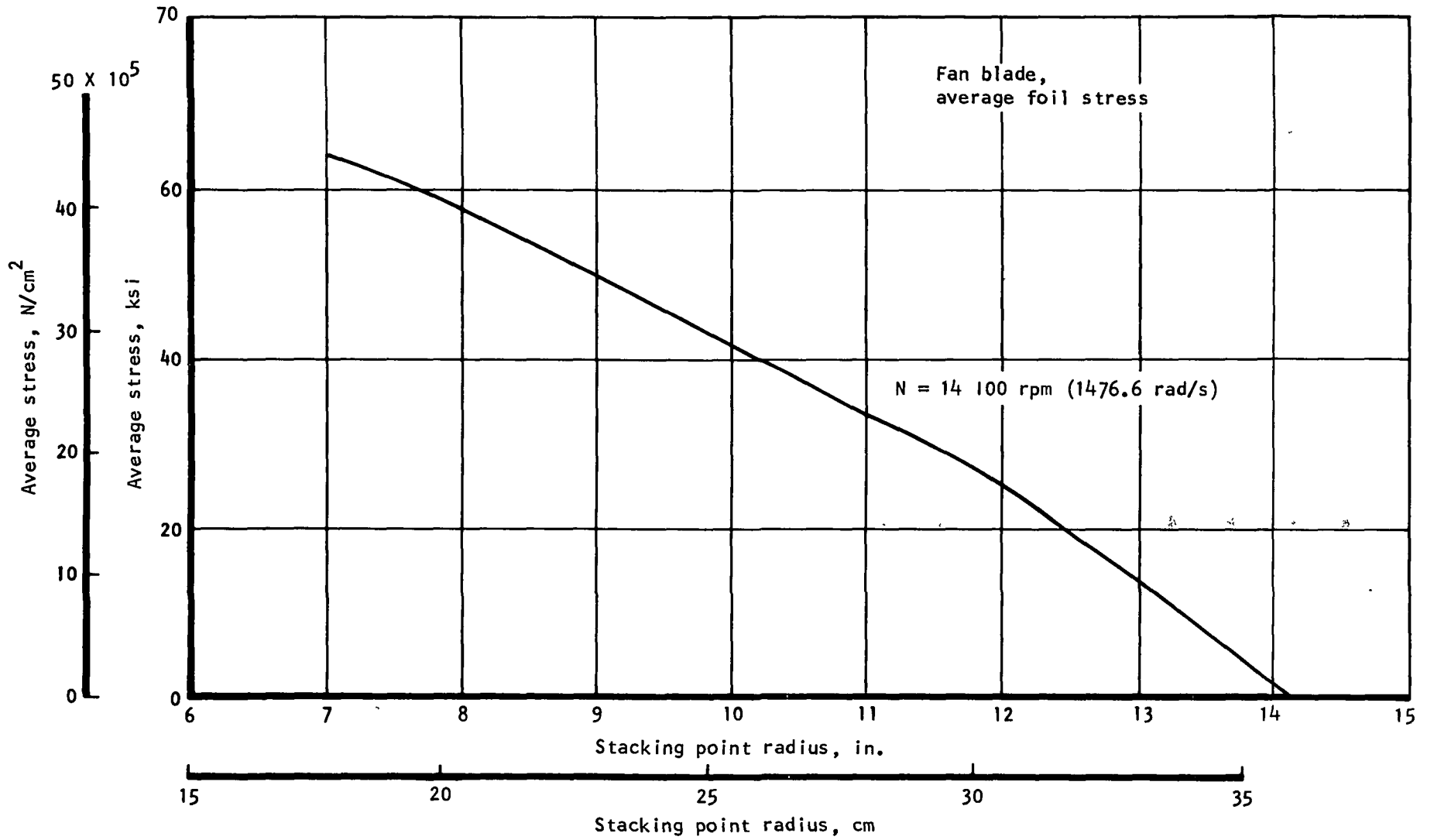
Figure 40.--Blade Average Foil Stress vs Radius.

S-71888

20
(13 79 x 10³)

30
(20 69 x 10³)

40
(27 58 x 10³)

20
(13 79 x 10³)

30
(20 69 x 10³)

40
(27 58 x 10³)

50
(34 48 x 10³)

65
(44 82 x 10³)

45
(31 03 X 10³)

Suction side

Pressure side
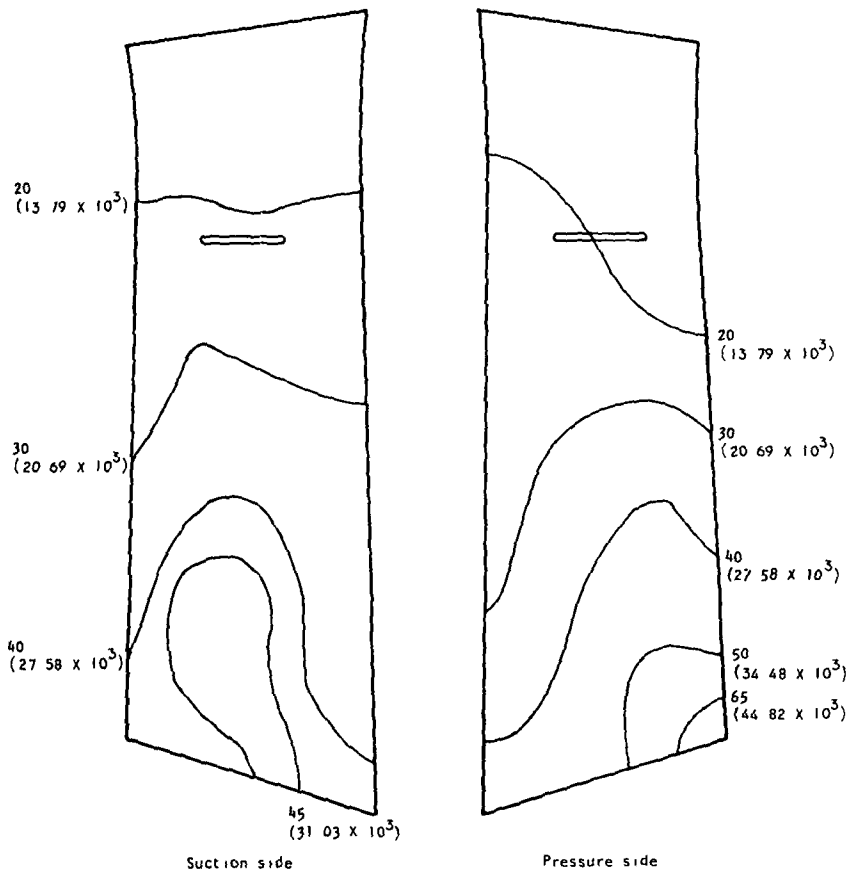
Blade built
to this tilt

Equivalent stress ksi (N/cm²)
N, 12 800 rpm (1340 4 rad/s)

S-71895

10 (6 90 X 10³)

10
(6 90 X 10³)

10 (6 90 X 10³)

5
(3 45 x 10³)

10
(6 90 X 10³)

10
(6 90 X 10³)

10 (6 90 X 10³)

Suction side

Pressure side

Equivalent stress, ksi (N/cm²)
N, 12 800 rpm (1340.4 rad/s)

S-71892

(a)   Blade Stress Distribution Due to
Aerodynamic and Centrifugal Loads,
0.0175 in./in. (cm/cm) Tangential Tilt.
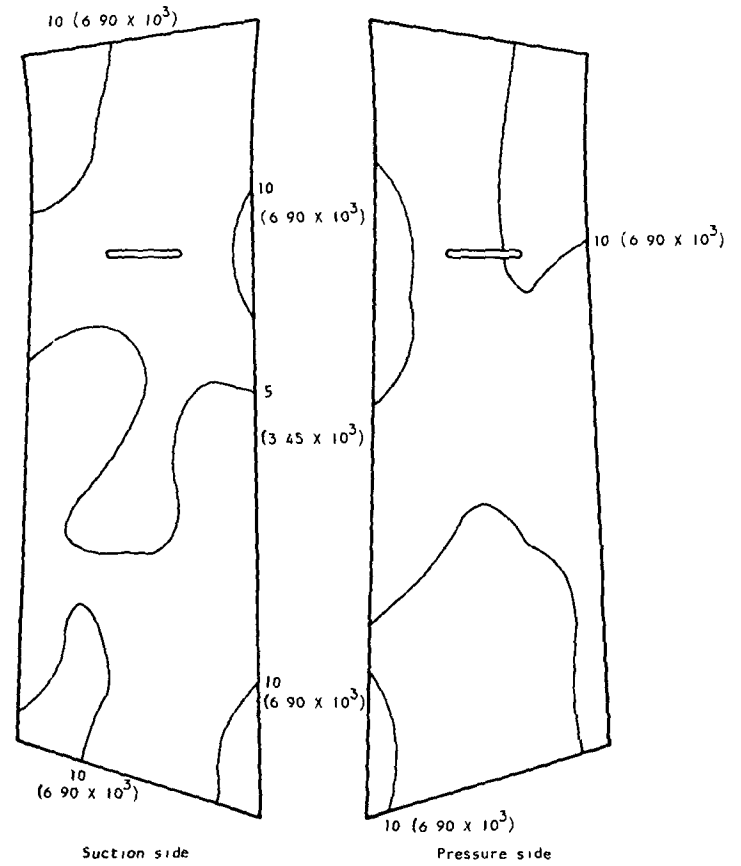
(b)   Blade Stress Distribution,
Aerodynamic Loads Only.

S-78047

Figure 41.--Blade Stress Distribution.

The midspan damper stress distributions are shown in fig. 42. The damper was made as thin as possible for aerodynamic reasons and a slight taper with thickness increasing from the overhang to the blade junction was required to minimize the stresses. The maximum stress at 100 percent speed is 80 ksi $(552 \times 10^2 \text{ N/cm}^2)$, which is less than the allowable 102 ksi $(704 \times 10^2 \text{ N/cm}^2)$.

The stacking axis displacements and blade untwist are shown in figs. 43 and 44, respectively. The tilt optimization of the blade at the aerodynamic design speed has reduced these displacements to the small magnitudes shown in the figures.

Blade vibration.--The blade interference diagram for the first three modes is shown in fig. 45. A frequency band is shown, based on the effective lock-up range that can be obtained from the midspan damper. The midspan dampers were designed to lock up at 50 percent speed. The midspan becomes effective prior to a two-per-revolution (2E) interference with the first flexural mode of a nonsupported blade. As shown in fig. 45, no blade resonances are expected at design speed. The first flexure mode occurs between 3E and 4E, the first torsion mode between 4E and 5E and the second bending mode between 6E and 8E. Resonances will occur at speeds below design speed, but are not expected to result in high stresses. The effect of blade dimensional tolerance on blade frequency is minor ($\pm$ 1.25 percent).

Fig. 46 is a modified Goodman diagram showing the allowable vibratory stress as a function of steady (mean) stress. The foil midchord at the midspan damper has been chosen as the critical point for vibratory stress. The allowable alternating vibratory stress (30 ksi or $207 \times 10^2 \text{ N/cm}^2$) is shown in fig. 46.

Mode shapes for zero speed and 14 100 rpm (1476.6 rad/s) are shown in fig. 47. The second flexural mode is a complex shape and cannot be considered a true second flex. Nodal lines are drawn from the results of displacement vectors obtained from the vibration program. The measured mode shapes based on a bench test are presented for comparison for the zero-speed case in the appropriate figures. Both the measured and calculated results were with the blade dovetail and midspan damper clamped. Good correlation is shown between the measured and calculated results.

Equivalent stress ksi (N/cm^2)

N = 14 100 rpm (1476.6 rad/s)
Midspan damper radius = 12.0 in. (30.48 cm)

Leading edge

10 (6.895×10^3)

20 (13.79×10^3)

40 (27.58×10^3)

20 (13.79×10^3)

10   20   40   60   70 80
(6.895×10^3) (13.79×10^3) (41.37×10^3) (55.16×10^3)

Foil intersection

S-71904
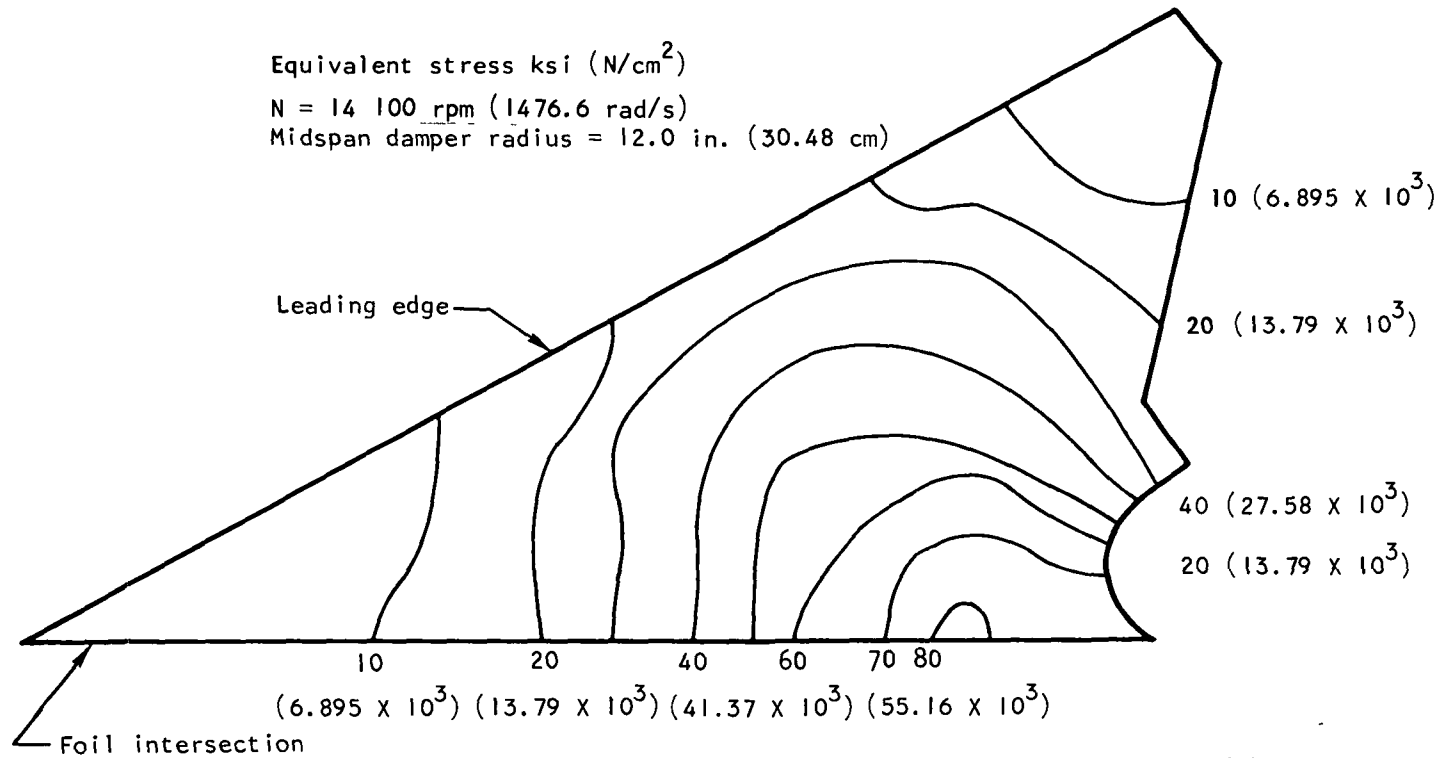
Figure 42.--Blade Midspan Damper Stress Distribution.
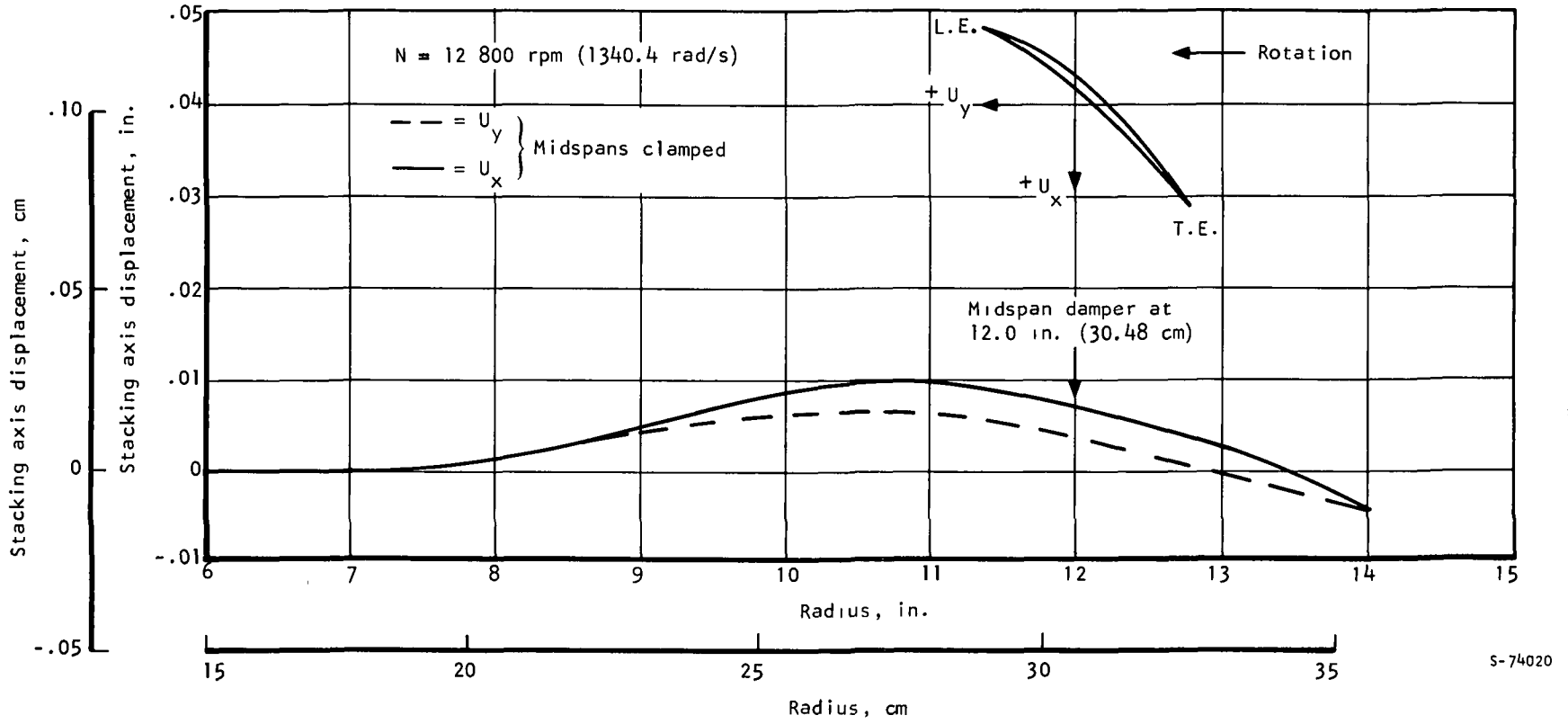
Figure 43.—Stacking Axis Displacement.
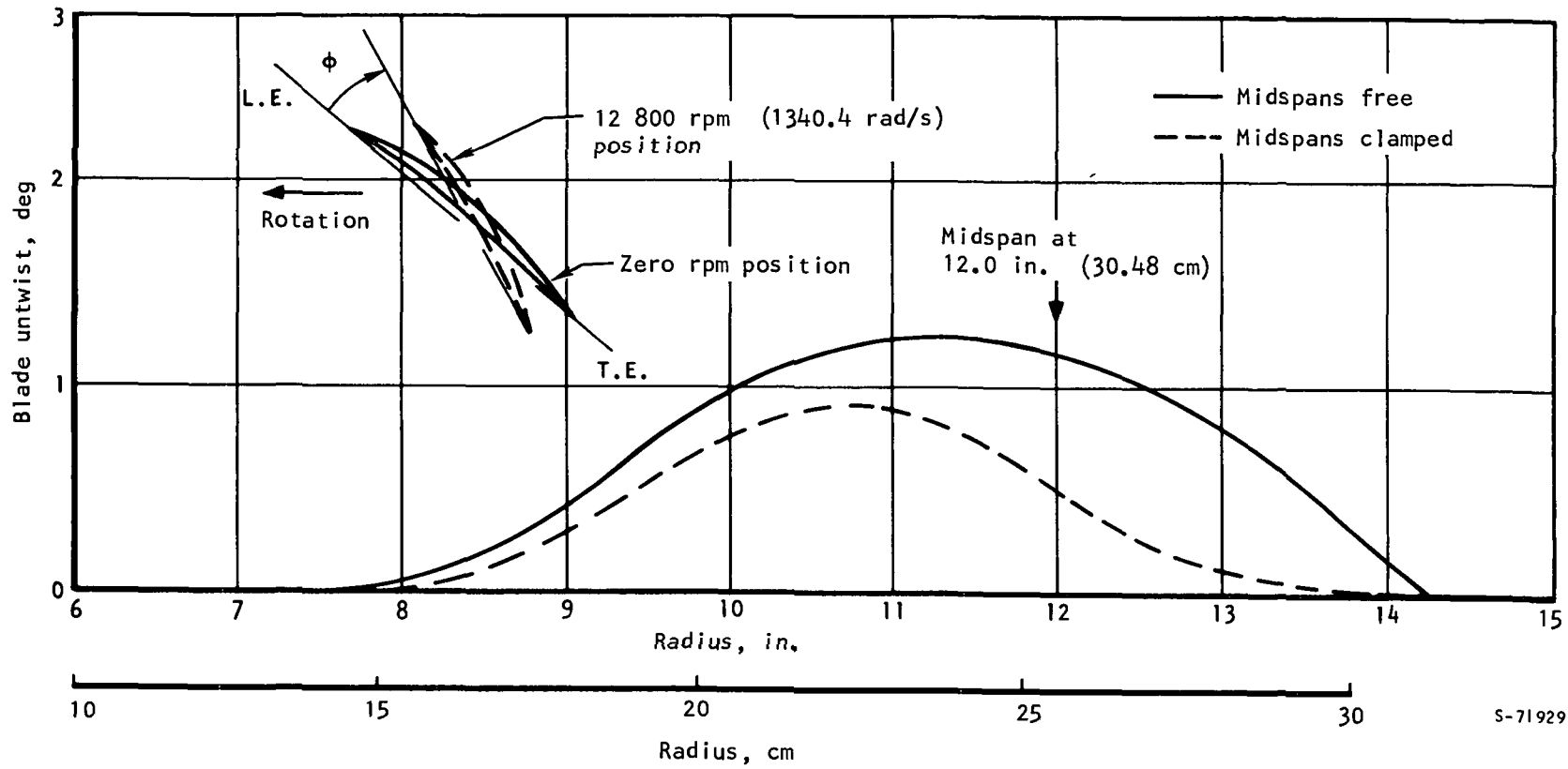
Figure 44.--Blade Untwist.

S-71929
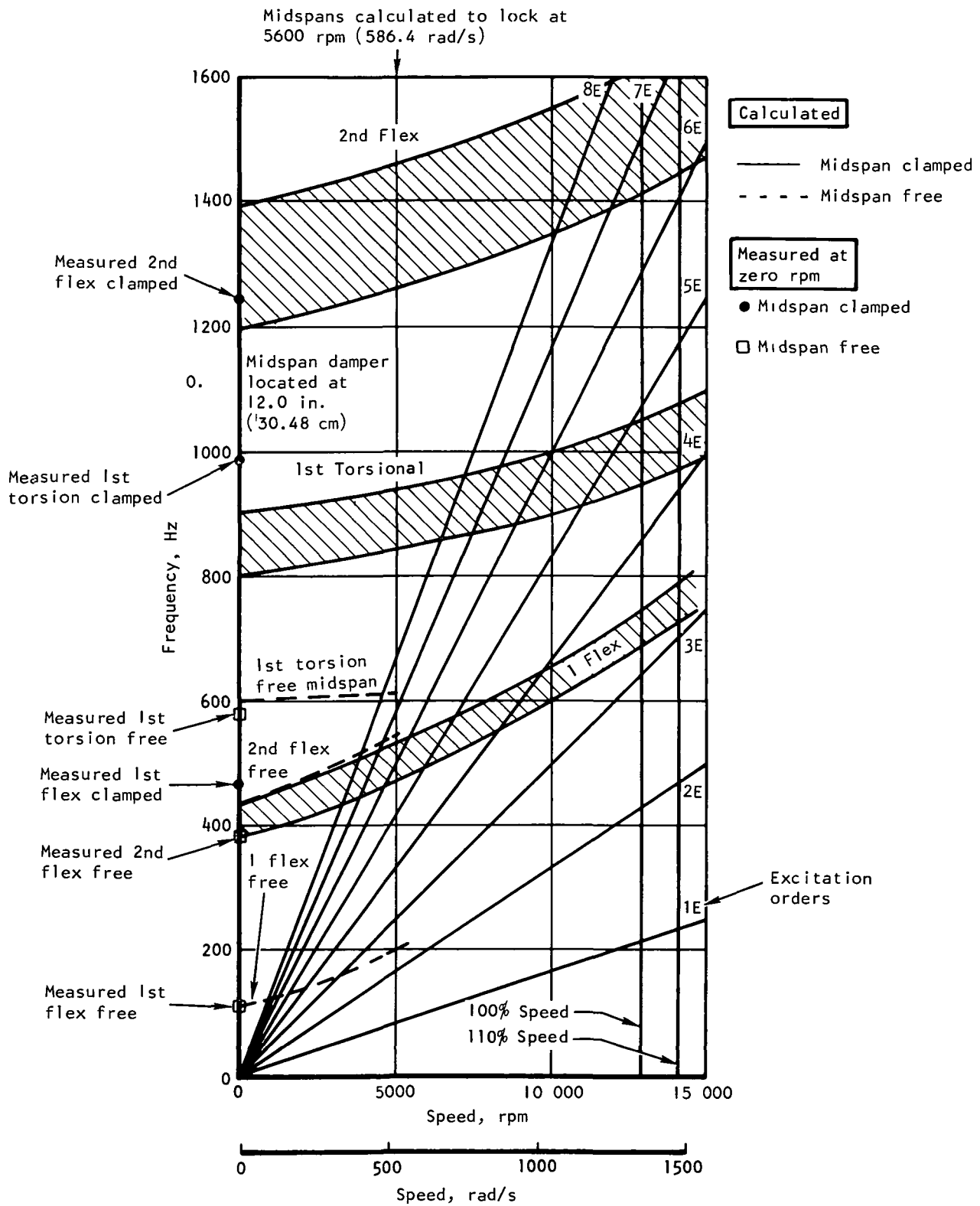
Figure 45.--Blade Interference Diagram.
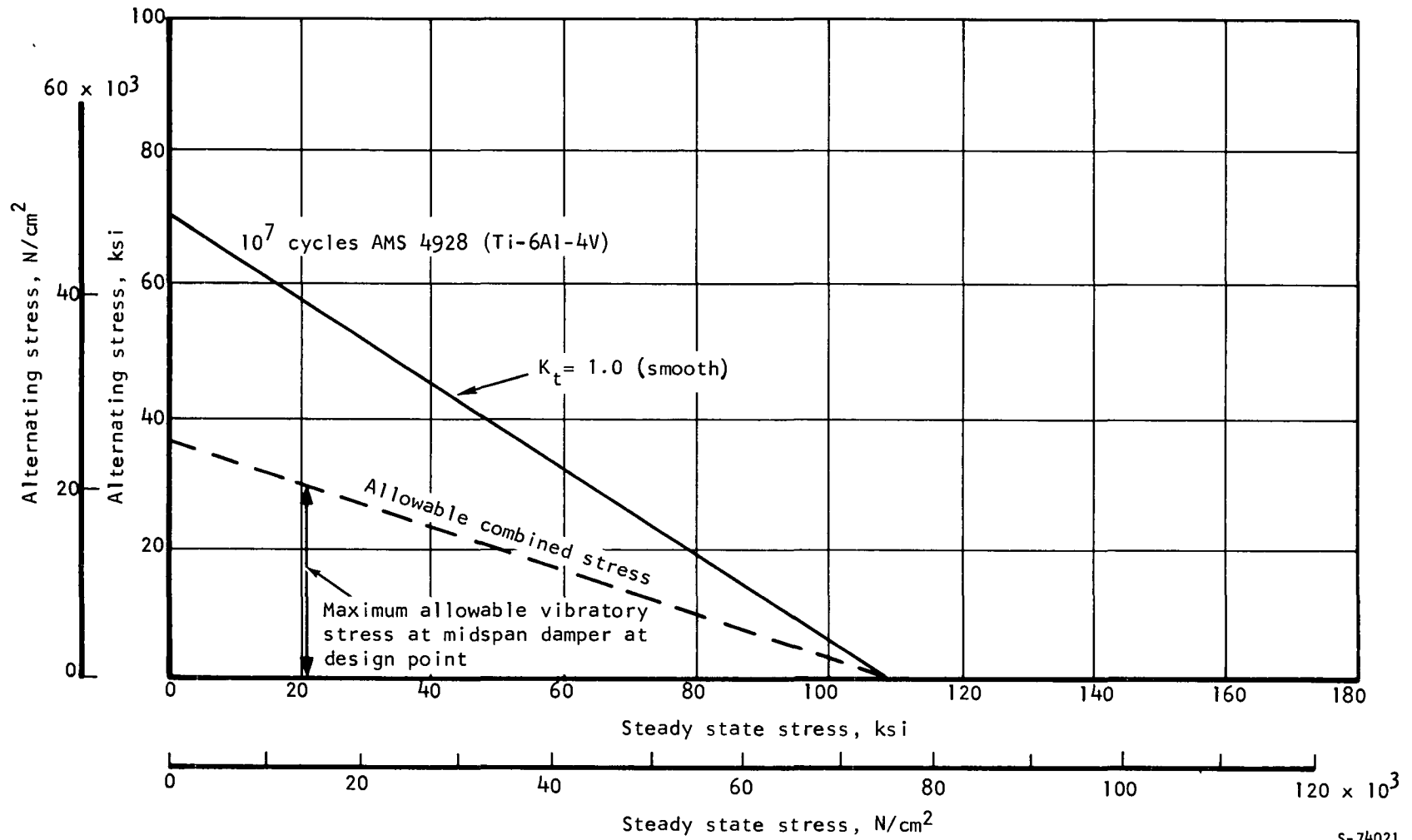
Figure 46.--Blade Goodman-Solderburg Diagram.

S-74021

109

Peak amplitude

Midspan damper

1st flex
zero rpm
432 Hz calculated
550 Hz measured

1st flex
781 Hz
14 100 rpm
(1476.6 rad/s)

1st torsion
zero rpm

904 Hz calculated

1000 Hz measured

1st torsion
1071 Hz
14 100 rpm
(1476.6 rad/s)

2nd flex - complex
zero rpm

1390 Hz calculated

1257 Hz measured

2nd flex - complex
1655 Hz

14 100 rpm
(1476.6 rad/s)
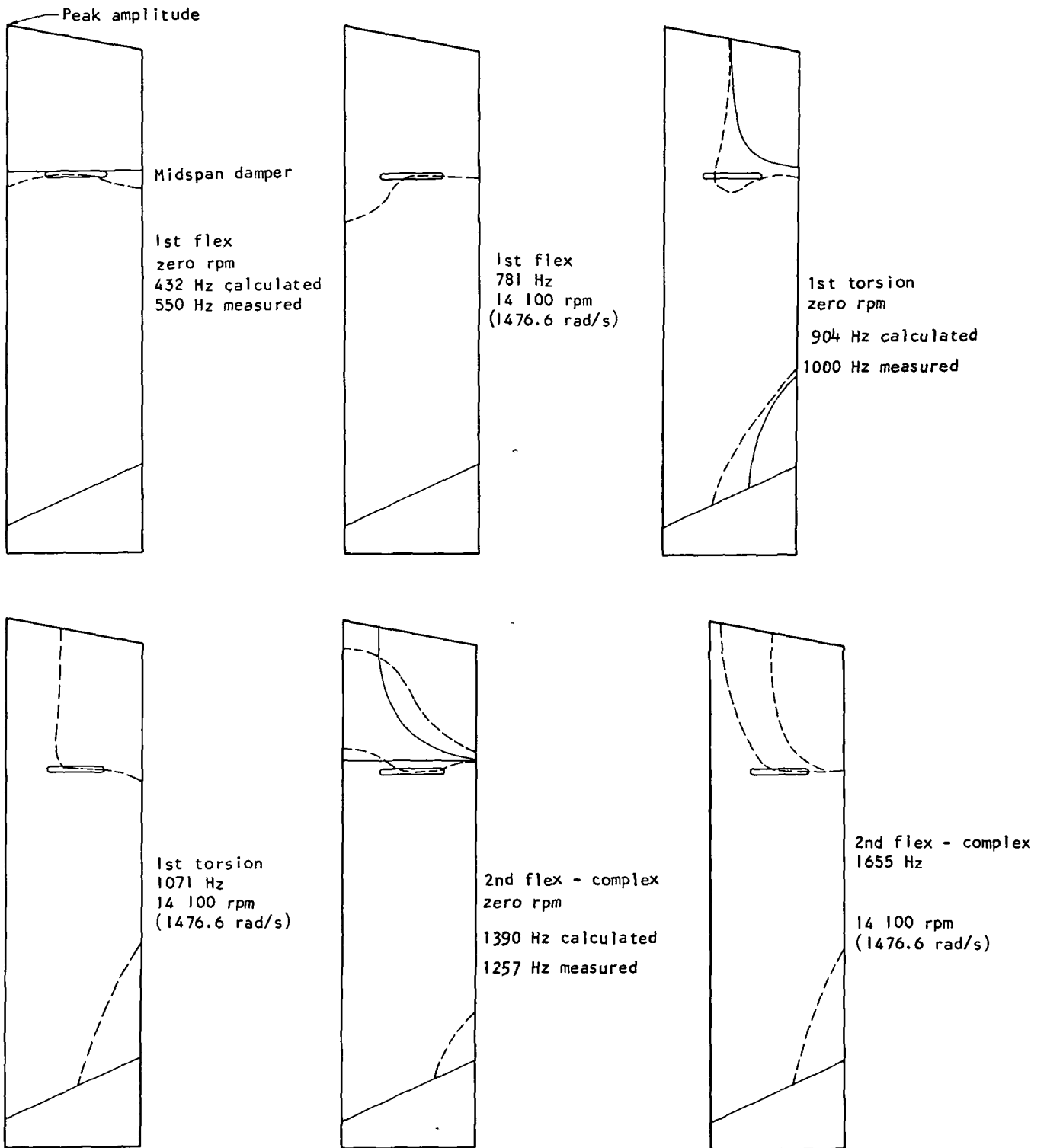
Note: Midspan damper located at 12.0 in. (30.48 cm)
Midspan and root clamped.
— — — — — — Calculated
————————— Bench test measurements

S-78048

Figure 47.--Blade Mode Shapes.

110

Blade flutter.--Flutter is a self-excited blade vibration that occurs primarily in the torsional mode or coupled bending torsional mode.

The effect of the midspan damper location on the torsional flutter was initially investigated by considering the blade to be split into two parts built ·in at the damper. One part is the portion extending radially inward from the damper and the other part extends radially outward from the damper. The flutter parameter versus midspan damper radial position for each of these independent blade parts and also for the complete blade, is shown in fig. 48. The optimum position of the midspan damper is 12.4 in. (31.5 cm) as can be seen from this figure. If -the midspan damper could be considered to lock the foil with 100 percent rigidity (cantilevered outboard from the damper), a flutter parameter of 1.6 could be obtained with a single damper located at the optimized radius. The achievable rigidity of the damper as shown by the cross-hatched region in fig. 48 can produce a flutter parameter between 1.1 and 1.2, where the flutter parameter is defined as $\omega C/V'$. A flutter parameter of 1.6 is considered conservatively safe and blades with a parameter as low as 1.0 have operated successfully.

ω = blade frequency, rad/s

C = chord, ft (or cm)

V' = relative velocity, ft/s (or m/s)

The damper was positioned at a 12.0 in. (30.48 cm) radius giving a flutter parameter in torsion between 1.1 and 1.2 (fig. 47) at 100 percent of normal operating speed. This final position was chosen as a compromise between anticipated flutter stability and midspan damper Mach number. Positioning the midspan damper out beyond 12.0 in. (30.48 cm) would have placed it at a radius at which supersonic through-flow was expected and would have compromised the achievement of this design flow condition.

Fig. 49 shows the relationship of C/V' versus radius. As can be seen, it is essentially a constant that makes the flutter parameter independent of the radial reference station used. The tip section was used as the reference station in the calculations.

Rotor Disk

Disk stresses.--The tangential and radial stresses versus radius are shown in fig. 50. The bore and web stresses are within the allowable values given in the design criteria. The disk average tangential stress is 64 100 psi (421×10^2 N/cm^2) at the overspeed point of 14 100 rpm (1476.6 rad/s).
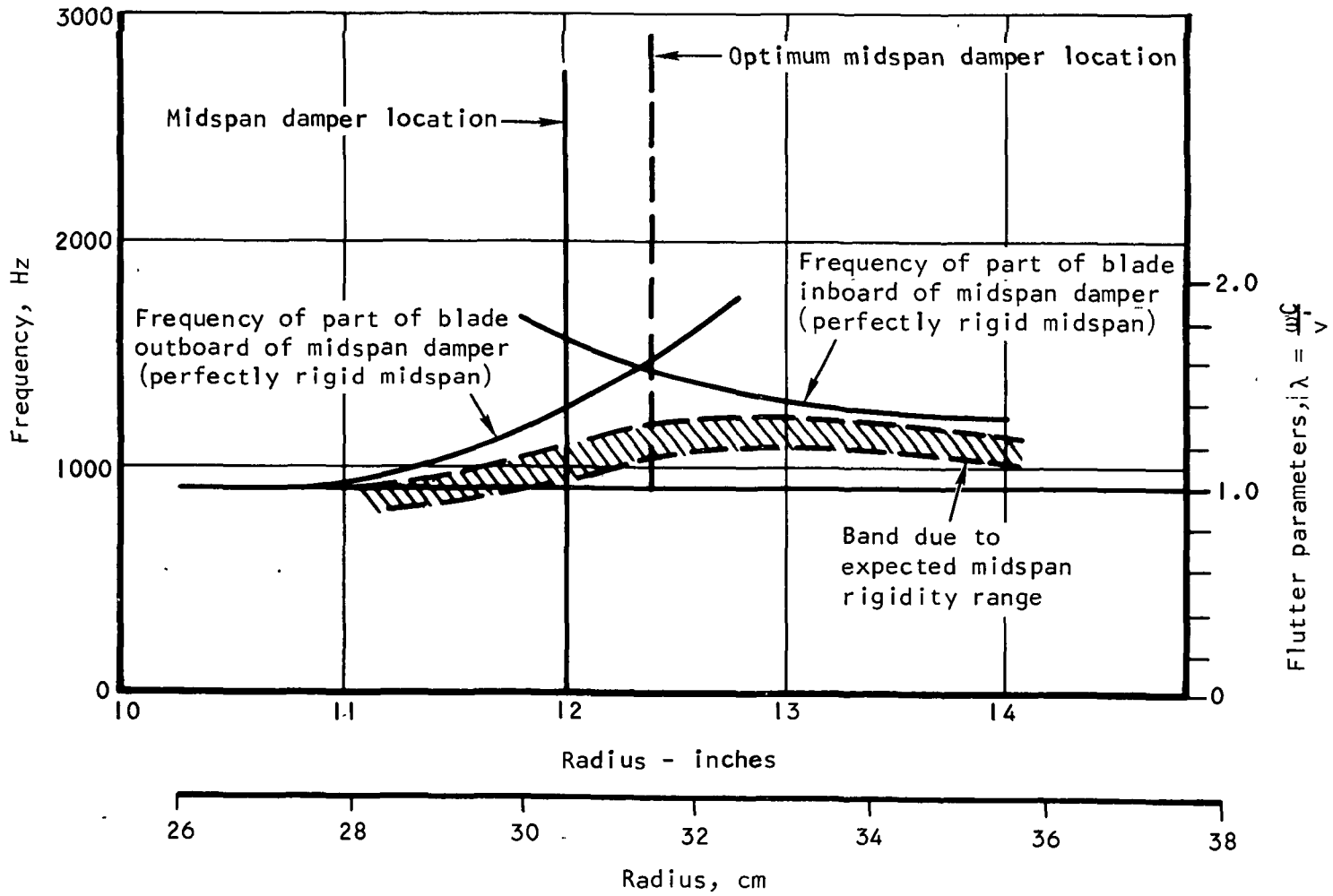
Figure 48.--Blade First Torsional Frequency and Flutter
Parameter vs Midspan Damper Location.

S-73034
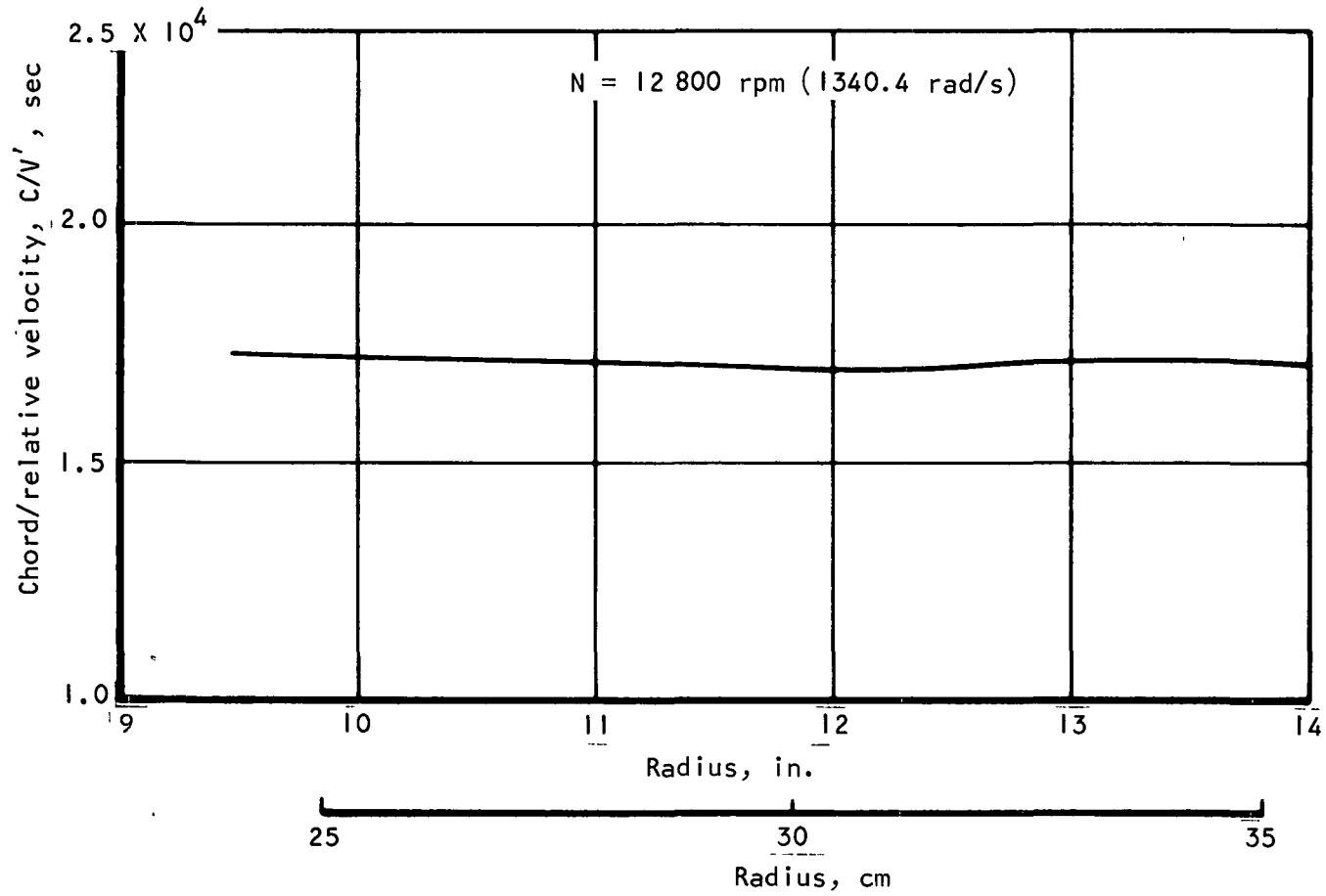
Figure 49.--Blade Chord Divided by Relative Velocity.

S-71925
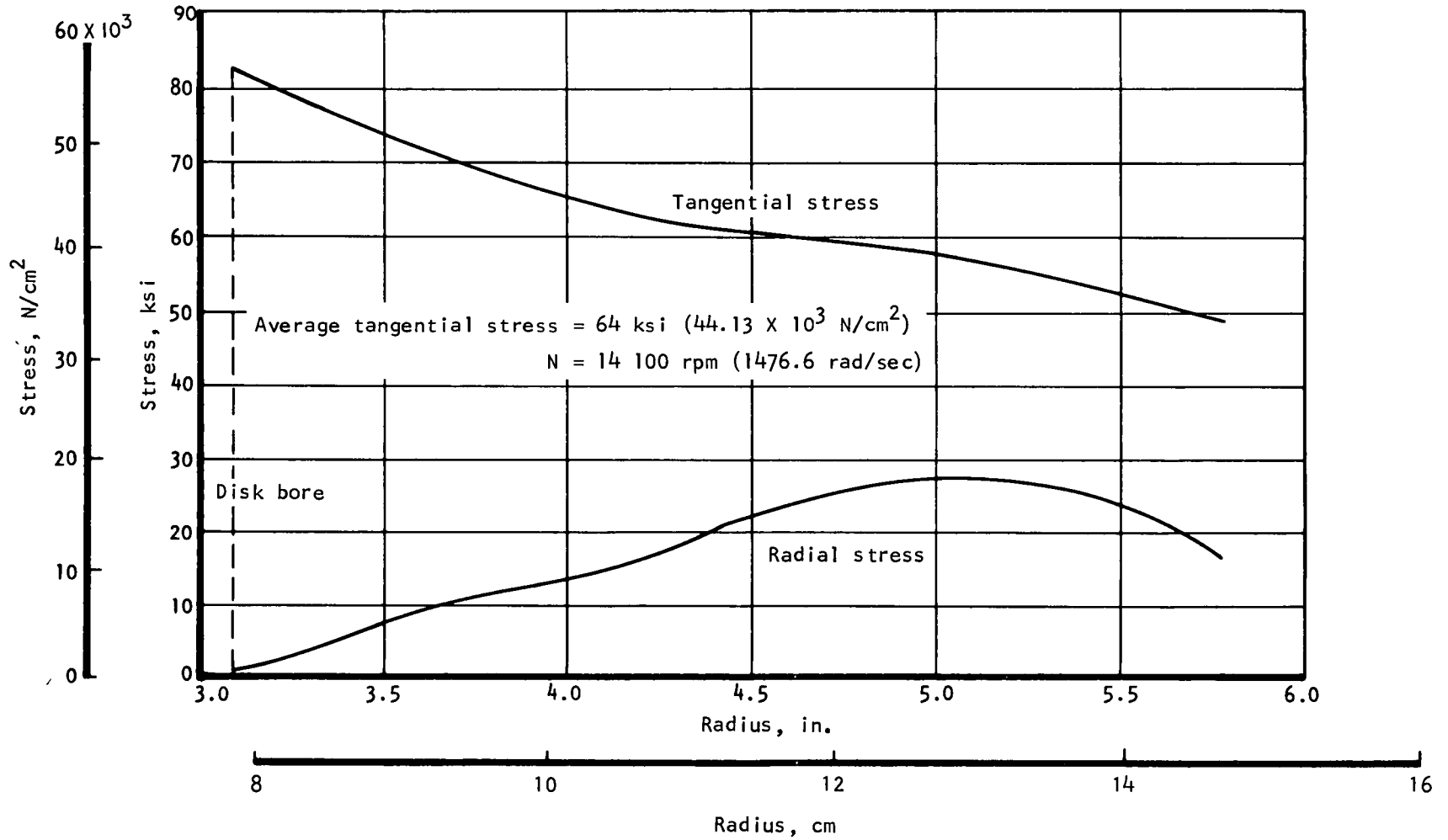
Figure 50.--Disk Centrifugal Stress vs Radius.

S-71884

Burst and shedding speeds.--The minimum shedding speeds for the foil and dovetail and minimum disk burst speeds were determined for the worst tolerances and maximum temperature conditions. These shedding speeds were:

Blade foil	18 400 rpm (1927 rad/s)
Blade shank	22 900 rpm (2400 rad/s)
Disk shank	18 500 rpm (1938 rad/s)
Disk burst	18 100 rpm (1895 rad/s)

The required minimum burst and shedding speed is 17 600 rpm (1843.1 rad/s), which is 125 percent of the mechanical design speed. The disk, which is the most critical element, exceeds the minimum required shedding speed by 3.0 percent.

Radial growth.--The radial growths of the hub and tip leading and trailing edges are summarized in table 5. This table presents the centrifugal, thermal, and total growth separately at the mechanical design speed. As expected, the maximum radial growth of 0.0432 in. (0.11 cm) occurs at the blade tip leading edge.

TABLE 5

HUB AND TIP RADIAL GROWTH

	Hub		Tip	
	in.	cm	in.	cm
Centrifugal growth, N = 14 100 rpm				
Leading edge	0.016	0.0406	0.034	0.0864
Trailing edge	.016	.0406	.028	.0711
Thermal growth, disk temperature = 150°F (339°K) blade temperature = 250°F (395°K)				
Leading edge	.0025	6.35×10^{-3}	.0092	.0234
Trailing edge	.0028	7.11×10^{-3}	.0083	.0211
Total growth				
Leading edge	.0185	.0470	.0432	.1097
Trailing edge	.0188	.0478	.0363	.0922

Blade/Disk Attachment

Attachment stresses.--The dovetail attachment stresses in the blade to disk have been summarized in table 6. Neck, tang, and combined stresses are shown. The combined fillet stress is a combination of tang bending and neck tension excluding stress concentration effects, while the maximum fillet stress which effects the low cycle fatigue life of the attachment includes the stress concentration factor. All the calculated stresses show a positive margin of safety based on the design criteria given previously. The disk, which is the weakest link as a result of using existing tooling, has a 0.03 margin of safety on the maximum fillet stress. The allowable stress levels are based on a 10 000-starts requirement and can be deviated from for this test rig application.

Stator Vane

Geometric definition.--The geometric summary of the final stator vane design is presented in tabular form in table 7.

Steady-stress.--The maximum airfoil steady-state stress is 6000 psi (41.4 $\times 10^2$ N/cm^2) and is induced by gas bending loads. This stress is well below the allowable.

Vibration.--The calculated natural frequencies of the fan stator are shown in fig. 51. The only exciting force will come from the 40 fan rotor blade wakes. Whenever the 40-excitations-per-revolution line crosses a natural frequency, a possible resonance condition with an amplification of the vibratory stress level exists. Examination of the excitation diagram reveals possible resonances throughout the operating speed range; however no resonance problems are expected. The first four natural frequencies will not be excited above 5000 rpm (522 rad/s) and can be passed through rapidly during rig running without causing any problems. The allowable vibratory stress based on a modified Goodman diagram is 34 ksi (234 $\times 10^2$ N/cm^2) as shown in fig. 52.

Stator vane flutter.--The frequency parameter, $\lambda = \omega C/V'$, was calculated for torsional flutter. The calculated value of 2.75 is well above the conservative minimum of 1.6, indicating stable operation.

Spool Critical Speed

The critical speed analysis of the fan spool and facility drive system shows that no resonance problems will occur within the rig operating speed range. The first critical speed of the system with synchronous precession (whirl ratio = 1) is 16 370 rpm (1714.3 rad/s), which provides a 16-percent margin over the maximum speed. The second critical speed is calculated to be 23 050 rpm (2413.8 rad/s).

TABLE 6

BLADE-TO-DISK DOVETAIL ATTACHMENT STRESSES

	Blade				Disk			
	Allowable	Nominal	Peak	Margin of Safety	Allowable	Nominal	Peak	Margin of safety
Neck tension or tang bending	87.4 (603×10^2)	36.4 (251×10^2)	46.3 (319×10^2)	0.88	87.4 (603×10^2)	61.0 (421×10^2)	76.3 (526×10^2)	0.15
Combined fillet	121.3 (838×10^2)	69.1 (476×10^2)	86.5 (596×10^2)	.40	121.3 (838×10^2)	94.7 (790×10^2)	114.5 (790×10^2)	.06
Maximum fillet (low cycle fatigue)	181.4 (1252×10^2)	0 0	127.2 (877×10^2)	.43	181.4 (1252×10^2)	0 0	177.0 (122×10^3)	.03
Bearing	121.3 (838×10^2)	47.7 (329×10^2)	71.8 (495×10^2)	.69	121.3 (838×10^2)	47.7 (329×10^2)	71.8 (495×10^2)	.69
Shear	50.7 (350×10^2)	23.1 (159×10^2)	27.0 (186×10^2)	.83	50.7 (350×10^2)	21.9 (151×10^2)	25.6 (177×10^2)	.93

NOTES:
(1) All stresses in ksi and (N/cm^2)
(2) All stresses calculated at 100 percent speed 14 100 rpm (1476.6 rad/s)
(3) Margin of safety is based upon the larger of (1.2 X nominal) or (calculated peak)
       Margin of safety = (allowable stress/calculated stress) - 1
(4) Allowable stresses include:
       5-percent reduction for surface finish and leading rate
       4.5-percent reduction for broach angle

TABLE 7

STATOR GEOMETRIC SUMMARY

|L-Plane Blade Sections, defined by the intersection of the blade and planes tangent to cylindrical surfaces|

Blade Height= 6.076 in. (0.1542m)   Number of vanes = 45   Airfoil Section

Hub/tip ratio = 0.560   Aspect ratio = 3.10   Double circular arc

Radius	in.	13.499	12.891	11.980	11.373	10.765	10.158	9.550	8.639	8.031
	m	0.3429	0.3274	0.3043	0.2889	0.2734	0.2580	0.2426	0.2194	0.2040
β_1^*		26.0	26.6	28.0	29.3	30.8	31.3	31.2	31.4	31.6
β_2^*		-7.5	-7.7	-8.4	-9.2	-10.2	-10.3	-9.8	-9.2	-9.0
Camber $\Delta\beta^*$		33.5	34.3	36.4	38.5	41.0	41.6	41.0	40.6	40.6
Stagger β_M^*		9.21	9.47	9.80	10.05	10.27	10.49	10.72	11.06	11.28
Axial chord	in.	1.926	1.926	1.926	1.926	1.926	1.926	1.926	1.926	1.926
	cm	4.89	4.89	4.89	4.89	4.89	4.89	4.89	4.89	4.89
Chord	in.	1.951	1.953	1.955	1.956	1.957	1.959	1.960	1.963	1.964
	cm	4.96	4.96	4.97	4.97	4.97	4.98	4.98	4.99	4.99
t_{max}/C		0.065	0.065	0.065	0.065	0.065	0.065	0.065	0.065	0.065
$r_{L.E.}/C$ & $r_{T.E.}/C$		0.004	0.004	0.004	0.004	0.004	0.004	0.004	0.004	0.004
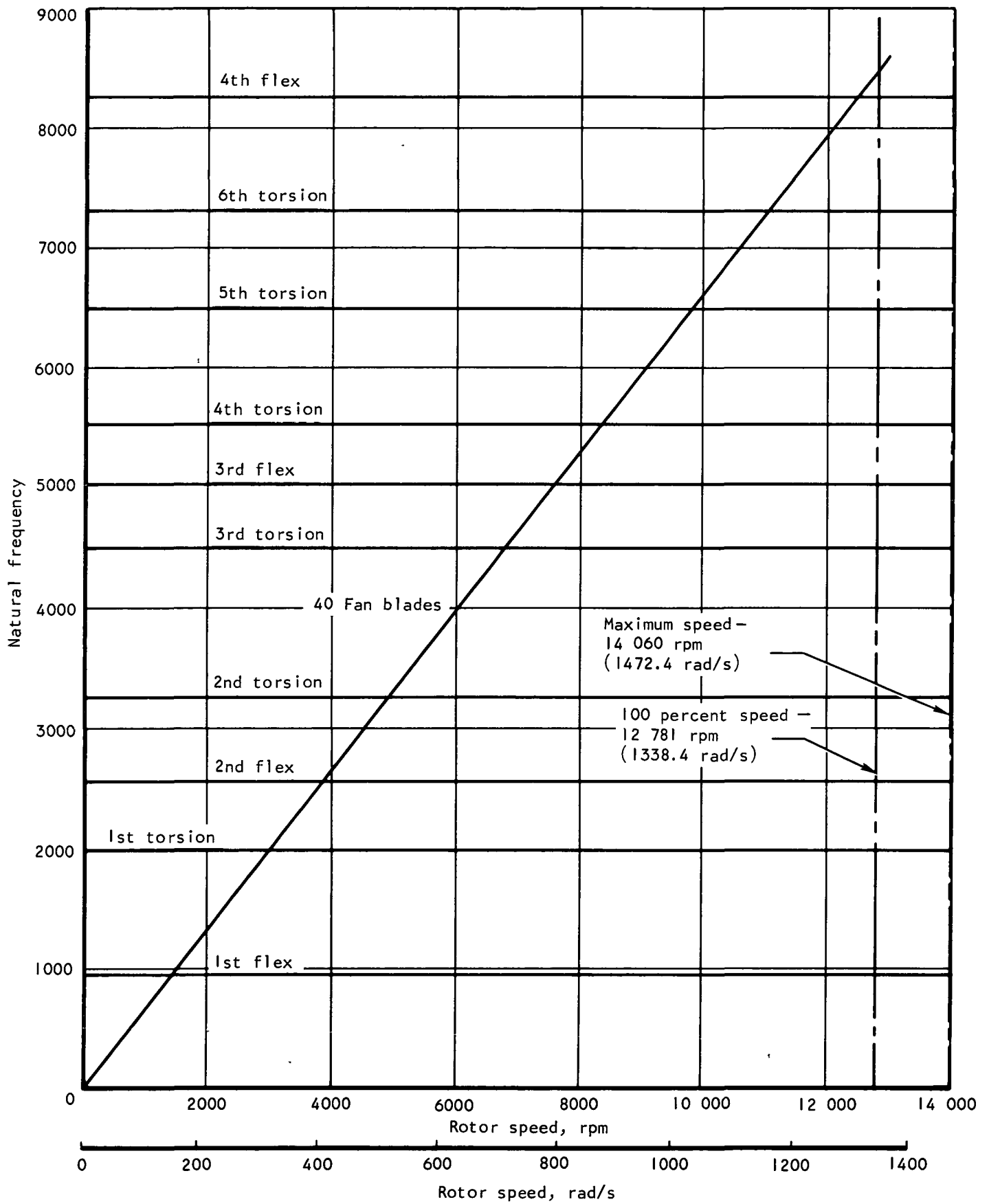
Figure 51.--Stator Vane Excitation.

S 71 P82

119
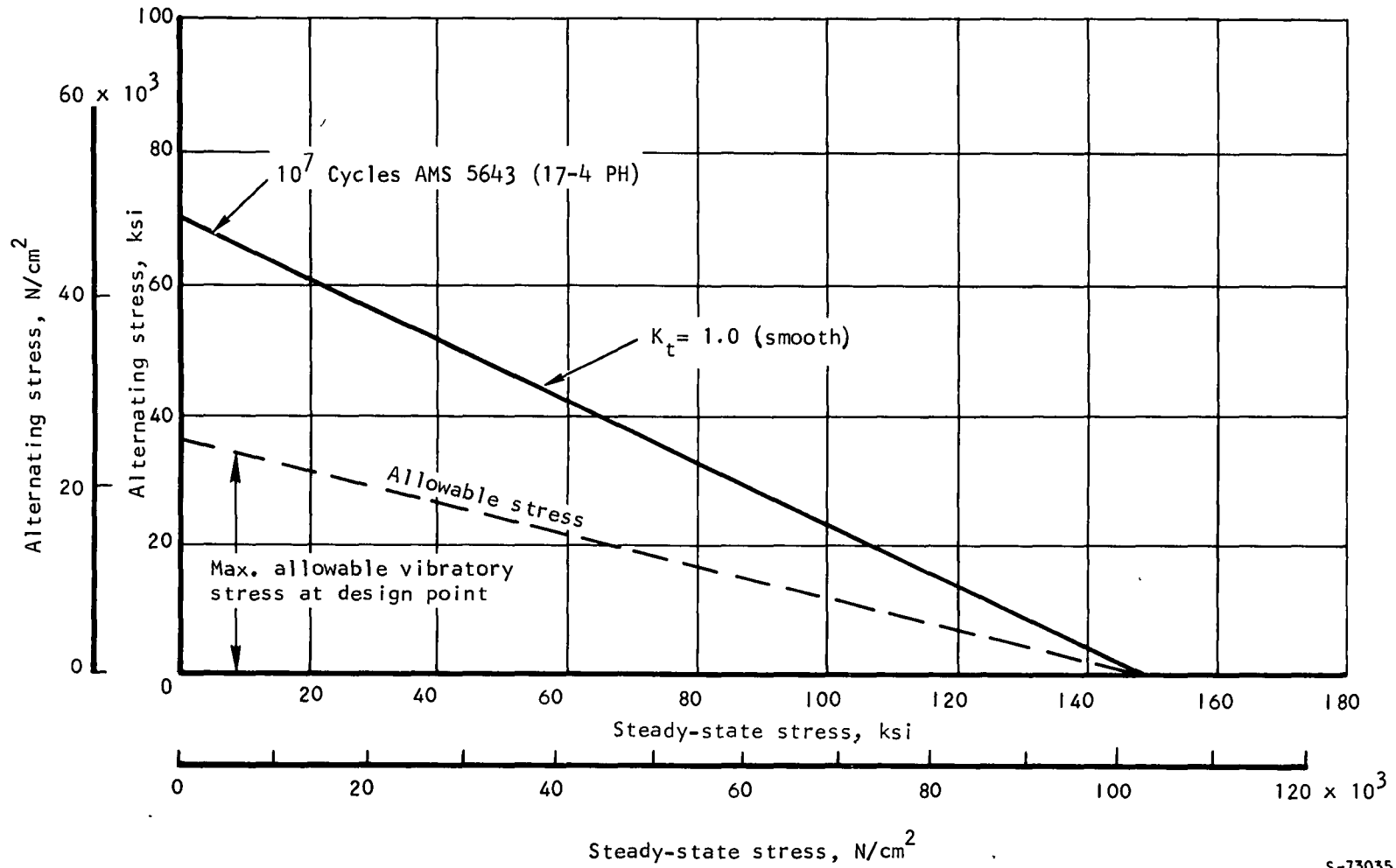
Figure 52.--Stator Vane Goodman-Soderburg Diagram.

APPENDIX A

THE CHARACTERISTIC COMPATIBILITY EQUATIONS

The purpose of this appendix is to derive the characteristic compatibility equations which apply to the flow in the outboard regions of the rotor. The derivation is divided into the following sections:

(1) General discussion

(2) Assumptions

(3) Governing differential equations

(4) Governing differential relationships

(5) The compatibility equations in $P-\beta$ form

(6) The compatibility equations in ξ^+, ξ^- form

(7) Derivatives of the unit vector $\bar{i}_s$

GENERAL DISCUSSION

Consider the steady, supersonic, planar flow of a gas in some shockless region R. At each point P in R, two directions (referred to as the positive and negative characteristic directions) may be defined. The positive characteristic direction is oriented at an angle of $+\mu$ and the negative characteristic direction at an angle of $-\mu$ with respect to the velocity vector at P. The angle μ is the Mach angle, defined as

$$\sin \mu = \frac{1}{M} \tag{A-1}$$

A curve passing through point P, and tangent everywhere along its length to the local positive characteristic direction, is referred to as the positive characteristic through P. Similarly, a curve through P everywhere tangent to the negative characteristic direction is called the negative characteristic through P. The positive and negative characteristic curves through P are denoted by C_p^+ and C_p^-, respectively. If the subscript p is not specified, then C^+ and C^- refer to arbitrary positive and negative characteristics.

Consider again the above flow field, with the additional constraints that the field be adiabatic and have constant entropy and total enthalpy, and that the gas be an inviscid, thermally perfect gas of constant composition. The theory of characteristics as applied to the mathematical model of this flow field indicates that the field possesses a rather surprising property. This property is that the quantities ξ^+ and ξ^-, defined as $\xi^+ = \frac{\nu - \beta}{2}$ and $\xi^- = \frac{\nu + \beta}{2}$

121

are invariant on the positive and negative characteristics, respectively, independent of how these characteristics weave and wind through the field. This property may be stated in differential form in the following manner

$$d\xi^+ = 0 \text{ on } C^+ \tag{A-2}$$

$$d\xi^- = 0 \text{ on } C^- \tag{A-3}$$

or more compactly as

$$d\xi^\pm = 0 \text{ on } C^\pm \tag{A-4}$$

Eq. (A-4) is referred to as the characteristic compatibility equation for this particular flow field.

The extreme simplicity of eq. (A-4) allows flow problems which satisfy the above field constraints to be analyzed in a simple, though tedious, manner by the so-called "method of characteristics." The technique is, in fact, simple enough to be done by hand.

Many flow fields which violate some of the above constraints can still be solved using the method of characteristics; however, the compatibility equations and consequently the solution technique become more complex. In general, the additional complexity is sufficient to make hand calculations impractical, and recourse must be made to high-speed digital computers.

ASSUMPTIONS

In deriving the compatibility equations which apply to the stream tube flows in the outboard regions of the rotor, the following assumptions are made:

(1) The fluid is constrained to flow within an axisymmetric stream-tube of specified geometry.

(2) The fluid is an inviscid, thermally perfect gas with constant composition and zero thermal conductivity.

(3) The flow field is steady and fully supersonic relative to a coordinate system which is fixed to the rotor.

(4) Electric, magnetic, gravitational, and thermal radiation effects are neglected.

Assumption (1) above is particularly significant in that it reduces the fully three-dimensional problem to a quasi-three-dimensional problem. As a consequence, effects associated with the blade geometry on other stream tubes will not be accounted for except indirectly, insofar as they affect the local stream-tube geometry via the axisymmetric flow analysis.

122

GOVERNING DIFFERENTIAL EQUATIONS

Within the accuracy of the above assumptions, the flow in the outboard regions of a rotor is governed by the following differential equations relative to a coordinate system fixed to the rotor.

Continuity:

$$\frac{1}{\rho} \overline{V}' \cdot \nabla \rho + \nabla \cdot \overline{V}' = 0 \tag{A-5}$$

As presented by Wu (ref. 9) the momentum equation is written as follows:

$$(\overline{V}' \cdot \nabla)\overline{V}' + 2\overline{\omega} \wedge \overline{V}' - \omega^2 \overline{r} + \frac{\nabla p}{\rho} = 0 \tag{A-6}$$

Also, from ref. 9, eq. (14a) for steady isentropic flow,

$$\nabla I = \overline{V}' \wedge (\nabla \wedge \overline{V}') \tag{A-7}$$

where I is the enthalpy function:

$$I = H - \omega(V_\theta r)$$

Taking the dot product of $\overline{V}'$ on both sides of eq. (A-7) yields

$$\overline{V}' \cdot \nabla I = 0 \tag{A-8}$$

Owing to the fact that $\overline{V}' \cdot \overline{V}' \wedge (\nabla \wedge \overline{V}') \equiv 0$

From the equation of state and the conditions of isentropy, the following is obtained:

$$\frac{p}{p_o} = \left(\frac{\rho}{\rho_o}\right)^\gamma \tag{A-9}$$

where the subscript, o, refers to an arbitrary reference state.

For the purposes of this analysis, the system of eqs. (A-5) through (A-9), is more conveniently handled in a less conventional form developed as follows:

From eq. (A-9),

$$\frac{1}{\gamma} \log_e \left(\frac{p}{p_o}\right) = \log_e \left(\frac{\rho}{\rho_o}\right) \tag{A-10}$$

Defining a pressure function P as

$$P = \frac{1}{\gamma} \log_e \left(\frac{p}{p_o} \right) \tag{A-11}$$

and taking the gradient of eq. (A-10) yields

$$\frac{\nabla p}{\rho} = \nabla P$$

Substitution into eq. (A-5) yields

$$\overline{V}' \cdot \nabla P + \nabla \cdot \overline{V}' = 0 \tag{A-12}$$

From eq. (A-11)

$$\nabla P = \frac{1}{\gamma} \frac{\nabla p}{p}$$

or

$$\frac{\gamma p}{\rho} \nabla P = \frac{\nabla p}{\rho}$$

but

$$c^2 = \frac{\gamma p}{\rho}$$

therefore

$$\frac{\nabla p}{\rho} = c^2 \nabla P$$

where C is the sonic velocity. Hence, eq. (A-6) becomes

$$(\overline{V}' \cdot \nabla) \overline{V}' + 2\omega \wedge \overline{V}' - \omega^2 \overline{r} + c^2 \nabla P = 0 \tag{A-13}$$

GOVERNING DIFFERENTIAL RELATIONSHIPS

For convenience, eqs. (A-12) and (A-13) are converted into a system of differential relationships relative to the unit vector direction $\overline{i}_s$, $\overline{i}_n$, and $\overline{i}_N$, where $\overline{i}_s$ is parallel to the velocity at each point, $\overline{i}_n$ is normal to $\overline{i}_s$ and lies in the axisymmetric stream surface, and $\overline{i}_N$ is normal to both $\overline{i}_s$ and $\overline{i}_n$ (see fig. A-1). Eqs. (A-12) and (A-13) are resolved into these intrinsic components as follows:

Since

$$\overline{V}' = \overline{i}_s V'$$

124
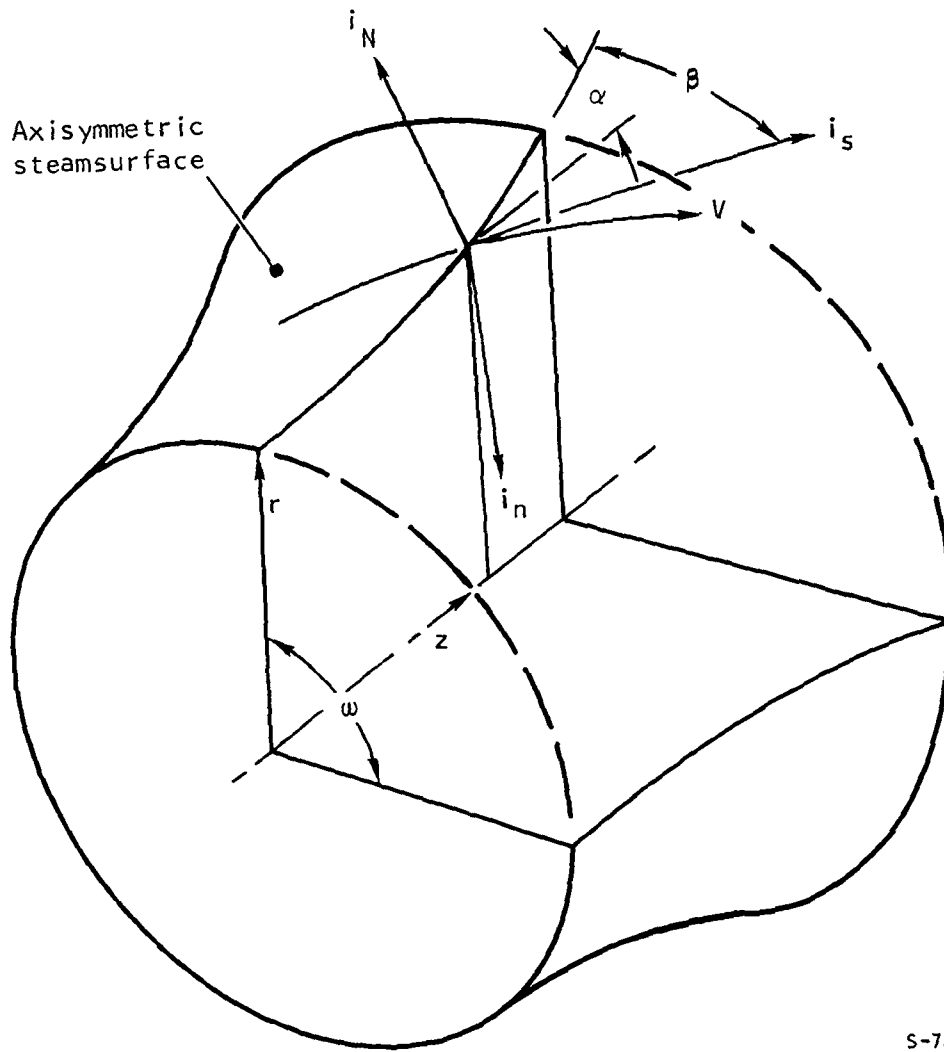
Figure A-I.--Coordinate System - Derivation of Characteristic
Compatibility Equations.

S-73033

and

$$\nabla P = \bar{i}_s \frac{\partial P}{\partial s} + \bar{i}_n \frac{\partial P}{\partial n} + \bar{i}_N \frac{\partial P}{\partial N}$$

we obtain

$$\bar{V}' \cdot \nabla P = V' \frac{\partial P}{\partial s} \qquad (A\text{-}14)$$

Also,

$$\nabla \cdot \bar{V}' = \bar{i}_s \cdot \frac{\partial}{\partial s}(\bar{i}_s V') + \bar{i}_n \cdot \frac{\partial}{\partial n}(\bar{i}_s V') + \bar{i}_N \cdot \frac{\partial}{\partial N}(\bar{i}_s V')$$

$$= \frac{\partial V'}{\partial s} + V'\left(\bar{i}_n \cdot \frac{\partial \bar{i}_s}{\partial n} + \bar{i}_n \cdot \frac{\partial \bar{i}_s}{\partial N}\right) \qquad (A\text{-}15)$$

Egs. (A-14) and (A-15) substituted into eq. (A-12) yield

$$V' \frac{\partial P}{\partial s} + \frac{\partial V'}{\partial s} + V'\left(\bar{i}_n \cdot \frac{\partial \bar{i}_s}{\partial n} + \bar{i}_N \cdot \frac{\partial \bar{i}_s}{\partial N}\right) \qquad (A\text{-}16)$$

The first two terms of eq. (A-13) are as follows:

$$(\bar{V}' \cdot \nabla)\bar{V}' = V' \frac{\partial}{\partial s}(\bar{i}_s V') \qquad (A\text{-}17)$$

$$= V'\left(\bar{i}_s \frac{\partial V'}{\partial s} + V' \frac{\partial \bar{i}_s}{\partial s}\right)$$

$$= \bar{i}_s V' \frac{\partial V'}{\partial s} + V'^2 \frac{\partial \bar{i}_s}{\partial s}$$

$$2\bar{\omega}\wedge\bar{V}' = 2 \begin{vmatrix} \bar{i}_s & \bar{i}_n & \bar{i}_N \\ \omega & \omega_n & \omega_N \\ V' & 0 & 0 \end{vmatrix}$$

$$= 2V'(\bar{i}_n \omega_N - \bar{i}_N \omega_n) \qquad (A\text{-}18)$$

Accordingly, eq. (A-13) becomes

$$\bar{i}_s V' \frac{\partial V'}{\partial s} + V'^2 \frac{\partial \bar{i}_s}{\partial s} + 2V'(\bar{i}_n \omega_N - \bar{i}_N \omega_n)$$

$$- \bar{i}_r \omega^2 r + c^2\left(\bar{i}_s \frac{\partial P}{\partial s} + \bar{i}_n \frac{\partial P}{\partial N} + \bar{i}_n \frac{\partial P}{\partial N}\right) = 0 \qquad (A\text{-}19)$$

126

In eqs. (A-16) and (A-19), s, n, and N refer to displacements in the $\bar{i}_s$, $\bar{i}_n$, and $\bar{i}_N$ directions, respectively. Eqs. (A-16) and (A-19) do not represent a set of differential equations with s, n, and N as independent variables. Since the metric coefficients have not been included in the derivations, these three variables do not define a coordinate system. More correctly, eqs. (A-16) and (A-19) should be viewed as a system of differential relationships which is valid at each point in the field.

The expressions for $\bar{i}_r$ and derivatives of $\bar{i}_s$ are presented in terms of the unit vectors $\bar{i}_s$, $\bar{i}_n$, and $\bar{i}_N$ under the headings of Derivatives of the Unit Vector $\bar{i}_s$ at the end of this appendix. In terms of these relationships, eq. (A-16) reduces to

$$V'\frac{\partial P}{\partial s} + \frac{\partial V'}{\partial s} + V'\left(\frac{\partial \beta}{\partial n} + \frac{\sin \alpha \cos \beta}{r} + \cos \beta \frac{\partial \alpha}{\partial N}\right) = 0 \qquad (A-20)$$

and eq. (A-19) may be rewritten as

$$\bar{i}_s\left(V'\frac{\partial V'}{\partial s} - \omega^2 r \cos \beta \sin \alpha + c^2 \frac{\partial P}{\partial s}\right) + V'^2 \frac{\partial \bar{i}_s}{\partial s}$$

$$+ \bar{i}_n\left(2V'\omega \sin \alpha + \omega^2 r \sin \beta \sin \alpha + c^2 \frac{\partial P}{\partial n}\right)$$

$$+ \bar{i}_N\left(- 2V'\omega \sin \beta \cos \alpha - \omega^2 r \cos \alpha + c^2 \frac{\partial P}{\partial N}\right) = 0 \qquad (A-21)$$

Substituting the expression for the derivative of $\bar{i}_s$ in terms of the unit vectors into eq. (A-17) and resolving the resulting equation into its components yields:

$$V'\frac{\partial V'}{\partial s} - \omega^2 r \cos \beta \sin \alpha + c^2 \frac{\partial P}{\partial s} = 0 \qquad (A-22)$$

$$V'^2\left(\frac{\partial \beta}{\partial s} + \frac{\sin \alpha \sin \beta}{r}\right) + 2V'\omega \sin \alpha + \omega^2 r \sin \beta \sin \alpha + c^2 \frac{\partial P}{\partial n} = 0 \qquad (A-23)$$

$$V'^2\left(\cos \beta \frac{\partial \alpha}{\partial s} - \frac{\sin^2 \beta \cos \alpha}{r}\right) - 2V'\omega \sin \beta \cos \alpha - \omega^2 r \cos \alpha + c^2 \frac{\partial P}{\partial N} = 0 \qquad (A-24)$$

Since the flow is constrained to flow in a specified axisymmetric stream-tube eq. (A-24) is extraneous, serving simply to define the pressure gradient necessary to support this stream tube.

Multiplying eq. (A-20) by V' and subtracting it from eq. (A-22) yields, (after suitable algebraic manipulation of the resulting equation and eq. (A-23)):

$$\frac{M^2 - 1}{M} \frac{\partial P}{\partial s} + \frac{\partial \beta}{\partial n} = - K_1 \qquad (A-25)$$

$$\frac{1}{M^2} \frac{\partial P}{\partial n} + \frac{\partial \beta}{\partial s} = - K_2 \qquad (A-26)$$

where

$$K_1 = \frac{\sin \alpha}{r} \cos \beta \left(1 + \frac{U^2}{V'^2}\right) + \cos \beta \frac{\partial \alpha}{\partial N} \qquad (A-27)$$

$$K_2 = \frac{\sin \alpha}{r} \left[\sin \beta \left(1 + \frac{U^2}{V'^2}\right) + \frac{2U}{V'} \right] \qquad (A-28)$$

Noting that by definition

$$\sin \mu = \frac{1}{M} \qquad (A-29)$$

$$\cos \mu = \frac{\sqrt{M^2 - 1}}{M} \qquad (A-30)$$

Eqs. (A-25) and (A-26) can be rewritten as

$$\frac{\sin 2\mu}{2} \cos \mu \frac{\partial P}{\partial s} + \sin \mu \frac{\partial \beta}{\partial n} = - \sin \mu K_1 \qquad (A-31)$$

$$\frac{\sin 2\mu}{2} \sin \mu \frac{\partial P}{\partial n} + \cos \mu \frac{\partial \beta}{\partial s} = - \cos \mu K_2 \qquad (A-32)$$

Adding and subtracting eqs. (A-31) from (A-32) yields

$$\frac{\sin 2\mu}{2} \left(\cos \mu \frac{\partial P}{\partial s} \pm \sin \mu \frac{\partial P}{\partial n}\right) \pm \left(\cos \mu \frac{\partial \beta}{\partial s} \pm \sin \mu \frac{\partial \beta}{\partial n}\right) = - (\sin \mu K_1 \pm \cos \mu K_2) \qquad (A-33)$$

The parenthetical expressions on the left hand side of eq. (A-33) represent direction derivatives in the positive and negative characteristic directions. Hence, in terms of the notation of eq. (A-4), eq. (A-33) becomes

$$\frac{\sin 2\mu}{2} dP \pm d\beta = - K_4^{\pm} \, dl \text{ on } C^{\pm} \qquad (A-34)$$

where dl is a differential displacement in the appropriate characteristic direction and $K_4^{\pm}$ is given as

$$K_4^{\pm} = \frac{\cos \beta}{M} \frac{\partial \alpha}{\partial N} \pm \frac{\sin \alpha}{r} \left[\sin (\beta \pm \mu) \left(1 + \frac{u^2}{V'^2}\right) \pm \cos \mu \frac{2U}{V'}\right] \qquad (A-35)$$

Eqs (A-34) and A-35) represent the characteristic compatibility equations in terms of the pressure variable P and the flow angle β. For development of the blade sections, it is more convenient to express the compatibility equations in terms of the variables ξ^+ and ξ^-. The conversion from the P - β to the ξ^+ - ξ^- form is accomplished below.

THE COMPATIBILITY EQUATIONS IN ξ^+, ξ^- FORM

The pressure function P, eq. (A-11), can be expressed as

$$P = \frac{1}{\gamma} \log_e \left(\frac{p}{P_{tr}} \frac{P_{tr}}{P_o}\right)$$

$$= \frac{1}{\gamma} \left[\log_e \left(\frac{p}{P_{tr}}\right) + \log_e \left(\frac{P_{tr}}{P_o}\right)\right]$$

where P_{tr} is the local value of relative stagnation pressure. The differential of P is

$$dP = \frac{1}{\gamma} \frac{d\left(\frac{p}{P_{tr}}\right)}{\frac{p}{P_{tr}}} + \frac{1}{\gamma} \frac{dP_{tr}}{P_{tr}}$$

In the first term

$$\frac{p}{P_{tr}} = \frac{1}{\left(1 + \frac{\gamma-1}{2} M^2\right)^{\frac{\gamma}{\gamma-1}}}$$

$$\log_e \left(\frac{p}{P_{tr}}\right) = -\frac{\gamma}{\gamma-1} \log_e \left(1 + \frac{\gamma-1}{2} M^2\right)$$

$$\frac{1}{\gamma} \frac{d\left(\frac{p}{P_{tr}}\right)}{\frac{p}{P_{tr}}} = -\frac{1}{2} \frac{d(M^2)}{1 + \frac{\gamma-1}{2} M^2}$$

In the second term

$$\frac{P_{tr}}{P_o} = \left(\frac{T_{tr}}{t_o}\right)^{\frac{\gamma}{\gamma-1}}$$

$$\log_e P_{tr} - \log_e P_o = \frac{\gamma}{\gamma-1}\left(\log_e T_{tr} - \log_e t_o\right)$$

$$\frac{1}{\gamma} \frac{d\,P_{tr}}{P_{tr}} = \frac{1}{\gamma-1} \frac{d\,T_{tr}}{T_{tr}}$$

Therefore,

$$dP = -\frac{1}{2} \frac{d(M^2)}{\left(1 + \frac{\gamma-1}{2}M^2\right)} + \frac{1}{\gamma-1} \frac{dT_{tr}}{T_{tr}} \qquad (A\text{-}36)$$

The differential of ν, the Prandtl-Meyer angle is

$$d\nu = \frac{\sqrt{M^2 - 1}}{2M^2\left(1 + \frac{\gamma-1}{2}M^2\right)} d\left(M^2\right) \qquad (A\text{-}37)$$

Noting that

$$\frac{\sin 2\mu}{2} = \sin \mu \cos \mu = \frac{\sqrt{M^2 - 1}}{M^2}$$

Eq. (A-36) yields

$$\frac{\sin 2\mu}{2} dP = -\frac{\sqrt{M^2 - 1}}{2M^2\left(1 + \frac{\gamma-1}{2}M^2\right)} d(M^2) + \frac{\sin 2\mu}{2(\gamma-1)} \frac{dT_{tr}}{T_{tr}}$$

Accordingly, eq. (A-34) becomes

$$d\nu \pm d\beta = K_4^{\pm}\, dl + \frac{\sin 2\mu}{2(\gamma - 1)} \frac{dT_{tr}}{T_{tr}} \quad \text{on } C^{\pm} \qquad (A\text{-}38)$$

Since
$$d\nu \pm d\beta = 2d\xi^{\pm}$$

eq. (A-38) becomes

$$2\frac{d\xi^{\pm}}{dl} = K_4^{\pm} + \frac{\sin 2\mu}{2(\gamma - 1)T_{tr}} \frac{dT_{tr}}{dr} \frac{dr}{dl} \quad (\text{on } C^{\pm}) \qquad (A\text{-}39)$$

130

The relative stagnation temperature T_{tr} is

$$T_{tr} = T_o + \frac{\omega^2}{2C_p} (r^2 - r_o^2) \qquad (A-40)$$

Therefore,

$$\frac{dT_{tr}}{dr} = \frac{\omega^2 r}{C_p} = \frac{U^2}{C_p r}$$

Also,

$$c_{tr}^2 = (\gamma - 1)C_p T_{tr} \qquad (A-41)$$

Substitution of eqs. (A-40) and (A-41) into (A-39) yields

$$2d\xi^{\pm} = \left[K_4^{\pm} + \frac{\sin 2\mu}{2r} \frac{U^2}{c_{tr}^2} \frac{dr}{dl} \right] dl \quad (\text{on } c^{\pm}) \qquad (A-42)$$

The following substitutions are made into K_4 (eq. A-35) and into the second term of eq. (A-42)

$$\frac{\partial \alpha}{\partial N} = \frac{1}{h} \frac{dh}{dm}$$

$$V'^2 = M^2 c^2$$

$$\frac{1}{r} \left(\frac{dr}{dl} \right)^{\pm} = \cos (\beta \pm \mu) \frac{\sin \alpha}{r} \quad (\text{on } c^{\pm})$$

and

$$\frac{\sin 2\mu}{2} = \frac{\cos \mu}{M}$$

Finally, eq. (A-42) is written

$$d\xi^{\pm} = \epsilon^{\pm} dl \quad (\text{on } c^{\pm}) \qquad (A-43)$$

where

$$\epsilon^{\pm} = \frac{\cos \beta}{2M} \left(\frac{1}{h} \frac{dh}{dm} \right) \pm \frac{\sin \alpha}{2r} \left\{ \left(1 + \frac{U^2}{M^2 c^2} \right) \sin (\beta \pm \mu) \right.$$

$$\left. + \frac{\sin 2\mu}{2} \left[\frac{U^2}{c_{tr}^2} \cos (\beta \pm \mu) \pm \frac{2U}{C} \right] \right\} \qquad (A-44)$$

131

Consider the intrinsic unit vectors, $\bar{i}_s$, $\bar{i}_n$, and $\bar{i}_N$ originating from the same point as the cylindrical coordinate unit vectors, $\bar{i}_z$, $\bar{i}_o$, and $\bar{i}_r$, fig. A-2. · The geometrical relationships between the two sets of unit vectors are developed as follows.

From the terminus of the $\bar{i}_s$ vector, a normal is drawn to the $\bar{i}_z$, $\bar{i}_r$ plane (component 3) followed by a normal drawn in the $\bar{i}_z$, $\bar{i}_r$ plane to the $\bar{i}_z$ vector (component 2) and concluded by a segment on the $\bar{i}_z$ vector to its origin (component 1). (The foregoing components are numbered in descending order because the imaginary path followed during this construction is opposite in direction to the vector sum defining $\bar{i}_s$.) Tracing from the origin along the foregoing orthogonal segments to the $\bar{i}_s$ terminus defines the magnitude and sense of the following components.

Component 3: $\bar{i}_\theta$ sin β

Component 2: $\bar{i}_r$ cos β sin α

Component 1: $\bar{i}_z$ cos β cos α

Accordingly

$$\bar{i}_s = \bar{i}_z \cos \beta \cos \alpha + \bar{i}_r \cos \beta \sin \alpha + \bar{i}_\theta \sin \beta \qquad \text{(A-45)}$$

Similarly, the $\bar{i}_n$ unit vector is resolved into $\bar{i}_z$, $\bar{i}_r$, and $\bar{i}_\theta$ components by means of (3) a normal from the $\bar{i}_n$ terminus to the $\bar{i}_\theta$, $\bar{i}_r$ plane, (2) a normal drawn in the $\bar{i}_\theta$, $\bar{i}_r$ plane to the $\bar{i}_\theta$ vector, and (1) a segment on the $\bar{i}_\theta$ vector to its origin. As before, the magnitude and sense of the components are:

Component 3: $-\bar{i}_z$ sin β cos α

Component 2: $-\bar{i}_r$ sin β sin α

Component 1: $\bar{i}_\theta$ cos β

and the vector sum yields

$$\bar{i}_n = \bar{i}_\theta \cos \beta - \bar{i}_r \sin \beta \sin \alpha + i_z \sin \beta \cos \alpha \qquad \text{(A-46)}$$

The $\bar{i}_N$ unit vector lies in the $\bar{i}_z$, $\bar{i}_r$ plane; its components are

$$\bar{i}_n = - \bar{i}_z \sin \alpha + \bar{i}_r \cos \alpha \qquad \text{(A-47)}$$

132

Line of intersection, $\bar{i}_s$, $\bar{i}_n$ plane with $\bar{i}_Z$, $\bar{i}_R$ plane

R

N

α

s

Z

Rθ

β

$\bar{i}_r$

$\bar{i}_s$

β

n β

$\bar{i}_\theta$

$\bar{i}_N$

Unit vectors

α

③

$\bar{i}_n$

②

i_Z

Unit vectors

Unit vectors

①

P

① $\bar{i}_s$ component 1 = $\bar{i}_Z$ cos β cos α

② $\bar{i}_s$ component 2 = $\bar{i}_r$ cos β sin α

③ $\bar{i}_s$ component 3 = $\bar{i}_\theta$ sin β

S-74065
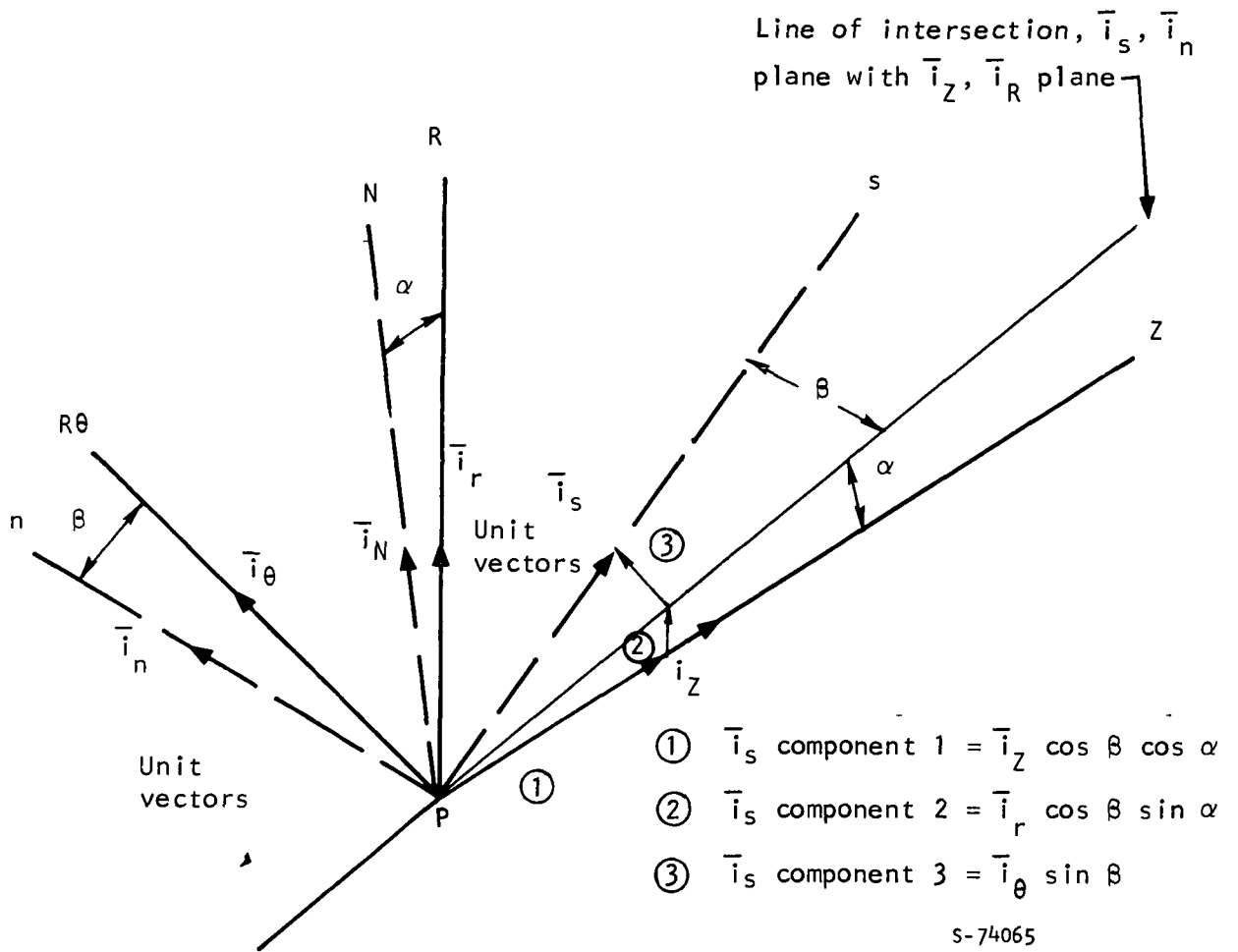
Notes: Axes Z, R, and N lie in the meridional plane.
Axis s is tangent to the velocity vector at P.
Axes s, Rθ, and n lie in a plane tangent to P
on the stream surface.
The axes illustrated are not, in general,
coordinate axes, but define the unit vector
directions.

Figure A-2.--Unit Vector Relationships, Cylindrical
and Intrinsic Coordinates.

133

The foregoing reasoning applied to the resolution of $\bar{i}_z$, $\bar{i}_r$, and $\bar{i}_\theta$ into their intrinsic components yields

$$\bar{i}_r = \bar{i}_s \cos \beta \sin \alpha - \bar{i}_n \sin \beta \sin \alpha + \bar{i}_N \cos \alpha \qquad \text{(A-48)}$$

$$\bar{i}_\theta = \bar{i}_s \sin \beta + \bar{i}_n \cos \beta \qquad \text{(A-49)}$$

$$\bar{i}_z = \bar{i}_s \cos \beta \cos \alpha - \bar{i}_n \sin \beta \cos \alpha - \bar{i}_N \sin \alpha \qquad \text{(A-50)}$$

Taking the derivative of $\bar{i}_s$ eq. (A-45) with respect to any arbitrary variable X (noting that the unit vector, $\bar{i}_z$, is invariant) yields

$$\frac{\partial \bar{i}_s}{\partial X} = - \bar{i}_z \cos \beta \sin \alpha \frac{\partial \alpha}{\partial X} - \bar{i}_z \sin \beta \cos \alpha \frac{\partial \beta}{\partial X}$$

$$- \bar{i}_r \sin \beta \sin \alpha \frac{\partial \beta}{\partial X} + \bar{i}_r \cos \beta \cos \alpha \frac{\partial \alpha}{\partial X}$$

$$+ \bar{i}_\theta \cos \beta \frac{\partial \beta}{\partial X} + \frac{\partial \bar{i}_r}{\partial X} \cos \beta \sin \alpha + \frac{\partial \bar{i}_\theta}{\partial X} \sin \beta \qquad \text{(A-51)}$$

and

$$\frac{\partial \bar{i}_s}{\partial X} = \cos \beta \; (- \bar{i}_z \sin \alpha + \bar{i}_r \cos \alpha) \frac{\partial \alpha}{\partial X}$$

$$+ (- \bar{i}_z \sin \beta \cos \alpha - \bar{i}_r \sin \beta \sin \alpha + \bar{i}_\theta \cos \beta) \frac{\partial \beta}{\partial X}$$

$$+ \frac{\partial \bar{i}_r}{\partial X} \cos \beta \sin \alpha + \frac{\partial \bar{i}_\theta}{\partial X} \sin \beta \qquad \text{(A-52)}$$

Substitution of eqs. (A-46) and (A-47) into eq. (A-51) yields the following:

$$\frac{\partial \bar{i}_s}{\partial X} = \bar{i}_N \cos \beta \frac{\partial \alpha}{\partial X} + \bar{i}_n \frac{\partial \beta}{\partial X} + \frac{\partial \bar{i}_r}{\partial X} \cos \beta \sin \alpha + \frac{\partial \bar{i}_\theta}{\partial X} \sin \beta \qquad \text{(A-53)}$$

134

Since the variable X operates on $\bar{i}_r$ and $\bar{i}_\theta$ through the polar coordinate, θ (i.e., changes in $\bar{i}_r$ or $\bar{i}_\theta$ comprise rotations about the Z axis), the following are obtained (fig. A-3):

$$\frac{\partial \bar{i}_r}{\partial X} = \frac{\partial \bar{i}_r}{\partial \theta} \frac{\partial \theta}{\partial X}$$

$$= \bar{i}_\theta \frac{\partial \theta}{\partial X} \tag{A-54}$$

$$\frac{\partial \bar{i}_\theta}{\partial X} = \frac{\partial \bar{i}_\theta}{\partial \theta} \frac{\partial \theta}{\partial X}$$

$$= -\bar{i}_r \frac{\partial \theta}{\partial X} \tag{A-55}$$

Substitution of eqs. (A-25b) and (A-25c) into eqs. (A-27a) and (A-27b) yields

$$\frac{\partial \bar{i}_r}{\partial X} = (\bar{i}_s \sin \beta + \bar{i}_n \cos \beta) \frac{\partial \theta}{\partial X} \tag{A-56}$$

and

$$\frac{\partial \bar{i}_\theta}{\partial X} = - (\bar{i}_s \cos \beta \sin \alpha - \bar{i}_n \sin \beta \sin \alpha + \bar{i}_N \cos \alpha) \frac{\partial \theta}{\partial X} \tag{A-57}$$

From eqs. (A-53), (A-56), and (A-57)

$$\frac{\partial \bar{i}_s}{\partial X} = \bar{i}_n \left(\frac{\partial \beta}{\partial X} + \sin \alpha \frac{\partial \theta}{\partial X} \right)$$

$$+ \bar{i}_N \left(\cos \beta \frac{\partial \alpha}{\partial X} - \sin \beta \cos \alpha \frac{\partial \theta}{\partial X} \right) \tag{A-58}$$

The general variable X is now identified successively as s, n, and N. The partial derivatives, $\frac{\partial \theta}{\partial s}$, $\frac{\partial \theta}{\partial n}$, and $\frac{\partial \theta}{\partial N}$ are evaluated from geometrical considerations. For an incremental translation Δs along the s-axis, a translation in θ results:

$$\Delta s \sin \beta = r \Delta \theta$$

Accordingly,

$$\frac{\partial \theta}{\partial s} = \frac{\sin \beta}{r} \tag{A-59}$$
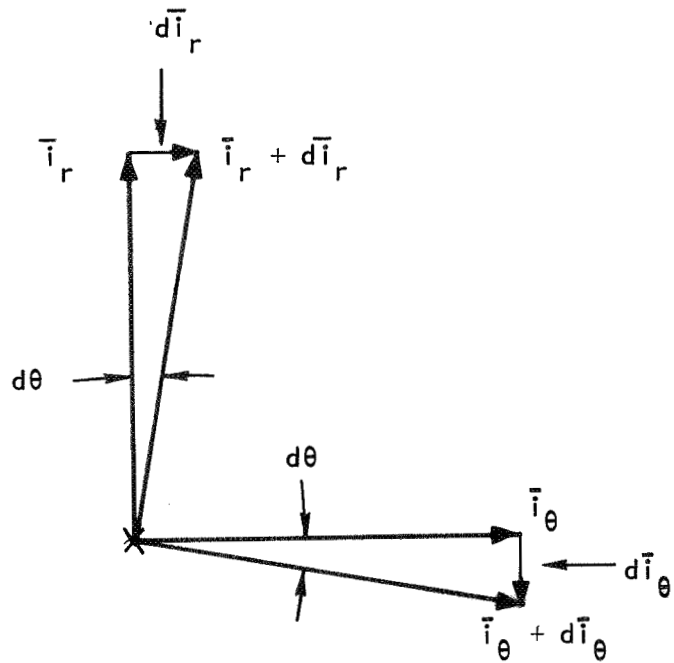
$$d\overline{i}_r = \overline{i}_\theta \, d\theta$$

$$d\overline{i}_\theta = -\,\overline{i}_r \, d\theta$$

S-74066

Figure A-3.--Vector Changes in Unit Vectors, $\overline{i}_r$ and $\overline{i}_\theta$.

136

Similarly, for a translation along the n-axis,

$$\Delta n \cos \beta = r \Delta \theta$$

$$\frac{\partial \theta}{\partial n} = \frac{\cos \beta}{r} \qquad \text{(A-60)}$$

However, the N-axis lies in the meridional (z, r) plane. A translation along the N-axis yields no change in θ:

$$\frac{\partial \theta}{\partial N} = 0 \qquad \text{(A-61)}$$

Finally, eqs. (A-58 through (A-61) yield

$$\frac{\partial \overline{i}_s}{\partial s} = \overline{i}_n \left(\frac{\partial \beta}{\partial s} + \frac{\sin \alpha \, \sin \beta}{r} \right) + \overline{i}_N \left(\cos \beta \, \frac{\partial \alpha}{\partial s} - \frac{\sin^2 \beta \, \cos \alpha}{r} \right) \qquad \text{(A-62)}$$

$$\frac{\partial \overline{i}_s}{\partial n} = \overline{i}_n \left(\frac{\partial \beta}{\partial n} + \frac{\sin \alpha \, \cos \beta}{r} \right) + \overline{i}_N \left(\cos \beta \, \frac{\partial \alpha}{\partial n} - \frac{\sin \beta \, \cos \beta \, \cos \alpha}{r} \right) \qquad \text{(A-63)}$$

$$\frac{\partial \overline{i}_s}{\partial N} = \overline{i}_n \, \frac{\partial \beta}{\partial n} + \overline{i}_N \, \cos \beta \, \frac{\partial \alpha}{\partial N} \qquad \text{(A-64)}$$

137

APPENDIX B

TRAILING EDGE MIXING CALCULATION

The equations used to calculate the trailing edge blockage and the inviscid core flow conditions are derived by relating the core plus boundary layer flow to the uniform downstream flow.

Consider a vanishingly thin control volume enclosing the trailing edge region of two adjacent blades as shown in fig. B-1. The fluid density, pressure, velocity, and flow angle at the discharge plane of the control volume (denoted by ρ_e, p_e, V'_e, and β'_e, respectively) are assumed to be uniform and equal to the corresponding section discharge values calculated by the axisymmetric program. The corresponding flow quantities at the inlet of the control volume (denoted by ρ, p, V', and β', respectively) are assumed to be nonuniform. The pressure acting on the trailing edge of the blade is assumed to be uniform and is denoted by p_b.

The conservation of mass, meridional momentum, and tangential momentum applied to the control volume results in the following three equations:

$$\int_0^{Y_c} \rho V' \cos \beta' \, dy = \rho_e V'_e \cos \beta'_e Y_e \qquad (B-1)$$

$$gp_b \left(Y_e - Y_c \right) + A + \int_0^{Y_c} \rho V'^2 \cos^2 \beta' \, dy = gp_e Y_e + \rho_e V'^2_e \cos^2 \beta'_e Y_e \qquad (B-2)$$

where

$$A = g \int_0^{Y_c} p \, dy$$

$$\int_0^{Y_c} \rho V'^2 \cos \beta' \sin \beta' \, dy = \rho_e V'^2_e \cos \beta'_e \sin \beta'_e Y_e \qquad (B-3)$$

138
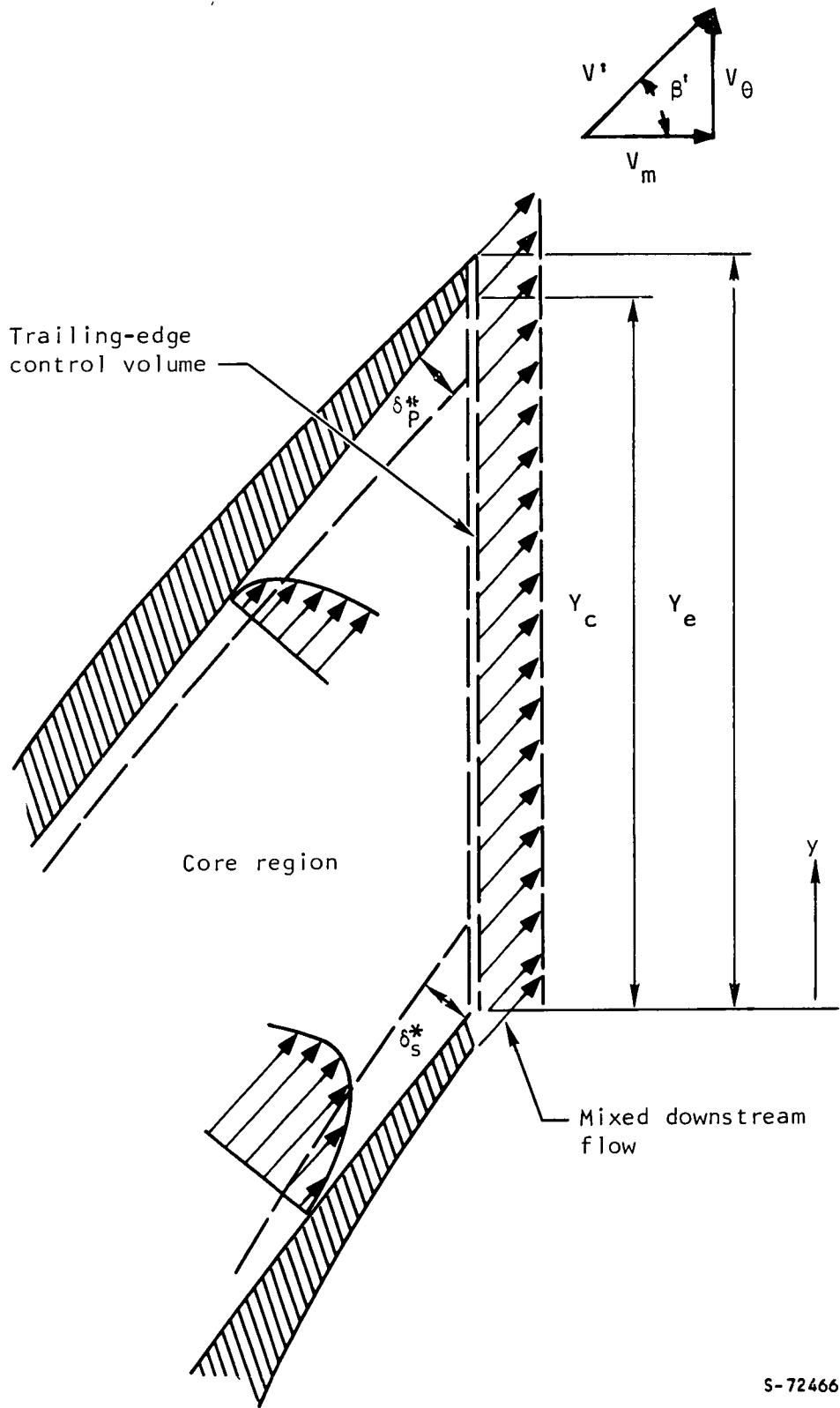
Figure B-I.--Rotor Blade Trailing Edge Flow Mixing Model.

S-72466

If the flow in the inviscid core region is assumed to be uniform, and the corresponding flow properties are denoted by the subscript c, then eqs. (B-1), (B-2), and (B-3) can be rewritten as

$$\frac{1}{Y_c} \int_0^{Y_c} \left(1 - \frac{\rho V' \cos \beta'}{\rho_c V'_c \cos \beta'_c} \right) dy = F_1 \qquad \text{(B-4)}$$

$$\frac{1}{Y_c} \int_0^{Y_c} \left(1 - \frac{\rho V'^2 \cos^2 \beta'}{\rho_c V'^2_c \cos^2 \beta'_c} \right) dy = F_2 - F_p \qquad \text{(B-5)}$$

$$\frac{1}{Y_c} \int_0^{Y_c} \left(1 - \frac{\rho V'^2 \sin \beta' \cos \beta'}{\rho_c V'^2_c \sin \beta'_c \cos \beta'_c} \right) dy = F_3 \qquad \text{(B-6)}$$

where

$$F_1 = 1 - \frac{\rho_e V_{me} Y_e}{\rho_c V_{mc} Y_c} \qquad \text{(B-7)}$$

$$F_2 = 1 - \frac{\rho_e}{\rho_c} \left(\frac{V_{me}}{V_{mc}} \right)^2 \frac{Y_e}{Y_c} \qquad \text{(B-8)}$$

$$F_3 = 1 - \frac{\rho_e V_{me} V'_{\theta e} Y_e}{\rho_c V_{mc} V'_{\theta c} Y_c} \qquad \text{(B-9)}$$

$$F_p = \left[\frac{P_e Y_e - P_c Y_c - P_b (Y_e - Y_c)}{\rho_c V^2_{mc} Y_c} \right] g \qquad \text{(B-10)}$$

and where V_m and V'_θ are the meridional and tangential components of V'. In the core region, the integrands of the above equations are zero, whereas in the boundary layer region, the integrands are nonzero. In order to evaluate these integrals in terms of boundary layer parameters, assume that the flow angle in the boundary layer is the same as in the core, and change the variable of integration from dy to dn where

140

$$dy = \frac{dn}{\cos \beta'_c} \qquad (B-11)$$

and the upper limit of the integral becomes $Y'_c = Y_c \cos \beta'_c$.

The integrals in eq. (B-4) and the integrals in eqs. (B-5) and (B-6) may then be written respectively as

$$I1 = \frac{1}{\cos \beta'_c} \int_0^{Y'_c} \left(1 - \frac{\rho V'}{\rho_c V'_c}\right) dn \qquad (B-12)$$

$$I2 = \frac{1}{\cos \beta'_c} \int_0^{Y'_c} \left(1 - \frac{\rho V'^2}{\rho_c V'^2_c}\right) dn \qquad (B-13)$$

Algebraic expansion of the integrand of I2 yields

$$I2 = \frac{1}{\cos \beta'_c} \left[\int_0^{Y'_c} \left(1 - \frac{\rho V'}{\rho_c V'_c}\right) dn + \int_0^{Y'_c} \frac{\rho V'}{\rho_c V'_c} \left(1 - \frac{V'}{V'_c}\right) dn \right] \qquad (B-14)$$

If δ^* and θ^* are used to denote the sum of the displacement and momentum thicknesses, respectively, of the pressure and suction surfaces at the trailing edge, then it follows that the first integral is

$$I1 = \frac{\delta^*}{\cos \beta'_c} \qquad (B-15)$$

and the second integral is

$$I2 = \frac{1}{\cos \beta'_c} (\delta^* + \theta^*) \qquad (B-16)$$

Substituting eqs. (B-15) and (B-16) into eqs. (B-4), (B-5), and (B-6) and noting the previous assumption that the flow direction is the same for the core and boundary layer flow yields

$$\frac{\delta^*}{Y_c \cos \beta'_c} = F_1 \qquad (B-17)$$

$$\frac{\delta^* + \theta^*}{Y_c \cos \beta'_c} = F_2 - F_p \qquad (B-18)$$

141

$$\frac{\delta^* + \theta^*}{Y_c \cos \beta_c'} = F_3 \qquad \text{(B-19)}$$

Finally, simultaneous solution of the preceding three equations with appropriate substitutions for the F terms of eqs. (B-7), (B-8), and (B-9) yields

$$V_{\theta c}' = \frac{V_{\theta e}'}{1 - \left(\frac{\frac{\delta^*}{Y_c} H}{\cos \beta_c' - \frac{\delta^*}{Y_c}}\right)} \qquad \text{(B-20)}$$

where

$H = \frac{\delta^*}{\theta^*}$ defines the boundary layer form factor.

Eqs. (B-17), (B-18) and (B-19) can be handled numerically in the following manner:

(1) The relative total temperature and' total pressure of the core flow are determined from the flow conditions upstream of the control volume. In cases where the section is assumed to be operating in the unstarted mode, the core relative total pressure is reduced from the ideal value by an amount consistent with the calculated bow shock loss.

(2) A discharge "shape factor" H is specified by the designer. If a shape factor of 1.5 is assumed to correspond to a flat-plate boundary layer, and a shape factor of 2.5 is assumed to correspond to a boundary layer at the point of incipient separation, then the choice of a discharge shape factor between these two values would appear reasonable. In the present rotor design, a value of 2.0 was used.

(3) A value for the overall trailing edge blockage λ (the sum of the boundary layer displacement thickness and the trailing edge metal blockage) is assumed.

(4) With the information from steps 1, 2 and 3, the continuity equation in the form

$$\rho_c V_{mc} (1 - \lambda) = \rho_e V_{me}$$

plus eq. (B-20) is used to calculate the core flow conditions and, consequently, the values of F_1, F_2, F_3, and F_p in eqs. (B-7) through (B-10).

(5) The shape factor is calculated using eqs. (B-17) and (B-19). If the value is not equal to the specified value, a new value of blockage factor is assumed, and steps 4 and 5 are repeated until agreement is achieved.

At present, no convergence problems have been encountered in applying the trailing edge blockage calculation.

The flow conditions leaving the control volume for streamline No. 4 as calculated from the axisymmetric flow analysis are: ·

$$M_e = 1.094$$

$$\beta'_e = 60.24 \text{ deg}$$

$$V_{me} = 624.9 \text{ ft/s } (190.8 \text{ m/s})$$

$$V'_{\theta e} = 1092.7 \text{ ft/s } (333.7 \text{ m/s})$$

$$P_e = 2491 \text{ lbf/ft}^2 \ (1.193 \times 10^5 \text{N/m}^2)$$

$$P_{te} = 5282 \text{ lbf/ft}^2 \ (2.529 \times 10^5 \text{N/m}^2)$$

$$\rho_e = 0.0848 \text{ lbm/ft}^3 \ (1.358 \text{ Kgm/m}^3)$$

$$T_{te} = 682.5^\circ\text{R } (379.2^\circ\text{K})$$

The core fluid properties (assuming no upstream shock loss) are

$$P_{tc} = 5529 \text{ lbf/ft}^2 \ (2.647 \times 10^5 \text{N/m}^2)$$

$$T_{tc} = 682.5^\circ\text{R } (379.2^\circ\text{K})$$

The discharge pitch and the core pitch (trailing edge tail radius = 0.0073 in.) are

$$Y_e = 2.103 \text{ in. } (5.342 \text{ cm})$$

$$Y_c = 2.089 \text{ in. } (5.306 \text{ cm})$$

With the trailing edge back pressure assumed to be equal to the core static pressure and the trailing edge shape factor specified as 2.0, the trailing edge blockage and core absolute swirl velocity are

$$\lambda = 6.18 \text{ percent}$$

$$V_{\theta C(abs)} = -281.5 \text{ ft/s} \ (-86.0 \text{ m/s})$$

The corresponding core flow conditions are

$$M_C = 1.143$$

$$\beta_C = 59.35 \text{ deg}$$

$$V_{mc} = 664.5 \text{ ft/s} \ (202.9 \text{ m/s})$$

$$V'_{\theta C} = 1121.3 \text{ ft/s} \ (342.4 \text{ m/s})$$

$$\rho_C = 0.085 \text{ lbm/ft}^3 \ (1.362 \text{ Kgm/m}^2)$$

The corresponding boundary layer parameters are:

$$\delta^* = 0.0512 \text{ in.} \ (0.130 \text{ cm})$$

$$\theta^* = 0.0256 \text{ in.} \ (0.0650 \text{ cm})$$

The discharge absolute swirl velocity calculated by the axisymmetric flow analysis program is

$$V_{\theta e(abs)} = -310.1 \text{ ft/s} \ (-94.7 \text{ m/s})$$

As a consequence, the absolute total temperature of the core flow is lower than the corresponding temperature of the downstream flow field. The difference is accounted for in terms of the higher total temperature associated with boundary layer fluid.

Similarly, the core static pressure is lower than the static pressure of the downstream flow, the difference being the result of the momentum exchange involved in the mixing process.

144

APPENDIX C

LEADING EDGE SHOCK CALCULATIONS--STARTED MODE

Once the strength of the leading edge shock is set, either by calculation for the outboard section, or by design input for the central sections, the problem remains of calculating the shape of the shock in the blade passage and the point where the shock intersects the suction surface. The techniques used to determine the shock shape and the intersection point are described in the following discussion.

TWO-DIMENSIONAL ISOLATED WEDGE

Consider a two-dimensional wedge with wedge angle δ and circular leading edge nose radius r in a supersonic flow field at zero incidence (see fig. C-1). If the wedge is assumed to extend to downstream infinity, then theoretically the supersonic upstream Mach number can only be sustained if δ is less than some maximum attachment angle δ_m, which is a function of the specified upstream Mach number. Assuming that δ is less than δ_m, then a shock wave will stand forward of the finite leading edge of the wedge as shown in the figure. At points far removed from the wedge, the shock angle is asymptotic to the ideal shock angle for a sharp wedge of the same included angle. In the region of the leading edge, the shock gradually becomes stronger until it becomes a normal shock on the wedge centerline. Following the technique described in ref. 4, the shock is assumed to have a hyperbolic shape described by the equation

$$\bar{X}^2 - \bar{Y}^2 \cot^2 \sigma_\infty = 1 \tag{C-1}$$

where σ_∞ is the shock angle far from the wedge, and $\bar{X}$ and $\bar{Y}$ are the X and Y coordinates normalized to X_0 (fig. C-1). The local shock angle σ is $d\bar{Y}/d\bar{X}$; accordingly differentiating eq. (C-1) yields

$$\cot^2 \sigma = (1 - \frac{1}{\bar{X}^2}) \cot^2 \sigma_\infty \tag{C-2}$$

At some point on the shock, the discharge Mach number from the shock is just sonic. This point will be called the sonic point. The sonic line dividing the subsonic flow in the leading edge region from the supersonic flow far from the wedge begins at the sonic point and ends somewhere on the wedge surface. Specifically, the sonic line is assumed to terminate on the wedge surface at the point m where the wedge surface angle corresponds to δ_m (ref. 4). Obviously, this point lies on the leading edge radius at

$$\bar{X}_m = \bar{X}_c - \bar{r} \sin \delta_m \tag{C-3}$$
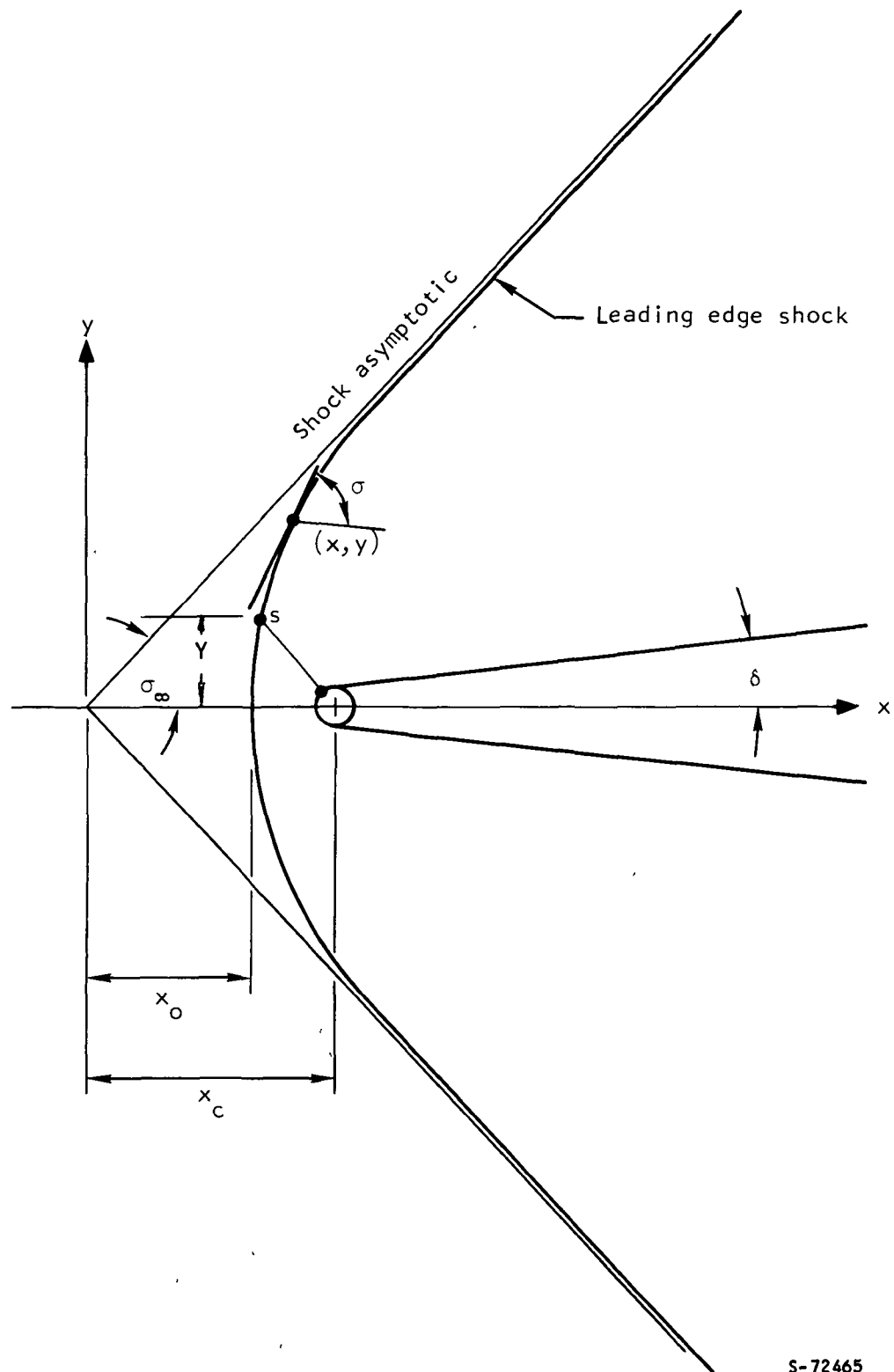
145

Figure C-1.--Two-Dimensional Leading Edge Shock Geometry.

$$\overline{Y}_m = \overline{r} \cos \delta_m \cdot \tag{C-4}$$

The symbol $\overline{r}$ represents the blade leading edge radius normalized by X_o. In addition, the sonic line is assumed to be straight, of normalized length $\overline{\ell}$, and oriented at an angle $\delta_a + 90$ where δ_a is the average of δ_s and δ_m. The location of the termination point in terms of $\overline{\ell}$ is

$$\overline{X}_m = \overline{X}_s + \overline{\ell} \sin \delta_a \tag{C-5}$$

$$\overline{Y}_m = \overline{Y}_s - \overline{\ell} \cos \delta_a \tag{C-6}$$

For two-dimensional flow, the value of $\overline{\ell}$ is approximately related to $\overline{Y}_s$ by continuity as follows:

$$\frac{\overline{\ell}}{\overline{Y}_s} = \left(\frac{A^*}{A}\right)_\infty e^{\frac{\Delta S}{R}} \tag{C-7}$$

where the subscript ∞ denotes the freestream flow before the shock, the area ratio is based on the upstream Mach number, and ΔS is the average entropy rise of the fluid passing through the shock between $\overline{Y}_s$ and the wedge centerline.

The latter quantity can be determined by (1) taking a number of equally spaced points between $\overline{Y}_s$ and the centerline, (2) using eq. (C-2) to calculate the associated shock angle (and consequently the entropy rise at the point), and (3) averaging the entropy rise over all such points.

Combining eqs. (C-4), (C-6), and (C-7)

$$\overline{r} = \frac{\overline{Y}_s}{\cos \delta_m} \left[1 - \left(\frac{A^*}{A}\right)_\infty e^{\frac{\Delta S}{R}} \cos \delta_a \right] \tag{C-8}$$

Eq. (C-6) may be used to calculate $\overline{r}$. For a specified leading edge radius, the value of X_o (and consequently the physical dimensions of all other normalized quantities) is

$$X_o = \frac{r}{\overline{r}} \tag{C-9}$$

Eq. (C-3) yields

$$\overline{X}_c = \overline{X}_m + \overline{r} \sin \delta_m$$

$$= \overline{X}_s + \overline{\ell} \sin \delta_a + \overline{r} \sin \delta_m \tag{C-10}$$

147

The shock standoff distance (from the center of the leading edge radius) is

$$X_{so} = X_o \, (\overline{X}_c - 1) \qquad \text{(C-11)}$$

THREE-DIMENSIONAL CASE

In determining the location of the shock in the quasi-three-dimensional section, the shock is first treated as a simple two-dimensional shock in the manner described above. The flow angle into the shock is then assumed to vary linearly across the blade passage from the value at the wedge to the value at the shock intersection point on the suction surface. The inclination of the shock in the field is then assumed to be equal to the local flow angle minus the shock angle calculated for the simple two-dimensional shock a similar distance from the wedge centerline. In addition, the standoff distance of the shock is assumed to be the same as in the two-dimensional case. With the standoff point and shock inclination angle determined in the above manner, the shock location is determined by

$$m_{sh} = m_{so}$$

$$\theta_{sh} = \theta_{so}$$

$$m_{sh_j} = m_{sh_{j-1}} + \Delta Y \cos \left(\beta_{sh_{j-1/2}} \right)$$

$$\theta_{sh_j} = \theta_{sh_{j-1}} + \Delta Y \sin \left(\beta_{sh_{j-1/2}} \right) \qquad \text{(C-12)}$$

Since the suction surface angle at the shock intersection point is not known a priori, the above technique implies an iterative solution. Rather than iterate for the suction surface, an approximate technique was used in the section design program.

LEADING EDGE SHOCK SHAPE--STREAMLINE NO. 4

The Mach number into the streamline No. 4 leading edge wedge and the magnitude of the wedge angle are,

$$M_1 = 1.502$$

$$\delta_1 = 4.34 \text{ deg}$$

148

The corresponding downstream Mach number and shock angle far from the leading edge radius are

$$M_\infty = 1.351$$

$$\sigma_\infty = 46.91 \text{ deg}$$

The maximum deflection angle, sonic deflection angle, and sonic shock angle corresponding to the inlet Mach number are

$$\delta_m = 12.17 \text{ deg}$$

$$\delta_s = 11.75 \text{ deg}$$

$$\sigma_s = 62.24 \text{ deg}$$

The corresponding values of $\bar{X}_s$ and $\bar{Y}_s$ from eqs. (C-1) and (C-2) are

$$\bar{X}_s = 1.210$$

$$\bar{Y}_s = 0.728$$

The average entropy rise to the sonic point, normalized to R is

$$\frac{\overline{\Delta S}}{R} = 0.0524$$

The corresponding value of $\bar{\ell}$ and $\bar{r}$ are

$$\bar{\ell} = 0.651$$

$$\bar{r} = 0.0927$$

The actual leading edge radius and the value for X_0 are

$$r = 0.0073 \text{ in.}$$

$$X_0 = 0.079$$

The value for $\bar{X}_c$ and the shock standoff distance (from the center of the leading edge radius) are

$$\overline{X}_c = 1.360$$

$$X_{so} = 0.028$$

LEADING EDGE SHOCK BLOCKAGE

In Appendix D, a correction for leading edge shock loss is incorporated into the overall leading edge blocking calculation for development of suction surface. The technique used to calculate the magnitude of this correction is discussed in the following paragraphs.

Consider a streamtube of width $\overline{dy}_1$ at a distance $\overline{y}_1$ above the wedge centerline upstream of the shock. The shock angle, and hence the entropy rise of the fluid in the streamtube, can be calculated from eqs. (C-1) and (C-2).

Downstream of the shock, the streamtube is located at a normal distance y from the wedge and has the width dy. Since the streamtube flow area is proportional to streamtube width, and the shock pressure recovery, in terms of entropy rise, is

$$\frac{pt2}{pt1} = e^{-\frac{\Delta S}{R}} \qquad (C-13)$$

the relationship between streamtube widths upstream and downstream of the shock is as follows:

$$dy = \left[\frac{\left(\frac{A^*}{A}\right)_1}{\left(\frac{A^*}{A}\right)_2} \; e^{\frac{\Delta S}{R}} \right] dy_1 \qquad (C-14)$$

where the subscripts 1 and 2 refer to conditions before and after the shock, $(A/A^*)_1$ and $(A/A^*)_2$ are the A^*/A values corresponding to the upstream and downstream Mach numbers, respectively, and the exponential term accounts for the change in A^* across the shock. Eq. (C-14) is written as

$$dy = \Gamma \; dy_1 \qquad (C-15)$$

150

where Γ represents the term in brackets in eq. (C-14). The normal distance Y_a of any arbitrary streamtube above the wedge surface can then be determined by integrating eq. (C-15) from the wedge centerline to Y_{1a}, i.e.,

$$Y_a = \int_0^{Y_{1a}} \Gamma \, dy_1 \qquad (C-16)$$

The blockage associated with the shock losses in the vicinity of the leading edge is taken to be the difference, normalized by the leading edge radius, between Y_a for the real shock wave and Y_a (denoted Y_{ai}) for the idealized shock wave attached to an infinitely sharp wedge. Denoting this quantity as Y yields

$$Y = \frac{(Y_a - Y_{ai})}{r}$$

or

$$Y = \frac{1}{r} \int_0^{Y_{1a}^r} (\Gamma - \Gamma_i) \, dy_1 \qquad (C-17)$$

Since the suction surface wedge angle is zero, $\Gamma_i = 1$. Extending the upper limit of integrations to infinity yields, finally

$$Y = \frac{1}{r} \int_0^\infty (\Gamma - 1) \, dy_1 \qquad (C-18)$$

LEADING EDGE SHOCK BLOCKAGE--STREAMLINE NO. 4

Setting the wedge angle to zero and using the same inlet Mach number and leading edge radius, the calculated shock parameters for streamline No. 4 are as follows

$$M_1 = 1.502$$

$$\delta = 0$$

$$M_{2i} = 1.502$$

151

$$\sigma_{2i} = 41.74$$

$$\delta_m = 12.17$$

$$\delta_s = 11.75$$

$$\sigma_s = 62.24$$

$$\bar{x}_s = 1.133$$

$$\bar{Y}_s = 0.474$$

$$\bar{\ell} = 0.425$$

$$\bar{r} = 0.060$$

$$x_o = 0.121$$

$$x_c = 0.150$$

$$\Delta x = 0.029$$

It may be noted that despite the differences in the intermediate numbers, the shock standoff distance calculated for the upper and lower surfaces (δ = 0 deg and δ = 4.34 deg, respectively) are approximately the same. This at least provides some justification for treating the actual wedge of 4.34 deg at an angle of attack of 2.17 deg as a superposition of an 8.68-deg wedge and a 0-deg wedge, each at a 0-deg angle of attack.

The normalized shock blockage for the above shock as calculated by a 50-step numerical integration to the upper limit $5\,\bar{Y}_s$ is

$$Y_s = 0.332$$

The corresponding incidence angle correction to streamline no. 4 is

$$i_f = 0.17 \text{ deg}$$

152

APPENDIX D

CASCADE START MARGIN

TWO-DIMENSIONAL CASCADES

Experimental studies of high-solidity, two-dimensional cascades with supersonic inlet flow indicate that at high back pressures, such cascades, in general, operate with a strong normal shock on the suction surface forming a bow wave ahead of the leading edge of the adjacent blade. As the back pressure is reduced with inlet Mach number held constant, the incidence angle decreases and the suction surface shock moves aft. Continued reduction generally results in one of two possible occurrences: either the cascade chokes or the shock reaches the leading edge of the adjacent blade. In the latter case, further reduction of cascade back pressure causes the suction surface shock to "jump" past the effective throat of the cascade, and to be replaced by an oblique shock system in the leading edge region. When this phenomena occurs, the cascade is said to be operating in the "started mode." Prior to this occurrence, the cascade is operating in the "unstarted mode." Once the cascade starts, the incidence angle no longer changes with changes in cascade back pressure. The incidence angle at which start occurs (hereafter referred to as the "start incidence") is, in general, only a function of the inlet Mach number for a particular cascade. Further reductions in back pressure tend to draw the trailing edge normal shock out of the trailing edge region, and for sections which are similar in shape to the outboard rotor sections, this will result in fully supersonic operation of the cascade.

START MARGIN DEFINITION

In order to ensure the starting of a cascade operated in the manner described above, the cascade passages should be sufficiently open to allow the cascade to reach the start incidence without choking. The start margin is defined as the percentage by which the metal passage area exceeds the minimum allowable area. For calculating the start margin, the operating conditions closest to choke are assumed to occur with the cascade at start incidence with the unstarted inlet shock structure. This condition need not be the critical condition for cascades operating at high Mach numbers with low flow angles. The minimum allowable passage area in this case is simply the sonic area for conditions downstream of the inlet normal shock. In general, cascade experience indicates that start margins of 3 to 4 percent are adequate to insure starting. The distribution of that margin for rotor sections 1 to 8 is presented in fig. D-1.

In order to calculate the start margin for a particular cascade, it is necessary to determine the starting incidence angle and the Mach number into the passage inlet normal shock. An approximate expression for the start incidence angle and shock Mach number for the simple case of a two-dimensional cascade with a straight suction surface is derived below. The application of this approximate expression to the design of the rotor outboard sections is discussed later in this appendix.
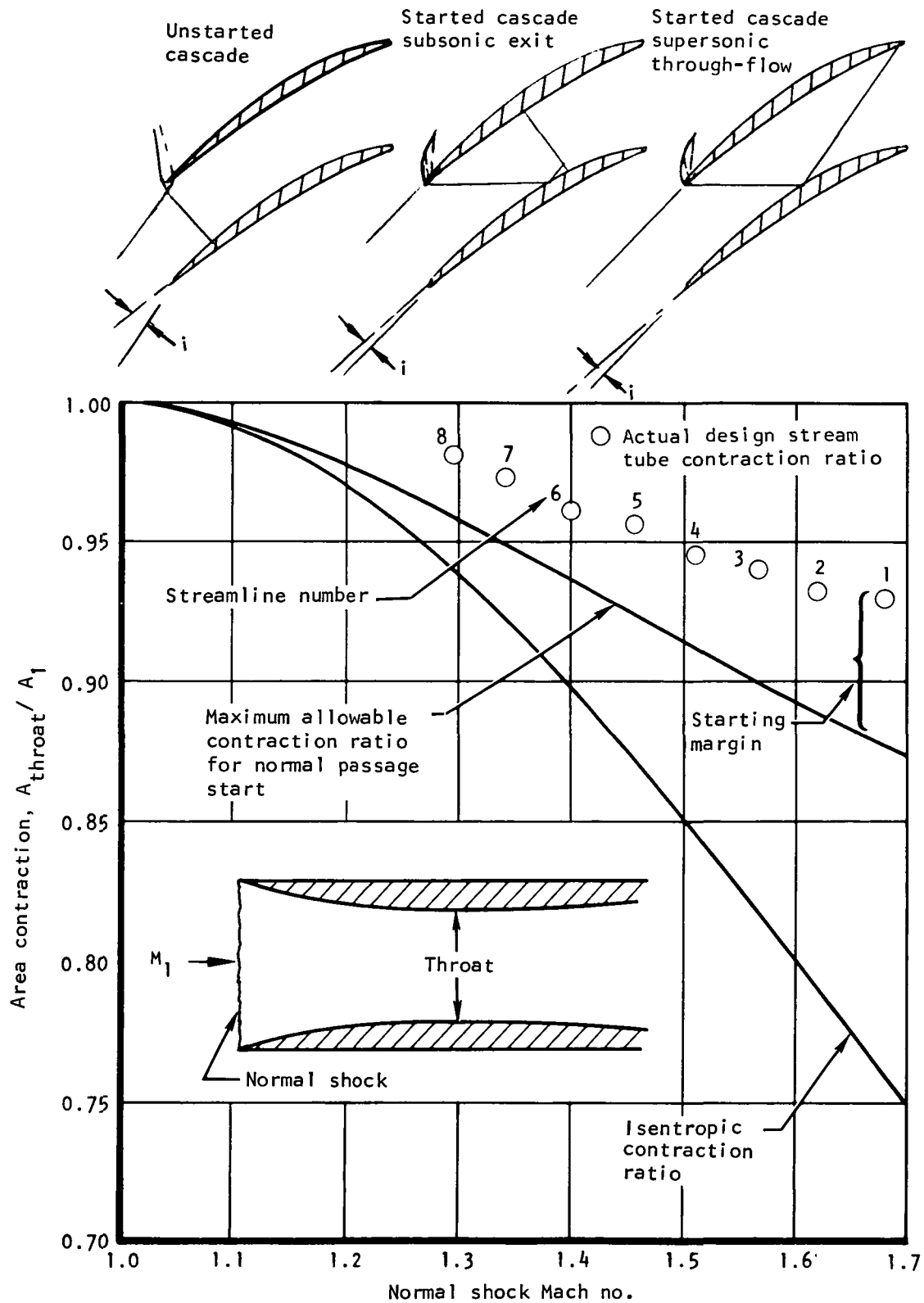
Figure D-1.--Start Margin.

S-71906

STARTING INCIDENCE

Consider the flow field for a started cascade with an external wave pattern as illustrated in fig. D-2. Let the upstream Mach number and flow angle be denoted as M_1 and β_1, respectively, and the corresponding quantities on the suction surface downstream of the wedges as M_s and β_s. The start incidence relative to the suction surface i_s is by definition

$$i_s = \beta_\infty - \beta_s \qquad\qquad (D-1)$$

for started flow. The corresponding suction surface Mach number (and hence the Mach number into the passage inlet in the unstarted mode) can be calculated approximately if the suction side bow wave losses are neglected

$$\nu_1 = \nu_\infty + i_s \qquad\qquad (D-2)$$

where ν is the Prandtl-Meyer expansion angle.

The upstream flow area per blade per unit span is given by

$$A_\infty = Y \cos \beta_\infty \qquad\qquad (D-3)$$

where Y is the cascade pitch. The passage inlet flow area per unit span is given by

$$A_I = Y \cos \beta_s - t \qquad\qquad (D-4)$$

where t is the suction surface metal blockage. The change in flow area normalized to the inlet area is therefore

$$\frac{A_I - A_\infty}{A_\infty} = \frac{\Delta A}{A_\infty} = \frac{Y \cos (\beta_\infty - i_s) - t}{Y \cos \beta_\infty} - 1 \qquad\qquad (D-5)$$

For small incidence angles such that $\cos i_s \approx 1$ and $\sin i_s \approx i_s$, this area change is approximately

$$\frac{\Delta A}{A_\infty} = (\tan \beta_\infty) i_s - \frac{t}{Y \cos \beta_\infty} \qquad\qquad (D-6)$$

Eq. (D-6) then relates, for a given cascade, the required starting area margin to the starting incidence with respect to the blade suction surface. From continuity requirements, the change in flow capability (induced by the change in Mach number) between the upstream and suction surfaces must equal the change in available flow area. It can be shown that for small values of

Leading edge
oblique shock

t

A_I

M_S

β_s

M_∞

β_∞

Upstream flow
conditions

S-72464
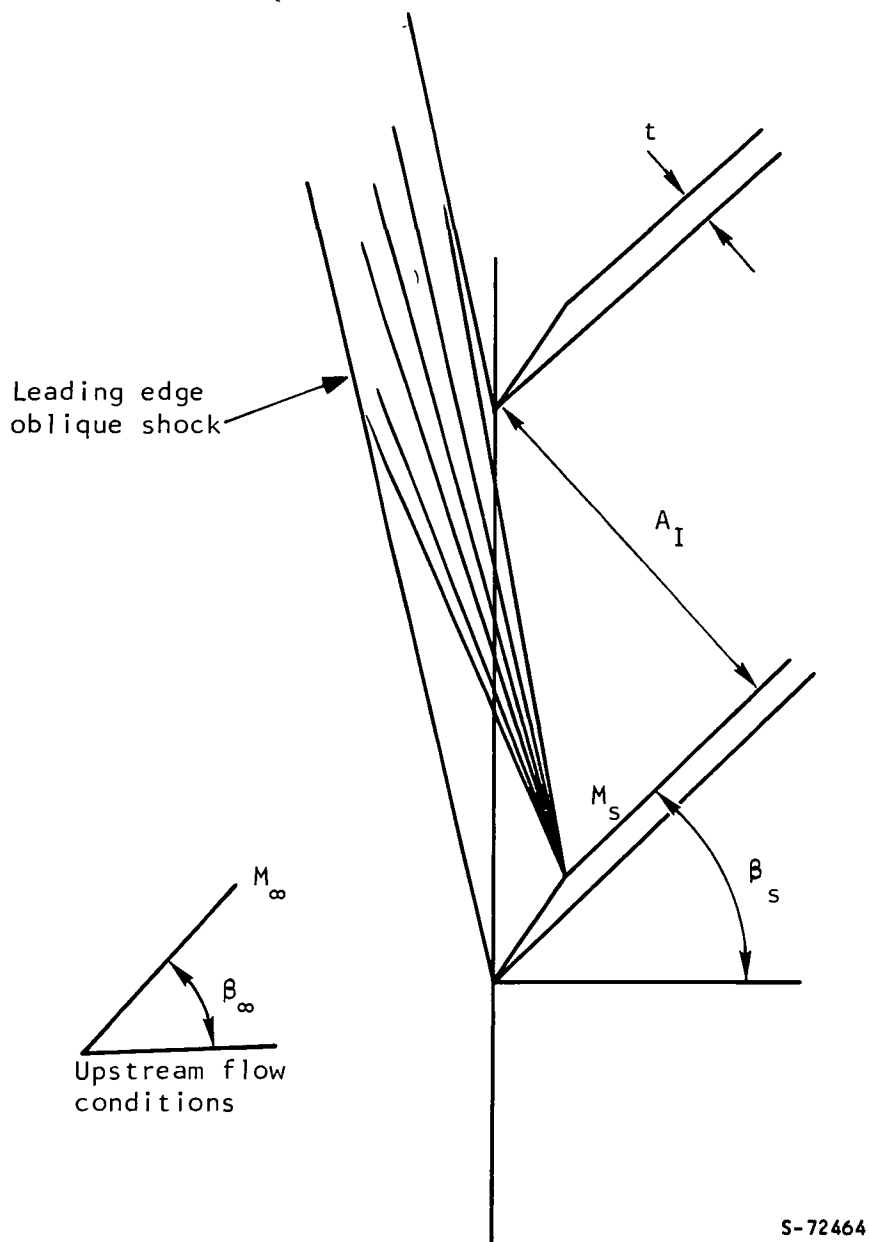
Figure D-2.--Leading Edge Region of a Single Two-Dimensional Cascade
with Straight Suction Surface in the Started Mode.

i_s and a weak oblique shock from the leading edge, the change in flow capacity is approximated by

$$\frac{\Delta A_f}{A_\infty} \approx i_s \sqrt{M_\infty^2 - 1} \qquad \text{(D-7)}$$

Eq. (D-7) then defines the approximate, required area margin in terms of the upstream Mach number for the fixed cascade. Equating eqs. (D-6) and (D-7) yields

$$i_s = \frac{\dfrac{t}{Y \cos \beta_\infty}}{\tan \beta_\infty - \sqrt{M_\infty^2 - 1}} \qquad \text{(D-8)}$$

THE OUTBOARD ROTOR SECTIONS

At the design point, the design intent is to have the outboard sections operating in the started mode, the upper central section operating in the started mode with a strong, second shock internally, and the lower central sections operating in the unstarted mode. Due to the expectation of a continuous leading edge shock surface, a gradual transition from started sections near the tip to unstarted sections near the hub is anticipated. There is no operating point analogous to this transition region in the two-dimensional cascade. The extent of this transition region, the manner in which it occurs, and the nature of the flow within it are questions that require further analytical and experimental investigations.

In addition to the structure of the leading edge wave pattern at specified speed and back pressure, the behavior of this wave pattern at a specified speed and varying back pressure is open to investigation. In particular, to determine if the transition region moves smoothly up and down the blade with varying back pressure, or "jumps" into and out of the rotor at certain critical values of back pressure with a consequent abrupt starting or unstarting of the tip section. The latter case would most probably be observable as a hysteresis phenomena in the fan operating map. Although this behavior has been looked for in many transonic and supersonic compressors, hysteresis of performance has not been observed. However, for entirely supersonic rotors there have been occasions where the sound level has made abrupt changes up and down.

Independent of whether smooth or abrupt transitions occur, a question exists as to whether the rotor sections require more or less start margin than the corresponding two-dimensional cascades. This question is significant in that the start margin is a major parameter in the design of the outboard sections. In the present rotor design, no benefit was assumed to accrue relative to start margin due to the three-dimensional nature of the rotor flow field.

The techniques used to calculate the start incidence and the corresponding start margin for the outboard section are discussed below.

SUCTION SURFACE DEVELOPMENT

The suction surface of the outboard rotor section as far aft as the first captured Mach line is developed by means of a direct analogy with the simplified two-dimensional cascade discussed previously. The corresponding simplified two-dimensional cascade quantities in the analogy are listed below.

(1) Straight suction surface aft of the leading edge wedge

(2) Flow conditions specified at upstream infinity

(3) Leading edge wedge blockage

(4) Uniform Mach number and flow conditions on the straight suction surface after correction for leading edge wedge blockage

Analogous three-dimensional section items in the analogy are given in the following list.

(1) Free streamline suction surface aft of the leading edge radius

(2) Calculated axisymmetric inlet conditions

(3) Leading edge radius and shock loss blockages

(4) Varying Mach number and flow conditions along the calculated free streamline after correction for leading edge radius and shock loss blockages

In setting the finite leading edge radius equivalent to the leading edge wedge blockage, it is assumed that the dividing streamline is parallel to the free streamline and, hypothetically, passes through the leading edge center. Consistent with this assumption, the suction surface thickness associated with the leading edge radius is set equal to the leading edge radius. The "leading edge shock blockage" refers to effective blockage associated with the detached position of the leading edge shock in the immediate vicinity of the leading edge radius. The technique used to calculate this blockage is presented in Appendix C.

The free streamline suction surface incidence is calculated as the sum of two incidence angles i_s and i_f. The former accounts for the leading edge radius blockage and is calculated by replacing t by $r_{L.E.}$ in eq. (D-8). The latter accounts for the shock blockage and is calculated as

$$i_f = Y \, i_s \qquad\qquad (D-9)$$

The technique used to calculate Y is discussed in Appendix C.

158

The total incidence correction is used to calculate the free streamline inlet Mach number.

In summary, a free streamline suction surface is used in an attempt to reduce the wave disturbances upstream of the section, with the free streamline flow condition specified in a manner which is (at least to a first approximation) consistent with started flow at the design point.

APPLICATION TO STREAMLINE NO. 4

For streamline no. 4, the inlet Mach number and flow angle are

$$M_1 = 1.479$$

$$\beta_1 = 62.85 \text{ deg} .$$

and the leading edge nose radius and leading edge pitch are

$$r = 0.0073 \text{ in. } (0.01854 \text{ cm})$$

$$Y = 2.13 \text{ in. } (5.41 \text{ cm})$$

The incidence correction i_s calculated from eq. (D-8) is 0.50; the shock blockage correction per eq. (D-9) for streamline no. 4 is

$$i_f = 0.17$$

and hence, the total incidence is

$$i_s + i_f = 0.67 \text{ deg}$$

The values of Mach number and flow angle used in the free streamline calculations are

$$M_{1 \text{ corr}} = 1.502$$

$$\beta_{1 \text{ corr}} = 62.17 \text{ deg}$$

The shock blockage correction was introduced into the blade calculation procedure via the incidence factor term discussed in the text. The actual value used in the calculation was 0.18 deg rather than the more correct value of 0.17 deg.

APPENDIX E

NOMENCLATURE

C   Chord, in. (cm)

D   Diffusion parameter

$$\text{rotor} = 1 - V_2'/V_1' + \frac{r_2 V_{\theta 2} - r_1 V_{\theta 1}}{(r_1 + r_2) V_1' \sigma}$$

$$\text{stator} = 1 - V_3/V_2 + \frac{r_2 V_{\theta 2} - r_3 V_{\theta 3}}{(r_2 + r_3) V_2 \sigma}$$

DCA   Double circular arc

f   Ratio of suction surface to total boundary

Layer displacement thickness

F_S Suction surface transition factor

F_P Pressure surface transition factor

Ft_u Ultimate tensile stress

Ft_y Tensile yield stress

g   Gravitational acceleration, ft/s^2 (m/s^2)

h   Radial height of stream tube, consistent units

H   Boundary layer form factor, δ^*/θ

i   Blade incidence angle, deg

i_f Section incidence correction due to inlet shock loss

i_s Section incidence correction due to leading edge thickness

j   Arbitrary index

ℓ Sonic line between leading edge radius and the bow wave

m   Meridional distance in radial-axial plane, in. (cm)

M   Mach number

MCA   Multiple circular arc

N   Rotational speed, rpm (rad/s)

P   Total pressure, psia (N/cm^2)

p   Static pressure, psia (N/cm^2)

Q   Loss parameter $e^{-\frac{\Delta S}{R}} = \dfrac{P_1/P_2}{(T_1/T_2)^{\gamma/\gamma-1}}$

Nb   Blade number

r   Radius, in. (cm)

R   Gas constant, ft-lb_f/lb_m-$^\circ$R (m-N/kg - $^\circ$K)

S   Entropy

T   Temperature, $^\circ$R ($^\circ$K)

t   Blade thickness, in. (cm)

$t_{m/C}$ Maximum thickness to chord ratio

U   Wheel tip speed, ft/s (m/s)

V   Absolute velocity, ft/s (m/s)

W   Airflow, lb/s (kg/s)

Y   Blade pitch, in. (m)

Z   Axial distance, in. (m)

α Streamline in radial-axial plane, deg

β Flow angle measured from meridional, deg

β_m Stagger angle, deg

β^*_{1ss} Inlet suction surface angle, deg

γ Ratio of specific heats, C_p/C_v

δ Ratio of total pressure to NASA standard sea level pressure of 14.696 psia (10.133 N/cm^2)

δ_1 Leading edge shock strength, deg

δ_2 Trailing edge shock strength, deg

δ_k Pressure surface kink angle, deg

δ_{TE} Trailing edge wedge angle, deg

δ^o Deviation angle with respect to blade metal mean camberline, deg

δ^* Displacement thickness, deg

δ^{**} Deviation angle with respect to envelope meanline, deg

ϵ Function characteristic equation

η Adiabatic efficiency

$$\text{rotor} = \frac{(P_2/P_1)^{\gamma-1/\gamma} - 1}{(T_2/T_1) - 1}$$

$$\text{stage} = \frac{(P_3/P_1)^{\gamma-1/\gamma} - 1}{(T_3/T_1) - 1}$$

λ Parameter modifying the subsonic section surface curvature distribution

μ Mach angle

ν Prandtl-Meyer expansion angle, deg

ξ^- Characteristic parameter, $\dfrac{\nu + \beta}{2}$

ξ^+ Characteristic parameter, $\dfrac{\nu - \beta}{2}$

ρ Fluid density, lb/ft^3 (kg/m^3)

σ Blade solidity

       = conical chord/blade spacing (based on average radius)

ϕ Streamline slope angle, deg

ω Angular velocity, rad/s

$\bar{\omega}$ Total pressure loss coefficient

$$\text{rotor} = \frac{(P_2')_{id} - P_2'}{P_1' - P_1}$$

$$\text{where } (P_2')_{id} = P_1' \left\{ 1 + \frac{\gamma-1}{2} \left(\frac{U_2^2}{a_{01}^2} \right) \left[1 - \left(\frac{r_1}{r_2} \right)^2 \right] \right\}^{\gamma/\gamma-1}$$

and a_{01} = upstream total acoustic velocity

$$\text{stator} = \frac{P_2 - P_3}{P_2 - P_2}$$

$\bar{\omega}_p$ Profile loss coefficient

$\bar{\omega}_s$ Shock loss coefficient

Subscripts

1   Rotor leading-edge station

2   Rotor trailing-edge, stator leading-edge station

3   Stator trailing-edge station

∞ Freestream just upstream of cascade

s, or ss   Suction surface

p   Pressure surface

fs   free stream

T   Tip

MCL   mean camber line

M   Meridional component

LE   Leading edge

TE   Trailing edge

ex   exit

θ Tangential component

z   Axial component

r   Radial component

Superscripts

*   Critical condition

**   Blade envelope parameter

'   Relative to rotating part

REFERENCES

1. Bogdonoff, Seymour M.: Some Experimental Studies of the Separation of Supersonic Turbulent Boundary Layers. AFOSTN-56-64, Report No. 336, ASTIA No. AD-81056, June 1955.

2. Chapman, Dean R.; Kuehn, Donald M.; and Larson, Howard K.: Investigation of Separated Flows in Supersonic and Subsonic Streams With Emphasis on the Effect of Transition. NACA TR-1356, 1958.

3. Monsarrat, N. T.; Keenan, M. J.; and Tramm, P. C.: Design Report Single-Stage Evaluation of Highly-Loaded High-Mach-Number Compressor Stages. NASA CR-72562 PWA-3546, July 16, 1969.

4. Erwin, John R.; Wright, Linwood C.; and Kantrowitz, Arthur: Investigation of an Experimental Supersonic Axial Flow Compressor. NACA RM L6J016, 1947.

5. Keenan, M. J.; and Bartok, J. A.: Experimental Evaluation of Transonic Stators - Final Report. NASA CR 72298, 1969.

6. Johnsen, I. A.; and Bullock, R. O.: Aerodynamic Design of Axial-Flow Compressors. NASA SP-36, 1965.

7. Wright, L.C., Schwind, R.: Throat-Area Determination for a Cascade of Double-Circular-Arc Blades. NACA RM E55H25a, 1955.

8. Department of Defense: Metallic Materials and Elements for Aerospace Vehicle Structures. MIL-HDBK-5B, 1 September 1971.

9. Wu Chung-Hua: A General Through-Flow Theory of Fluid Flow with Subsonic or Supersonic Velocity in Turbomachines of Arbitrary Hub and Casing Shapes. NACA TN-2302, March 1951.

DISTRIBUTION LIST

CONTRACT NAS3-13498

Copies

1. NASA-Lewis Research Center
   21000 Brookpark Road
   Cleveland, Ohio 44135

Attention:		Copies
Report Control Office	MS 5-5	1
Technical Utilization Office	MS 3-19	1
Library	MS 60-3	2
Fluid System Components Div.	MS 5-3	1
Compressor Branch	MS 5-9	5
Dr. B. Lubarsky	MS 3-3	1
R. S. Ruggeri	MS 5-9	1
M. J. Hartmann	MS 5-9	1
W. A. Benser	MS 5-9	1
D. M. Sandercock	MS 5-9	1
L. J. Herrig	MS 501-4	1
T. F. Gelder	MS 5-9	1
C. L. Ball	MS 5-9	1
L. Reid	MS 5-9	1
L. W. Schopen	MS 500-206	1
S. Lieblein	MS 501-5	1
C. L. Meyer	MS 60-4	1
J. H. Povolny	MS 60-4	1
C. H. Voit	MS 5-3	1
E. E. Bailey	MS 5-9	33

2. NASA Scientific and Technical Information Facility
   P. O. Box 33
   College Park, Maryland 20740
   Attention: NASA Representative   10

3. NASA Headquarters
   Washington, D. C. 20546
   Attention: N. F. Rekos (RLC)   1

4. U. S. Army Aviation Materiel Laboratory
   Fort Eustis, Virginia 23604
   Attention: John White   1

5. Headquarters
   Wright-Patterson AFB, Ohio 45433
   Attention: J. L. Wilkins, SESOS   1
                 S. Kobelak, APTP   1
                 R. P. Carmichael, SESSP   1

6. Department of the Navy
    Naval Air Systems Command
    Propulsion Division, AIR 536
    Washington, D. C.   20360   1

7. Department of Navy
    Bureau of Ships
    Washington, D. C.   20360
    Attention: G. L. Graves   1

8. NASA-Langley Research Center
    Technical Library
    Hampton, Virginia   23365
    Attention: Mark R. Nichols   1
                John V. Becker   1

9. The Boeing Company
    Commercial Airplane Group
    P. O. Box 3707
    Seattle, Washington   98124
    Attention: G. J. Schott, G-8410, MS 73-14   1

10. Douglas Aircraft Company
    3855 Lakewood Boulevard
    Long Beach, California   90801
    Attention: J. E. Merriman   1
                Technical Information Ctr. C1-250

11. Pratt & Whitney Aircraft
    Florida Research & Development Center
    P. O. Box 2691
    West Palm Beach, Florida   33402
    Attention: J. Brent   1
                H. D. Stetson   1
                W. R. Alley   1
                R. E. Davis   1
                R. W. Rockenbach   1
                B. A. Jones   1
                J. A. Fligg   1

12. Pratt & Whitney Aircraft
    400 Main Street
    East Hartford, Connecticut   06108
    Attention: R. E. Palatine   1
                T. G. Slaiby   1
                H. V. Marman   1
                M. J. Keenan   1
                B. B. Smyth   1
                A. A. Mikolajczak   1
                Library (UARL)   1
                W. M. Foley (UARL)   1

13. Allison Division, GMC
     Department 8894, Plant 8
     P. O. Box 894
     Indianapolis, Indiana 46206
     Attention: J. N. Barney   1
                 G. E. Holbrook   1
                 B. A. Hopkins   1
                 R. J. Loughery   1
                 Library   1
                 J. L. Dillard   1
                 P. Tramm   1

14. Northern Research and Engineering
     219 Vassar Street
     Cambridge, Massachusetts 02139
     Attention: K. Ginwala   1

15. General Electric Company
     Flight Propulsion Division
     Cincinnati, Ohio 45215
     Attention: J. W. Blanton J-19   1
                 W. G. Cornell K-49   1
                 D. Prince H-79   1
                 E. E. Hood/J. C. Pirtle J-165   1
                 J. F. Klapproth H-42   1
                 J. W. McBride H-44   1
                 L. H. Smith H-50   1
                 S. N. Suciu H-32   1
                 J. B. Taylor J-168   1
                 Technical Information Ctr. N-32   1
                 Marlen Miller H-50   1
                 C. C. Koch H-79   1

16. General Electric Company
     1000 Western Avenue
     Lynn, Massachesetts 01910
     Attention: D. P. Edkins - Bldg. 2-40   1
                 F. F. Ehrich - Bldg. 2-40   1
                 L. H. King   - Bldg. 2-40   1
                 R. E. Neitzel- Bldg. 2-40   1
                 Dr. C. W. Smith - Library -
                                 Bldg. 2-40M   1

17. Curtiss-Wright Corporation
     Wright Aeronautical
     Wood-Ridge, New Jersey 07075
     Attention: S. Lombardo   1
                 G. Provenzale   1

18. AirResearch Manufacturing Company
    402 South 36th Street
    Phoenix, Arizona 85034
    Attention: Robert O. Bullock   1
              Jack Erwin   - Dept. 32-1 - J   1
              Don Seyler   - Dept. 32-1 - J   1
              Jack Switzer - Dept. 32-1 - M   1
              G. L. Perrone   1

19. AiResearch Manufacturing Company
    2525 West 190th Street
    Torrance, California 90509
    Attention: R. Kobayashi   1
              Bob Carmody   1
              Library   1
              R. Jackson   1

20. Union Carbide Corporation
    Nuclear Division
    Oak Ridge Gaseous Diffusion Plant
    P. O. Box "P"
    Oak Ridge, Tennessee 37830
    Attention: R. G. Jordan   1
              D. W. Burton, K-1001, K-25   1

21. Avco Corporation
    Lycoming Division
    550 South Main Street
    Stratford, Connecticut 06497
    Attention: Clause W. Bolton   1

22. Teledyne Cae
    1330 Laskey Road
    Toledo, Ohio 43601
    Attention: Eli H. Benstein   1
              Howard C. Walch   1

23. Solar
    San Diego, California 92112
    Attention: P. A. Pitt   1
              J. Watkins   1

24. Goodyear Atomic Corporation
    Box 628
    Piketon, Ohio 45661
    Attention: C. O. Langebrake   2

25. Iowa State University of Science & Tech.
    Ames, Iowa 50010
    Attention: Professor George K. Serovy
                Dept. of Mechanical Engineering   1

26. Hamilton Standard Division of United
        Aircraft Corporation
    Windsor Locks, Connecticut 06096
    Attention: Mr. Carl Rohrback
                Head of Aerodynamics and
                    Hydrodynamics   1

27. Westinghouse Electric Corporation
    Small Steam and Gas Turbine Engineering B-4
    Lester Branch
    P. O. Box 9175
    Philadelphia, Pennsylvania 19113
    Attention: Mr. S. M. DeCorso   1

28. Williams Research Corporation
    P. O. Box 95
    Walled Lake, Michigan 48088
    Attention: J. Richard Joy
                Supervisor, Analytical Section   1

29. Lockheed Missile and Space Company
    P. O. Box 879
    Mountain View, California 94040
    Attention: Technical Library   1

30. The Boeing Company
    224 N. Wilkinson
    Dayton, Ohio 45402
    Attention: James D. Raisbeck   1

31. Chrysler Corporation
    Research Office
    Dept. 9000
    P. O. Box 1118
    Detroit, Michigan 48231
    Attention: James Furlong   1

32. Elliott Company
    Jeannette, Pennsylvania 15644
    Attention: J. Rodger Schields
                Director-Engineering   1

Copies

33. Dresser Industries Inc.
    Clark Gas Turbine Division
    16530 Peninsula Boulevard
    P. O. Box 9989
    Houston, Texas 77015
    Attention: R. V. Reddy   1

34. California Institute of Technology
    Pasadena, California 91109
    Attention: Prof. Duncan Rannie   1

35. Massachusetts Institute of Technology
    Cambridge, Massachusetts 02139
    Attention: Dr. J. L. Kerrebrock   1

36. Caterpillar Tractor Company
    Peoria, Illinois 61601
    Attention: J. Wiggins   1

37. Penn State University
    Department of Aerospace Engineering
    233 Hammond Building
    University Park, Pennsylvania 16802
    Attention: Prof. B. Lakshminarayana   1

38. Texas A&M University
    Department of Mechanical Engineering
    College Station, Texas 77843
    Attention: Dr. Meherwan P. Boyce P.E.   1